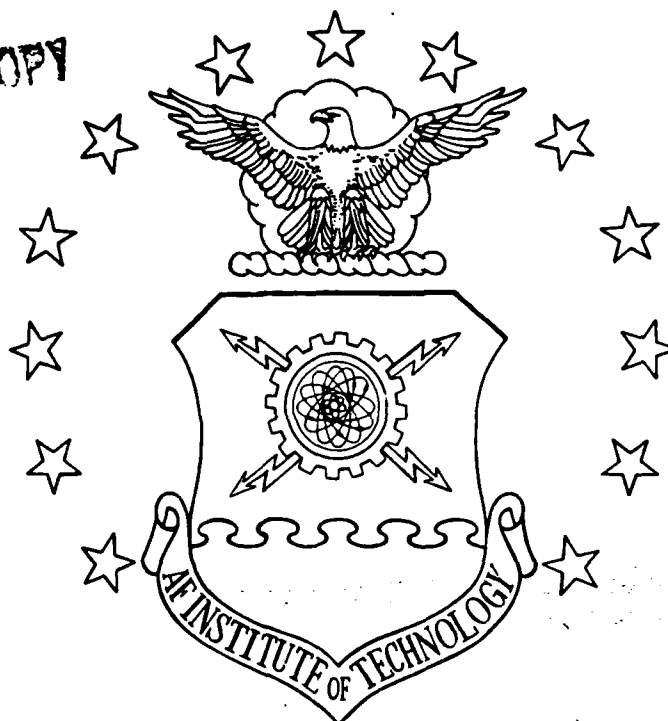


DTIC FILE COPY

AD-A216 378



INVESTIGATION OF COLLAPSE  
CHARACTERISTICS OF CYLINDRICAL COMPOSITE  
PANELS WITH LARGE CUTOUTS

THESIS

Scott A. Schimmels  
Captain, USAF

AFIT/GAE/ENY/89D-33

**DISTRIBUTION STATEMENT A**

Approved for public release  
Distribution Unlimited

DEPARTMENT OF THE AIR FORCE  
AIR UNIVERSITY

**AIR FORCE INSTITUTE OF TECHNOLOGY**

Wright-Patterson Air Force Base, Ohio

90 01 02 085

DTIC  
ELECTE  
JAN 03 1990

S

D

CS

29

1

DTIC  
ELECTE  
JAN 03 1990  
S D D

INVESTIGATION OF COLLAPSE  
CHARACTERISTICS OF CYLINDRICAL COMPOSITE  
PANELS WITH LARGE CUTOUTS

THESIS

Scott A. Schimmels  
Captain, USAF

AFIT/GAE/ENY/89D-33

Approved for public release, distribution unlimited

INVESTIGATION OF COLLAPSE  
CHARACTERISTICS OF CYLINDRICAL COMPOSITE  
PANELS WITH LARGE CUTOUTS

THESIS

Presented to the Faculty of the School of Engineering  
of the Air Force Institute of Technology  
Air University  
In Partial Fulfillment of the  
Requirements for the Degree of  
Master of Science in Aeronautical Engineering

Scott A. Schimmels  
Captain, USAF

December, 1989



Accession For	
NTIS	CRA&I <input checked="checked" type="checkbox"/>
DTIC	TAB <input type="checkbox"/>
Unannounced <input type="checkbox"/>	
Justification	
By	
Distribution /	
Availability Codes	
Dist	Avail and/or Special
A-1	

Approved for public release: distribution unlimited

## ACKNOWLEDGEMENTS

I wish to express my deepest thanks to Dr Anthony Palazotto for his patience, expertise, and wit as he guided me through and over all the roadblocks I managed to create for myself during this effort.

I would like to thank all the people of the Flight Dynamics Laboratory for assisting me in the completion of this thesis, with specials thanks to Jack Smith for making the panels and for Messrs. Don Cook and Larry Bates for running (and even re-running) the panel tests.

Many thanks to Kris Larsen and Jack Phillips for their patience with my lack of understanding of VMS, UNIX, and "What is a Cyber?"

To the gang in the Bullpen: Thanks to Zeke, Hoobs, Ralph, Kevin, Ray, Gene, Sid, "Papa" Papka, and the rest of the Aero/Astro gang for adding hilarity and a sense of reality to this adventure. By the way guys, the STAGS queue is free and clear for all to see.

Most of all, to my wife Jeanne. Without her love, patience, understanding, and support, my sanity would definitely be in question and you would not be reading this.

This thesis research is part of an overall effort in composite nonlinear shell analysis sponsored by AFOSR, Dr Anthony N. Palazotto principal investigator.

## TABLE OF CONTENTS

	Page
Acknowledgements.....	ii
List of Figures.....	v
List of Tables.....	xiii
List of Symbols.....	xiv
Abstract.....	xix
I. Introduction.....	1-1
1. Background.....	1-1
2. Objective.....	1-4
3. Scope.....	1-10
II. Theory Development.....	2-1
1. Strain-Displacement Relations.....	2-1
2. STAGSC-1 Theory.....	2-10
3. SHELL Theory.....	2-42
III. Experimental Methods.....	3-1
1. Manufacturing.....	3-1
2. Axial Compression.....	3-5
3. Residual Stress.....	3-16
IV. Finite Element Modeling.....	4-1
1. Panel Properties, Boundary Conditions....	4-1
2. Grid Selection.....	4-4
V. Results and Discussion.....	5-1
1. Analytical Results - STAGS.....	5-1
1) V Free vs V Fixed.....	5-2
2) Imperfections.....	5-11
3) Geometric Imperfections (Cutouts) & Eccentricity Effects.....	5-24
4) Boundary Conditions.....	5-35
5) Panel Geometry.....	5-44
2. Analytical Result - SHELL.....	5-54
3. Experimental Results.....	5-57
4. Residual Stress.....	5-87
VI. Conclusions.....	6-1
VII. Recommendations.....	7-1
VIII. Bibliography.....	8-1

Appendix A, Derivation of STAGC-1 Nonlinear Strain Displacement Equations.....	A-1
Appendix B, Derivation of 3-D Nonlinear Strain Displacement Equations.....	B-1
Appendix C, Variational Formulation.....	C-1
Appendix D, Classical Laminated Plate Theory.....	D-1
Appendix E, Anisotropic Thick Cylindrical Shell Theory.....	E-1
Appendix F, Derivation of the Tangent Stiffness Matrix.....	F-1
Appendix G, Using STAGSC-1.....	G-1
Appendix H, Miscellaneous Information.....	H-1
Vita.....	V-1

## LIST OF FIGURES

Figure		Page
1.1	Panel with Simply Supported Vertical Edges...	1-6
1.2	Panel with Unsupported Vertical Edges.....	1-7
1.3	Panel with 4" Cutout, Centered.....	1-8
1.4	Panel with 4" Cutout, Offset 1".....	1-9
2.1	Point M Located in 3-D Space by Position Vector $\bar{r}$ . Vector $d\bar{r}$ has length $ds$ .....	2-3
2.2	Segment MN Deforms to $M^*N^*$ Through Displacement Vector $u$ .....	2-7
2.3	Cylindrical Shell Section Showing Coordinate and Displacement Directions [17].....	2-13
2.4	Fiber Reinforced Lamina Definitions.....	2-18
2.5	STAGS 411 Quadrilateral Element [26].....	2-29
2.6	Flat Plate Element Representing a Curved Shell [42].....	2-31
2.7	Load Displacement Curve for Typical Cylindrical Panel.....	2-34
2.8	Quadrilateral Element Local Reference Systems [42].....	2-40
2.9	Cylindrical Shell Geometry [51].....	2-48
2.10	Basic Procedure for Modified Riks Method.....	2-67
3.1	Schematic of Cutting Support.....	3-2
3.2	Picture of Hole Cutting Support.....	3-3
3.3	Picture of Finished Product.....	3-4
3.4	Experimental Setup, Axial Compression.....	3-6
3.5	Close-up of Panel in Specialized Supports....	3-7
3.6	LVDT Positions, 8" Panel, No Cutout.....	3-9

3.7	LVDT Positions, 8" Panel, 4" Cutout, Centered.....	3-9
3.8	LVDT Positions, 8" Panel, 4" Cutout, 1" Offset.....	3-10
3.9	LVDT Positions, 12" Panel, No Cutout.....	3-10
3.10	LVDT Positions, 12" Panel, 4" Cutout, Centered.....	3-11
3.11	LVDT Positions, 12" Panel, 4" Cutout, 1" Offset.....	3-11
3.12	Strain Gage Positions, Panels with Cutouts...	3-13
3.13	Strain Gage Positions, Panels without Cutouts.....	3-14
3.14	Load vs Strain, Collapse of Solid Panel.....	3-15
3.15	Strain Rosette Positions, Front View.....	3-17
3.16	Strain Rosette Positions, Rear View.....	3-18
3.17	Picture of Panel Before Cutting Process.....	3-19
3.18	Picture of Panel Cutting Process.....	3-20
3.19	Picture of Panel, After Removing Cutout, Unloaded.....	3-21
4.1	Properties for Composite Panels.....	4-2
4.2	STAGS QUAF 411 Element [26].....	4-6
4.3	STAGS Grid for 8" Panel, No Cutout.....	4-7
4.4	STAGS Grid for 8" Panel, Centered Cutout.....	4-8
4.5	STAGS Grid for 8" Panel, Offset Cutout.....	4-9
4.6	STAGS Grid for 12" Panel, Centered Cutout....	4-10
4.7	SHELL 36 DOF Element.....	4-11
4.8	SHELL Grid for 1/4 8" Panel, No Cutout.....	4-12
4.9	SHELL Grid for 1/4 8" Panel, Centered Cutout.	4-12



4.10	SHELL Grid for 1/4 8" Panel, Offset Cutout...	4-13
4.11	Half Model for SHELL Incorporating Course Mesh.....	4-23
4.12	Full Model for SHELL Incorporating Course Mesh.....	4-14
5.1	Equilibrium Load Distribution along Top of Solid Panel at Collapse.....	5-3
5.2	Equilibrium Load Distribution along Top of 4" Cutout Panel at Collapse.....	5-3
5.3	Load Displacement, v Free and Fixed, 12" Panel, Experimental Results Compared.....	5-5
5.4	Load Displacement, v Free and Fixed, 8" Panel, Experimental Results Compared.....	5-6
5.5	Radial Displacement Contour, 12" Wide Panel, No Cutout, v Free, Total Load = 4754 lbs (100% of Collapse Load).....	5-7
5.6	Radial Displacement Contour, 12" Wide Panel, No Cutout, v Fixed, Total Load = 5060 lbs (100% of Collapse Load).....	5-8
5.7	Radial Displacement Contour, 8" Wide Panel, No Cutout, v Free, Total Load = 3174 lbs (100% of Collapse Load).....	5-9
5.8	Radial Displacement Contour, 8" Wide Panel, No Cutout, v Fixed, Total Load = 3761 lbs (100% of Collapse Load).....	5-10
5.9	Load Displacement, 12" Simply Supported Panel, Comparing Perfect vs Imperfection.....	5-14
5.10	Load Displacement, 8" Simply Supported Panel, Comparing Perfect vs Imperfection.....	5-15
5.11	Load-Displacement, 12" Unsupported Panel, Comparing Perfect vs Imperfection.....	5-16
5.12	Load-Displacement, 8" Unsupported Panel, Comparing Perfect vs Imperfection.....	5-17

5.13	Raidal Displacement Contour, 12" Wide Panel No Cutout, Simply Supported, No Imperfection Total Load = 5060 lbs (100% of Collapse Load).....	5-19
5.14	Radial Displacement Contour, 12" Wide Panel No Cutout, Simply Supported, Imperfection Total Load = 5060 lbs (100% of Collapse Load).....	5-20
5.15	Radial Displacement Contour, 8" Wide Panel No Cutout, Simply Supported, No Imperfection Total Load = 5060 lbs (100% of Collapse Load).....	5-21
5.16	Radial Displacement Contour, 8" Wide Panel No Cutout, Simply Supported, Imperfection Total Load = 5060 lbs (100% of Collapse Load).....	5-22
5.17	Load-Displacement, 12" Simply Supported Panel, Comparing Geometric Imperfections.....	5-26
5.18	Load-Displacement, 8" Simply Supported Panel, Comparing Geometric Imperfections.....	5-27
5.19	Load-Displacement, 12" Unsupported Panel, Comparing Geometric Imperfections.....	5-28
5.20	Load-Displacement, 8" Unsupported Panel, Comparing Geometric Imperfections.....	5-29
5.21	Bifurcation/Nonlinear Collapse Load for Varying Cutout Sizes and Locations.....	5-31
5.22	Values of $N_x$ Along Side of Cutout, 12" Simply Supported Panel.....	5-32
5.23	Values of $N_x$ Along Side of Cutout, 8" Simply Supported Panel.....	5-34
5.24	Load-Displacement, 12" Panels, No Cutout.....	5-36
5.25	Load-Displacement, 12" Panels, 4" Cutout, Centered.....	5-37
5.26	Load-Displacement, 12" Panels, 4" Cutout, 1" Offset.....	5-38

5.27	Load-Displacement, 8" Panels, No Cutout.....	5-39
5.28	Load-Displacement, 8" Panels, 4" Cutout, Centered.....	5-40
5.29	Load-Displacement, 8" Panels, 4" Cutout, 1" Offset.....	5-41
5.30	Comparing Simply Supported/Unsupported Panels	5-43
5.31	Load-Displacement, Simply Supported Panels with No Cutout.....	5-46
5.32	Load-Displacement, Simply Supported Panels with 4" Cutout, Centered.....	5-47
5.33	Load-Displacement, Simply Supported Panels with 4" Cutout, 1" Offset.....	5-48
5.34	Load-Displacement, Unsupported Panels with No Cutout.....	5-49
5.35	Load-Displacement, Unsupported Panels with 4" Cutout, Centered.....	5-50
5.36	Load-Displacement, Unsupported Panels with 4" Cutout, 1" Offset.....	5-51
5.37	Comparing 12"/8" Panels for Similar Boundary Conditions and Geometric Imperfections.....	5-53
5.38	Load-Displacement, 8" Panel, Unsupported with 4" Cutout, Centered.....	5-56
5.39	Load-Displacement, 12" Panel, Simply Supported, No Cutout.....	5-58
5.40	Load-Displacement, 12" Panel, Simply Supported, 4" Cutout, Centered.....	5-59
5.41	Load-Displacement, 12" Panel, Simply Supported, 4" Cutout, 1" Offset.....	5-60
5.42	Load-Displacement, 8" Panel, Simply Supported, No Cutout.....	5-61
5.43	Load-Displacement, 8" Panel, Simply Supported, 4" Cutout, Centered.....	5-62

5.44	Load-Displacement, 8" Panel, Simply Supported, 4" Cutout, 1" Offset.....	5-63
5.45	Load-Displacement, 12" Panel, Unsupported, No Cutout.....	5-64
5.46	Load-Displacement, 12" Panel, Unsupported, 4" Cutout, Centered.....	5-65
5.47	Load-Displacement, 12" Panel, Unsupported, 4" Cutout, 1" Offset.....	5-66
5.48	Load-Displacement, 8" Panel, Unsupported, No Cutout.....	5-67
5.49	Load-Displacement, 8" Panel, Unsupported, 4" Cutout, Centered.....	5-68
5.50	Load-Displacement, 8" Panel, Unsupported, 4" Cutout, 1" Offset.....	5-69
5.51	STAGS/Experimental Collapse Ratios for 12" Simply Supported Panels.....	5-73
5.52	STAGS/Experimental Collapse Ratios for 8" Simply Supported Panels.....	5-74
5.53	STAGS/Experimental Collapse Ratios for 12" Unsupported Panels.....	5-75
5.54	STAGS/Experimental Collapse Ratios for 8" Unsupported Panels.....	5-76
5.55	Picture of 12" Simply Supported Panel with 4" Cutout, Centered Prior to Collapse Snap - Through.....	5-79
5.56	Pictures of 12" Simply Supported Panel with 4" Cutout, Centered After Collapse Snap - Through.....	5-80
5.57	Picture of 12" Unsupported Panel with No Cutout, Centered Prior to Collapse Snap - Through.....	5-81
5.58	Picture of 12" Unsupported Panel with No Cutout, Centered After Collapse Snap - Through.....	5-82

5.59	Picture of 12" Unsupported Panel with 4" Cutout, Centered Prior to Collapse Snap - Through.....	5-83
5.60	Pictures of 12" Unsupported Panel with 4" Cutout, Centered After Collapse Snap - Through.....	5-84
5.61	Picture of 8" Unsupported Panel with 4" Cutout, Centered Prior to Collapse Snap - Through.....	5-85
5.62	Pictures of 8" Unsupported Panel with 4" Cutout, Centered After Collapse Snap - Through.....	5-86
5.63	Circumferential Stress Near Cutout Edge at Collapse as Compared to Stress Change Measured.....	5-89
5.64	Schematic of Residual Stress Test Showing Placement of Strain Rosettes.....	5-90
5.65	Circumferential Stress Near Cutout Edge at Collapse as Compared to Stress Change Measured.....	5-93
A.1	Line Element in Undeformed and Deformed State [26].....	A-3
B.1	Shell Panel Coordinates and Degrees of Freedom.....	B-2
B.2	Transverse Shear Strain Models.....	B-4
D.1	Coordinate Systems, Displacements, and Force and Moment Resultants.....	D-2
D.2	Principal (x,y,z) and Material (1,2,3) Axis Systems.....	D-5
D.3	Geometry of an N-Layered Laminate [45].....	D-6
E.1	Lamina Material Coordinates.....	E-2
E.2	Arbitrary Lamina Coordinates.....	E-5
E.3	Geometry of an N-Layered Laminate [45].....	E-8

G.1	Typical Command File for Batch Execution.....	G-1
G.2	VMS Syntax for Submitting Batch File.....	G-2
G.3	Input Deck for 12x12 Panel, Simply Supported, No Cutout.....	G-3
G.4	Input Deck for 12x12 Panel, Simply Supported, 4" Cutout, Centered.....	G-4
G.5	Input Deck for 12x12 Panel, Simply Supported, 4" Cutout, 1" Offset.....	G-5
G.6	Input Deck for 8x12 Panel, Simply Supported, 4" Cutout, Centered.....	G-6
G.7	Input Deck for 12x11 Panel, Unsupported, 4" Cutout.....	G-7
G.8	Input Deck for 8x11 Panel, Unsupported, 4" Cutout.....	G-8
G.9	Input Deck for 12x12 Panel, Simply Supported, No Cutout, with Imperfection.....	G-9
G.10	Input Deck for 12x12 Panel, Simply Supported, No Cutout, with V Free.....	G-10
G.11	Typical Command File for Batch Restart.....	G-11
G.12	Modified Control File for Restart Execution..	G-12

## LIST OF TABLES

Table		Page
2.1	Contracted Notation for STAGS.....	2-17
2.2	SHELL Contracted Notation.....	2-49
3.1	Experimental Test Plan.....	3-2
5.1	Results by Comparing Perfect vs Imperfect Panels.....	5-13
5.2	Panel Results by Comparing Boundary Conditions.....	5-42
5.3	Panel Results by Comparing Panel Geometry	5-52
5.4	Comparing SHELL Models with Coarse Mesh Size (1" Elements) vs Experimental Results.....	5-55
5.5	Comparing SHELL Models with Half Mesh Size (1/2" Elements) vs Experimental Results.....	5-55
5.6	Panel Results by Comparing Experiment vs STAGS.....	5-71
H.1	Individual Panel Results - STAGS - Collapse Load, lbs.....	H-1
H.2	Individual Panel Results - STAGS - Top Edge Displacement, in.....	H-2
H.3	Individual Panel Results - SHELL - Collapse Load, lbs.....	H-3
H.4	Individual Panel Results - SHELL - Top Edge Displacement, in .....	H-3
H.5	Individual Panel Results - Experimental..	H-4

# LIST OF SYMBOLS

$a_i, a_r, a_s$	Displacement Vectors
$A_{ij}$	Extensional Stiffness Matrix
$A_{rs}$	STAGS Constant Stiffness Matrix
$B_{ij}$	Coupling Stiffness Matrix
$ds, ds^*$	Differential Length of Line Segment, Deformed Differential Length
$dx, dx^*$	Differential Length in X-direction, Deformed Differential Length
$dy, dy^*$	Differential Length in Y-direction, Deformed Differential Length
$D_{ij}$	Bending Stiffness Matrix
$d_{ij}, d_{ijk}, d_{ijkl}$	Elements of Elasticity Tensor
DOF	Degrees of Freedom
$E_1$	Longitudinal Modulus of Elasticity
$E_2$	Transverse Modulus of Elasticity
$f_r(q_r)$	Error Function
$g_{ij}$	Metric Tensor - Cylindrical Coordinates
$G_{12}, G_{13}, G_{23}$	Torsional Moduli of Elasticity
$G_{ij}$	Metric Tensor - Cartesian Coordinates
$h_i$	Shape Factors
J	Jacobian
K	SHELL Constant Stiffness Matrix
$M_x, M_y, M_{xy}$	Moment Resultants
$N_x, N_y, N_{xy}$	Force Resultants



$N_1$	SHELL Linear Dependent Stiffness Matrix
$N_2$	SHELL Quadratic Dependent Stiffness Matrix
$N1_{rs}$	STAGS Linear Dependent Stiffness Matrix
$N2_{rs}$	STAGS Quadratic Dependent Stiffness Matrix
$P$	Applied Load Vector
$Q_{ij}$	Reduced Stiffnesses
$\bar{Q}_{ij}$	Transformed Reduced Stiffness
$\bar{r}$	Position Vector
$R_x, R_y$	Principal Radii of Curvature
$R_u, R_v, R_w$	Rotations about x, y, and z axes
$t$	Panel Thickness
$t_{ij}$	Tangential Displacement DOF
$u, v, w$	Displacements in x, y, and z directions
$U, U_1, U_2$	Internal Strain Energy
$V$	Total Potential Energy
$W$	Work of Applied Forces
$X, Y, Z$	Spacial Coordinates
$X', Y', Z'$	Shell Coordinates
$z$	Transverse Nodal Displacements
$Z_n$	Distance from Midplane
$1, 2$	Fiber, Transverse Directions (Laminate)
$\alpha_\gamma$	Square Root of Metric Tensor
$\delta$	First Variation
$\delta^2$	Second Variation

$\epsilon_i$	Normal Strain
$\epsilon_i^o$	Normal Strain at the Midplane
$\gamma$	Shear Strain
$\chi_x, \chi_y, \chi_z$	Curvatures
$\chi_j^i$	Curvature Terms in Eqn (2.72)
$\chi_{ip}$	Curvature Terms in Eqn (2.73)
$\eta$	Isoparametric Coordinate
$\xi$	Isoparametric Coordinate
$\mu$	Micro ( $10^{-6}$ )
$\nu_{12}$	Poisson's Ratio
$\nu_{21}$	Poisson's Ratio
$\Omega$	Shell Middle Surface
$\Pi_p$	Potential Energy
$\phi$	Rotational Terms
$\lambda_i$	Load Fraction for Solution Step i
$\phi_1, \phi_2$	Higher Order Shear Terms for SHELL Strain-Displacement Relations
$\theta$	Opening Angle of Cylindrical Panel Arc
$\theta_1, \theta_2$	Higher Order Shear Terms for SHELL Strain-Displacement Relations
$\theta_x, \theta_y, \theta_z$	Rotations about the Subscript Axis
$\sigma$	Normal Stress
$\tau$	Shear Stress
$\Delta s$	Increment along Equilibrium Path for Riks Solver
[A] - [T]	Elasticity Arrays in Eqns (2.80) and

(2.81)

[B]	Product of [L] and [N]
[D]	Material Matrix
[K]	Stiffness Matrix
[L]	Differential Operator Matrix
[N]	Shape Functions
[R]	Matrix of Derivatives
[B <sub>0</sub> ]	Constant [B] Matrix
[B <sub>L</sub> ]	[B] Matrix which is Function of Displacements
[K <sub>0</sub> ]	Linear Portion of Stiffness Matrix
[K <sub>L</sub> ]	Nonlinear Portion of Stiffness Matrix
[K <sub>T</sub> ]	Tangent Stiffness Matrix
[K <sub>σ</sub> ]	Initial Stress Matrix
(a)	Vector of Displacements
(ε)	Vector of Strains
(σ)	Vector of Stresses
(θ)	Matrix of Derivatives
(Ψ)	Sum of External and Internal Generalized Forces
[Ψ(a)]	Sum of External and Internal Generalized Forces as a Function of Displacement
(ε <sub>0</sub> ), (σ)	Vectors of Initial Strain and Stress, Respectively
(ξ)	Generalized Vector of ε Terms
(ξ <sup>0</sup> )	Generalized Vector of ε <sup>0</sup> Terms
[X]	Generalized Matrix of Curvature Terms, x

( $\mathbf{z}$ )

Generalized Vector of Nodal  
Displacements,  $\mathbf{z}$

Subscript "e" indicates element reference

Subscript "g" indicates global reference

Superscript "b" indicates bending terms

Superscript "p" indicates in-plane terms

Superscript "o" indicates midsurface value

( $\cdot$ )<sub>i</sub> indicates derivative with respect to  $i$

ABSTRACT

In order to better understand the collapse properties of composite shells, an analysis of cylindrical panels with large cutout (11% and 16.7%) with simply supported and unsupported (free) vertical edges is conducted using two finite element programs (STAGSC-1 and SHELL). Cutouts, their locations, boundary conditions, and panel width are varied to see how each affected the collapse load. In addition, the shape and magnitude of the residual strain due to placing the cutout in the panel is evaluated.

It is found that the panel collapses at lower load (a reduction of 50-80%) when a cutout is introduced, if the vertical supports are removed, or if the panel width is reduced. The panel collapses at higher loads (an increase of 3-10%) when eccentricity (17%-25%) in cutout location is introduced. Initial imperfections in the solid panels create a reduced panel stiffness which reduces the collapse load. The new version of STAGS (1986) is seen to accurately predict panel response in terms of load and displacement. SHELL incorporates through-the-thickness shear which reduces panel stiffness and gives closer approximation of experimental results than STAGS. It was determined that if the cylindrical composite panel undergoes rotations of greater than  $15-17^\circ$ , or displacements larger than five times the panel thickness, transverse shear effects must be addressed in the

analytical model(s). This requires using the SHELL code to accurately predict panel response for axial compression. If the panel does not undergo such rigorous displacements and/or rotations, then STAGSC-1 code will give accurate predictions. The STAGSC-1 code is adequate for all the models considered, but does not incorporate a transverse shear strain model. Hence, the rationale for incorporating SHELL within this research effort. Residual stress does exist when a cutout is introduced to the panel. This stress is significant ( $\approx 750$  psi) but does not dominate the panel's response when compared to the effect of geometric imperfections.

INVESTIGATION OF COLLAPSE  
CHARACTERISTICS OF CYLINDRICAL COMPOSITE  
PANELS WITH LARGE CUTOUTS

1. INTRODUCTION

1.1 Background

Large, lightweight shell structures are used extensively in aircraft for both strength and stability. These shell structures are greatly influenced by either reinforced or non-reinforced cutouts, cutout eccentricity, and mixed boundary conditions. Due to these influences and with recent advances, a vast number of these shells are made from composite materials. These composite materials are desired primarily due to the ability of the designer to tailor the material properties in a structure to withstand the load environment. This material tailoring leads to, in general, a lighter structure than similar metal structures thereby reducing the overall weight of a system; a critical factor in aerospace design. Therefore, from a practical point of view, there is a need to further research into composite shell structures and the effect of cutouts, cutout eccentricity and boundary conditions on the stability of shell structures.

The basic area of work on shells is very broad. A good portion of this work deals with geometrically linear problem solving. Ugral [1] shows a basic layout of linear shell theory. Other works such as Saada [2], Sanders [3] and Leissa [4] deal with shells from a nonlinear point of view.

Very few references can be found dealing with buckling of composite shell structures (such as panels or plates) under axial compression with cutouts. In contrast, numerous studies have been carried out on isotropic plates and cylindrical panels without cutouts [5-10]. These studies center around various boundary conditions and their affect on the buckling load. If one considers the area of axially loaded isotropic panels with cutouts [11-15], mainly, panels with centered circular cutouts were analyzed numerically by finite difference techniques to determine the buckling and bifurcation loads.

As mentioned earlier, composite panels are an important part of aerospace structures due to their excellent strength-to-weight and stiffness-to-weight ratios. Composite cylindrical panels without cutouts have been studied [16-20], but very little work can be found in dealing with composite panels with cutouts. Janisse [21], Lee [22], Hermesen [23], Dennis [24], and Knight and Starnes [30-31] are authors who have studied the problem of cutouts in composite cylindrical panels. Janisse [21] found that



the collapse characteristics of composite cylindrical panels are dependent upon ply lay up and size of the cutout. Lee [22] studied the effects of the cutout aspect ratio and concluded that as the surface area of the cutout increased the buckling load decreased with the effects of nonlinearity becoming more pronounced. Hermesen [23] concluded that eccentricity of small cutouts will reduce the buckling load and that the larger cutouts induce nonlinear response throughout the entire loading range. Dennis [24] developed a two-dimensional shell theory completely described by orthogonal curvilinear coordinates. This theory encompasses large displacement and rotational geometric nonlinearity for small strain situations. Additionally, the theory includes a parabolic transverse shear stress and strain distribution through the shell thickness. Linneman [25] has an excellent presentation of the theoretical development of anisotropic cylindrical shell theory and the corresponding equations of motion and appropriate boundary conditions.

With the ever increasing capability of the modern computer, many shells are analyzed numerically. Most of the recent computer work is finite element based. Cook [26] has a very well written section on nonlinear solution techniques while the Structural Analysis for General Shells (STAGS) theory manual [27] and Zienkiewicz [28] have sections that deal specifically with shells and geometrically nonlinear

finite element solutions.

Other references are concerned with experimental research on composite shell structures. This is of particular importance in order to validate closed form and finite element solutions. References in this area include works by Lee [29], Tisler [32-35], and Egan [36-37].

This thesis addresses all of these aspects of composite shells and includes three aspects that are not well documented. These three aspects incorporate nonlinear analysis with experimental testing. One aspect relates to the comparison of the shell's response to axial loading when the vertical edges are completely unsupported as compared to simply supported edges, thereby increasing large geometric displacement and rotational nonlinearity. Another aspect is investigating the eccentricity (17-25%) of large cutouts (11-17% reduction in surface area) and the combining this effect with various boundary conditions. The final aspect relates to the experimental determination of residual stress generated by removing large cutouts and analytically determining the effect this residual stress has on the buckling characteristics. There is very little documentation on laminated cylindrical shells in the areas considered by this thesis.

## 1.2 Objectives

The major purpose of this thesis is determining if a nonlinear finite element analysis of a laminated cylindrical shell produces results that correlate well with results from experimentally tested panels. The program(s) used to do this analysis are (1) the Structural Analysis for General Shells (STAGSC-1) computer program (1986 version) and (2) Dennis' [24,40-41] two-dimensional theory (SHELL) that incorporates a parabolic transverse shear strain energy distribution through the thickness. The shell(s) are axially loaded with an external distributed load along the top surface.

The second purpose is investigating the effect of various boundary conditions, simple supported vs unsupported vertical edges, (see Figs 1.1 and 1.2), and eccentricity of the cutout location to the shells' collapse characteristics (Figs 1.3 and 1.4), and determine what effect transverse shear strain energy has during large geometric displacement and/or rotations.

A third purpose is comparing analytical and experimental results. The final purpose is a residual stress analysis. This analysis is concerned with determining the magnitude and shape of the stress when removing the cutout, then determining the effect of this stress to the

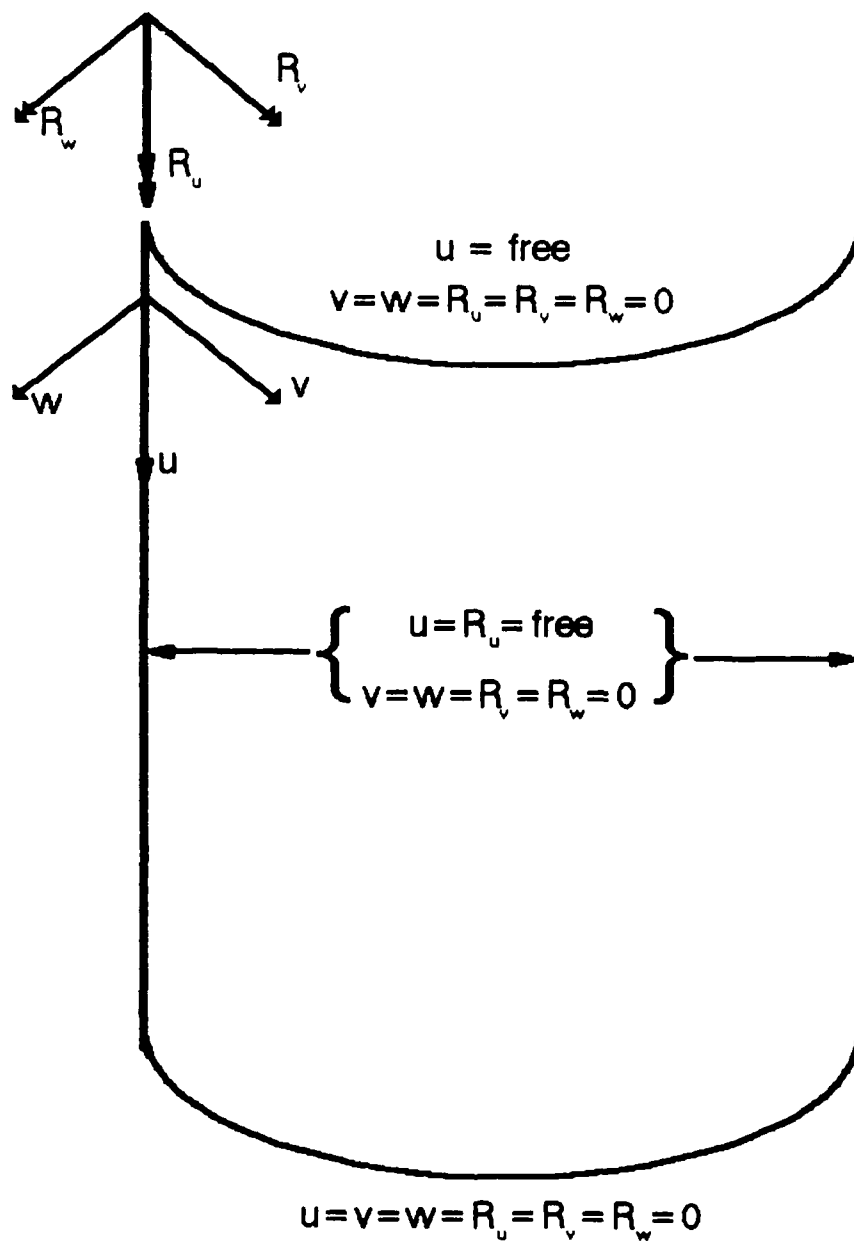


Fig 1.1 Panel with Simply Supported Vertical Edges

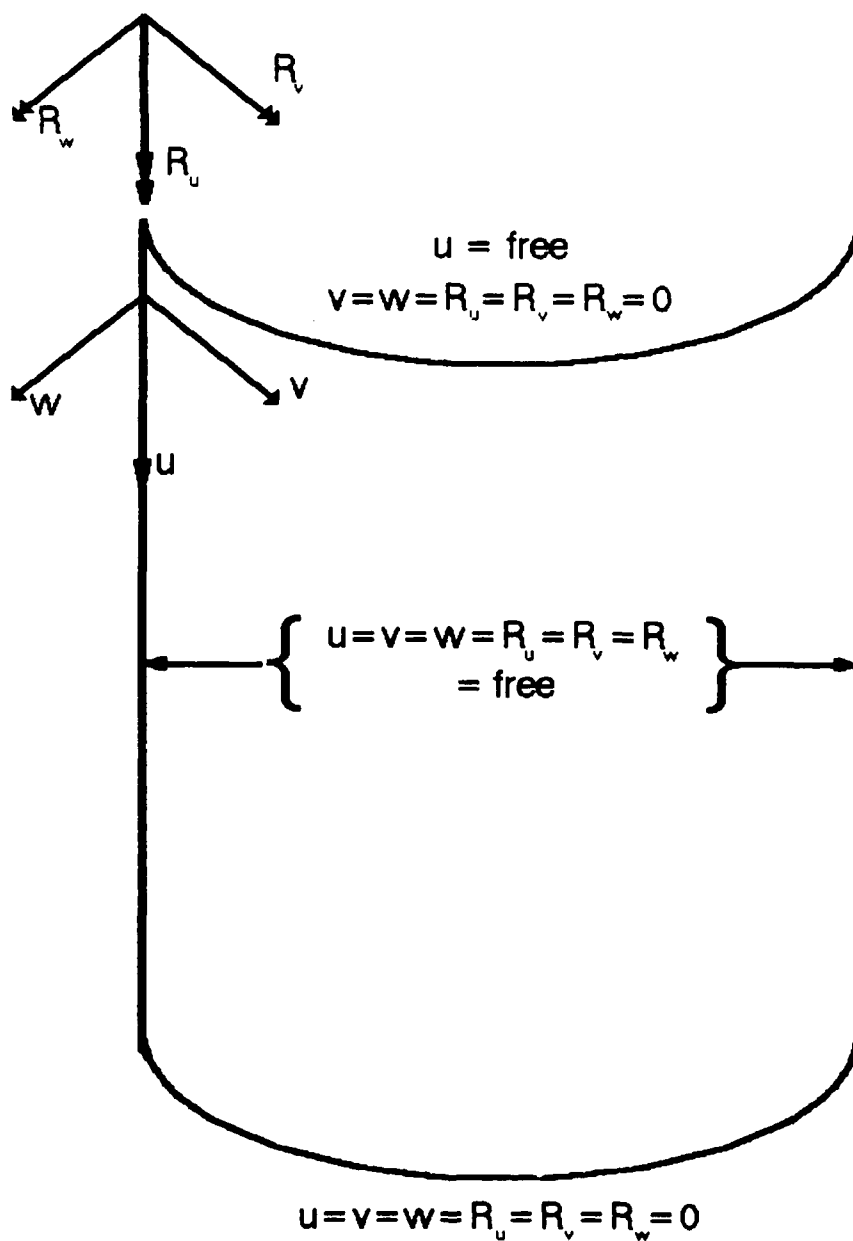


Fig 1.2 Panel with Unsupported Vertical Edges

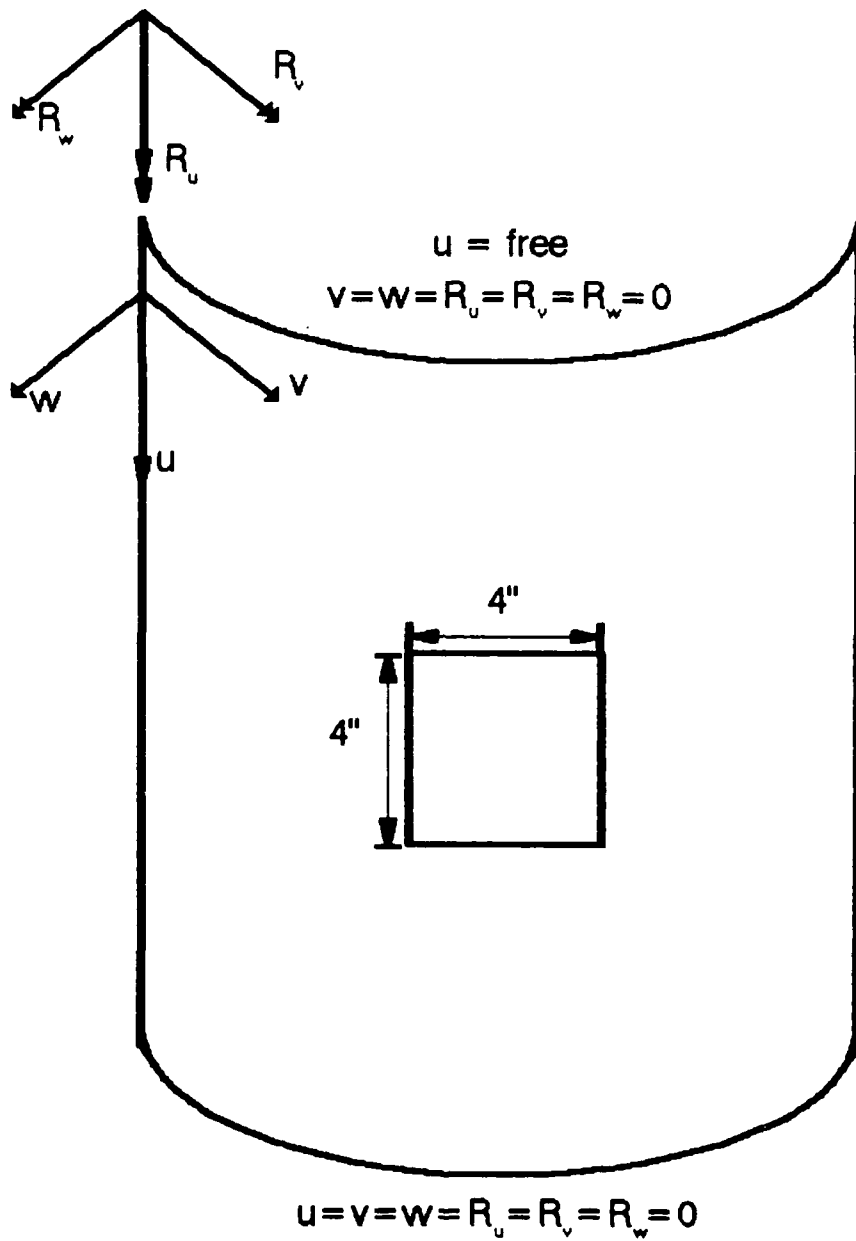


Fig 1.3 Panel with 4" Cutout, Centered

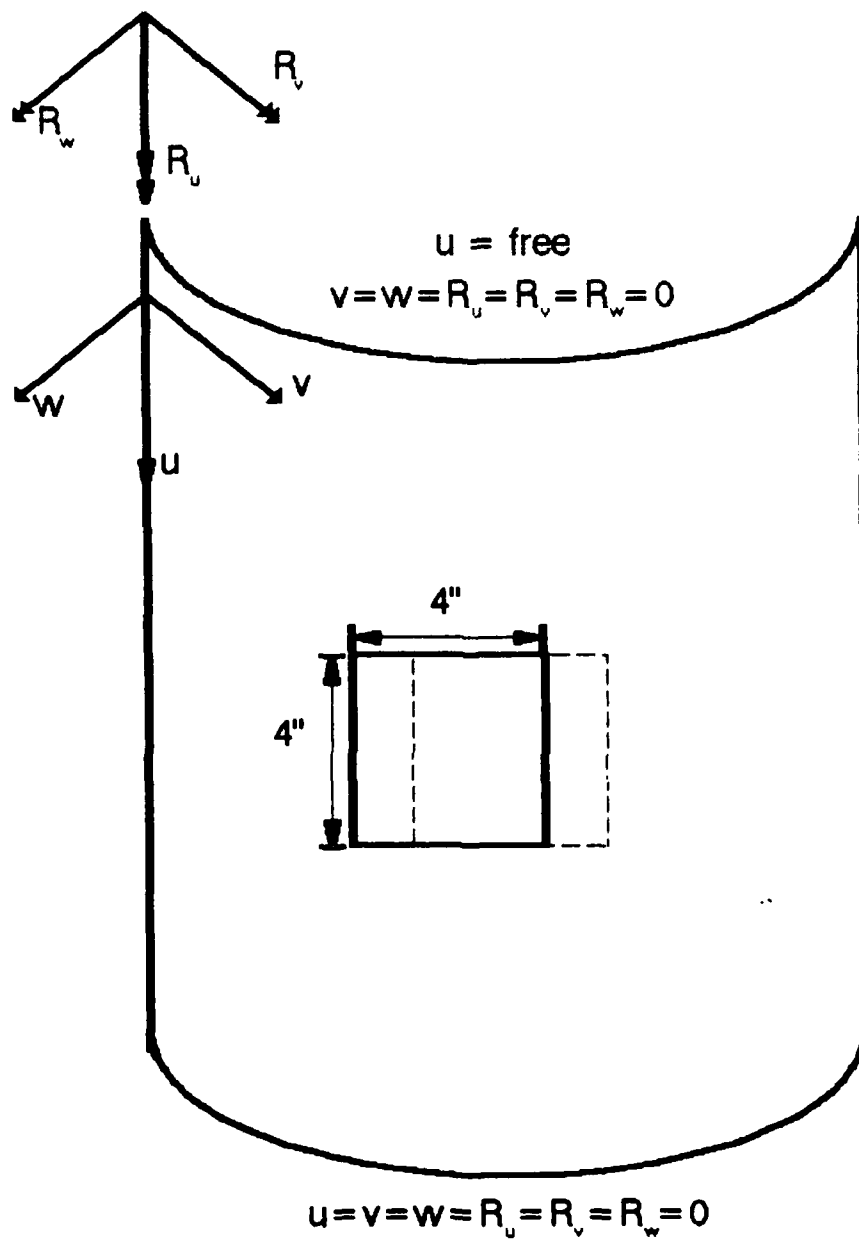


Fig 1.4 Panel with 4" Cutout, Offset 1"

shell's collapse. The results are used to better understand the effects of large displacements and rotations on a finite element analysis.

### 1.3 Scope

A total of twelve models are run on STAGS and six models are run on SHELL to determine displacements due to an external, axially-applied distributed load. The models, developed from previous work [35,41], included the material properties of the experimental test specimens and incorporated a modified Riks technique based on the "constant arc length" method [39]. The models are run with a nonlinear analysis using STAGSC-1 and SHELL with linear analysis runs for comparison purposes.

Next, the results are compared to experimental results. The experimental results are obtained by the Flight Dynamics Laboratory, Wright Research & Development Center, Wright-Patterson AFB, Ohio.

Finally, experimentally derived residual stress parameters are incorporated into one nonlinear analysis model to compare residual stress effects on nonlinear collapse characteristics.



## 2. THEORETICAL DEVELOPMENT

The first step in the theoretical development for this thesis is the derivation of a displacement field for a general shell based upon nonlinear kinematics. This is done to give the reader an understanding of the complex nonlinear relationships that govern a arbitrary, cylindrical, composite shell's response to axial loading. Next, the theory governing STAGSC-1 analysis is developed for a plate element. This development includes kinematics, classical laminated plate theory, and the solution techniques. Next, the theory governing SHELL analysis is developed similarly for a cylindrical shell. The work developed subsequently is a review of many references on shell theory. It is presented to the reader for completeness only. The writer does not intend to imply originality.

### 2.1 Derivation of General Nonlinear Shell Strain Displacement Equations

Since this thesis is concerned with three dimensional curvilinear shells, a basic understanding of the underlying kinematics (in orthogonal curvilinear coordinates) is necessary. Therefore, a brief presentation is made of the derivation of the strain tensor giving the exact relations

in orthogonal curvilinear coordinates. These relations are presented in several elasticity texts, see [2] for example.

Consider a point M of Fig 2.1 that is located in 3-D space by the position vector,  $\bar{r}$ . The point M has Cartesian coordinates,  $x_i$ , as shown in Eqn (2.1).

$$\bar{r} = x_i \bar{i}_i \quad i = 1,2,3 \quad (2.1)$$

where,

$x_i$  = Cartesian coordinates

$\bar{i}_i$  = Cartesian basis vectors

A summation convention on repeated indices applies unless otherwise stated, and barred quantities refer to vectors.

The point M can also be represented with curvilinear coordinates  $y_i$ . The Cartesian coordinates are related to the curvilinear coordinates through transformations of the form shown in Eqn (2.2):

$$\begin{aligned} x_i &= x_i(y_1, y_2, y_3) = x_i(y_j) \\ y_i &= y_i(x_1, x_2, x_3) = y_i(x_j) \end{aligned} \quad (2.2)$$

Basis vectors,  $\bar{a}_i$ , of the curvilinear system are found by taking the differential of the position vector,  $\bar{r}$ .

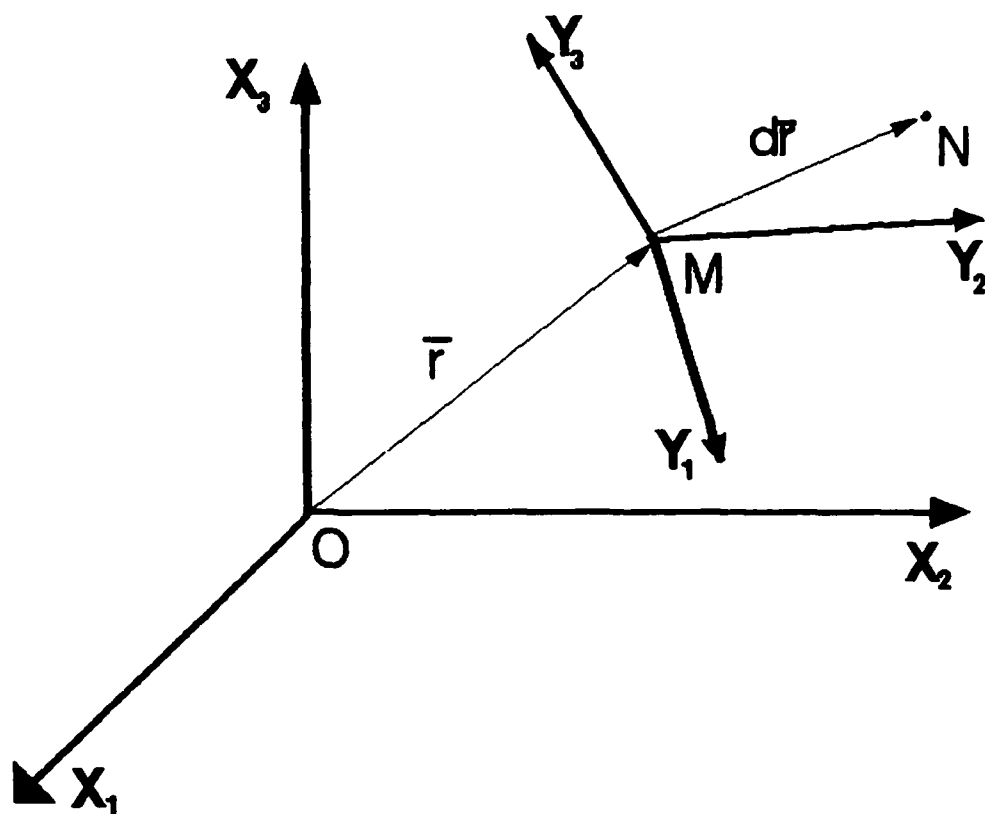


Fig 2.1 Point M Located in 3-D Space by Position Vector  $\bar{r}$ .  
Vector  $d\bar{r}$  has length  $ds$ .

From Eqn (2.1),

$$d\vec{r} = dx_i \vec{i}_i \quad (2.3)$$

The length,  $ds$ , of the infinitesimal line segment MN (see vector  $d\vec{r}$  of Fig 2.1) is then given by,

$$(ds)^2 = d\vec{r} \cdot d\vec{r} \quad (2.4)$$

The length  $ds$  is independent of coordinate systems and therefore from Eqn (2.2),

$$d\vec{r} = \bar{a}_1 dy_1 + \bar{a}_2 dy_2 + \bar{a}_3 dy_3 \quad (2.5)$$

where

$$\bar{a}_i = \frac{\partial \vec{r}}{\partial y_i} = \vec{r}_{,i}$$

A curvilinear basis vector,  $\bar{a}_i$ , is tangent to the  $Y_i$  coordinate line. From Eqns (2.4) and (2.5) we can write,

$$(ds)^2 = (\bar{a}_i \cdot \bar{a}_j) dy_i dy_j = g_{ij} dy_i dy_j \quad (2.6)$$

where,

$$g_{ij} = \bar{a}_i \cdot \bar{a}_j$$

The elements of  $g_{ij}$  form a symmetric tensor called the metric tensor that links the two coordinate systems  $X_i$  and  $Y_i$  through the invariant property of length. The  $Y_i$  coordinate system is called orthogonal if its metric tensor is diagonal, i.e., when  $g_{ij} = 0$  for  $i \neq j$ . This is assumed from this point on.

Next, consider the infinitesimal line segment, MN, of length  $ds$  now embedded in a differential volume element, see Fig 2.2. This differential volume is linearly transformed, i.e., deformed, to a new configuration where the line segment is now of length  $ds^*$ , and whose transformed coordinate system has a metric tensor  $G_{ij}$ . As a result of deformation, the line segment MN of Fig 2.2 moves to  $M^*N^*$  represented by the displacement vector,  $\bar{u}$ . By subtracting the original and deformed squared lengths of the line segment, the Green's strain tensor,  $\gamma_{ij}$ , is defined as shown in Eqn (2.7).

$$(ds^*)^2 - (ds)^2 = 2\gamma_{ij} dy_i dy_j \quad (2.7)$$

Previously defined quantities then give,

$$2\gamma_{ij} = G_{ij} - g_{ij} = \bar{a}_i \cdot \bar{u}_{,j} + \bar{a}_j \cdot \bar{u}_{,i} + \bar{u}_{,i} \cdot \bar{u}_{,j} \quad (2.8)$$

The physical strains,  $\epsilon_{ij}$ , are then found from,

$$\epsilon_{ij} = \frac{\gamma_{ij}}{h_i h_j} \quad (2.9)$$

In Eqn (2.9), the  $h_i$  are called scale factors and are defined by  $g_{ii} = h_i^2$  (no sum) and the  $\gamma_{ij}$  are shown in Eqn (B.10) where the  $u_i$  are the coordinates of the displacement vector,  $\bar{u}$ . In the general large strain case, the  $\epsilon_{ii}$  (no sum) are related to the elongations of the fibers of the differential volume element and the  $\epsilon_{ij}$  ( $i \neq j$ ) are related to the shears (the difference from ninety degrees the originally perpendicular fibers are oriented to after deformation). For the case of small strains ( $\epsilon < .04$ ) [41], the  $\epsilon_{ii}$  (no sum) are the elongations and the  $\epsilon_{ij}$  ( $i \neq j$ ) are the shears. That is to say, for large strains, the  $\epsilon_{ij}$  have no physical meanings; but for small strains, the  $\epsilon_{ij}$  have the engineering definitions. The elongations and shears are identically zero for rigid body displacements and rotations of the body under loading [41]. In this way, there are no theoretical limitations on the magnitudes of displacement and rotation elements of which the body can undergo [41]. One important limitation of Eqn (2.10) is that it applies

only to small strain quantities. Therefore, if large strains exist, Eqn (2.10) is no longer valid. This theory applies only for large displacements and/or moderately large rotations with small strains (e.g. no plasticity).

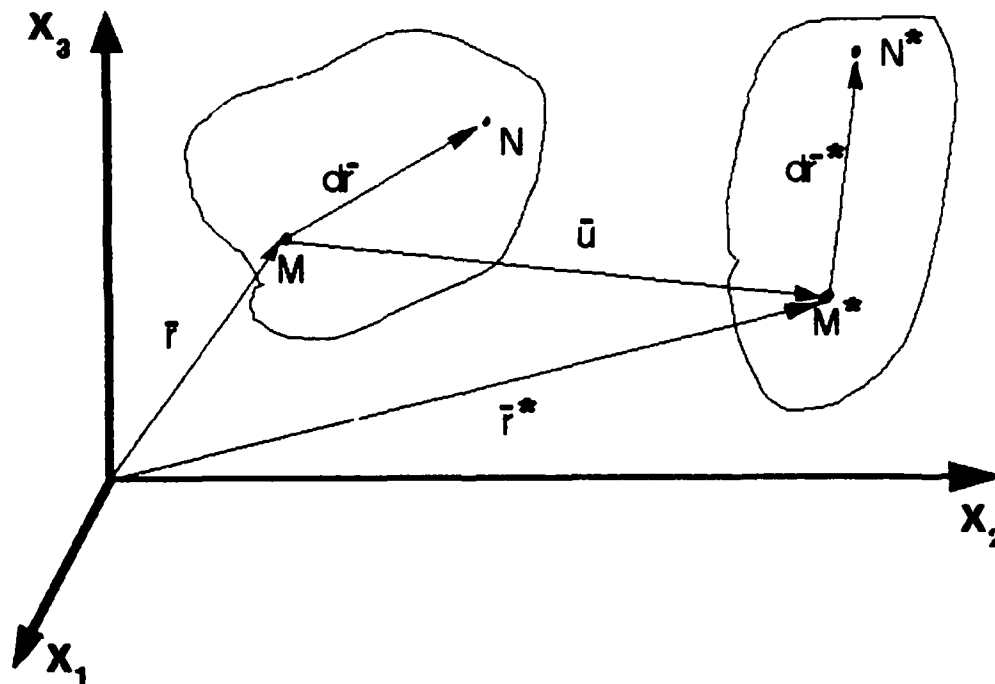


Fig 2.2 Segment  $MN$  Deforms to  $M^*N^*$  Through Displacement Vector  $u$ .

$$\begin{aligned}
\gamma_{11} &= h_1 \frac{\partial u_1}{\partial y_1} + \frac{h_1 u_2}{h_2} \frac{\partial h_1}{\partial y_2} + \frac{h_1 u_3}{h_3} \frac{\partial h_1}{\partial y_3} \\
&\quad + \frac{1}{2} \left( \frac{\partial u_1}{\partial y_1} + \frac{u_2}{h_2} \frac{\partial h_1}{\partial y_2} + \frac{u_3}{h_3} \frac{\partial h_1}{\partial y_3} \right)^2 \\
&\quad + \frac{1}{2} \left( \frac{\partial u_2}{\partial y_1} - \frac{u_1}{h_2} \frac{\partial h_1}{\partial y_2} \right)^2 + \frac{1}{2} \left( \frac{\partial u_3}{\partial y_1} - \frac{u_1}{h_3} \frac{\partial h_1}{\partial y_3} \right)^2 \\
\gamma_{22} &= h_2 \frac{\partial u_2}{\partial y_2} + \frac{h_2 u_3}{h_3} \frac{\partial h_2}{\partial y_3} + \frac{h_2 u_1}{h_1} \frac{\partial h_2}{\partial y_1} \\
&\quad + \frac{1}{2} \left( \frac{\partial u_2}{\partial y_2} + \frac{u_3}{h_3} \frac{\partial h_2}{\partial y_3} + \frac{u_1}{h_1} \frac{\partial h_2}{\partial y_1} \right)^2 \\
&\quad + \frac{1}{2} \left( \frac{\partial u_3}{\partial y_2} - \frac{u_2}{h_3} \frac{\partial h_2}{\partial y_3} \right)^2 + \frac{1}{2} \left( \frac{\partial u_1}{\partial y_2} - \frac{u_2}{h_1} \frac{\partial h_2}{\partial y_1} \right)^2 \\
\gamma_{33} &= h_3 \frac{\partial u_3}{\partial y_3} + \frac{h_3 u_1}{h_1} \frac{\partial h_3}{\partial y_1} + \frac{h_3 u_2}{h_2} \frac{\partial h_3}{\partial y_2} \\
&\quad + \frac{1}{2} \left( \frac{\partial u_3}{\partial y_3} + \frac{u_1}{h_1} \frac{\partial h_3}{\partial y_1} + \frac{u_2}{h_2} \frac{\partial h_3}{\partial y_2} \right)^2 \\
&\quad + \frac{1}{2} \left( \frac{\partial u_1}{\partial y_3} - \frac{u_3}{h_1} \frac{\partial h_3}{\partial y_1} \right)^2 + \frac{1}{2} \left( \frac{\partial u_2}{\partial y_3} - \frac{u_3}{h_2} \frac{\partial h_3}{\partial y_2} \right)^2 \\
\gamma_{12} &= \frac{1}{2} \left( h_1 \frac{\partial u_1}{\partial y_2} + h_2 \frac{\partial u_2}{\partial y_1} - u_2 \frac{\partial h_2}{\partial y_1} - u_1 \frac{\partial h_1}{\partial y_2} \right) \\
&\quad + \frac{1}{2} \left( \frac{\partial u_1}{\partial y_2} - \frac{u_2}{h_1} \frac{\partial h_2}{\partial y_1} \right) \left( \frac{\partial u_1}{\partial y_1} + \frac{u_2}{h_2} \frac{\partial h_1}{\partial y_2} + \frac{u_3}{h_3} \frac{\partial h_1}{\partial y_3} \right) \\
&\quad + \frac{1}{2} \left( \frac{\partial u_2}{\partial y_1} - \frac{u_1}{h_2} \frac{\partial h_1}{\partial y_2} \right) \left( \frac{\partial u_2}{\partial y_2} + \frac{u_1}{h_1} \frac{\partial h_2}{\partial y_1} + \frac{u_3}{h_3} \frac{\partial h_2}{\partial y_3} \right) \\
&\quad + \frac{1}{2} \left( \frac{\partial u_3}{\partial y_1} - \frac{u_1}{h_3} \frac{\partial h_1}{\partial y_3} \right) \left( \frac{\partial u_3}{\partial y_2} - \frac{u_2}{h_3} \frac{\partial h_2}{\partial y_3} \right)
\end{aligned} \tag{2.10}$$



$$\begin{aligned}
\gamma_{13} = & \frac{1}{2} \left( h_3 \frac{\partial u_3}{\partial y_1} + h_1 \frac{\partial u_1}{\partial y_3} - u_1 \frac{\partial h_1}{\partial y_3} - u_3 \frac{\partial h_3}{\partial y_1} \right) \\
& + \frac{1}{2} \left( \frac{\partial u_1}{\partial y_3} - \frac{u_3}{h_1} \frac{\partial h_3}{\partial y_1} \right) \left( \frac{\partial u_1}{\partial y_1} + \frac{u_3}{h_3} \frac{\partial h_1}{\partial y_3} + \frac{u_2}{h_2} \frac{\partial h_1}{\partial y_2} \right) \\
& + \frac{1}{2} \left( \frac{\partial u_3}{\partial y_1} - \frac{u_1}{h_3} \frac{\partial h_1}{\partial y_3} \right) \left( \frac{\partial u_3}{\partial y_3} + \frac{u_1}{h_1} \frac{\partial h_3}{\partial y_1} + \frac{u_2}{h_2} \frac{\partial h_3}{\partial y_2} \right) \\
& + \frac{1}{2} \left( \frac{\partial u_2}{\partial y_1} - \frac{u_1}{h_2} \frac{\partial h_1}{\partial y_2} \right) \left( \frac{\partial u_2}{\partial y_3} - \frac{u_3}{h_2} \frac{\partial h_3}{\partial y_2} \right) \\
\gamma_{23} = & \frac{1}{2} \left( h_3 \frac{\partial u_3}{\partial y_2} + h_2 \frac{\partial u_2}{\partial y_3} - u_2 \frac{\partial h_2}{\partial y_3} - u_3 \frac{\partial h_3}{\partial y_2} \right) \\
& + \frac{1}{2} \left( \frac{\partial u_2}{\partial y_3} - \frac{u_3}{h_2} \frac{\partial h_3}{\partial y_2} \right) \left( \frac{\partial u_2}{\partial y_2} + \frac{u_3}{h_3} \frac{\partial h_2}{\partial y_3} + \frac{u_1}{h_1} \frac{\partial h_2}{\partial y_1} \right) \\
& + \frac{1}{2} \left( \frac{\partial u_3}{\partial y_2} - \frac{u_2}{h_3} \frac{\partial h_2}{\partial y_3} \right) \left( \frac{\partial u_3}{\partial y_3} + \frac{u_2}{h_2} \frac{\partial h_3}{\partial y_2} + \frac{u_1}{h_1} \frac{\partial h_3}{\partial y_1} \right) \\
& + \frac{1}{2} \left( \frac{\partial u_1}{\partial y_2} - \frac{u_2}{h_1} \frac{\partial h_2}{\partial y_1} \right) \left( \frac{\partial u_1}{\partial y_3} - \frac{u_3}{h_1} \frac{\partial h_3}{\partial y_1} \right)
\end{aligned} \tag{2.10}$$

cont.

## 2.2 STAGSC-1 Theory

The Structural Analysis for General Shells (STAGS) computer program, developed by Lockheed Palo Alto Research Laboratory, was first operational in 1967. Its primary purpose is the analysis of thin shelled structures. From 1967-1976 the program was based on the finite difference method. In 1979 a new version of STAGS, STAGSC-1, was released and is based entirely on the finite element method [42]. The 1986 STAGSC-1 VAX Computer version is used in this thesis. Of the many capabilities in the STAGS program, the primary one used herein is the nonlinear static analysis. The basic finite element used in STAGSC-1 is the flat plate element that facets the shell surface to approximate its curvature. A look at the theory for this flat plate element and the theory used in STAGS is presented in the following sections, based primarily upon Egan's work (see [37]). While this may not be the exact theory used in STAGSC-1, the following presentation is an attempt through researching documentation to give some insight into the internal make-up of the STAGS's code.

### 2.2.1 Nonlinear Shell Theory

A review of Sanders' nonlinear shell theory is presented so that the reader may understand strain-displacement relations in a shell. This presentation will, in the subsequent section, provide an insight to the theory used in STAGSC-1.

The classical thin shell theory derived by Sanders assumes that the shell is thin, the middle surface strains and rotations are small, and the displacements away from the surface are restricted by the Kirchhoff-Love hypothesis [3]. With these assumptions in mind the equations for the mid-surface and bending strains are [44]:

$$\begin{aligned}\epsilon_x^0 &= \frac{u_{,x}}{\alpha_x} + \frac{\alpha_{x,y}}{\alpha_x \alpha_y} v + \frac{w}{R_x} + \frac{1}{2} \phi_x^2 + \frac{1}{2} \phi^2 \\ \epsilon_y^0 &= \frac{v_{,y}}{\alpha_y} + \frac{\alpha_{y,x}}{\alpha_x \alpha_y} v + \frac{w}{R_y} + \frac{1}{2} \phi_y^2 - \frac{1}{2} \phi^2 \\ \gamma_{xy}^0 &= \frac{v_{,x}}{\alpha_x} + \frac{u_{,y}}{\alpha_y} - \frac{\alpha_{x,y}}{\alpha_x \alpha_y} u - \frac{\alpha_{y,x}}{\alpha_x \alpha_y} v - \phi_x \phi_y\end{aligned}\quad (2.11)$$

and

$$\begin{aligned}\chi_x &= \frac{\phi_{x,x}}{\alpha_x} + \frac{\alpha_{x,y} \phi_y}{\alpha_x \alpha_y} \\ \chi_y &= \frac{\phi_{y,y}}{\alpha_y} + \frac{\alpha_{y,x} \phi_x}{\alpha_x \alpha_y} \\ 2\chi_{xy} &= \frac{\phi_{y,x}}{\alpha_x} + \frac{\phi_{x,y}}{\alpha_y} - \frac{\alpha_{x,y} \phi_x}{\alpha_x \alpha_y} - \frac{\alpha_{y,x} \phi_y}{\alpha_x \alpha_y} + \frac{\phi}{R_x} + \frac{\phi}{R_y}\end{aligned}\quad (2.12)$$

where  $u$  and  $v$  denote displacements tangent to the mid-surface and  $w$  denotes displacement perpendicular to the shell's mid surface,  $R_x$  and  $R_y$  are the principal radii of curvature,  $\phi_x$ ,  $\phi_y$ , and  $\phi$  are in-plane rotational terms, and  $\alpha_x$  and  $\alpha_y$  are metric tensor coefficients. The rotational terms are given by [44]:

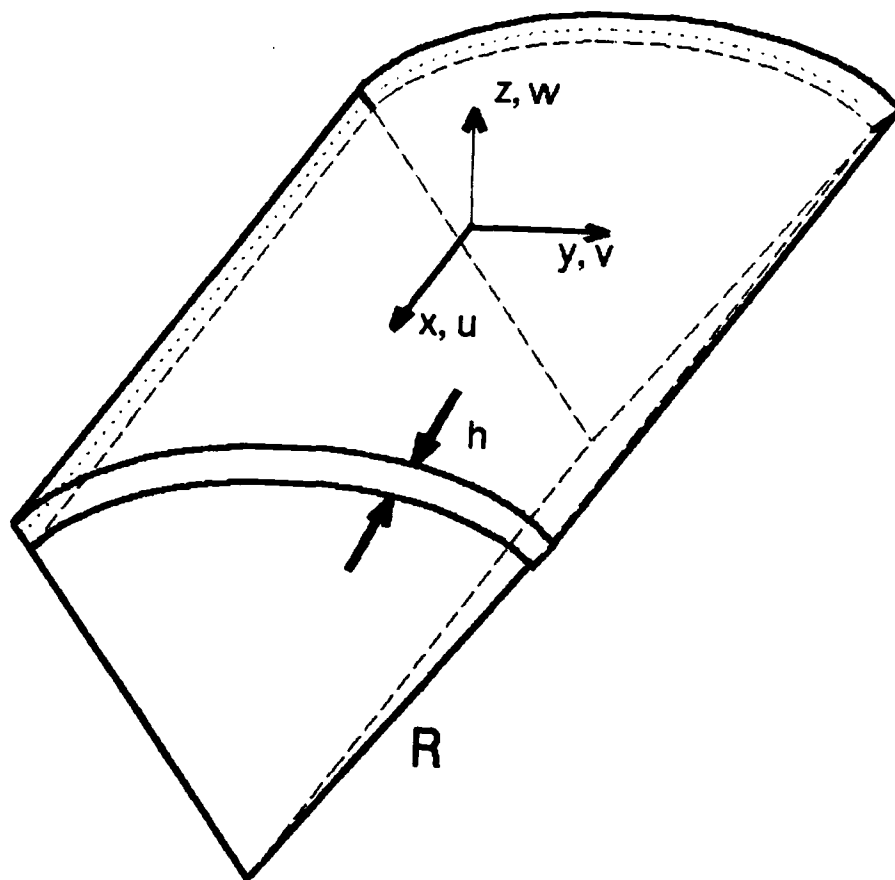
$$\begin{aligned}\phi_x &= -\frac{w_{,x}}{\alpha_x} + \frac{u}{R_x} \\ \phi_y &= -\frac{w_{,y}}{\alpha_y} + \frac{v}{R_y} \\ \phi &= \frac{1}{2\alpha_x\alpha_y} \left[ (\alpha_y v)_{,x} - (\alpha_x u)_{,y} \right]\end{aligned}\tag{2.13}$$

The metric coefficients, written in a form similar to Saada [2], are:

$$\begin{aligned}\alpha_x &= h_1 = \sqrt{E} \left( 1 + \frac{\xi_3}{R_x} \right) \\ \alpha_y &= h_2 = \sqrt{G} \left( 1 + \frac{\xi_3}{R_y} \right)\end{aligned}\tag{2.14}$$

where  $\xi_3$  is the distance from the mid-surface and  $E$  and  $G$  are functions of the shell geometry (not material constants).

For simplicity, a thin cylindrical shell is considered for the remainder of the development (see Fig 2.3). The



**Fig 2.3 Cylindrical Shell Section Showing Coordinate and Displacement Directions [17]**

reference surface for the shell is the mid-plane. For this cylindrical shell we let  $R_x \rightarrow \infty$ ,  $R_y = R$ ,  $\xi_3 = z$ , and assume that  $z \ll R$ . For this particular case Sanders' equations (Eqns (2.1) and (2.2)) reduce to [17]:

$$\begin{aligned}\epsilon_x^o &= u_{,x} + \frac{1}{2} \phi_x^2 + \frac{1}{2} \phi^2 \\ \epsilon_y^o &= v_{,y} + \frac{1}{2} \phi_x^2 - \frac{1}{2} \phi^2 \\ \gamma_{xy}^o &= v_{,x} + u_{,y} + \phi_x \phi_y\end{aligned}\tag{2.15}$$

and

$$\begin{aligned}\chi_x &= \phi_{x,x} \\ \chi_y &= \phi_{y,y} \\ 2\chi_{xy} &= 2\chi_{yx} = \phi_{y,x} + \phi_{x,y} + \frac{\phi}{R_y}\end{aligned}\tag{2.16}$$

Now, Eqns (2.15) and (2.16) can be written with the Kirchhoff-Love hypothesis to obtain the full strain expression:

$$\begin{Bmatrix} \epsilon_x \\ \epsilon_y \\ 2\gamma_{xy} \end{Bmatrix} = \begin{Bmatrix} \epsilon_x^o \\ \epsilon_y^o \\ \gamma_{xy}^o \end{Bmatrix} - z \begin{Bmatrix} \chi_x \\ \chi_y \\ 2\chi_{xy} \end{Bmatrix}\tag{2.17}$$

### 2.2.2 Strain-Displacement Relations

As stated earlier, STAGS uses flat plates to approximate the curved surface of a shell. These plate elements are thin, therefore a state of plane stress can be assumed with  $\gamma_{xz}$ ,  $\gamma_{yx}$ ,  $\epsilon_z$ , and  $\sigma_z$  equal to zero, and the in-plane displacements,  $u$  and  $v$ , as well as the normal displacement,  $w$ , functionally depending on only two space variables [26]. As in Sanders' equations for a thin shell, STAGS uses the Kirchhoff-Love hypothesis for strains away from the mid-plane. The complete derivation of the nonlinear kinematics relations is given in Appendix A.

If the Kirchhoff-Love hypothesis is considered for out of plane strain terms (see Appendix A) and combined with the in-plane strain terms from Eqn (2.20), the resulting expressions for strains in the plate are given by:

$$\begin{aligned}\epsilon_x &= \epsilon_x^0 - ZW_{,xx} \\ \epsilon_y &= \epsilon_y^0 - ZW_{,yy} \\ \gamma_{xy} &= \gamma_{xy}^0 - 2ZW_{,xy}\end{aligned}\tag{2.18}$$

Eqn (2.18) shows the nonlinear kinematic equations which appear to be used in STAGSC-1. These kinematic relations allow for large displacements and moderate

rotations (due to Kirchhoff-Love hypothesis) and will be used in the following section to demonstrate the general form of the tangent stiffness matrix.

### 2.2.3 Constitutive Development

As was stated in Section 2.2.2, a state of plane stress is assumed for the plate element. The following contracted notation in Table 2.1 is used for the constitutive development where Fig 2.4 demonstrates the relationship between the subscripts.

Table 2.1 Contracted Notation for STAGS

stress		strain		plate
explicit	contracted	explicit	contracted	coordinates
$\sigma_{11}$	$\sigma_1$	$\epsilon_{11}$	$\epsilon_1$	x → 1
$\sigma_{22}$	$\sigma_2$	$\epsilon_{22}$	$\epsilon_2$	y → 2
$\sigma_{33}$	$\sigma_3$	$\epsilon_{33}$	$\epsilon_3$	z → 3
				shear:
$\sigma_{23}$	$\sigma_4$	$2\epsilon_{23}$	$\epsilon_4$	y-z → 4
$\sigma_{13}$	$\sigma_5$	$2\epsilon_{13}$	$\epsilon_5$	x-z → 5
$\sigma_{12}$	$\sigma_6$	$2\epsilon_{12}$	$\epsilon_6$	x-y → 6



The research in this thesis is limited to material response in the linear regime, but complexity arises due to the directional response of the oriented plies in the laminate. The constitutive relations between stress and strain for a laminate of arbitrarily oriented transversely isotropic plies is developed. These relations are then summed over the lamina thickness of the directional constitutive equation for each ply, to arrive at the total laminate's effective stress-strain relation. See Appendix D for complete derivation based upon [45].

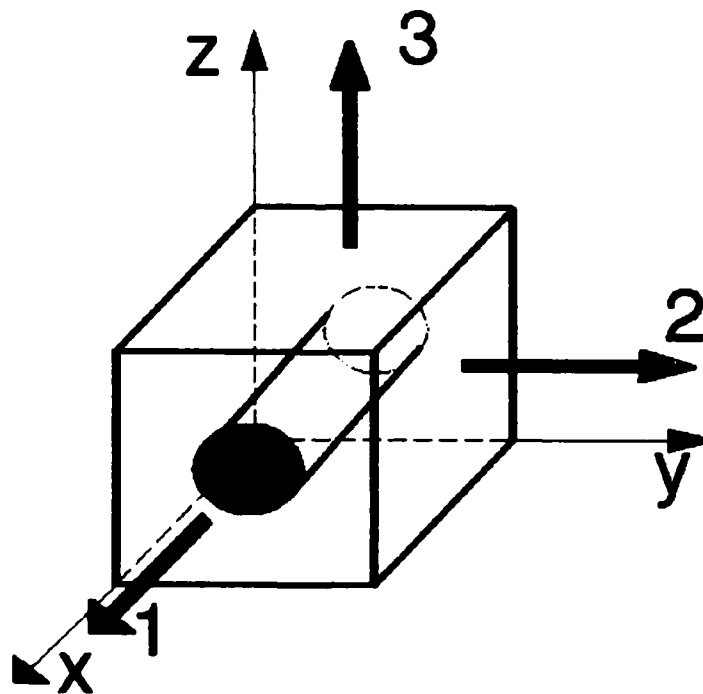


Fig 2.4 Fiber Reinforced Lamina Definitions

From basic elasticity relations, for isotropic material under purely extensional load, stress ( $\sigma$ ) and strain ( $\epsilon$ ) are related as:

$$\sigma = E\epsilon \quad (2.19)$$

with  $E$  being Young's modulus. For a general anisotropic material, Young's modulus can differ with different load orientations, so the equation expands to [45]:

$$\begin{Bmatrix} \sigma_1 \\ \sigma_2 \\ \sigma_3 \\ \sigma_4 \\ \sigma_5 \\ \sigma_6 \end{Bmatrix} = \begin{bmatrix} S_{11} & S_{12} & S_{13} & S_{14} & S_{15} & S_{16} \\ S_{21} & S_{22} & S_{23} & S_{24} & S_{25} & S_{26} \\ S_{31} & S_{32} & S_{33} & S_{34} & S_{35} & S_{36} \\ S_{41} & S_{42} & S_{43} & S_{44} & S_{45} & S_{46} \\ S_{51} & S_{52} & S_{53} & S_{54} & S_{55} & S_{56} \\ S_{61} & S_{62} & S_{63} & S_{64} & S_{65} & S_{66} \end{bmatrix} \begin{Bmatrix} \epsilon_1 \\ \epsilon_2 \\ \epsilon_3 \\ \epsilon_4 \\ \epsilon_5 \\ \epsilon_6 \end{Bmatrix} \quad (2.20)$$

where  $S_{ij}$  is the stiffness matrix of 36 independent terms defining the stress-strain relationship for loading in the  $i$ th direction. When the area of study is restricted to the energy conserving elastic regime, the matrix is symmetric ( $S_{12} = S_{21}$ ) resulting in 21 independent terms. In the case of fiber-reinforced composites, shown in Fig 2.4, the three mutually orthogonal planes of symmetry decouple shear strains from normal stresses and vice versa, and shear

stresses are decoupled from shear strains. This is the definition of an orthotropic material, which has only nine independent terms [45]:

$$\begin{Bmatrix} \sigma_1 \\ \sigma_2 \\ \sigma_3 \\ \sigma_4 \\ \sigma_5 \\ \sigma_6 \end{Bmatrix} = \begin{bmatrix} S_{11} & S_{12} & S_{13} & 0 & 0 & 0 \\ S_{12} & S_{22} & S_{23} & 0 & 0 & 0 \\ S_{12} & S_{23} & S_{33} & 0 & 0 & 0 \\ 0 & 0 & 0 & S_{44} & 0 & 0 \\ 0 & 0 & 0 & 0 & S_{55} & 0 \\ 0 & 0 & 0 & 0 & 0 & S_{66} \end{bmatrix} \begin{Bmatrix} \epsilon_1 \\ \epsilon_2 \\ \epsilon_3 \\ \epsilon_4 \\ \epsilon_5 \\ \epsilon_6 \end{Bmatrix} \quad (2.21)$$

Since the material responds equally to any direction of load in the plane perpendicular to the fiber longitudinal axis, so the 2 and 3 subscripts on  $S$  are interchangeable. This behavior is termed transverse isotropy, and it further reduces the number of independent terms to seven. Jones defines these stiffness terms with respect to the engineering constants  $E$  (Young's Modulus) and  $\nu$  (Poisson's ratio) [45] (refer to Appendix E, Eqn (E.2)).

Due to the thinness of the plies in the laminate, the assumption of plane stress is made ( $\sigma_3 = \sigma_4 = \sigma_5 = 0$ ) at this point. It should be noted that the limitation to this assumption is plane stress is no longer valid for thick plies. Using a simplistic criterion that  $t \leq 1/2\pi$  inches (see [54]) as the point when plane strain applies, one can

easily determine that the laminate ( $t = .004''$ ) is much less than the criteria and the plane stress assumption is valid. Solving for  $\epsilon_3$  in Eqn (2.21) after applying this assumption yields [45]:

$$\epsilon_3 = - (S_{13}/S_{33})\epsilon_1 - (S_{23}/S_{33})\epsilon_2 \quad (2.22)$$

Applying the plane stress assumption to Eqn (2.24) and using the relation of Eqn (2.21) to eliminate  $\epsilon_3$  produces the lamina constitutive relation:

$$\begin{Bmatrix} \sigma_1 \\ \sigma_2 \\ \sigma_6 \end{Bmatrix} = \begin{bmatrix} Q_{11} & Q_{12} & 0 \\ Q_{12} & Q_{22} & 0 \\ 0 & 0 & Q_{66} \end{bmatrix} \begin{Bmatrix} \epsilon_1 \\ \epsilon_2 \\ \epsilon_6 \end{Bmatrix} \quad (2.23)$$

where the  $Q_{ij}$  are the reduced stiffness coefficients related to the  $S_{ij}$ 's by [45]:

$$Q_{ij} = S_{ij} - (S_{i3}S_{j3})/S_{33} \quad (2.24)$$

where  $Q_{ij}$  is defined in Appendix D. Finally, in order to analyze the stack of plies, they must all be referenced to a global axis system and their effects summed [45]:

$$\{\sigma_i\}_k = [T][Q_{ij}]_k[T]^T\{\epsilon_i\}_k \quad (2.25)$$

where [T] is defined in Appendix E. With this transformation the constitutive relations become:

$$\left\{ \sigma_i \right\}_k = \left[ \bar{Q}_{ij} \right]_k \left\{ \epsilon_i \right\}_k \quad (2.26)$$

with the transformed reduced stiffness,  $\bar{Q}_{ij}$ , being defined in Appendix D.

#### 2.2.4 Derivation of the Tangent Stiffness Matrix

The tangent stiffness matrix is a nonlinear stiffness matrix used in the modified Newton-Raphson method for solving a nonlinear set of equations. There are other techniques for solving these equations, but STAGSC-1 uses the modified Newton-Raphson. Therefore, the derivation of the tangent stiffness matrix is of interest for this thesis. The tangent stiffness matrix is derived for a flat plate element, a STAGS type element, in a general way without reference to any specific shape functions. The specific shape functions, and their derivation, for the STAGS element is shown in [43]. It must also be pointed out that STAGS uses an isoparametric formulation, which requires the Jacobian for the element, whereas this formulation is given

in general coordinates to show the reader the steps involved in formulating a nonlinear stiffness matrix. A complete derivation of the tangent stiffness matrix is shown in Appendix F and in [37].

To start the derivation (see Appendix F for the complete derivation), a form of the tangent stiffness matrix is found from the energy expression. Consider  $(\psi)$ , the sum of the external and internal generalized forces (Appendix C, Eqn (C.14)), which is given as [28]:

$$(\psi) = \int_V [B]^T (\sigma) dV - (f) \quad (2.27)$$

where,

$(\sigma)$  = vector of stresses

$(f)$  = nodal forces of the element

In an equilibrium state,  $(\psi)$  (Eqn (2.27)) will equal zero. The strain displacement relations can be written (to include the  $[B]$  matrix) as [37]:

$$(\epsilon) = [L][N](a) = [B](a) \quad (2.28)$$

where,

$[L]$  = differential operator matrix

$[N]$  = element shape functions

$(a)$  = nodal displacement vector

In the case of a nonlinear stiffness matrix (i.e. tangent stiffness matrix),  $[B]$  is redefined as [28]:

$$[B] = [B_0] + [B_L] \quad (2.29)$$

where,

$$[B_0] = \text{constant}$$

$$[B_L] = \text{functions of displacements}$$

In order to use the Newton-Raphson method, a relation between  $\delta(a)$  and  $\delta(\psi)$  (see Section 2.2.7) must be found [37]. Taking the variation of Eqn (2.27) with respect to  $\delta(a)$  gives the relation needed (see Appendix F, Eqn (F.4)). Incorporating the elastic stress strain relations into the variational equations and defining stiffness matrices based on the appropriate terms yields [27]:

$$\begin{aligned} [K_0] &= \int_V [B_0]^T [D] [B_0] dV \\ [K_L] &= \int_V \left( [B_0]^T [D] [B_0] + [B_L]^T [D] [B_L] \right. \\ &\quad \left. + [B_L] [D] [B_0] \right) dV \\ [K_\sigma] \delta(a) &= \int_V \delta[B_L]^T(\sigma) dV \end{aligned} \quad (2.30)$$

where,

$[K_0]$  = linear stiffness matrix

$[K_L]$  = nonlinear stiffness matrix

$[K_\sigma]$  = initial stress matrix

The full expression for the tangent stiffness matrix can now be written as:

$$[K_T] = [K_0] + [K_L] + [K_\sigma] \quad (2.31)$$

With an expression for the elements contained in the tangent stiffness matrix (Eqn (2.31)), the derivation can proceed in determining the terms in each of the matrices that make up the tangent stiffness matrix.

After formulating the kinematic relation incorporating linear and nonlinear in-plane and bending strains (see Appendix F, Eqn (F.11)) [37], introducing the definition for the material matrix (see Appendix F, Eqn (F.12)) [37], and determining the displacement relations, the expression for the linear and nonlinear stiffness matrices ( $[K_0]$  and  $[K_L]$ ) are [37]:

$$_{(24 \times 24)}^{[K_0]} = \int_A \begin{bmatrix} [B_0^p]^T [A] [B_0^p] & [B_0^p]^T [B] [B_0^b] \\ [B_0^p]^T [B] [B_0^b] & [B_0^b]^T [D] [B_0^b] \end{bmatrix} dA \quad (2.32)$$



and

$$_{(24 \times 24)} [K_L] = \int_A \begin{bmatrix} [1] & [2] \\ [2] & [3] \end{bmatrix} dA \quad (2.33)$$

where,

$$\begin{aligned} _{(12 \times 12)} [1] &= [B_o^p]^T [A] [B_L^p] + [B_L^p]^T [A] [B_L^p] + [B_L^p]^T [A] [B_o^p] \\ _{(12 \times 12)} [2] &= [B_o^p]^T [A] [B_L^b] + [B_L^p]^T [A] [B_L^b] + [B_L^p]^T [B] [B_o^b] \\ _{(12 \times 12)} [3] &= [B_o^b]^T [A] [B_L^b] + [B_L^b]^T [B] [B_L^b] + [B_L^b]^T [B] [B_o^b] \end{aligned} \quad (2.34)$$

The final expression necessary for the tangent stiffness matrix is the initial stress matrix  $[K_o]$ . The initial stress matrix can be broken down into in-plane and bending components. Each of these components are then defined in terms of the appropriate stress resultants and displacement relations (see Appendix F, Eqns (F.35) to (F.42)) [37]. The final expressions for each initial stress matrix component are (Appendix F, Eqns (F.43) and (F.44)) [37]:

$$_{(12 \times 12)} [K_o^p] = \int_A _{(12 \times 4)} [G^p]^T \begin{bmatrix} N_x & N_{xy} & 0 & 0 \\ N_y & N_{xy} & 0 & 0 \\ 0 & 0 & N_x & N_{xy} \\ 0 & 0 & N_y & N_{xy} \end{bmatrix} _{(4 \times 12)} [G^p] dA \quad (2.35)$$

and

$$[K\sigma^b]_{(12 \times 12)} = \int_A [G^b]_{(12 \times 2)}^T \begin{bmatrix} N_x & N_{xy} \\ N_{xy} & N_y \end{bmatrix} [G^b]_{(2 \times 12)} dA \quad (2.36)$$

With Eqns (2.35) and (2.36), the full expression for the initial stress matrix can be written as:

$$[K\sigma]_{(24 \times 24)} = \begin{bmatrix} [K\sigma^p]_{(12 \times 12)} & 0 \\ 0 & [K\sigma^b]_{(12 \times 12)} \end{bmatrix} \quad (2.37)$$

#### 2.2.5 Plate Elements Representing a Shell

As stated earlier, STAGS, uses plate elements to represent the surface of the shell. The quadrilateral plate elements primarily used in this thesis are the STAGS QUAF 411 elements. The QUAF 411 element has 32 degrees of freedom; four rotations and three displacements at each corner node and an in-plane displacement at each of the four side nodes. This element is shown in Fig 2.5.

From examining Fig 2.5 it is noted that a degree of freedom not usually used in plate elements is included; the normal rotation  $\theta_z$ . This normal rotation, for the QUAF 411, is the average in-plane rotation of the two adjacent edges

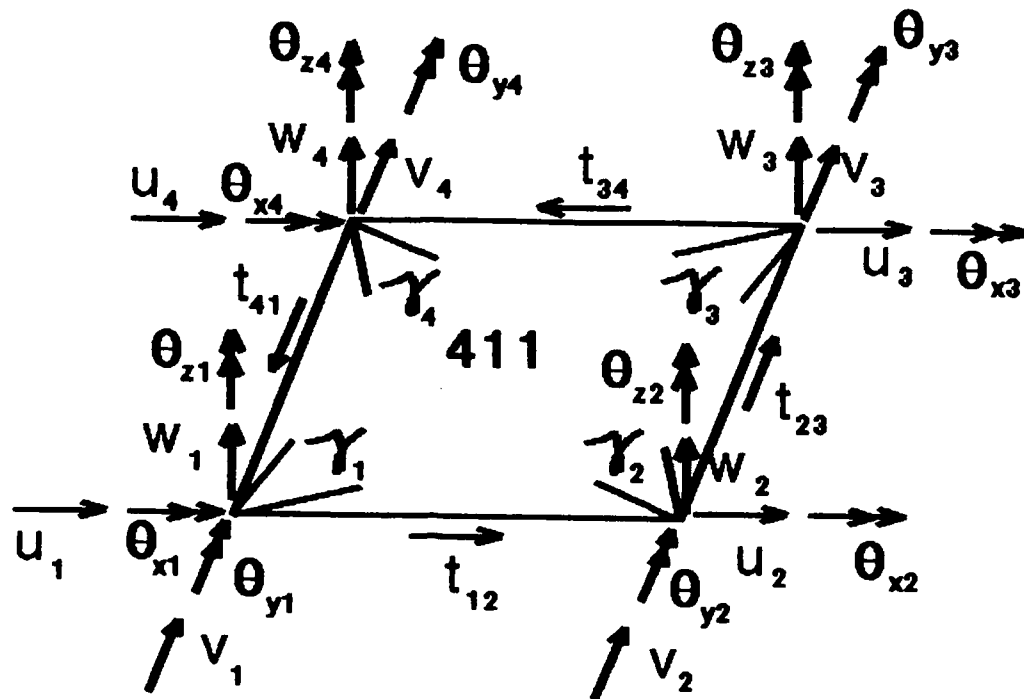


Fig 2.5 STAGS 411 Quadrilateral Element [26]

of the plate element. This degree of freedom is necessary when two flat plate elements meet at an angle to represent a curved shell [42].  $\theta_z$  takes the plate's activity and transforms it into a physical representation of a shell. A problem with this rotation is that it does not appear in the strain energy expression for the element.

To illustrate, consider two flat plate elements joined together at an angle  $\alpha$  as in Fig 2.6. These plates represent the curved surface of a shell. Once the rotations

of each element are transformed into the same reference system, compatibility is given as [42]:

$$\begin{aligned} \left( \theta_y^1 - \theta_y^2 \right) \cos(\alpha/2) - \left( \theta_z^1 + \theta_z^2 \right) \sin(\alpha/2) &= 0 \\ \left( \theta_z^1 - \theta_z^2 \right) \cos(\alpha/2) - \left( \theta_y^1 + \theta_y^2 \right) \sin(\alpha/2) &= 0 \end{aligned} \quad (2.38)$$

where the superscripts 1 and 2 are the associated element numbers. As the angle between the elements,  $\alpha$ , becomes smaller the system of equations in Eqn (2.38) becomes increasingly ill-conditioned and is singular at  $\alpha = 0$  [42]. Once this limit is reached,  $\theta_z$  is omitted and Eqn (2.38) is assumed as  $\theta_y^1 = \theta_y^2$ . The system of equations becomes flat plate relations.

Another problem associated with the use of flat elements representing a curved surface has to do with displacement conformity at an interface of two flat elements. For a flat element the lateral deflection,  $w$ , is usually represented by at least a cubic polynomial in order to handle the second derivatives associated with bending strain. The in-plane displacements,  $u$  and  $v$ , are usually represented with a linear or quadratic polynomial. If the compatibility relation for two adjacent flat elements is derived, the resulting expression is given as [42]:

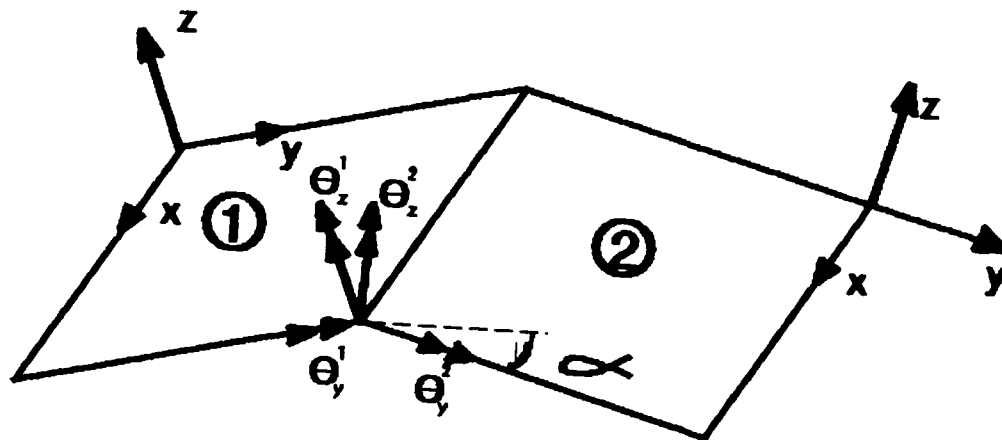


Fig 2.6 Flat Plate Element Representing a Curved Shell [42]

$$\begin{aligned}
 (v^1 - v^2) \cos(\alpha/2) - (w^1 + w^2) \sin(\alpha/2) &= 0 \\
 (w^1 - w^2) \cos(\alpha/2) - (v^1 + v^2) \sin(\alpha/2) &= 0
 \end{aligned}
 \tag{2.39}$$

If one examines Eqn (2.39) it is evident that the displacement compatibility along the interface of the two elements cannot be satisfied (if  $v$  is quadratic, it cannot fit the same curve as the cubic,  $w$ ) unless  $v$  and  $w$  are

represented by polynomials of the same order. To overcome this displacement nonconformity the QUA411 uses a third order polynomial to represent  $u$  in the  $y$ -direction (quadratic in  $y$ ) and  $v$  in the  $x$ -direction (quadratic in  $x$ ). The lateral deflection,  $w$ , is represented by a cubic polynomial in  $x$  and  $y$ . The QUA411 element adds a shear term,  $\gamma$ , at each corner node and an in-plane tangent displacement,  $t$ , at the side nodes [42]. Rotational compatibility is enforced only at the nodes, thus the 411 element is a nonconforming bending element. The derivation of the shape functions associated with these assumed displacement fields is given in [42].

#### 2.2.6 Equations of Motion

Since the analysis is static, the problem is one of solving the equation of static equilibrium, namely:

$$\sum \text{Forces} = 0 \quad (2.40)$$

During static equilibrium, the potential energy,  $\Pi_p$ , must be at a minimum and the first variation of potential energy,  $\delta\Pi_p$ , will be zero. This yields the equilibrium equation. For bifurcation analysis (either linear or nonlinear), the second variation,  $\delta^2\Pi_p$ , is also zero at the collapse point.

The nonlinear studies considered in this effort seek a limit point in the loading curve rather than an actual bifurcation point. It is well known that curved cylindrical panels have post buckling at decreased loads only, so the first limit point is the actual collapse load, as seen in Fig 2.7. As shown in Fig 2.7, the solution derived by linear bifurcation may be either higher or lower than the actual solution [44]. For a cylindrical panel with cutouts, the bifurcation value is too high. While with large cutouts the bifurcation values become too low [35]. The use of nonlinear bifurcation is limited and will not be used in this thesis.

The total potential energy in a body is the internal strain energy minus the work of the applied forces, or:

$$\Pi_p = U - W \quad (2.41)$$

Both  $U$  and  $W$  can be calculated based upon the displacement field, with (Eqn (C.5), Appendix C):

$$U = \frac{1}{2} \int_A (\epsilon^o)^T [D] (\epsilon^o) dA \quad (2.42)$$

where  $(\epsilon^o)$  and  $[D]$  are defined in Appendix D and reference [36]. The work done by the applied forces is (Eqn (C.12), Appendix C):

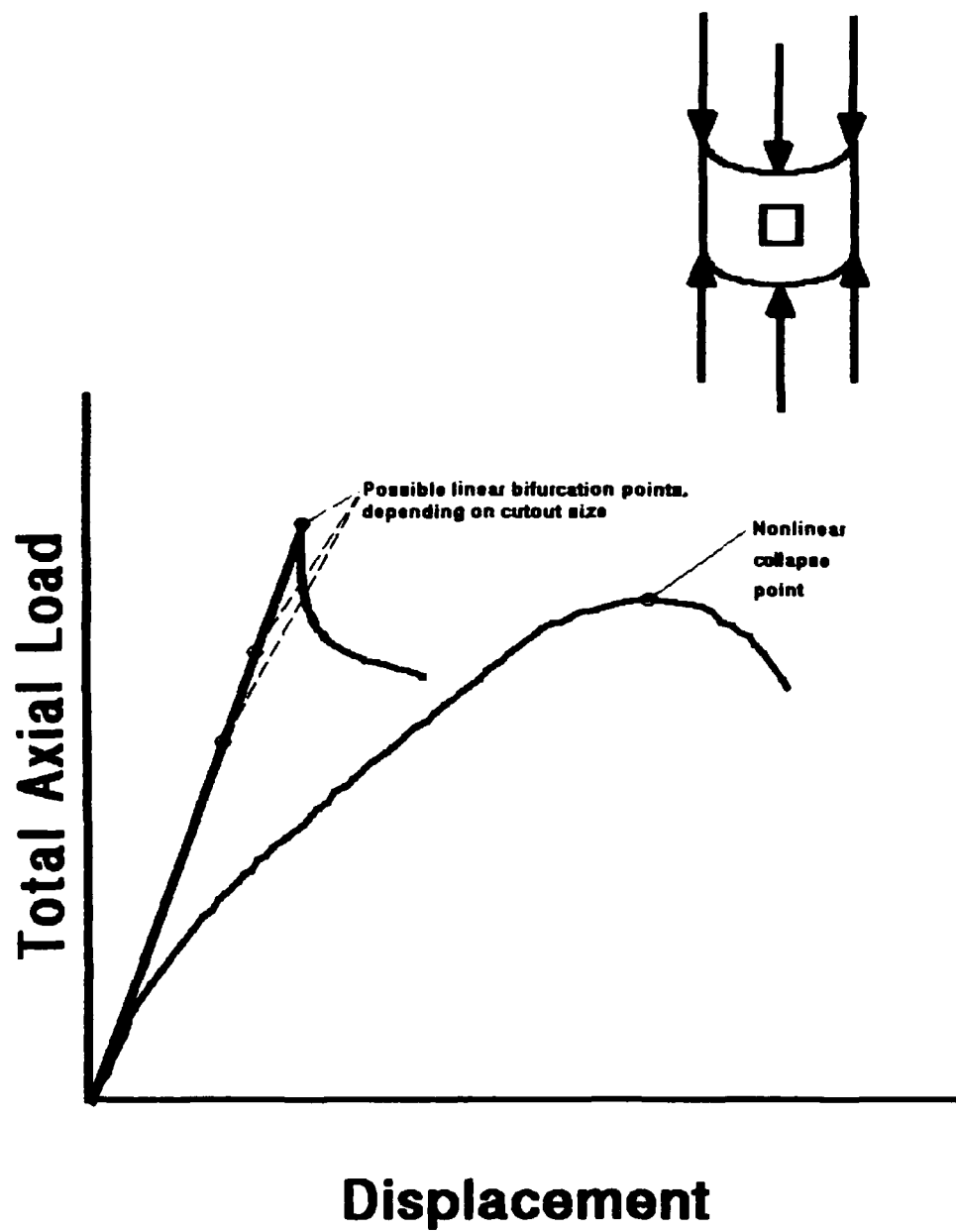


Fig 2.7 Load Displacement Curve for Typical Cylindrical Panel



$$W = (a)^T(f) \quad (2.43)$$

where,

(a) = vector of displacements

(f) = vector of externally applied forces

For applied displacements, STAGS calculates a load which results in the proper displacements.

The details of the modified Newton-Raphson method are given in the STAGS theory manual [26], by which a stiffness matrix from a previous step is used to estimate the displacement for a given load increment.

Although Bauld [16] used a finite difference formulation in solving the strain energy relationship, the method in determining the equation of motion is conceptually the same as STAGS. Bauld separated the strain energy into quadratic, cubic, and quartic displacement terms:

$$2U = d_{ij} a_i a_j + d_{ijk} a_i a_j a_k + d_{ijkl} a_i a_j a_k a_l \quad (2.44)$$

The tensors  $d_{ij}$ ,  $d_{ijk}$ , and  $d_{ijkl}$  are independent of the displacement vector  $a_i$  and are assumed to be symmetrized. Details for the tensor determination are found in [16]. Bauld goes on to give the total potential energy as:

$$\Pi_p = \left( \frac{1}{2} A_{rs} + \frac{1}{6} N1_{rs} + \frac{1}{12} N2_{rs} \right) a_r a_s - R_s a_s \quad (2.45)$$

$A_{rs}$  is the linear stiffness matrix with no dependence on the displacement vector,  $a$ .  $N1_{rs}$  and  $N2_{rs}$  are stiffness matrices with linear and quadratic dependence, respectively, on displacement.  $R_s$  is the applied surface force vector. Taking the first variation of this in order to satisfy minimum potential energy, one obtains the equilibrium equation:

$$\left( A_{rs} + \frac{1}{2} N1_{rs} + \frac{1}{3} N2_{rs} \right) a_r - R_s = 0 \quad (2.46)$$

### 2.2.7 Solution Techniques

The STAGSC-1 computer program uses a Newton-Raphson or a modified Newton-Raphson (user defined) solution technique to solve the nonlinear equilibrium equations. For a linear problem in STAGSC-1, the solution technique is much easier since the stiffness matrix is not a function of displacements. The linear set of equations is given as:

$$[K](a) = (f) \quad (2.47)$$

where  $[K]$  is the stiffness matrix (constant),  $(a)$  is the set of nodal degrees of freedom (nodal parameters), and  $(f)$  is the applied loads. STAGSC-1 uses a Cholesky triangular decomposition with forward and backward substitution to solve Eqn (2.47) for  $(a)$  [42]. The solution for the nonlinear equilibrium equations is much more involved and is considered next.

An explanation of the reference systems in STAGSC-1 is necessary before progressing. There are basically two reference systems defined: a global reference system (subscript  $g$ ) and a local element reference system (subscript  $e$ ). The global reference system is fixed in space and does not move. The local reference system uses an updated Lagrangian approach. The local reference system, called a corotational system, is fixed to the element and moves with the element during rigid body motion [25]. This allows for the removal of rigid body motion in the element before calculating strain. The present version of STAGSC-1 (1986) also redefines the standard way of representing a rotation as a vector quantity. Rotations are defined by a triad (three mutually perpendicular unit vectors) to accurately map local rotations since they depend on order of rotation. The previous versions of STAGS used vectors to describe rotations which with large rotations gave spurious results (vectors cannot track order of

rotations and are only good for small rotations). This is the reason the QUAF 411 element was developed. The 411 element handles larger rotations, but with increased cost [46]. The reader is referred to [47] for a complete discussion on this rotational formulation. Finally, differentiation and integration within the element are done with respect to this corotational system [25].

For the STAGSC-1 quadrilateral element, the local reference system is defined as follows: An approximation of the warped element surface is made by crossing the principal diagonals of the element to form a vector and the establishing a plane normal to this vector such that one of the nodes lies on this plane. This node is where the local reference system is established by taking the z-axis normal to the plane, the x or y axis is located along one of the element edges, and the remaining axis completes a Cartesian right-handed system (see Fig 2.8) [47]. All local deformations of the element are referenced to this local system during an iteration for a solution. Once a solution has been found in the global system the local coordinates are updated and a new local reference system is established. This movement of the local reference system appears to be Eulerian except that the local coordinates of a point change [25]. Strains and rotations in a local reference system are usually small enough so as to ignore the nonlinear

stiffness matrix  $[K_L]$  and sometimes even the initial stress matrix  $[K_\sigma]$  that are a part of the tangential stiffness matrix [25]. This is only true for the local system, the global tangent stiffness matrix must, in general, contain all the terms (see Eqn (2.31)). From thorough research of the STAGS documentation, it appears that STAGS uses the full tangent stiffness matrix in both the global and the local systems to overcome difficulties in solutions due to highly nonlinear problems.

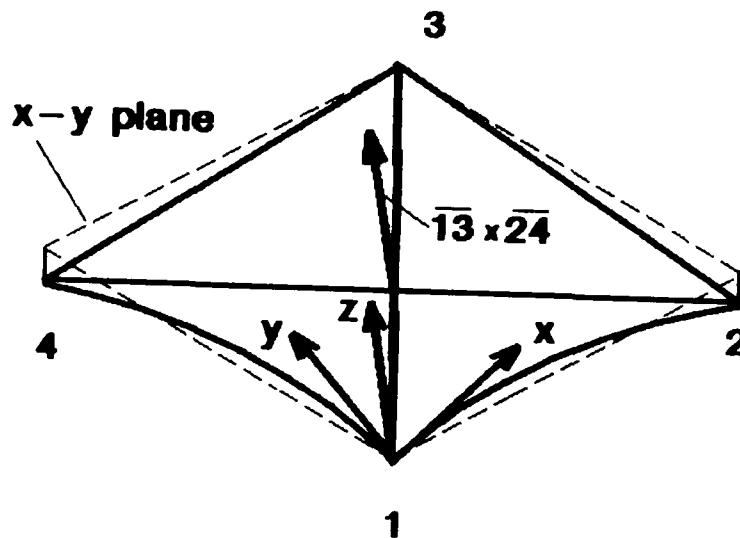


Fig 2.8 Quadrilateral Element Local Reference Systems [47]

With the reference systems defined, the Newton-Raphson solution techniques can be explained. To start, expand the expression for the sum of the external and internal forces,  $(\psi)$  (see Appendix C), in a Taylor expansion:

$$\left\{ \psi(a)^{n+1} \right\} = \left\{ \psi(a)^n \right\} + \left( \frac{d(\psi)}{d(a)} \right) (\Delta a)^n + \text{H.O.T.} = 0 \quad (2.48)$$

where H.O.T. means higher order terms and,

$$(a)^{n+1} = (a)^n + (\Delta a)^n \quad (2.49)$$

From Eqn (F.4) (see Appendix F):

$$\frac{d(\psi)}{d(a)} = [K_T] \quad (2.50)$$

where  $[K_T]$  is the tangent stiffness matrix, a function of displacements. If one uses the expression for  $(\psi)$  in Eqn (C.15) (Appendix C) and writes it as a function of displacements for the nonlinear problem one obtains [27]:

$$(\psi(a)) = [K(a)](a) - (f) \quad (2.51)$$

where,

$[K(a)](a)$  = internal resisting forces of the element

$(f)$  = externally applied loads

Inserting Eqns (2.50) and (2.51) into Eqn (2.482) and eliminating the higher order terms results in:

$$[K_T](\Delta a)^n = (f) - [K(a)^n](a)^n \quad (2.52)$$

The problem now is to find the displacements within the elements that balance the externally applied loads and the internal resisting forces (i.e. the sum of the right hand side of Eqn (2.52) equaling zero). Since an updated Lagrangian approach is being used, the internal deformations are relative to the local reference system, therefore the last expression in Eqn (2.52) needs to be written in terms of the local displacements. Rewriting Eqn (2.52) in terms of the local (subscript e) and global (subscript g) displacements results in [25]:

$$[K_T](\Delta a_g^n) = (f) - \sum [k(a_e)^n](a_e)^n \quad (2.53)$$

where,

$\sum [k(a_e)^n](a_e)^n$  = internal resisting forces transformed into the global system and summed

For simplicity, the Newton-Raphson solution technique is given as follows [25]:

1. Increment the applied load ( $f$ ).
2. Establish the local coordinates for each element.
3. Formulate the element tangent stiffness matrices in terms of their local degrees of freedom.
4. Transform the local tangent stiffness matrices to the global coordinate system and assemble them into the global stiffness matrix.
5. Compute the values of the local degrees of freedom ( $a_e$ ) (zero for the first iteration within each load step) from the global degrees of freedom ( $a_g$ ).
6. Calculate the element internal forces  $[k(a_e)](a_e)$ . Transform these forces to the global system and assemble them with the other element internal forces.
7. Solve Eqn (2.53) for ( $\Delta a_g$ ).
8. If the vector ( $\Delta a_g$ ) is not small enough (i.e. converges) return to step 3.

After the solution converges (step 8) return to step 1 and repeat. Once the solution has converged for the final load step ( $f$  has been incremented to equal the final load) the solution is complete.

An alternate solution technique is the modified Newton-Raphson method. This is the method used in STAGS for this effort. In this method the tangent stiffness matrix is



not reformulated at every iteration within a load step. The previously assembled stiffness matrix is used for successive iterations and is only refactored when the convergence rate dictates [25].

STAGS allows the user to control many of the parameters in the solution process to include: either using the full or modified Newton-Raphson method, control of the load step size, the number of attempts at a solution if convergence difficulties arise, and whether the Riks solution algorithm or the Thurston Equivalence Transformation method is used. For this effort, the Riks solution algorithm is used. This algorithm is explained in greater detail in Section 2.3.5.

### 2.3 SHELL Theory

SHELL was developed in 1986 by Scott Dennis as part of his Ph.D. dissertation [41]. Its primary purpose is the analysis of thin, cylindrical, shell structures. It is based entirely upon the finite element method. SHELL's primary capability is the nonlinear large displacement and moderate rotation characteristics of thin shells with the added feature of including through the thickness shear strain. The basic element used in SHELL is a cylindrical shell element that can exactly match the curvature of the shell surface. The nonlinear analysis is based upon either the Donnell approximations (similar to Von Karman plate relations but has curvature incorporated within the kinematic equations) or the exact nonlinear kinematic relations. And the additional feature, mentioned above, of this program is that SHELL incorporates a parabolic distribution for transverse shear strain.

For this effort, the exact nonlinear kinematic relations are discussed herein because of the larger rotations (on the order of  $\approx 30^\circ$ ) encountered in the panels that are not simply supported along the vertical edges (see Sections 3 and 4). These large rotations far exceed the assumptions made for the Donnell relations, thereby

invalidating them. A brief look at the theory for this cylindrical shell element and the governing relations used in SHELL is presented in the following sections.

Bathe and Ho [48] stated the following set of criteria for a desirable shell element:

- 1.) No spurious zero-energy modes should exist, so that reliable results can always be expected. No numerical fudge factors should be necessary, either.
- 2.) The element should be applicable to general shell structures, including those with beam stiffeners, cutouts, intersections, etc.
- 3.) The element should be cost-effective for linear as well as nonlinear static and dynamic analysis. This implies that the degrees of freedom is held to a minimum. It should allow analysis of large displacement and large rotation problems, and materially nonlinear situations.

Criterion 1 is achieved in this formulation. The code has not been developed beyond the research stage, so application to other than plate and cylindrical shell cases modeled with rectangular elements is not yet possible. However, the theory is not restricted geometrically, so criterion 2 is somewhat met. Material linearity is assumed in the formulation of the element, so criterion 3 is only partially

fulfilled. The incorporation of through thickness shear effects in a shell structure while maintaining a two dimensional analysis well satisfies the first part of this criterion, however.

The following development applies specifically to cylindrical geometry. Dennis [24] presents the general case of a doubly curved shell.

### 2.3.1 Geometry and Assumptions

The curvilinear orthogonal coordinate system and nomenclature used in this formulation of the laminated cylindrical shell is shown in Fig 2.9. The x-axis lies along the straight dimension of the panel; the s-axis follows the circumference, and the z-axis is everywhere normal to the shell middle surface, positive toward the center of curvature. The surface formed by the x and s axes lies in the center of the thickness of the panel, so the thickness coordinate is negative on the outer surface and positive on the inner surface. Displacements along the x, s and z axes are u, v and w respectively. In the early vectorial development the coordinate  $\theta$  is used instead of s for the purpose of generality, s is used when specializing to the cylindrical geometry. Since the structure analyzed here is an open shell, the angle  $\theta$  is also useful for

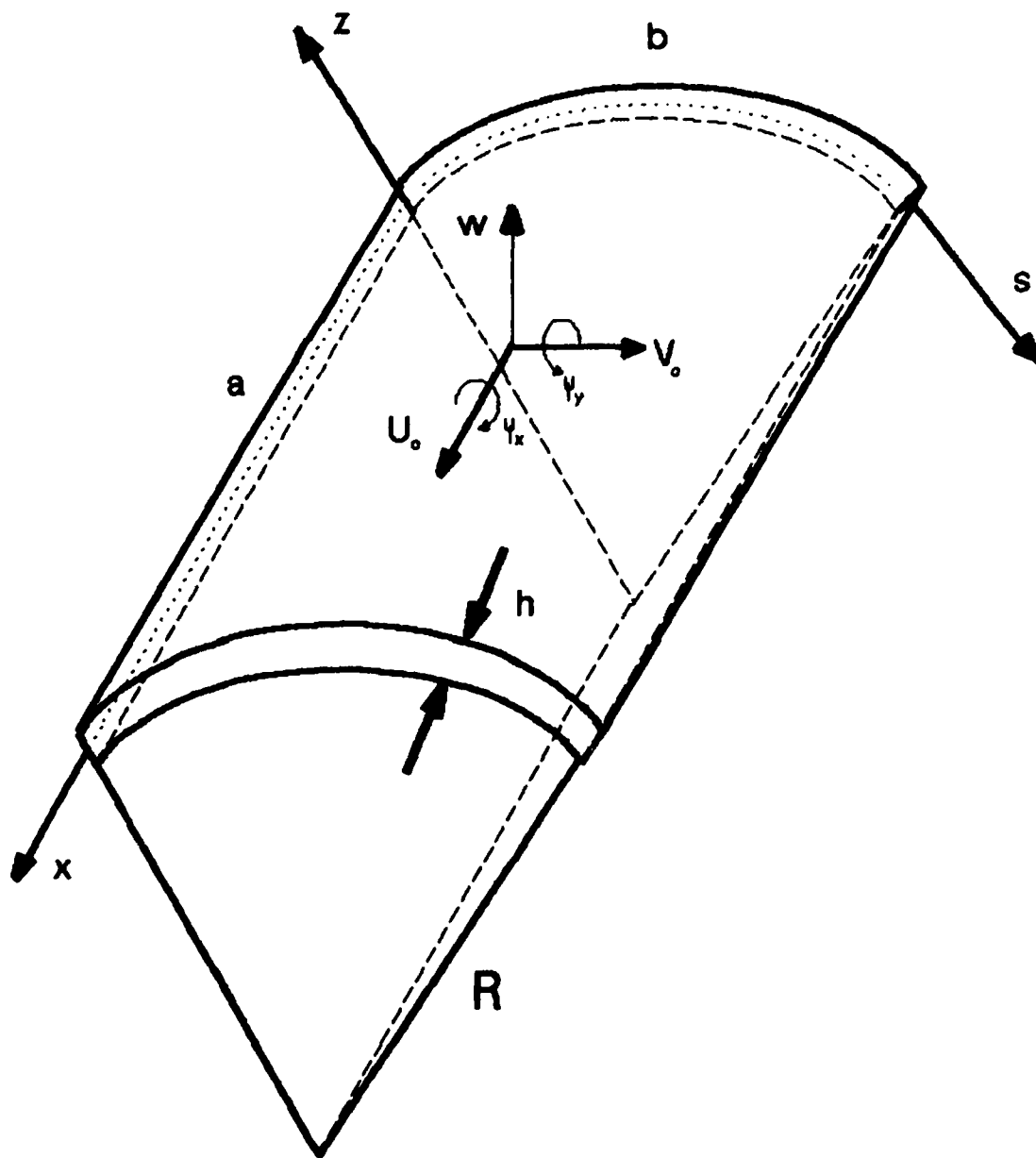


Fig 2.9 Cylindrical Shell Geometry

describing shallowness. The angle  $\phi$  specifies the orientation angle of each ply in the laminate. Subscripts denoting stress and strain orientation are explained in Table 2.2 and Figure 2.4.

Table 2.2. SHELL Contracted Notation

stress		strain		cylindrical
explicit	contracted	explicit	contracted	coordinates
$\sigma_{11}$	$\sigma_1$	$\epsilon_{11}$	$\epsilon_1$	x → 1
$\sigma_{22}$	$\sigma_2$	$\epsilon_{22}$	$\epsilon_2$	s → 2
$\sigma_{33}$	$\sigma_3$	$\epsilon_{33}$	$\epsilon_3$	z → 3
				shear:
$\sigma_{23}$	$\sigma_4$	$\epsilon_{23}$	$\epsilon_4$	s-z → 4
$\sigma_{13}$	$\sigma_5$	$\epsilon_{13}$	$\epsilon_5$	x-z → 5
$\sigma_{12}$	$\sigma_6$	$\epsilon_{12}$	$\epsilon_6$	x-s → 6

### 2.3.2 Constitutive Development

The development of the constitutive relations for SHELL is shown in Appendix E. It is identical to Section 2.2.2 except it assumes a modified plane stress relationship. This modified relationship allows  $\sigma_3 = 0$  but it assumes  $\sigma_4$  and  $\sigma_5$  are not equal to zero, thereby incorporating nonzero through the thickness shear stress. Therefore, following

the same logical progression in Section 2.2.2, but now incorporating the modified plane stress relation, the reduced stiffness constitutive relation becomes [45]:

$$\begin{Bmatrix} \sigma_1 \\ \sigma_2 \\ \sigma_6 \\ \sigma_4 \\ \sigma_5 \end{Bmatrix} = \begin{bmatrix} Q_{11} & Q_{12} & 0 & 0 & 0 \\ Q_{12} & Q_{22} & 0 & 0 & 0 \\ 0 & 0 & Q_{66} & 0 & 0 \\ 0 & 0 & 0 & Q_{44} & 0 \\ 0 & 0 & 0 & 0 & Q_{55} \end{bmatrix} \begin{Bmatrix} \epsilon_1 \\ \epsilon_2 \\ \epsilon_6 \\ \epsilon_4 \\ \epsilon_5 \end{Bmatrix} \quad (2.54)$$

where the  $Q_{ij}$  are reduced stiffness coefficients related to the  $S$ 's by

$$Q_{ij} = S_{ij} - \frac{S_{i3}S_{j3}}{S_{33}} \quad (2.55)$$

In terms of the engineering coefficients again,

$$\begin{aligned} Q_{11} &= \frac{E_1}{\Delta} \\ Q_{22} &= \frac{E_2}{\Delta} \\ Q_{12} &= \frac{\nu_{21}E_2}{\Delta} \\ Q_{44} &= G_{23} \\ Q_{55} &= G_{13} \\ Q_{66} &= G_{12} \end{aligned} \quad (2.56)$$

where,  $\Delta = 1 - v_{12}v_{21}$ .

Finally, in order to analyze a stack of plies, they must all be referenced to a global axis system and their effects summed (Appendix E, Eqn (E.6)):

$$\left\{ \sigma_i \right\}_k = \left[ \begin{array}{c} T \\ T \end{array} \right] \left[ \begin{array}{c} Q_{ij} \\ Q_{ij} \end{array} \right]_k \left[ \begin{array}{c} T \\ T \end{array} \right]^T \left\{ \varepsilon_i \right\}_k \quad (2.57)$$

where (see Appendix E, Eqn (E.5)),

$$\left[ \begin{array}{c} T \\ T \end{array} \right] = \left[ \begin{array}{ccc} c^2 & s^2 & -2cs \\ s^2 & c^2 & 2cs \\ cs & -cs & c^2 - s^2 \end{array} \right] \text{ for } \left[ \begin{array}{ccc} Q_{11} & Q_{12} & 0 \\ Q_{12} & Q_{22} & 0 \\ 0 & 0 & Q_{66} \end{array} \right]$$

$$\left[ \begin{array}{c} T \\ T \end{array} \right] = \left[ \begin{array}{cc} c & -s \\ s & c \end{array} \right] \text{ for } \left[ \begin{array}{cc} Q_{44} & 0 \\ 0 & Q_{55} \end{array} \right] \quad (2.58)$$

and  $c = \cos(\theta)$ ,  $s = \sin(\theta)$ . With this transformation the constitutive relations are:

$$\left\{ \sigma_i \right\}_k = \left[ \begin{array}{c} \bar{Q}_{ij} \\ \bar{Q}_{ij} \end{array} \right]_k \left\{ \varepsilon_i \right\}_k \quad (2.59)$$

and the transformed reduced stiffnesses are shown in Appendix E, Eqn (E.8).



### 2.3.3 Strain-Displacement Relations

The geometric nonlinearity arising from the panel's curvature is incorporated by the strain-displacement relations. It is also here that the through thickness shear effects are incorporated into the analysis. This development follows Dennis [41] who authored the computer code which employs these relations.

The incorporation of transverse shear effects is accomplished by assuming a modified state of plane stress for the lamina in which  $\sigma_3 = 0$  (and hence  $\epsilon_3 = 0$ ) but  $\sigma_4$  and  $\sigma_5$  are allowed to be small nonzero values. These transverse shear stresses are assumed to equal zero on the top and bottom surfaces of each ply, and the associated strains will vary parabolically through the ply thickness.

To proceed, keeping just the linear (first order) displacement terms for the transverse shear strains  $\epsilon_4$  and  $\epsilon_5$  we see that [2]:

$$\begin{aligned}\epsilon_4 &= \frac{1}{h_2} \left( u_{3,2} + h_2 u_{2,3} - u_2 h_{2,3} \right) \\ \epsilon_5 &= \frac{1}{h_1} \left( u_{3,1} + h_1 u_{1,3} - u_1 h_{1,3} \right)\end{aligned}\tag{2.60}$$

where the  $h_i$  are the coordinate system scale factors; for

the cylindrical geometry used in this work,  $h_1 = 1$  and  $h_2 = 1 - z/R$ .

The displacement equations in the thickness variable  $z$  which permit the incorporation of the desired through thickness feature are [41]:

$$\begin{aligned} u(x, \theta, z) &= u^0 + z\psi_1 + z^2\theta_1 + z^3\gamma_1 + z^4\theta_1 \\ v(x, \theta, z) &= v^0 \left(1 - \frac{z}{R}\right) + z\psi_2 + z^2\theta_2 + z^3\gamma_2 + z^4\theta_2 \quad (2.61) \\ w(x, \theta) &= w \end{aligned}$$

where  $u^0$ ,  $v^0$ ,  $w$ ,  $\psi_i$ ,  $\theta_i$ ,  $\gamma_i$  and  $\theta_i$  are functions of the coordinates  $x$  and  $\theta$ . The displacements  $u^0$  and  $v^0$  are of the shell middle surface; transverse displacement  $w$  is the same throughout the thickness since transverse normal strain is assumed negligible. The  $\psi_i$  terms are rotations of the surface normals in the  $x$  and  $s$  planes, and  $\theta_i$ ,  $\gamma_i$  and  $\theta_i$  are to be found by applying the assumption that transverse shear stresses  $\sigma_4$  and  $\sigma_5$  are zero on the shell surfaces. Substituting the equations for  $v$  and  $w$  into Eq (2.60) for  $\epsilon_4$  yields [41]:

$$\epsilon_4 = \frac{1}{1-z/R} \left[ w_{,2} + (1-z/R) \left( -\frac{v^0}{R} + \psi_2 + 2z\theta_2 + 3z^2\gamma_2 + 4z^3\theta_2 \right) + \frac{1}{R} \left\{ v^0 \left( 1 - \frac{z}{R} \right) + z\psi_2 + z^2\theta_2 + z^3\gamma_2 + z^4\theta_2 \right\} \right] \quad (2.62)$$

For zero transverse shear stress at the surfaces, the associated strain will also be zero. Enforcing this condition by substituting  $\pm h/2$  for  $z$  in Eqn (2.62), setting both resulting expressions to zero and hence equal to each other, then solving for the unknown variables produces [41]:

$$\begin{aligned} \theta_2 &= 0 \\ \theta_2 &= \frac{\gamma_2}{2R} \end{aligned} \quad (2.63)$$

$$\left[ 1 - \frac{h^2}{8R^2} \right] \gamma_2 = \frac{-4}{3h^2} (\psi_2 + w_{,2})$$

Note that an  $h/R$  value of  $1/5$  (quite high for practical aerospace shell geometries) allows neglect of the  $h/R$  term in the left side of Eqn (2.63). Replacing  $\theta_2$ ,  $\theta_2$  and  $\gamma_2$  in Eqn (2.62) with the results in Eqn (2.63) yields the transverse shear strain  $\epsilon_4$  in terms of transverse displacement  $w$  and rotation  $\psi_2$  [41]:

$$\epsilon_4 = \frac{1}{1-z/R} (w_{,2} + \psi_2) \left( 1 - \frac{4z^2}{h^2} + \frac{8z^3}{3h^2R} \right) \quad (2.64)$$

Note again that there are  $1/R$  terms to be neglected. Therefore, the transverse shear strain-displacement relations,  $\epsilon_4$ , along with a similar analysis with  $\epsilon_5$  (simpler since  $h_1 = 1$ ), become [41]:

$$\epsilon_4 = \frac{1}{1-z/R} (w_{,2} + \psi_2) \left( 1 - \frac{4z^2}{h^2} \right) \quad (2.65a)$$

$$\epsilon_5 = (w_{,1} + \psi_1) \left( 1 - \frac{4z^2}{h^2} \right) \quad (2.65b)$$

Replacing  $\theta_i$ ,  $\theta_i$  and  $\gamma_i$  in Eq (2.61) yields the displacement equations [41]:

$$\begin{aligned} u(x, \theta, z) &= u^0 + z\psi_1 - \frac{4}{3h^2} z^3 (\psi_1 + w_{,1}) \\ v(x, \theta, z) &= v^0 \left( 1 - \frac{z}{R} \right) + z\psi_2 - \frac{4}{3h^2} z^3 (\psi_2 + w_{,2}) \\ w(x, \theta) &= w \end{aligned} \quad (2.66)$$

At this point one can note that this formulation provides seven degrees of freedom:  $u$ ;  $v$ ;  $w$ ;  $w_{,1}$ ;  $w_{,2}$ ;  $\psi_1$  and  $\psi_2$ .

Now that we have displacement equations which incorporate a parabolic through thickness shear stress

distribution, the in-plane kinematic equations are derived for the shell middle surface. The fully general strain displacement relations are quite extensive; the theoretical development incorporating them can be found in Dennis' large displacement - moderate rotation general shell development [41]. The general strain displacement relations of Eqns (2.9) and (2.10) with the kinematics of Eqn (2.66) will give the in-plane shell strain displacement relations. These expressions can be specialized for a shell geometry of interest by defining the scale factors,  $h_i$ , used in Eqn (2.67) [41].

$$\begin{aligned} h_1 &= \alpha_1(1 - z/R_1) \\ h_2 &= \alpha_2(1 - z/R_2) \\ h_3 &= 1 \end{aligned} \tag{2.67}$$

where  $\alpha_\gamma^2 = g_{\gamma\gamma}$  (no sum).

Substituting Eqn (2.67) into Eqns (2.9) and (2.10) and carrying out the indicated differentiation yields for the in-plane strain-displacement equations [41]:

$$\begin{aligned}
\epsilon_1 &= \frac{\gamma_{11}}{h_1^2} = \epsilon_1^0 + z x_1^1 + z^2 x_1^2 + z^3 x_1^3 + z^4 x_1^4 + z^6 x_1^6 \\
\epsilon_2 &= \frac{\gamma_{22}}{h_2^2} = \epsilon_2^0 + z x_2^1 + z^2 x_2^2 + z^3 x_2^3 + z^4 x_2^4 + z^6 x_2^6 \\
\epsilon_6 &= \frac{2\gamma_{11}}{h_1 h_2} = \epsilon_6^0 + z x_6^1 + z^2 x_6^2 + z^3 x_6^3 + z^4 x_6^4 + z^6 x_6^6
\end{aligned} \tag{2.68}$$

where the  $\epsilon_j^0$  and the  $x_j^I$  terms ( $j=1,2,6$ ;  $I=1,2,3,4,6$ ) are functions of the displacements and the scale factors, and can be found in Appendix A of [41]. It is noted that the superscripts on the  $x_j^I$  are not exponents, they are individual strain components that correspond to the power of  $z$  that multiplies it, and the subscripts on  $x_j^I$  indicate the strain,  $\epsilon_1$ ,  $\epsilon_2$ , or  $\epsilon_6$  that these components correspond with.

The following equivalent representation of the strains is conducive to the matrix operations of the potential energy formulation in the next section. The in-plane strain displacement relations are represented by [41]:

$$\varepsilon_1 = \varepsilon_1^0 + z^p \chi_{1p} ; (p = 1, \dots, 7) \quad (2.69a)$$

where,

$$\varepsilon_1^0 = u_{,1} + \frac{1}{2} \left( u_{,1}^2 + v_{,1}^2 + w_{,1}^2 \right)$$

$$\varepsilon_2 = \varepsilon_2^0 + z^p \chi_{2p} ; (p = 1, \dots, 7) \quad (2.69b)$$

where,

$$\varepsilon_2^0 = v_{,2} - \frac{w}{R} + \frac{1}{2} \left( u_{,2}^2 + v_{,2}^2 + w_{,2}^2 + \frac{v^2}{R^2} + \frac{w^2}{R^2} \right) + \frac{vw_{,2}}{R} - \frac{v_{,2}w}{R}$$

$$\varepsilon_6 = \varepsilon_6^0 + z^p \chi_{6p} ; (p = 1, \dots, 7) \quad (2.69c)$$

where,

$$\varepsilon_6^0 = u_{,2} + v_{,1} + u_{,1}u_{,2} + v_{,1}v_{,2} + w_{,1}w_{,2} + \frac{1}{R} \left( vw_{,1} - v_{,1}w \right)$$

Note: The higher order bending strain-displacement relations,  $\chi_{ip}$  ( $i=1,2,6$ ;  $p=1,\dots,7$ ), are completely shown in [41].

The transverse shear strains (in similar form) are [41]:

$$\begin{aligned} \varepsilon_4 &= \varepsilon_4^0 + z^p \chi_{4p} ; & \varepsilon_4^0 &= w_{,2} + \psi_2 \\ \chi_{42} &= 3k(w_{,2} + \psi_2) \end{aligned} \quad (2.70a)$$

$$\chi_{4p} (p = 1, 3, 4, 5, 6, 7) = 0$$

$$\begin{aligned} \varepsilon_5 &= \varepsilon_5^0 + z^p \chi_{5p} ; & \varepsilon_5^0 &= w_{,1} + \psi_1 \\ \chi_{52} &= 3k(w_{,1} + \psi_1) \end{aligned} \quad (2.70b)$$

$$\chi_{5p} (p = 1, 3, 4, 5, 6, 7) = 0$$

This allows assembly of the strain displacement equations into a matrix format which will become convenient in the next section:

$$\begin{Bmatrix} \epsilon_1 \\ \epsilon_2 \\ \epsilon_6 \end{Bmatrix} = \begin{Bmatrix} \epsilon_1^0 \\ \epsilon_2^0 \\ \epsilon_6^0 \end{Bmatrix} + \begin{bmatrix} x_{11} & x_{12} & x_{13} & x_{14} & x_{15} & x_{16} & x_{17} \\ x_{21} & x_{22} & x_{23} & x_{24} & x_{25} & x_{26} & x_{27} \\ x_{61} & x_{62} & x_{63} & x_{64} & x_{65} & x_{66} & x_{67} \end{bmatrix} \begin{Bmatrix} z \\ z^2 \\ z^3 \\ z^4 \\ z^5 \\ z^6 \\ z^7 \end{Bmatrix} \quad (2.71)$$

$$\begin{Bmatrix} \epsilon_4 \\ \epsilon_5 \end{Bmatrix} = \begin{Bmatrix} \epsilon_4^0 \\ \epsilon_5^0 \end{Bmatrix} + \begin{bmatrix} x_{42} \\ x_{52} \end{bmatrix} z^2$$

In a general expression,

$$\{\epsilon\} = \{\epsilon^0\} + [x]\{z\} \quad (2.72)$$

It is worth noting that these kinematics avoid the common pitfall of shear locking, wherein the model becomes artificially stiff as the shell thickness is decreased. This is a problem with finite element formulations which incorporate constant or linearly distributed shear strain through the thickness, and it necessitates the use of a correction factor. However, examination of the compatibility relations associated with the



strain displacement equations developed in this section shows that the terms associated with transverse shear drop out as thickness is reduced to zero (see [41]).

Note the kinematics developed in this section are specifically for the cylindrical geometry. The analysis accomplished for this thesis uses the large displacement - moderate rotation formulations.

#### 2.3.4 Equations of Motion

The shell potential energy is the sum of the internal strain energy and the work done by external forces:

$$\Pi_p = U + V \quad (2.73)$$

where the internal strain energy is given by:

$$U = \int_{\Omega} \int_h \frac{1}{2} \left( [\bar{Q}] \{ \bar{\epsilon} \} \right)^T \{ \bar{\epsilon} \} d\Omega dh \quad (2.74)$$

where  $\Omega$  represents the shell middle surface. The internal strain energy  $U$  is composed of in plane and normal terms (set 1), and transverse shear terms (set 2). Expanding the expression for  $U_1$  and  $U_2$  by inserting Eq (2.69) through (2.72) into Eq (2.74) gives

$$\begin{aligned}
U_1 = \frac{1}{2} \int_{\Omega} \int_h \left[ \bar{Q}_{11} (\epsilon_1^o + z^p x_{1p})^2 + \bar{Q}_{22} (\epsilon_2^o + z^p x_{2p})^2 \right. \\
+ 2\bar{Q}_{12} (\epsilon_1^o + z^p x_{1p})(\epsilon_2^o + z^r x_{2r}) + \bar{Q}_{66} (\epsilon_6^o + z^p x_{6p})^2 \\
+ 2\bar{Q}_{16} (\epsilon_1^o + z^p x_{1p})(\epsilon_6^o + z^r x_{6r}) \\
\left. + 2\bar{Q}_{26} (\epsilon_2^o + z^p x_{2p})(\epsilon_6^o + z^r x_{6r}) \right] dz d\Omega
\end{aligned} \tag{2.75}$$

$$\begin{aligned}
U_2 = \frac{1}{2} \int_{\Omega} \int_h \left[ \bar{Q}_{44} (\epsilon_4^o + z^2 x_{42})^2 + \bar{Q}_{55} (\epsilon_5^o + z^2 x_{52})^2 \right. \\
\left. + 2\bar{Q}_{45} (\epsilon_4^o + z^2 x_{42})(\epsilon_5^o + z^2 x_{52}) \right] dz d\Omega
\end{aligned}$$

where  $p, r = 1, 2, \dots, 7$ . Integrating the  $z$  over  $\pm h/2$  yields the equation for strain energy as a function of the middle surface only, which is the desired formulation for this shell problem. A further simplification performed in the coding of the SHELL program is one of symmetry in ply lay-up. This results in the cancellation of elasticity arrays which are multiplied by odd powers of the transverse coordinate  $z$ . Rearranging (see [41]) yields the final forms of:

$$\begin{aligned}
U_1 = \frac{1}{2} \int_{\Omega} \{ \epsilon^o \}^T [A] \{ \epsilon^o \} d\Omega \\
+ \frac{1}{2} \int_{\Omega} 2 \{ \epsilon^o \}^T \left( [B] + [D] + [E] + [F] + [G] + [H] + [I] \right) \{ \chi \} d\Omega \\
+ \frac{1}{2} \int_{\Omega} \{ \chi \}^T \left( [D] + [E] + [F] + [G] + [H] + [I] + [J] + [K] + [L] \right. \\
\left. + [P] + [R] + [S] + [T] \right) \{ \chi \} d\Omega
\end{aligned} \tag{2.76a} \tag{1,2,6}$$

$$U_2 = \frac{1}{2} \int_{\Omega} \left( \{\mathbf{x}^0\}^T [\mathbf{A}] \{\mathbf{x}\} + 2\{\mathbf{x}^0\} [\mathbf{D}] [\mathbf{x}] + [\mathbf{x}]^T [\mathbf{F}] [\mathbf{x}] \right) d\Omega \quad (2.76b)$$

(4,5)

where  $\{[\mathbf{A}, \mathbf{B}, \mathbf{D}, \mathbf{E}, \mathbf{F}, \mathbf{G}, \mathbf{H}, \mathbf{I}, \mathbf{J}, \mathbf{K}, \mathbf{L}, \mathbf{P}, \mathbf{R}, \mathbf{S}, \mathbf{T}]\}$

$$= \int_h [\bar{\mathbf{Q}}] \{1, z, z^2, z^3, z^4, z^5, z^6, z^7, z^8, z^9, z^{10}, z^{11}, z^{12}, z^{13}, z^{14}\} dz. \quad (2.77)$$

### 2.3.5 Finite Element Formulation

The solution of the static finite element problem involves finding the equilibrium state between applied load and structural response. This state can be determined by finding where the system potential energy is stationary, i.e. where its variation is zero. Recall Eq (2.73):

$$\Pi_p = U + V \quad (2.78)$$

where now internal strain energy can be represented by

$$U = \frac{1}{2} \mathbf{a}^T \left[ \mathbf{K} + \mathbf{N}_1 + \mathbf{N}_2 \right] \mathbf{a} \quad (2.79)$$

where  $\mathbf{a}$  = column array of nodal displacements,  $\mathbf{K}$  = constant

stiffness terms,  $N_1$  = stiffness terms linear in displacement, and  $N_2$  = stiffness terms nonlinear in displacement. This collective group of stiffness terms is known as the tangent stiffness matrix  $K_T$ , since it defines the local slope of the load - displacement curve at any point of equilibrium. The external work can be represented as

$$V = - a^T \lambda P \quad (2.80)$$

where  $P$  is a column array of applied nodal loads and  $\lambda$  is a multiplier whose utility will be seen in the section on the solution algorithm. Equilibrium is defined as the state at which internal strain energy and external work balance; potential energy is at a relative minimum here. This point can be found by substituting Eqns (2.79) and (2.80) into Eqn (2.82) and taking the first variation:

$$\delta \Pi_p = \delta a^T [K_T a - \lambda P] = 0 \quad (2.81)$$

Since displacements  $\delta a$  are nonzero for all but the trivial solution, the bracketed expression must be zero for equilibrium. It is a function (call it  $g$ ) of  $a$  and  $\lambda$ :

$$K_T a - \lambda P = 0 = g(a, \lambda) \quad (2.82)$$

Since  $K_T$  varies with load and displacement, a numerical iterative solution is preferred to attempting to solve in closed form. Therefore, to determine the nodal displacements  $a$  for a given applied load  $P$ , Eqn (2.82) is solved iteratively by the modified Newton-Raphson method as discussed next.

The technique advanced by Riks [49] and Wempner [50] and demonstrated by Crisfield [55] of incrementing a desired arc length along the load-displacement curve, while solving iteratively via the modified Newton-Raphson method, is the solution technique used in this work. The modified Riks-Wempner algorithm, added to the SHELL program by Tsai and Palazotto [51], allows for tracing of the load-displacement response through both load reversing (snap through) and displacement reversing (snap back) critical points, so the most complex behavior can be continuously followed.

The essence of the Riks/Wempner method is that neither load  $P$  nor displacement  $a$  is independently controlled; rather, a selected arc length  $\Delta s$  of the load-displacement curve is incremented. The equilibrium condition is found which satisfies the constraint relation:

$$\Delta \bar{a}_{i+1}^T \Delta \bar{a}_{i+1} + \Delta \lambda_{i+1}^2 P^T P = \Delta s^2 \quad (2.83)$$

where  $\Delta \bar{a}_{i+1}$  is the incremental displacement for step  $i+1$ , and  $\Delta \lambda_{i+1}$  is the fraction of load  $P$  applied at step  $i+1$  (see Fig 2.10). The effect of constraint Eqn (2.83) is that each subsequent step solution is searched for on an arc of radius  $\Delta s$  from the current solution. The initial value for the quantity  $\Delta \lambda$  is specified in the problem data deck.

To apply the modified Newton-Raphson method, the first variation of Eq (2.84) is taken and applied at steps  $i$ :

$$K_T \delta a_i = \delta \lambda_i P - g(a_i, \lambda_i) \quad (2.84)$$

where

$$\delta a_i = \delta a_{i1} + \delta \lambda_i \delta a_{i2} \quad (2.85a)$$

and

$$\delta a_{i1} = -K_T^{-1} g(a_i, \lambda_i) \quad (\text{out-of-balance term}) \quad (2.85b)$$

$$\delta a_{i2} = K_T^{-1} P \quad (\text{linear term}) \quad (2.85c)$$

The displacement increment  $\Delta a_{i+1}$  and load parameter increment  $\Delta \lambda_{i+1}$  are updated by

$$\Delta a_{i+1} = \Delta a_i + \delta a_i \quad (2.86a)$$

and

$$\Delta \lambda_{i+1} = \Delta \lambda_i + \delta \lambda_i \quad (2.86b)$$

The linear solution at the beginning of each load step is defined by

$$\Delta a_1 = \Delta \lambda_1 \delta a_{12} \quad (2.87)$$

where  $\delta \lambda_1$  is the incremental loading parameter in the beginning of each load step. Crisfield [55] has shown that it is preferable to fix the "incremental length"  $\Delta s$ . The constraint relation is then replaced by

$$\Delta a_{i+1}^T \Delta a_{i+1} = \Delta s^2 \quad (2.88)$$

for all iterations,  $i$ . By substituting Eqn (2.86a) into Eqn (2.88), one obtains the following quadratic equation for the change,  $\delta \lambda_i$

$$a \delta \lambda_i^2 + 2b \delta \lambda_i + c = 0 \quad (2.89)$$

where

$$a = \delta a_{12}^T \delta a_{12}$$

$$b = (\Delta a_i + \delta a_{11})^T \delta a_{12}$$

$$c = (\Delta a_i + \delta a_{11})(\Delta a_i + \delta a_{11}) - \Delta s^2$$





The total displacement  $a_n$  and the total load parameter  $\lambda_n$  for the nth load step is updated by

$$a_n = a_{n-1} + \Delta a_n \quad (2.90a)$$

and

$$\lambda_n = \lambda_{n-1} + \lambda_n \quad (2.90b)$$

In brief, the algorithm proceeds for a given load step  $n$  as follows ( $i$  denotes the iteration). Refer to Fig 2.10:

a.) The tangent stiffness matrix  $K_T$  at the current deformed geometry is determined and held constant throughout the iteration. Select a reference load  $P$  and reference number of iteration for each load step as  $N_s$ , and the number of load steps  $M_s$ . A load parameter  $\lambda_1$  for the first load step, a maximum load parameter  $\lambda_{max}$ , and a convergence criteria  $\epsilon$  for each load step are also selected.

b.) If it is the first load step:

- 1) Calculate  $\delta a_{i2}$  from Eqn (2.85c)
- 2) Calculate the constant arc length  

$$\Delta s_1 = \Delta \lambda_0 (\delta a_{i2}^T \delta a_{i2})^{1/2}$$
- 3) Calculate  $\Delta a_1$  from Eqn (2.87)
- 4) Go to step (c-2)

c.) For any load step n:

1) For the first iteration:

(i)  $\Delta s_n = \Delta s_{n-1} (N_s / N_{s-1})$

(ii) Calculate  $\delta a_{i2}$  from Eqn (2.85c)

(iii)  $\Delta \lambda_1 = \pm \frac{\Delta s_n}{(\delta a_{i2}^T \delta a_{i2})^{1/2}}$

$\Delta \lambda_1$  is positive if  $\det(K_T)$  is positive

$\Delta \lambda_1$  is negative if  $\det(K_T)$  is negative

(iv) Calculate  $\Delta a_1$  from Eqn (2.87)

2) For any iteration i+1:

(i) Calculate the out-of-balance term  $\delta a_{i1}$   
from Eqn (2.85b)

(ii) Calculate the load parameter change  $\delta \lambda_i$   
from scalar quadratic equation (2.85).

Two roots are obtained as  $\delta \lambda_{i1}$  and  $\delta \lambda_{i2}$ .

If  $\delta \lambda_{i1}$  and  $\delta \lambda_{i2}$  are imaginary, let

$\Delta s_{n+1} = \Delta s_n / 2$ , and go to step (c-1-ii). If  
they are real roots, go to the next step.

(iii) Calculate the updated displacement

increment  $\Delta a_{i+1}^1$  and  $\Delta a_{i+1}^2$  from Eqn

(2.86a) for the two roots  $\delta \lambda_{i1}$  and  $\delta \lambda_{i2}$ .

(iv) Calculate the angle  $\theta_1$  between the  $\Delta a_1$

and  $\Delta a_{i+1}^1$ , and  $\theta_2$  between the  $\Delta a_1$  and

$\Delta a_{i+1}^2$ . If  $\theta_1$  is positive,  $\Delta a_{i+1} = \Delta a_{i+1}^1$

and  $\delta \lambda_i = \delta \lambda_{i1}$ . If  $\theta_2$  is positive,

$\Delta a_{i+1} = \Delta a_{i+1}^2$  and  $\delta \lambda_i = \delta \lambda_{i2}$ . If both  $\theta_1$  and  $\theta_2$  are positive,  $\delta \lambda_i$  takes the value closest to the linear solution  $\delta \lambda = -c/2b$ .

(v) Update the load parameter  $\Delta \lambda_i$  from Eqn (2.86b) and the total displacement

$$a_n = a_n + \Delta a_{i+1} - \Delta a_i$$

- 3) Repeat step (2) until the difference between the norms of the total displacement for two consecutive iterations is within  $\epsilon$  of the norms of the total displacement. The number of iterations to reach the convergent criteria is defined as  $N_n$ , and the final incremental load parameter for the nth load step is  $\Delta \lambda_m$ .
- 4) Update the total load parameter as from Eqn (2.90b).

d.) If the load step number  $n$  is equal to  $M_s$  or the total load parameter  $\lambda_n$  is larger than  $\lambda_{max}$ , stop. Otherwise go to step (c).

The efficiency of the algorithm is improved by scaling the step  $(n + 1)$ 's target  $\Delta s$  length by the ration of a user-selected desired number of iterations to the number of iterations needed to converge to step  $n$ . Thus, in near-linear parts of the load-displacement curve, wide spacing of solution points is allowed; when the curve rounds

corners (around limit points) the method has to iterate more to converge and hence  $\Delta s$  is reduced until the curve straightens out again.

The inability to solve for equilibrium at a limit load point is circumvented due to the nature of the stepping method. The technique shoots a tangent from the current equilibrium point, then searches an arc about the tip for the next solution point, so the exact limit load point is almost always skipped over. Auxiliary equations can be programmed to enable determination of the critical point [49].

### 3. EXPERIMENTAL METHODS

#### 3.1 Manufacturing

A total of 12 panels were fabricated for the axial compression experiments. Table 3.1 breaks down the various geometries and cutout placements used for the experimental portion of the study. Two additional panels were fabricated and used in the residual stress test, described in more detail below. All 14 panels were newly manufactured. The manufacturing process and materials for the new panels were the same used by Horban [52], Tisler [35], and Wilder [53] for their studies. All panels were C-scanned after being manufactured, thus ensuring that neither delaminations nor internal defects were present. The thickness was measured at twelve locations on each panel, and the average thickness for the panels was taken. Thickness variation within each panel was small ( $\approx 6\%$ ), and within the total group it was even smaller ( $\approx 3\%$ ).

A hole cutting process was developed during Tisler's work [35] to help remove damage caused by flattening of the panel during cutting. A wooden base, also with a radius of 12 inches, held the panel nearly in its original shape during cutting. Fiberglass and rubber sheets help reduce vibration damage, and a steel template guided the router

Table 3.1 Experimental Test Plan

	Unsupported Vertical Edges		Simply Supported Vertical Edges	
	8" x 11"	12" x 11"	8" x 12"	12" x 12"
No Cutout	X	X	X	X
4" Cutout	X	X	X	X
4" Cutout 1" Offset	X	X	X	X

used for cutting. A schematic of the cutting setup is given in Fig 3.1, along with photographs in Figs 3.2 and 3.3.

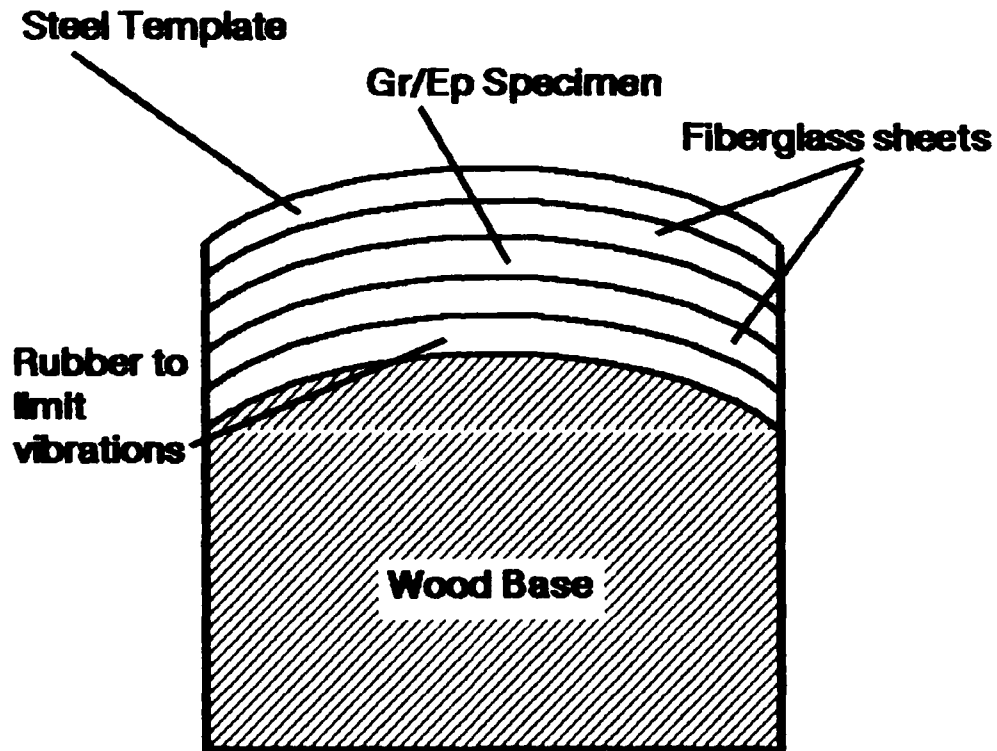


Fig 3.1 Schematic of Cutting Support

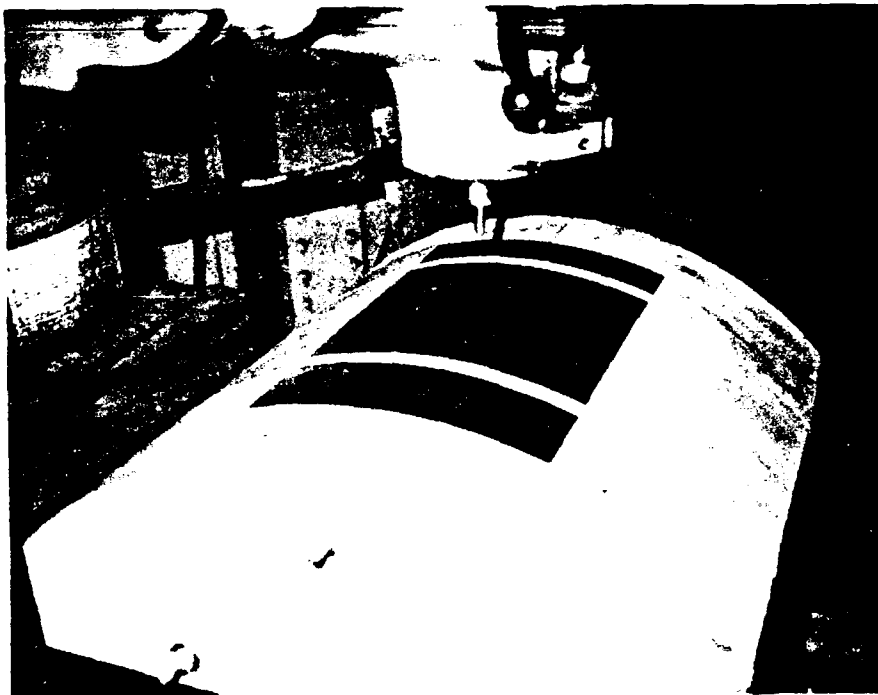


Fig 3.2 Picture of Hole Cutting Support



Fig 3.3 Picture of Finished Product



The corners of the square cutouts were slightly rounded ( $\approx 1/16$  inch radius). This was caused by the router used to cut the panels, and had the beneficial effect of removing stress singularities at the corners.

All the edges of the panel were cut the same way as was previously done [35,52,53]. NOTE: for those edges to be clamped or simply supported, the dimensions in the axial and circumferential directions were cut slightly larger (by  $1/2$  inch) to create a holding tab for the experimental fixture's supports. With these in place, the effective dimensions in the clamped or supported directions were shorter by one inch. It is crucial that the upper and lower edges be extremely close to being parallel to assure even loading. The actual edge cutting procedure is explained in more detail by Horban [52].

### 3.2 Axial Compression

The axial compression experimental setup (Fig 3.4) and the panel clamping devices (Fig 3.5) were essentially the same as used by Horban [52], Janisse [21], Tisler [35], and Wilder [53] for their studies of cutouts and delamination effects. Initial problems with the vertical boundary conditions and measurement of the top edge displacement [21] have been corrected, as described by Horban. All of the

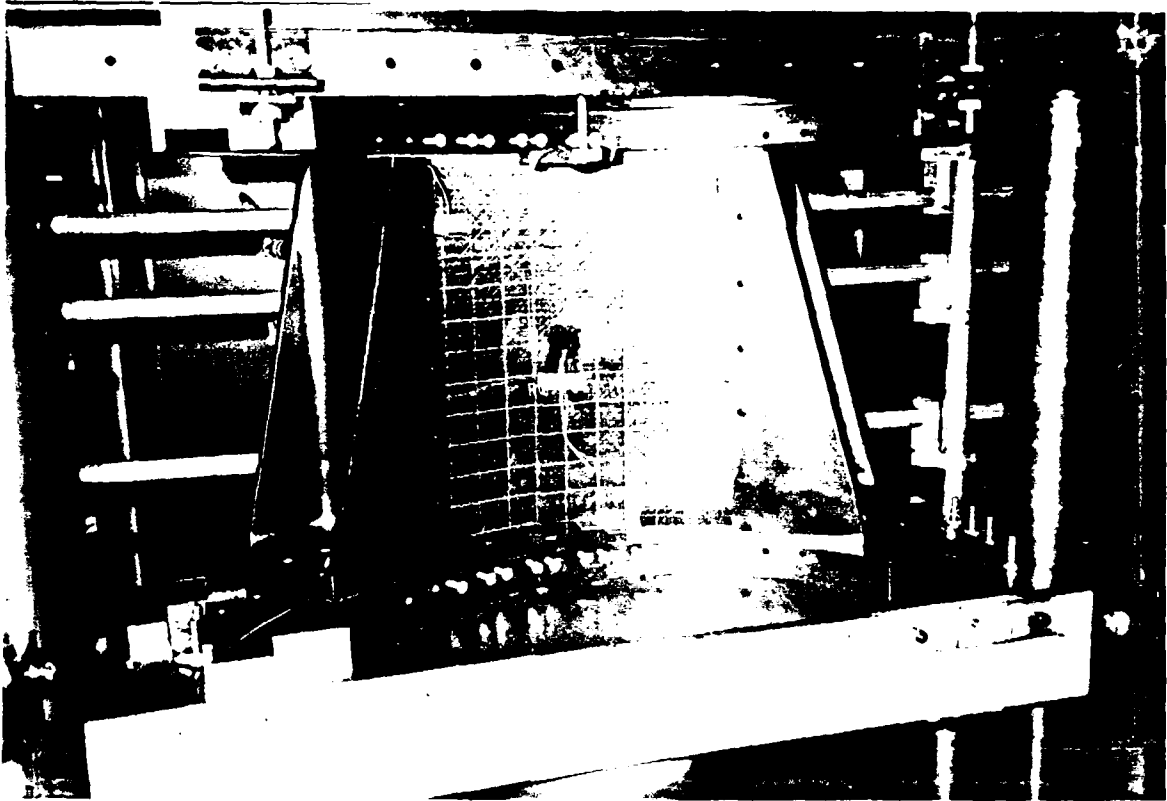


Fig 3.4 Experimental Setup, Axial Compression

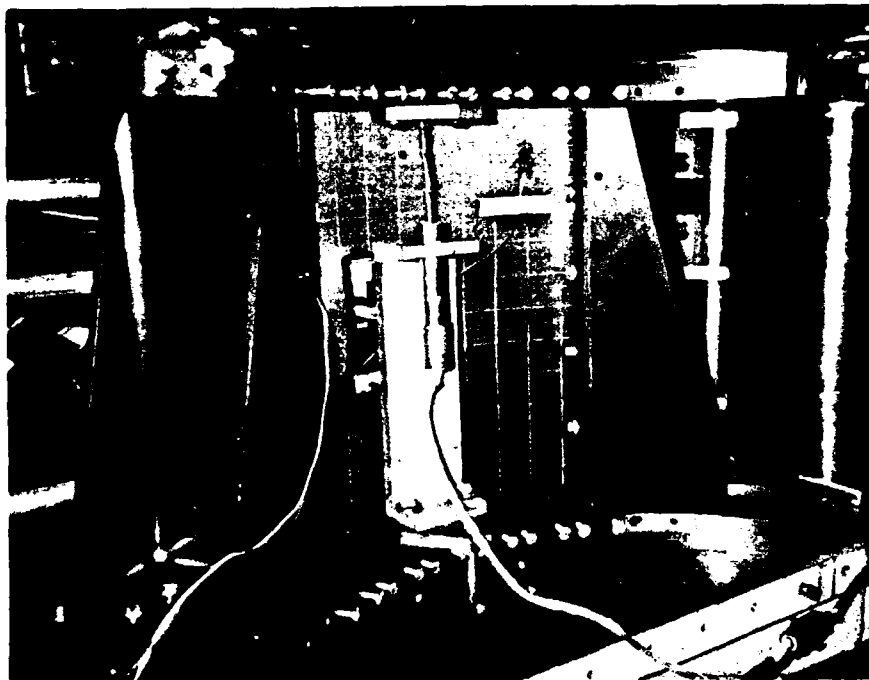


Fig 3.5 Close-up of Panel in Specialized Supports

edges were held by specialized fixtures, also explained in detail by Horban. The top and bottom were clamped ( $u = v = w = R_x = R_y = R_z = 0$ ), while the edges were assumed to be simply supported ( $u = R_x = \text{free}, v = w = R_y = R_z = 0$ ) or completely unsupported ( $u = v = w = R_x = R_y = R_z = \text{free}$ ). The assumption of  $v$  being fixed was later questioned after reviewing analytical vs experimental results (this will be discussed in greater detail in Section 5).

A vertically mounted Linear Variable Displacement Transducer (LVDT), in front of the panel in Fig 3.4, measured the top edge displacement, while a bank of LVDT's behind the panel measured out of plane displacement at 15 specified points. Figures 3.6 through 3.11 demonstrate the LVDT positions for the 8" and 12" panels with varying cutout positions. All the measured radial displacements were near the cutout. These were expected to be the largest displacements, and therefore would be the easiest to measure accurately.

The uniform displacement is applied from above with a 30K lb hydraulic compression machine. Although the bottom platen is moving upward, the positioning of the vertical supports makes the top edge the true applied displacement. A load cell measures the total applied load. Uniform displacement is slowly applied (.05"/min) until a maximum collapse load is reached at which point: (1) for the simply

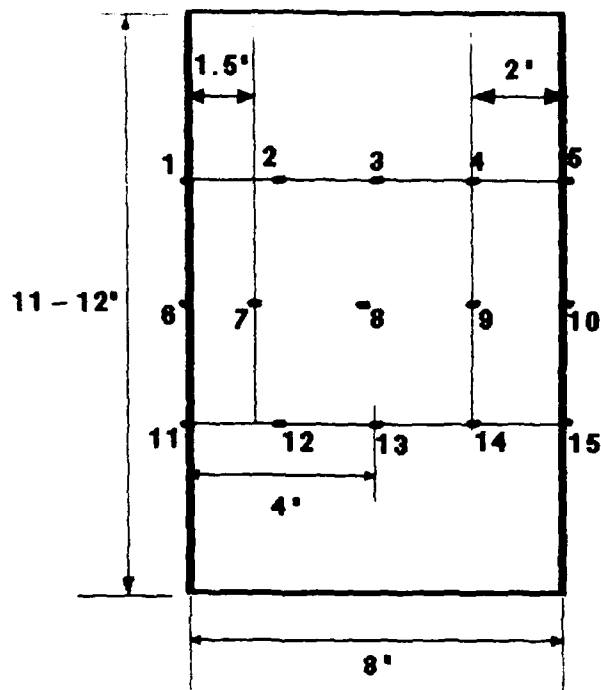


Fig 3.6 LVDT Positions, 8" Panel, No Cutout

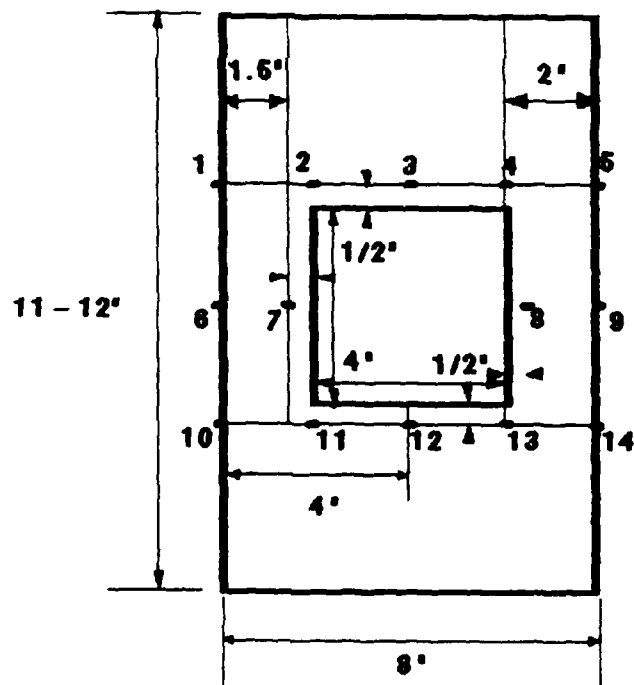


Fig 3.7 LVDT Positions, 8" Panel, 4" Cutout, Centered

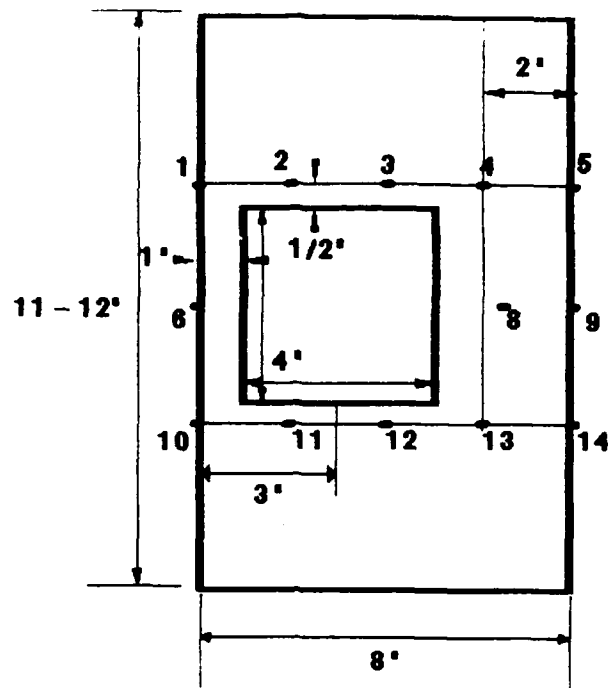


Fig 3.8 LVDT Positions, 8" Panel, 4" Cutout, 1" Offset

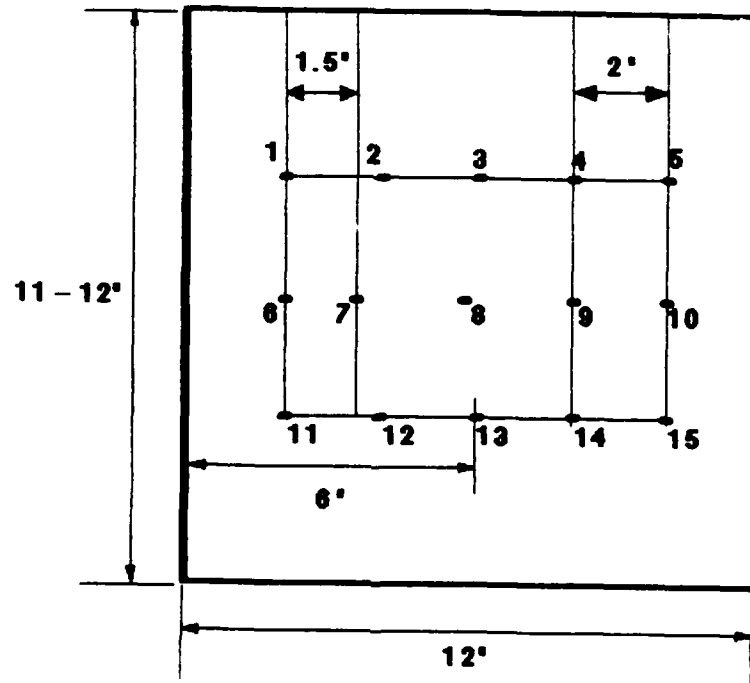


Fig 3.9 LVDT Positions, 12" Panel, No Cutout

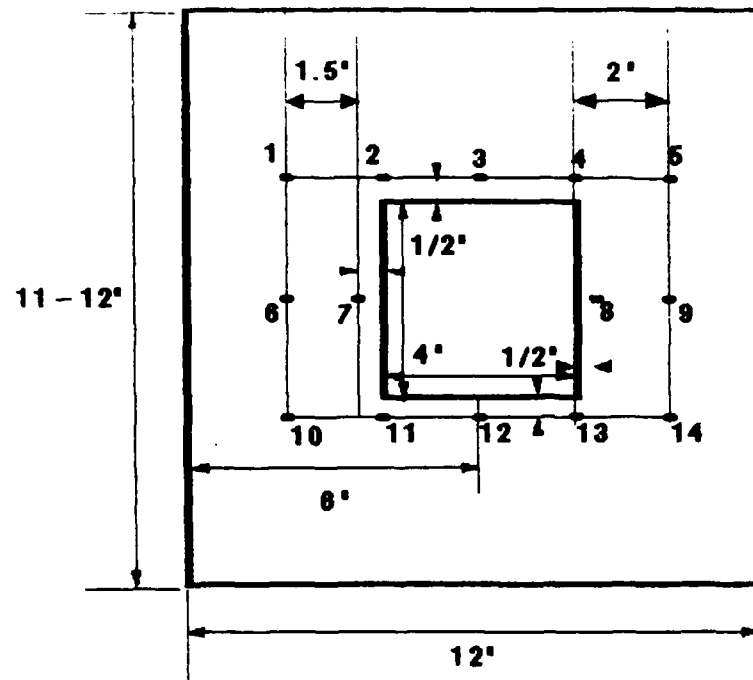


Fig 3.10 LVDT Positions, 12" Panel, 4" Cutout, Centered

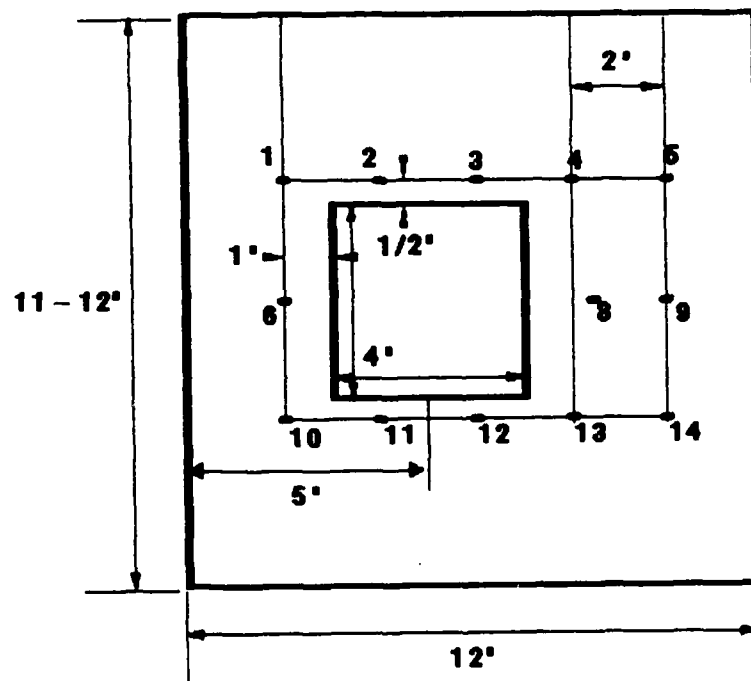


Fig 3.11 LVDT Positions, 12" Panel, 4" Cutout, 1" Offset

supported test specimens, the panel snaps suddenly into a new displacement shape and the load is reduced, or (2) for the unsupported test specimens, the panel continues to deform smoothly in the same displacement shape it started with, while the load peaks and then begins to drop off slowly. Two strain gages were positioned near the top (Fig 3.12) to ensure the applied load was evenly distributed. It is important that the load be applied evenly by centering the force in the middle of the panel to allow for symmetric load distribution. For those panels not containing cutouts, two additional strain gages were positioned at the geometric center of the panel (front and back), see Fig 3.13 for detail. These strain gages allowed for confirmation of the collapse load because the load vs strain curves diverged dramatically at collapse (an example is shown in Fig 3.14). All the data from the strain gages and LVDT's is saved on a VAX 11/780 computer, allowing for experimental graphs of the load displacement curves, both for the top edge and radial displacements. For a detailed discussion of the axial compression experimental procedure, including photographs and drawings of the boundary supports, see [21,53].

The imperfection amplitude was measured using an aluminum guide and a displacement gage [35]. The average amplitude of imperfections was found to be about the same as in the past ( $\approx 0.0060$  inches). Note that this is



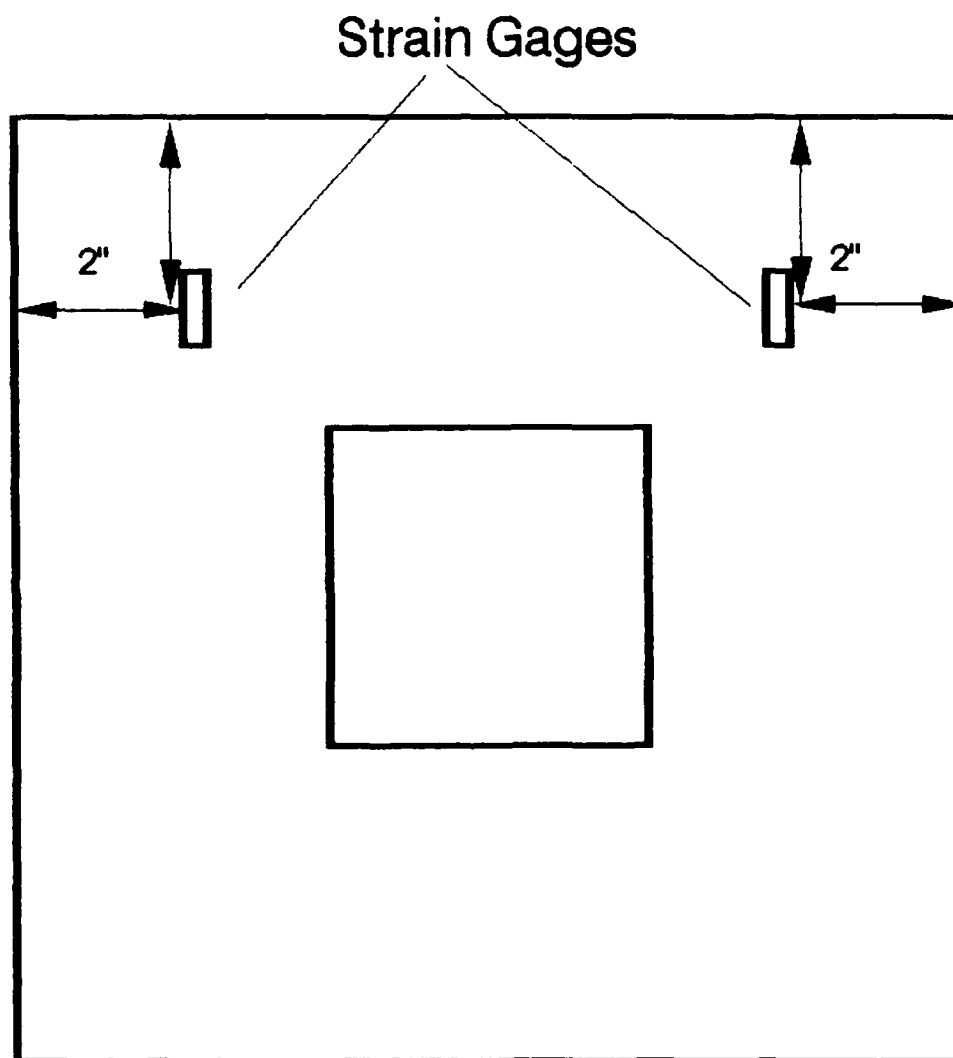
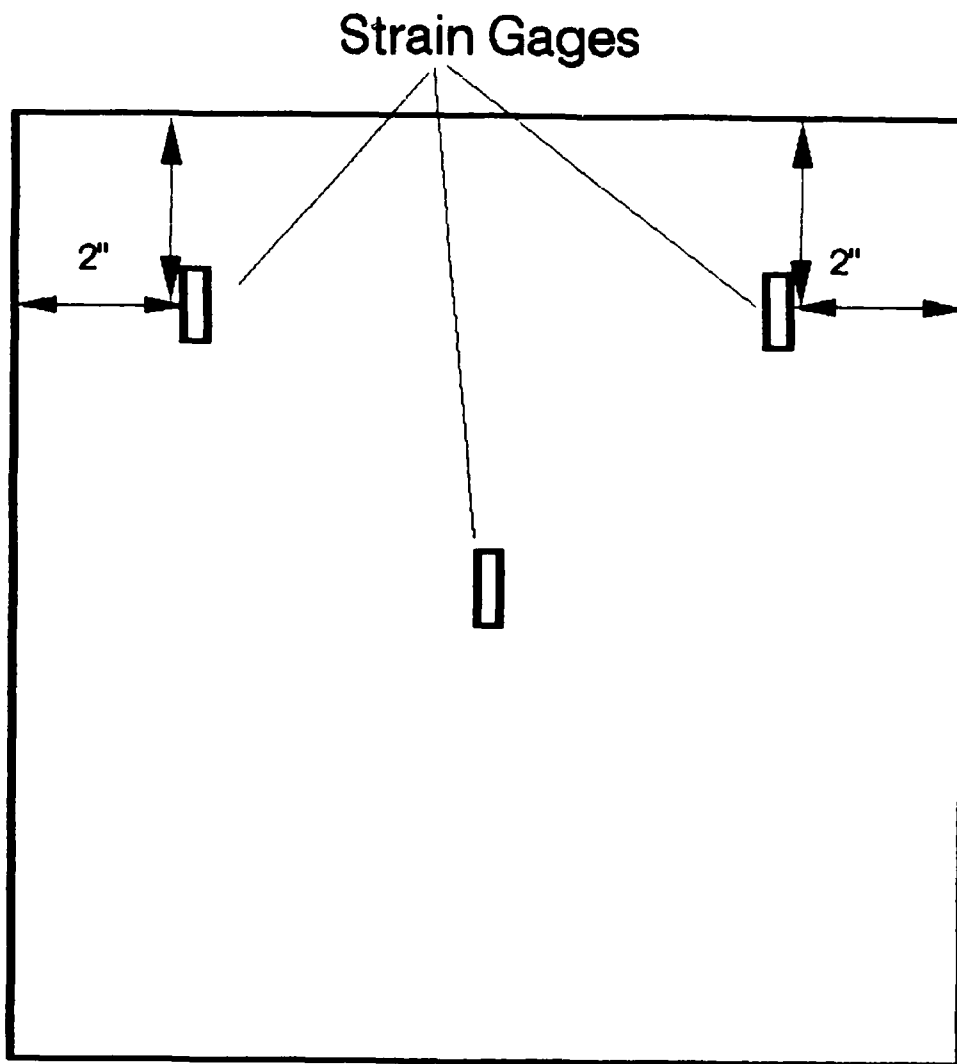


Fig 3.12 Strain Gage Positions, Panels With Cutouts



NOTE: FOR SOLID PANELS, 2 STRAIN  
GAGES ARE PLACED AT CENTER  
OF PANEL ON BOTH SIDES.

Fig 3.13 Strain Gage Positions, Panels Without Cutouts

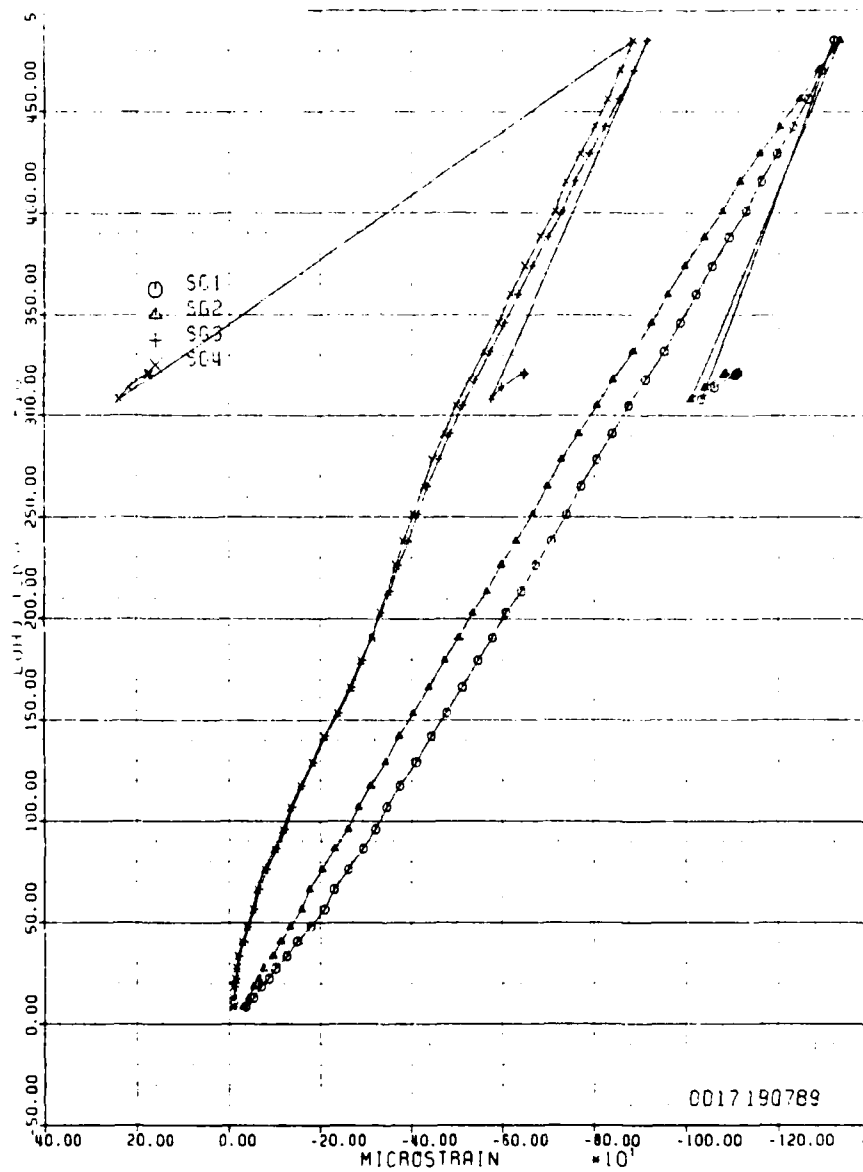


Fig 3.14 Load vs Strain, Collapse of Solid Panel

approximately the thickness of one ply and is substantially less than the panel thickness of 0.042 inches.

### 3.3 Residual Stress Test

For the determination of residual stress created by cutout removal, 16 strain rosettes are mounted along the edge of the cutout location (Figs 3.15 and 3.16). These rosettes are mounted prior to removing the cutout. Because of the type of router used, the rosettes are placed within 0.5 inches of the cutout edge only. Strain in the panel while free from any load, is recorded to create a baseline of strain data which determines the amount of residual stress created by removing the cutout (Fig 3.17). The panel is placed in the cutting setup, and again strain is recorded generating a baseline of strain data while the panel is strapped into the cutting setup. After the router punched a hole into the panel, strain is recorded (Fig 3.18), and strain is recorded after each side of the cutout template is completed by the router. Once the cutout is completely removed, strain is recorded again before the panel is removed from the cutout setup (Fig 3.19). The panel is removed from the cutout assembly and placed such that no loading is applied. Then strain is measured for a final time, for a total of nine strain measurements. Residual

stress is determined from any changes in the measured strain from the first and last strain measurements. The other measurements are recorded as an attempt to give a complete history of the cutout process and

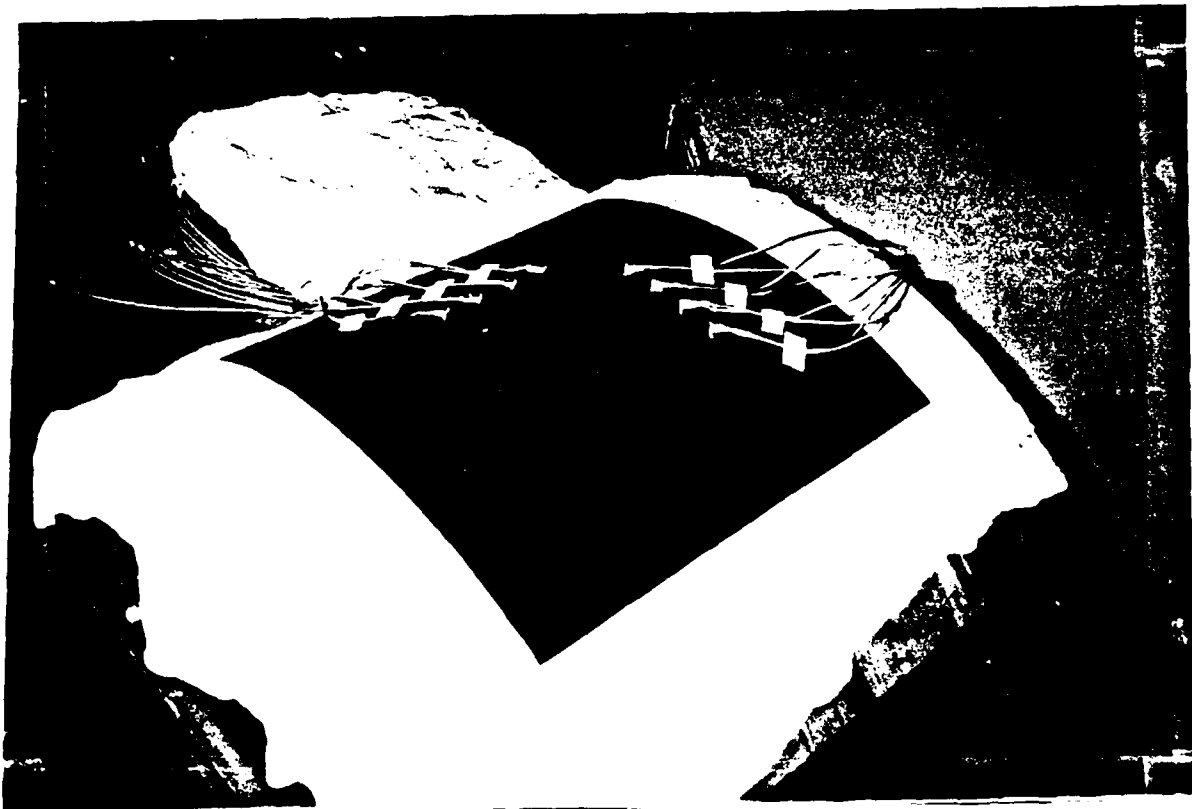


Fig 3.15 Strain Rosette Positions, Front View



Fig 3.16 Strain Rosette Positions, Rear View



Fig 3.17 Picture of Panel Before Cutting Process



Fig 3.18 Picture of Panel Cutting Process



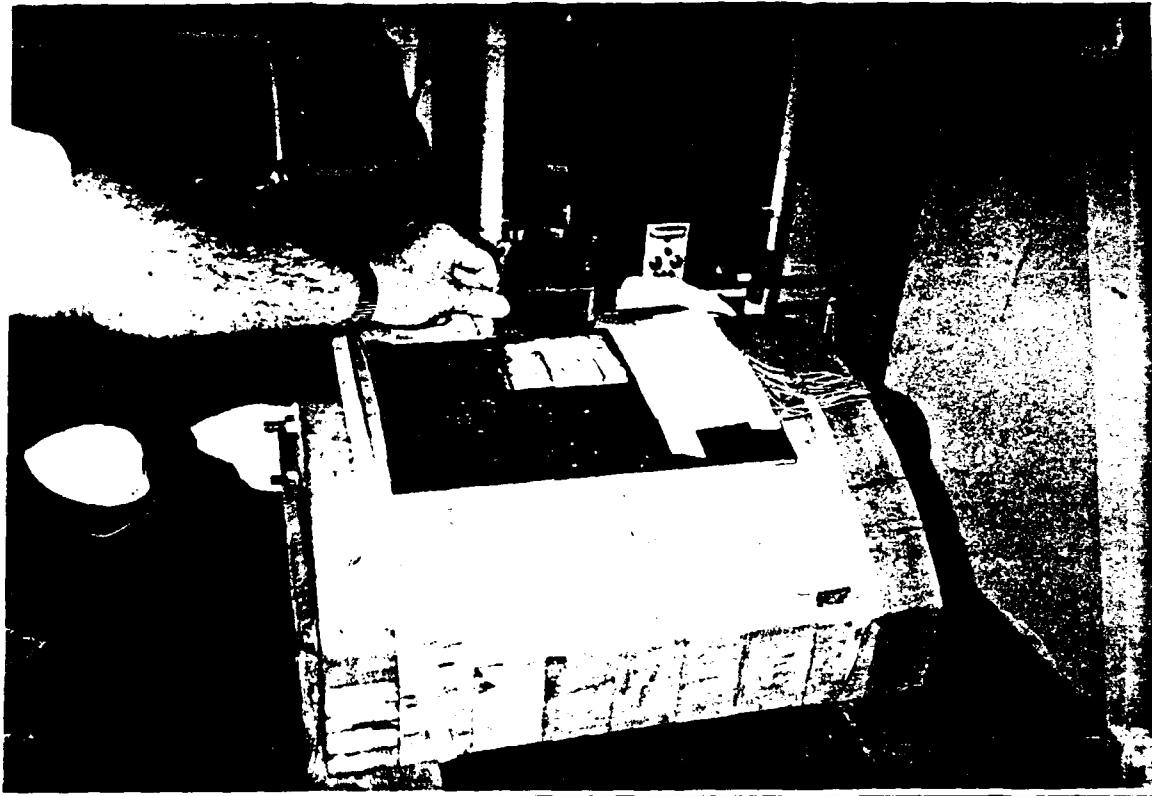


Fig 3.19 Picture of Panel, After Removing Cutout, Unloaded

aid in determining any anomalies that may be created by removing the cutout. The change in strain is attributed to cutting out a portion of the curved composite panel. A better approximation of the residual stress distribution is generated than in [35] but it by no means an exact distribution.

When a curved panel is cured from an elevated temperature, a residual stress forms. These stresses are considered to have two parts. The first is an in-plane stress, with no warping involved if the panel is symmetric and balanced. This stress can be easily calculated by assuming a flat plate with the ply lay-up used for this work. The second part comes from the curvature. As the curved panel is cured, the uneven lengths of the inner and outer plies create a bending stress. This is referred to as the bending residual stress.

The stress caused by curing a flat composite plate with the ply lay-up  $[0,-45,+45,90]_s$  is estimated using a curing temperature change of  $300^{\circ}\text{F}$ . This flat plate stress is found to be  $\approx 5$  ksi. A bending stress also comes about as a result of the panel's curvature, as discussed above. If a change occurs within the flat plate residual stress, the change should be the same in all directions since the panel is quasi-isotropic. If a change takes place in the bending residual stress, the change will predominantly be in

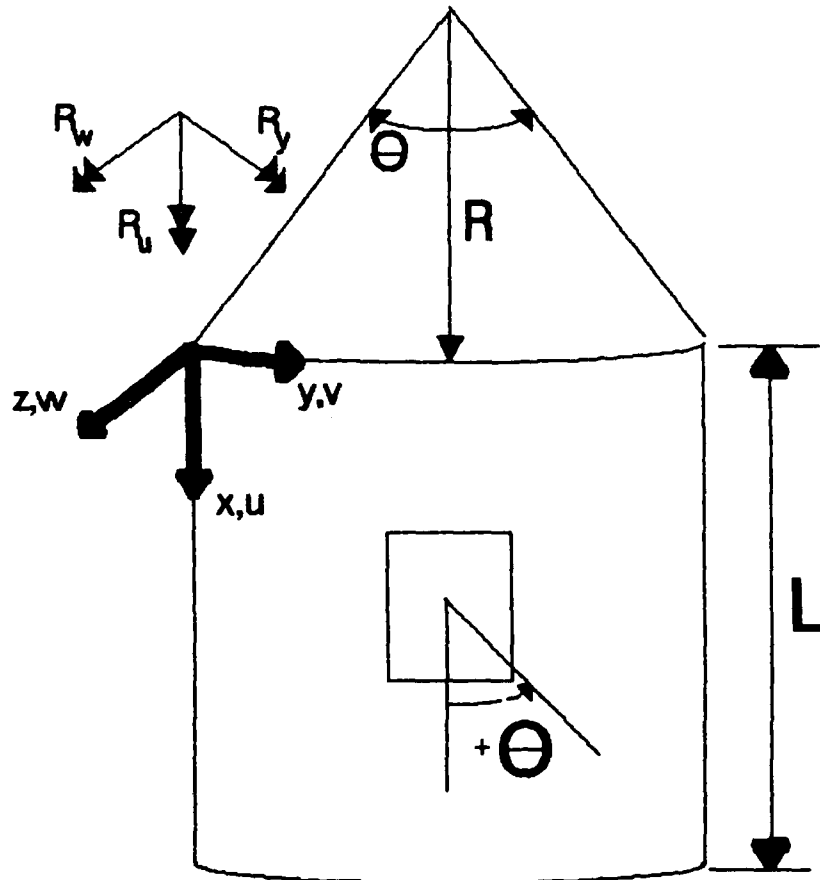
the circumferential direction, with limited change in the axial direction. By comparing the change in strain in the circumferential and axial directions, one can tell which component of the residual stress is affected by the cutout. Finally, changes in stress due to changes in strain are compared to the stresses present during axial compression to see if residual stress change warrants further study.

#### 4. FINITE ELEMENT MODELING

##### 4.1 Panel Properties and Analytical Boundaries

Once placed within the experimental setup, all panels have a radius of 12" but axial and circumferential dimensions varied. These are discussed in Table 3.1 of Section 3. Essentially, there are two classes of panels. One class is clamped on the top and bottom and had free vertical edges. Of this class, panels is either 8" or 12" in the circumferential direction and 11" in the axial direction. Each circumferential dimension (8" or 12") has three panels within its sub-class: one panel has no cutout, one panel has a 4" cutout centered within the panel, and the final panel has a 4" cutout offset one inch to measure eccentricity effects of the cutout. The other class is clamped on the top and bottom and has simply supported vertical edges. This class is broken down in the exact manner as the first class. The panel material properties, dimensions, and sign conventions in Fig 4.1. These material properties are determined experimentally through tensile test coupons and are used for the finite element model.

For the finite element models, as mentioned before, two boundary conditions are compared. In both models, the bottom boundary is clamped ( $u = v = w = R_u = R_v = R_w = 0$ ).



**Material:** Hercules AS4 – 3501 Graphite Epoxy

**Radius,  $R$ :** 12 inches

**Length,  $L$ :** 11 or 12 inches

**Circumferential Length:** 8" or 12"  $\circ$   $\circ$

**Ply Layup:**  $[0, -45, 45, 90]_4$ , angles as indicated

**Elastic Moduli:**  $E_1 = 20.461 \times 10^6$  psi

$E_2 = 1.3404 \times 10^6$  psi

**Shear Modulus:**  $G_{12} = .8638 \times 10^6$  psi

**Poisson's Ratios:**  $\nu_{12} = .301$   $\nu_{21} = .0205$

**Fig 4.1 Properties for Composite Panels**

And in both models, the top has a degree of freedom,  $u$ , free. For the one class, the vertical edge boundaries are free ( $u = v = w = R_u = R_v = R_w \neq 0$ ). For the other class, the vertical edge boundaries are assumed simply supported, both vertical rotation and movement ( $R_u$  and  $u$ ) are assumed free.

Both Janisse [21] and Tisler [35] compared simply supported panels and varied whether the degree of freedom,  $v$ , is fixed or free. Janisse [21] found this variation to have an almost negligible effect for a panel with a 2" cutout (3% difference), but anticipated the difference to be more pronounced for larger cutouts. Because the difference is so small for 2" cutouts, he did not have to consider whether the experimental edge boundary conditions were  $v$  free or  $v$  fixed. Tisler [35] on the other hand did consider this variation for a panel with a 4" cutout (18% difference) and found it to have a significant effect on the panel's global collapse load. Because of some disparity between early analytical (STAGS) and experimental results, those models not containing cutouts are run with the degree of freedom,  $v$ , free, and fixed, to determine which boundary condition better approximated the true experimental conditions.

## 4.2 Grid Selection

Based on thorough research into the previous works of Lee [22], Tisler [35], and Egan [37], the 411 element (Fig 4.2) proved to be the best choice for use in the nonlinear large displacement/moderate rotation analysis in STAGS. Unfortunately, the lack of a transition element made grid selection important. Again, careful analysis of Lee's and Tisler's work determined a refined grid utilizing a 0.5 inch element around the cutout provided the best results. Hence grids similar to those shown in Figs 4.3 through 4.6 are used. These grids are slightly more refined than Tisler's. This is due to the large displacements ( $\approx .02''$ ) and rotations ( $\approx 30^\circ$ ) experimentally measured, and analytically determined, for the panels with unsupported vertical edges. It must be noted that these refined grid selections require large amounts of computer time on the VAX computer systems (up to 90000 CPU seconds) in order to reach collapse load.

Based on Dennis' work [41], the 36 degree of freedom (DOF) element (Fig 4.7) proved to be the best choice for use in the nonlinear analysis in SHELL. Again grid selection was important, but another factor presented itself. In order to minimize the amount of CPU run-time needed to converge to an accurate solution (for the number of models that are

considered), it was decided to use only half size models (examples are shown in Figs 4.8-10) on the computer mainframes available (Elexi 6400 and VAX 8550) to converge to a solution using SHELL. Due to the asymmetrical displacement pattern that exists at the point of collapse, it is recognized these models will generate solutions with larger stiffnesses (thereby requiring larger collapse loads). An attempt was made to determine the percentage increase over the full model by using a comparison between full and half models using a coarser grid (see Figs 4.11 and 4.12). It is recognized that this comparison is in no way an accurate method in determining how much increase will exist for each model. This is just an attempt in arriving to a rough estimate as to a range of increase that could be applied to the half models and thereby reduce the artificial stiffness created by the model(s). The artificial stiffness arises due to the fact that the displacement pattern is asymmetrical. This asymmetry is created by the  $D_{16}$  and the  $D_{26}$  bending coefficients (which in turns affects the  $M_{xy}$  moment) coming in to play at the collapse of the panel. Once the percentage increase is determined, it is applied to the half model solutions as a means of removing the artificially induced stiffness.



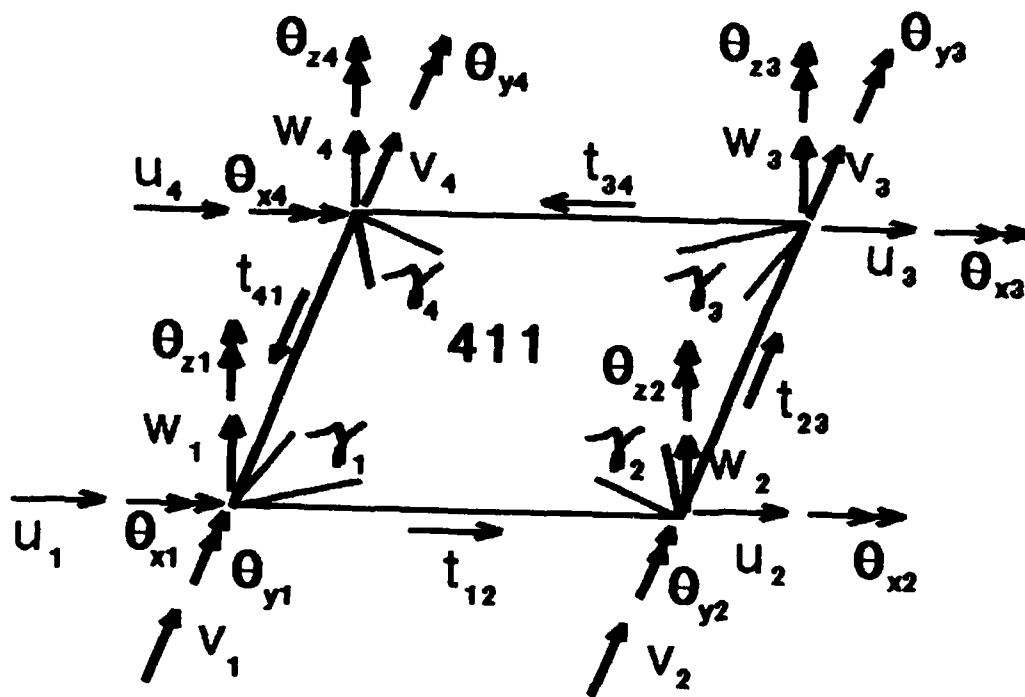


Fig 4.2 STAGS QUAF 411 Element

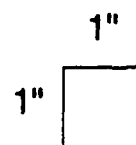
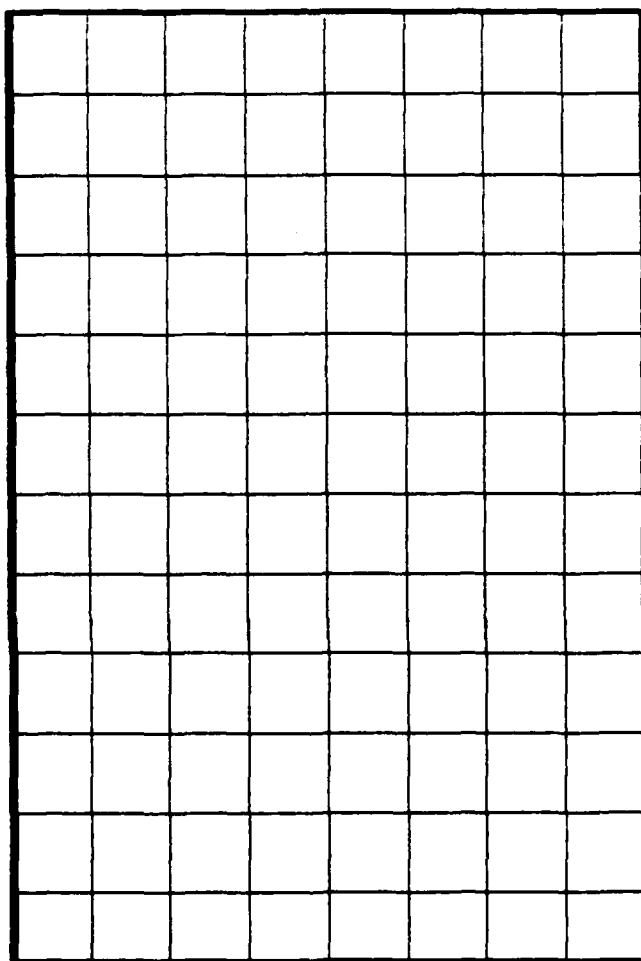
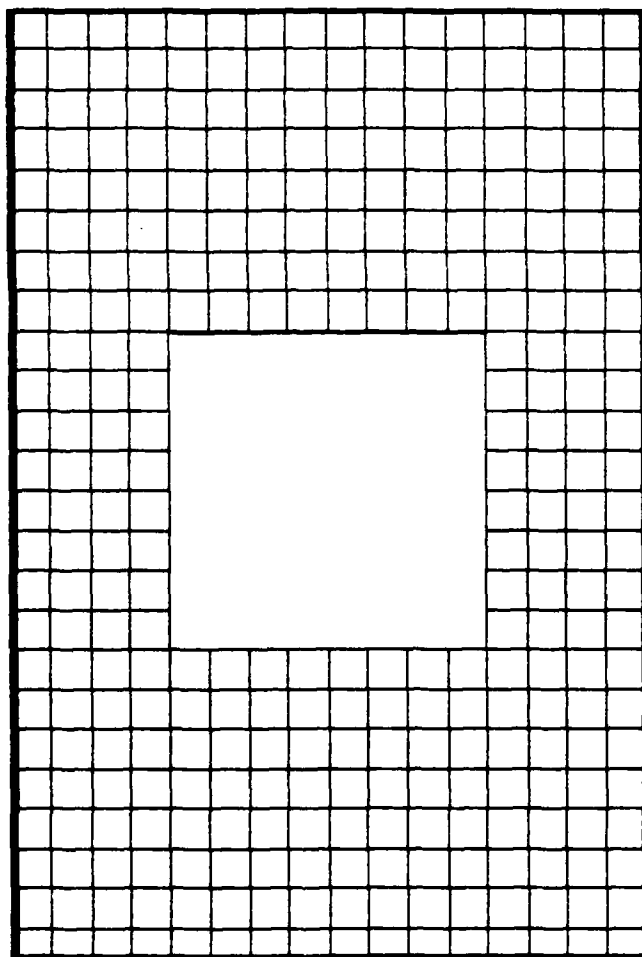
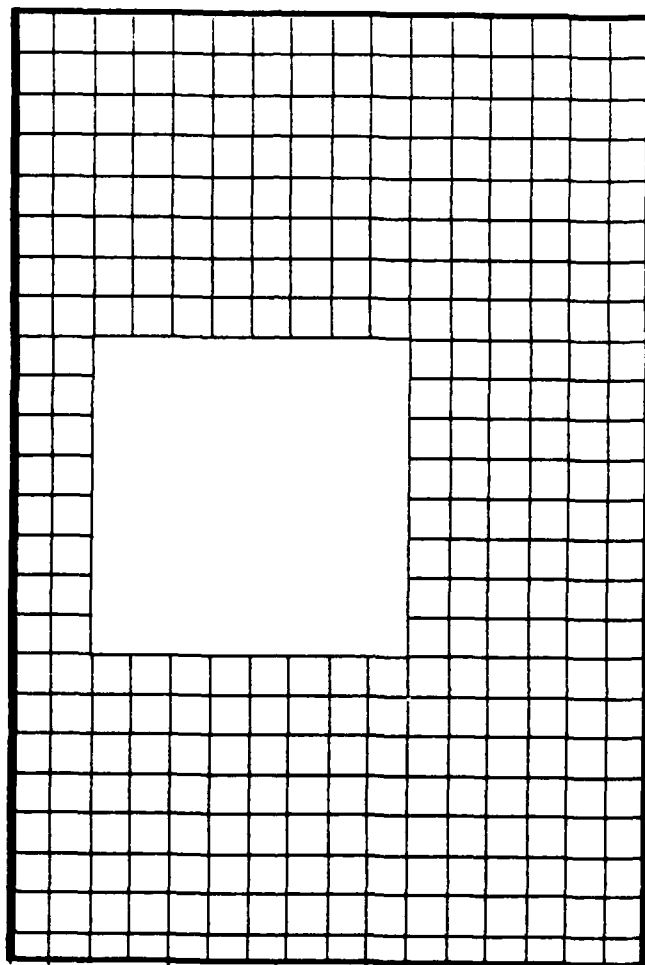


Fig 4.3 STAGS Grid for 8" Panel, No Cutout



1/2"  
1/2" □

Fig 4.4 STAGS Grid for 8" Panel, Centered Cutout




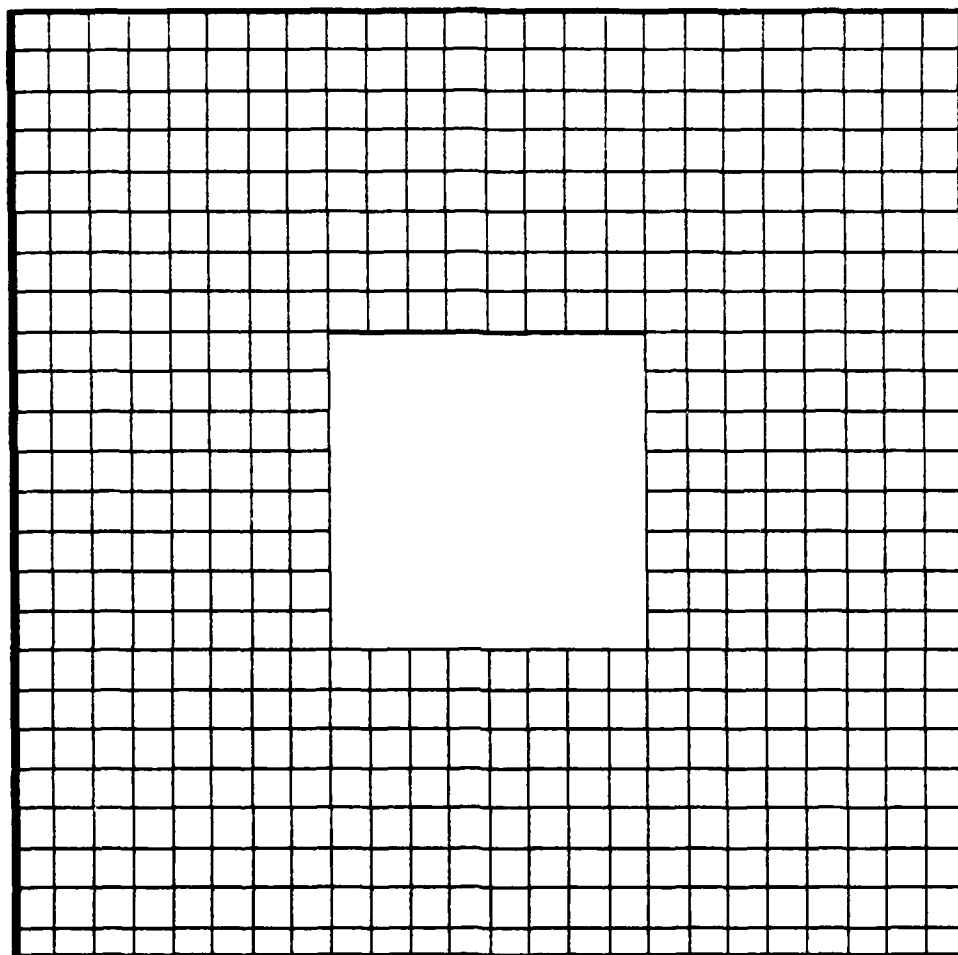
1/2"  
1/2" 

Fig 4.5 STAGS Grid for 8" Panel, Offset Cutout




$\frac{1}{2}$ "  
 $\frac{1}{2}$ " 

Fig 4.6 STAGS Grid for 12" Panel, Centered Cutout

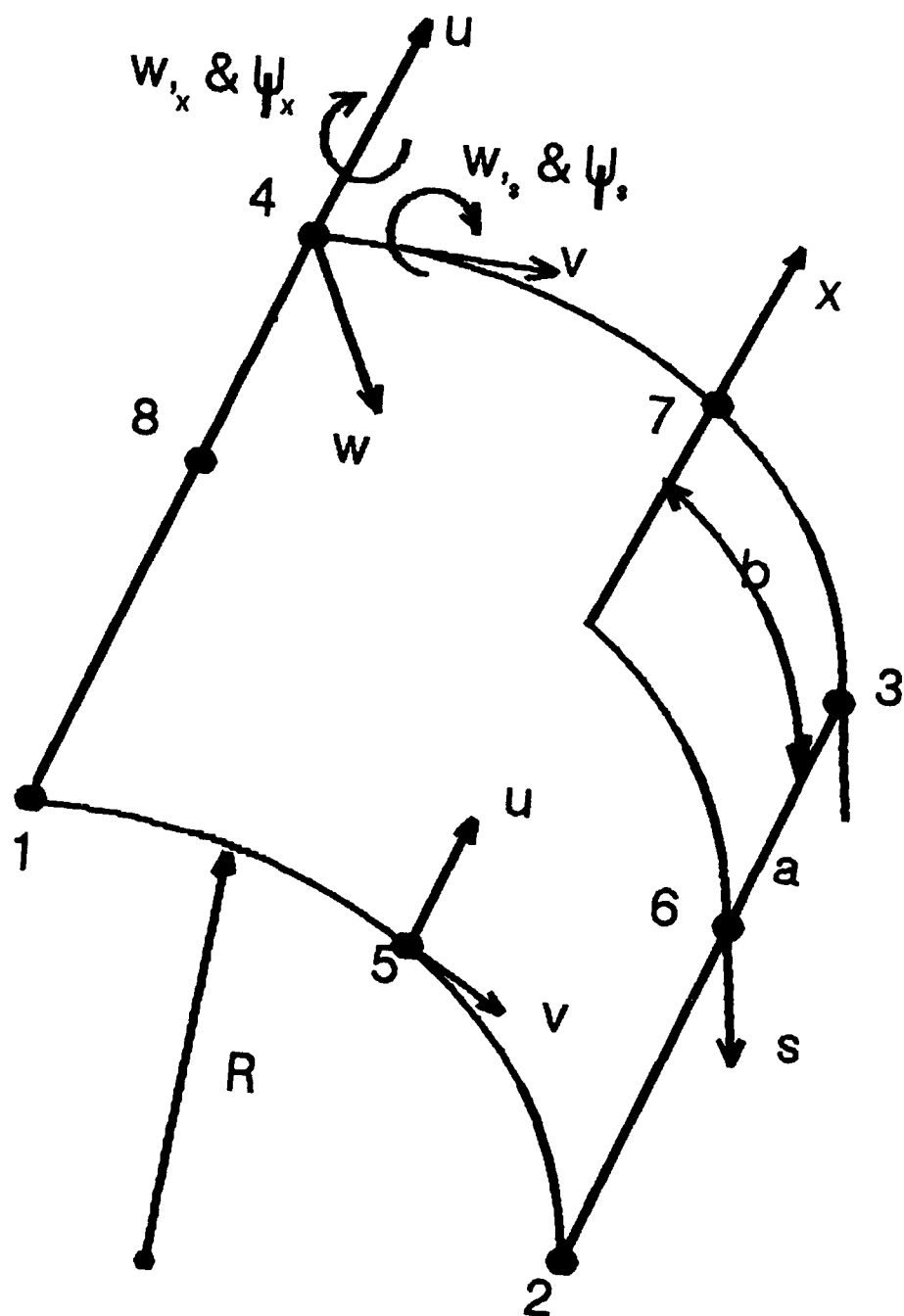
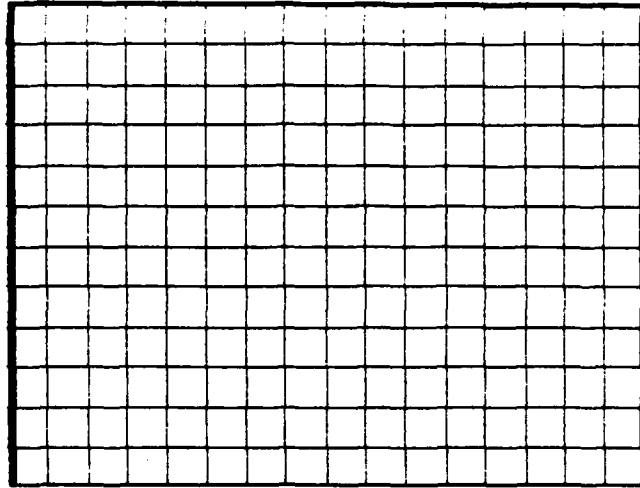
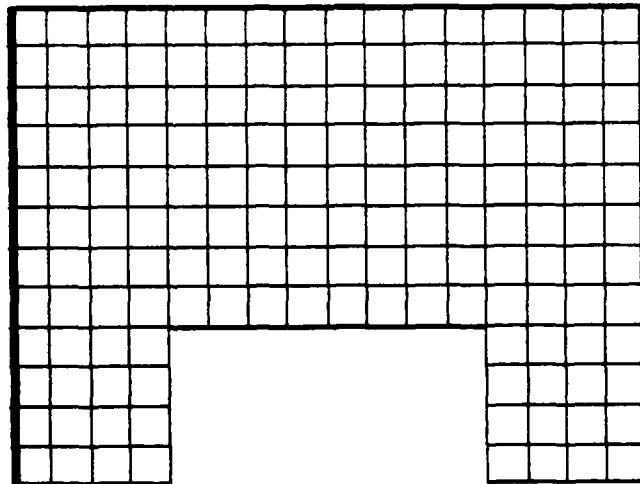


Fig 4.7 SHELL 36 DOF Element



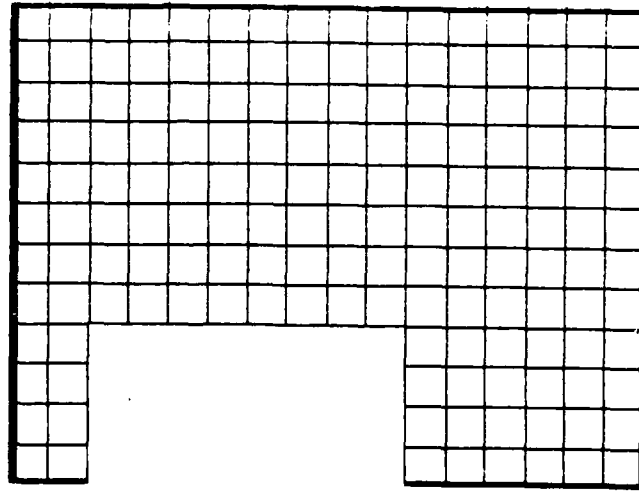
1/2"  
1/2" □

Fig 4.8 SHELL Grid for 1/2 8" Panel, No Cutout



1/2"  
1/2" □

Fig 4.9 SHELL Grid for 1/2 8" Panel, Centered Cutout



1/2"


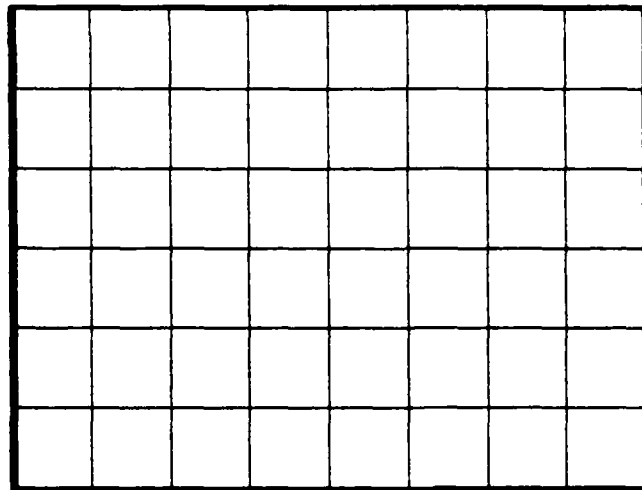
1/2" 

Fig 4.10 SHELL Grid for 1/2 8" Panel, Offset Cutout



1"


1" 

Fig 4.11 Half Model for SHELL Incorporating Course Mesh



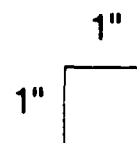
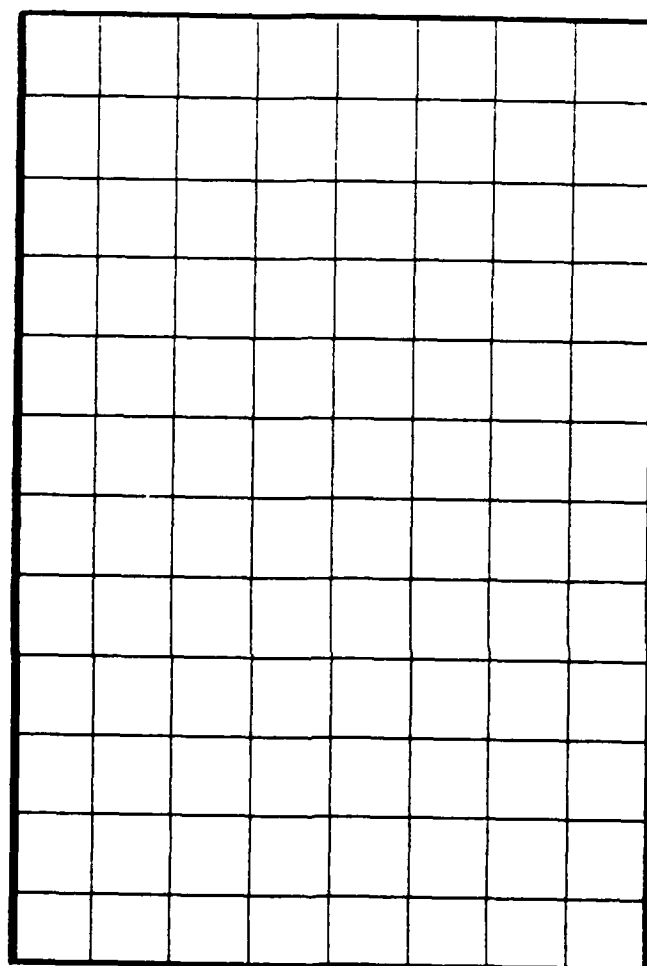


Fig 4.12 Full Model for SHELL Incorporating Course Mesh

## 5. RESULTS AND DISCUSSION

The main study area of this thesis is the correlation of analytical results with experimentally derived results. This correlation considers varying panel geometry, boundary conditions, geometric imperfection (cutout) effects including eccentricity effects, and through-the-thickness shear effects. Thus, in order to establish the critical characteristics of the effect that a true geometric imperfection (cutout) has on a composite panel, a study was carried out incorporating the previously mentioned comparisons. The results of these comparisons are discussed below. The discussion includes the analytical results from STAGS and SHELL, how these results correlate with experimentally derived results, and a brief discussion of determining residual stress experimentally.

### 5.1 Analytical Results - STAGS

Before beginning this discussion, it should be reiterated what conditions are being started with, since several parameters were varied. One begins with the assumption of a 12" wide panel, no cutout, no initial radial imperfections included, clamped along the top and bottom, and simply supported along the vertical edges (assuming  $v$

is fixed along the vertical edges). Then panel width, boundary conditions, geometric imperfections (cutouts), and eccentricity of cutout location are mentioned at the start of each model's discussion.

Based on previous work [35], it is assumed the loading condition is a top edge uniform displacement. During the experimental collapse tests, a top edge uniform displacement was applied, not a uniform load, to the panels through the test fixture. Tisler [35] determined that a uniform displacement load condition for STAGS best matches experimental results. With a uniform displacement, applied load is measured by summing the total axial force along the top. This is done by summing the equilibrium load values for each node along the top of the panel (Fig 5.1). This load is far from being a constant distribution when a large cutout (11-16% reduction in surface area) is present as seen in Fig 5.2. By summing the total axial force analytically, one can make comparisons with the total load measured experimentally.

#### 5.1.1 V Free vs V Fixed

During current and past cutout experiments [24,35], it became apparent that the assumed vertical boundary condition of v free was not entirely consistent. Teflon tape

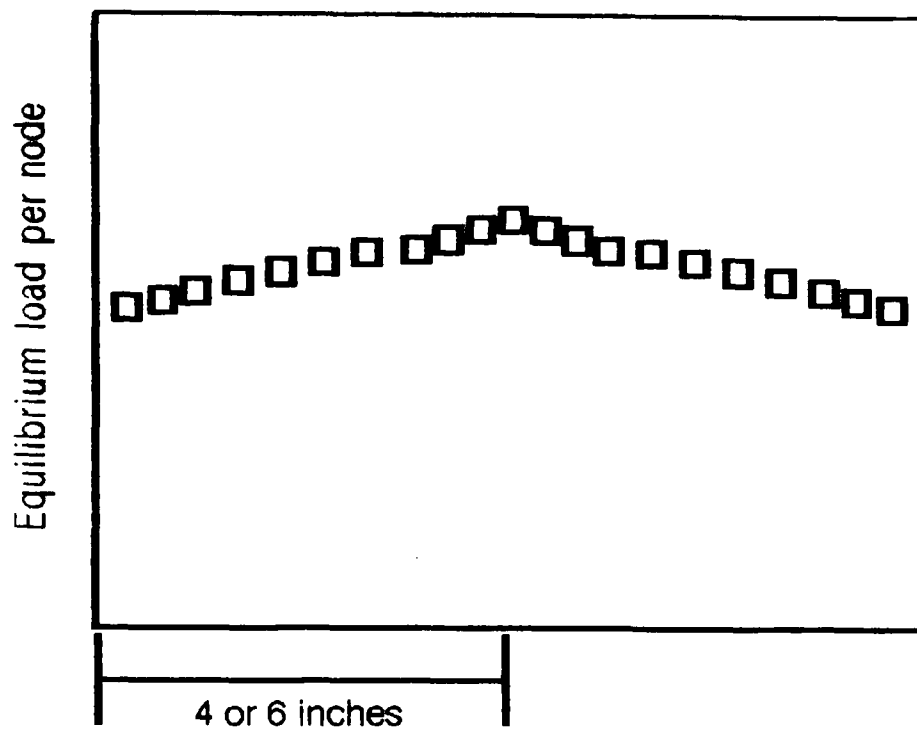


Fig 5.1 Equilibrium Load Distribution along Top of Solid Panel at Collapse

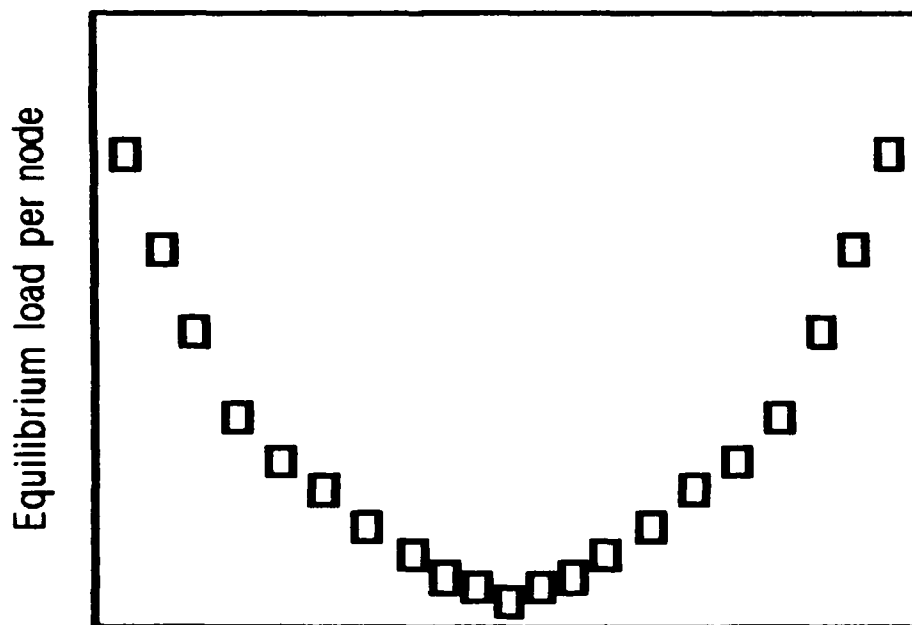
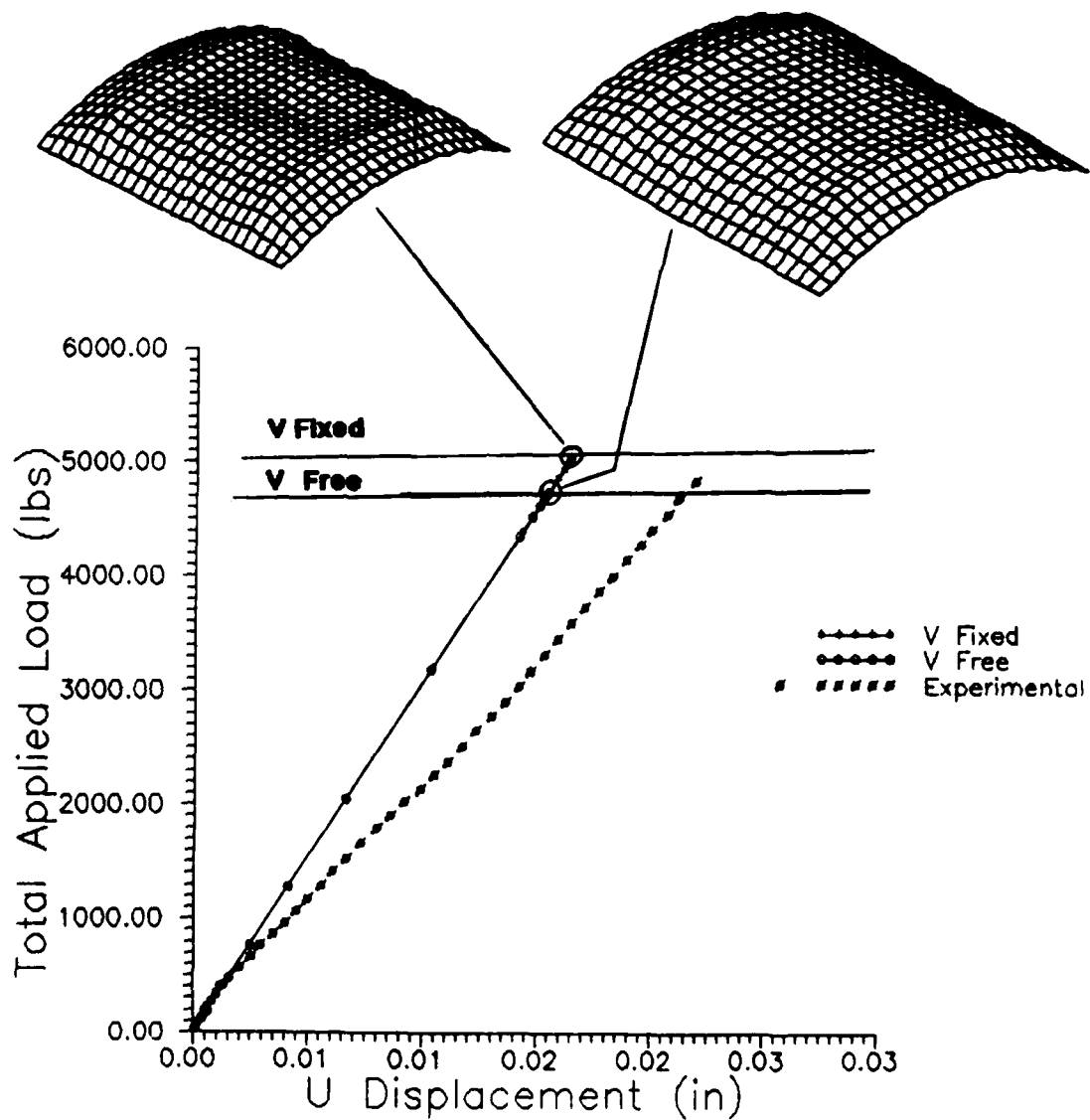


Fig 5.2 Equilibrium Load Distribution along Top of 4" Cutout Panel at Collapse

protected the edges and corners of the panel from being damaged by the experimental test setup. Although there was scarring of this tape during the tests (indicating the circumferential ( $v$ ) displacement was somewhat restricted), it was not clear if indicated  $v$  was completely fixed along the vertical edges. A comparison was carried out for the same model with  $v$  fixed and  $v$  free.

The added restriction of  $v$  fixed along the vertical edge allows for more of the load to be carried along the vertical edges, so one expects the panel with  $v$  fixed to carry more load before it collapsed. The load-displacement curves for a solid panel are shown in Figs 5.3 and 5.4, comparing  $v$  free to  $v$  fixed. It is seen, as expected, the fixed boundary condition results in a higher collapse load (about 10%) and top edge displacement. This collapse load increase is much greater than the 3% increase noted by Janisse [21] for 2" cutouts but less than the 18% increased noted by Tisler [35] for 5" cutouts. As Tisler noted, the radial displacements for the  $v$  fixed are greater than for  $v$  free (Figs 5.5-8). With  $v$  fixed, most of the bending and load carrying occurs at the vertical edges of the panel, while they are more evenly distributed for the  $v$  free condition.

When compared to experimental results for collapse load and displacement of the 12" panel with no cutout (Fig 5.3)



**Fig 5.3 Load-Displacement, v Free and Fixed, 12" Panel  
Experimental Results Compared**

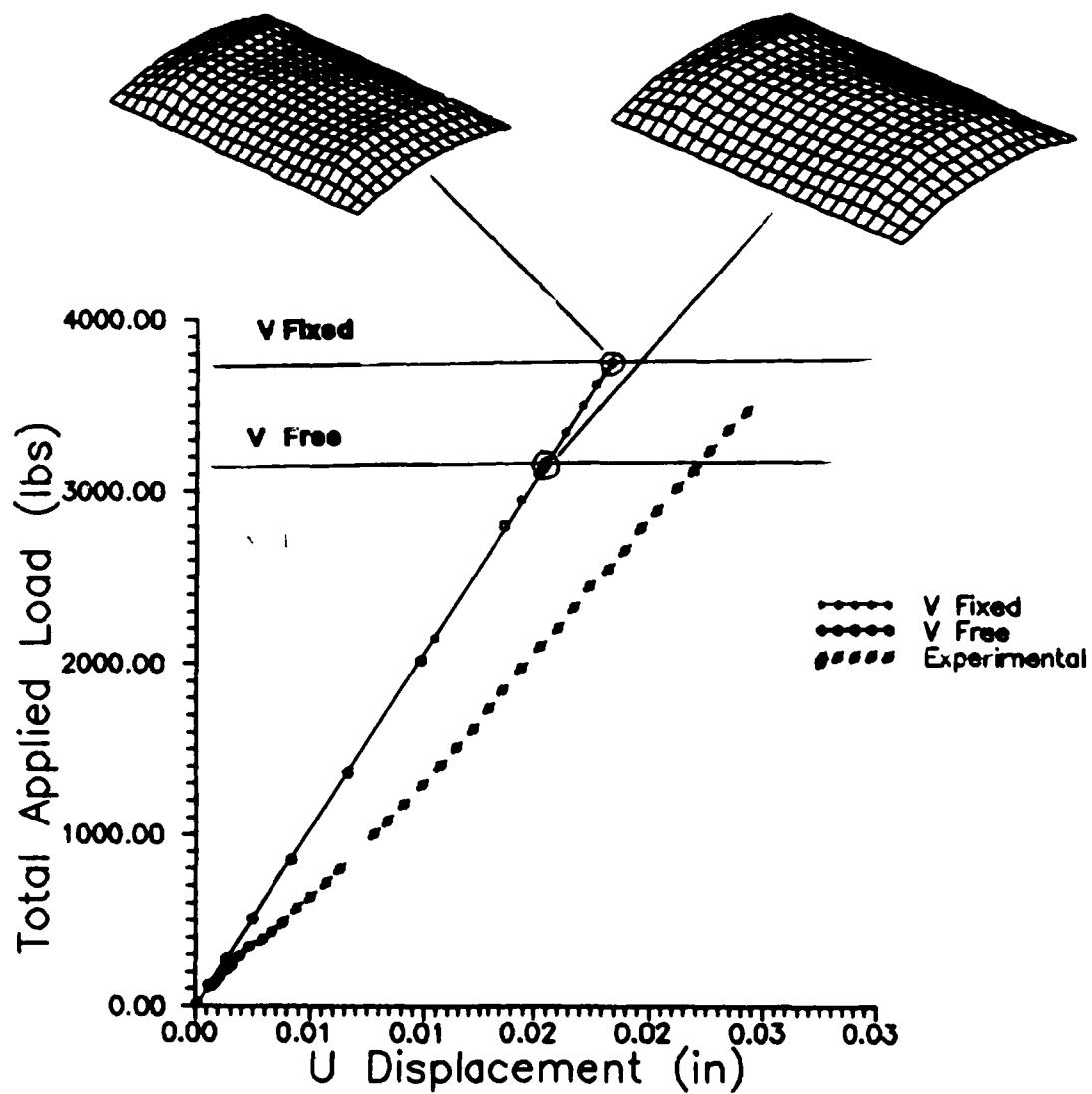


Fig 5.4 Load-Displacement, v Free and Fixed, 8" Panel  
Experimental Results Compared

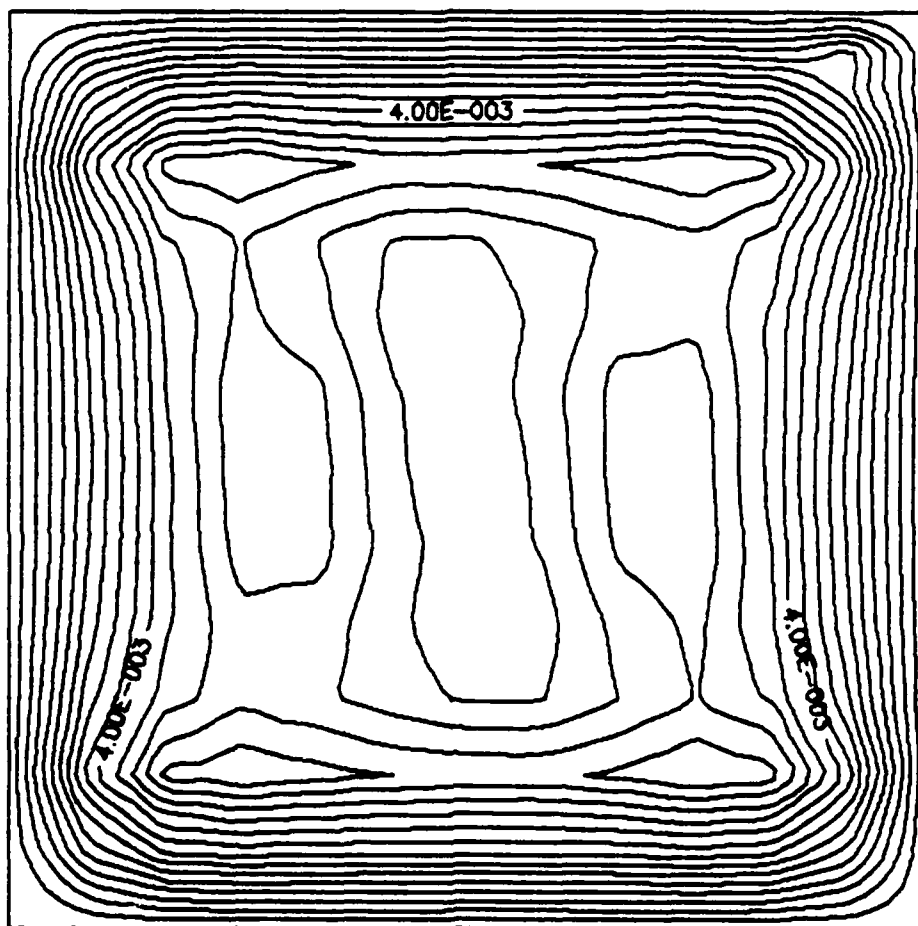


Fig 5.5 Radial Displacement Contour, 12" Wide Panel, No Cutout, v Free, Total Load = 4754 lbs (100% of Collapse Load).



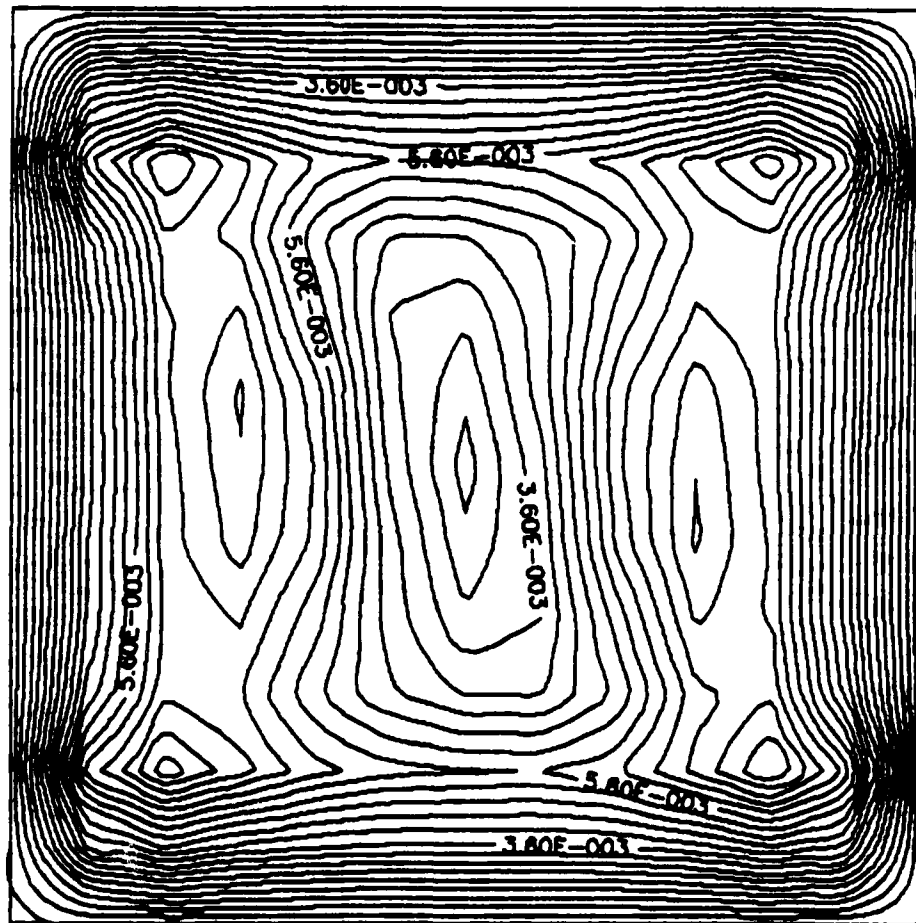


Fig 5.6 Radial Displacement Contour, 12" Wide Panel, No Cutout, v Fixed, Total Load = 5060 lbs (100% of Collapse Load).

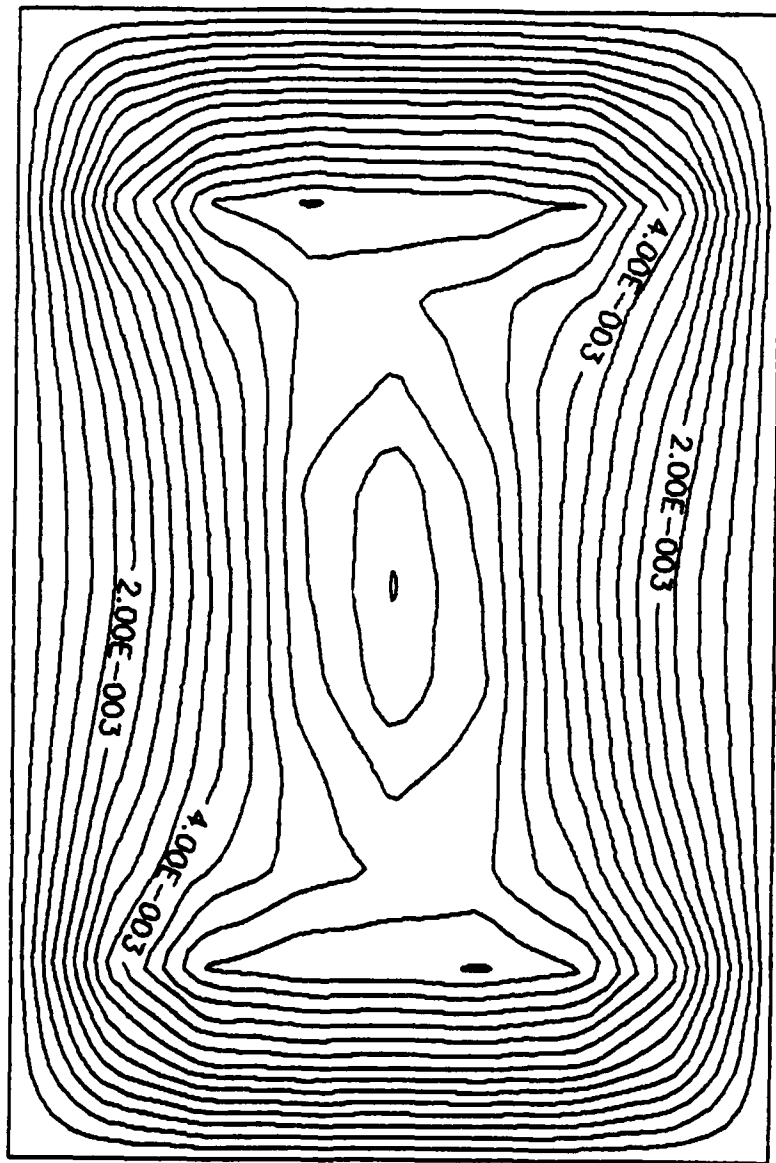
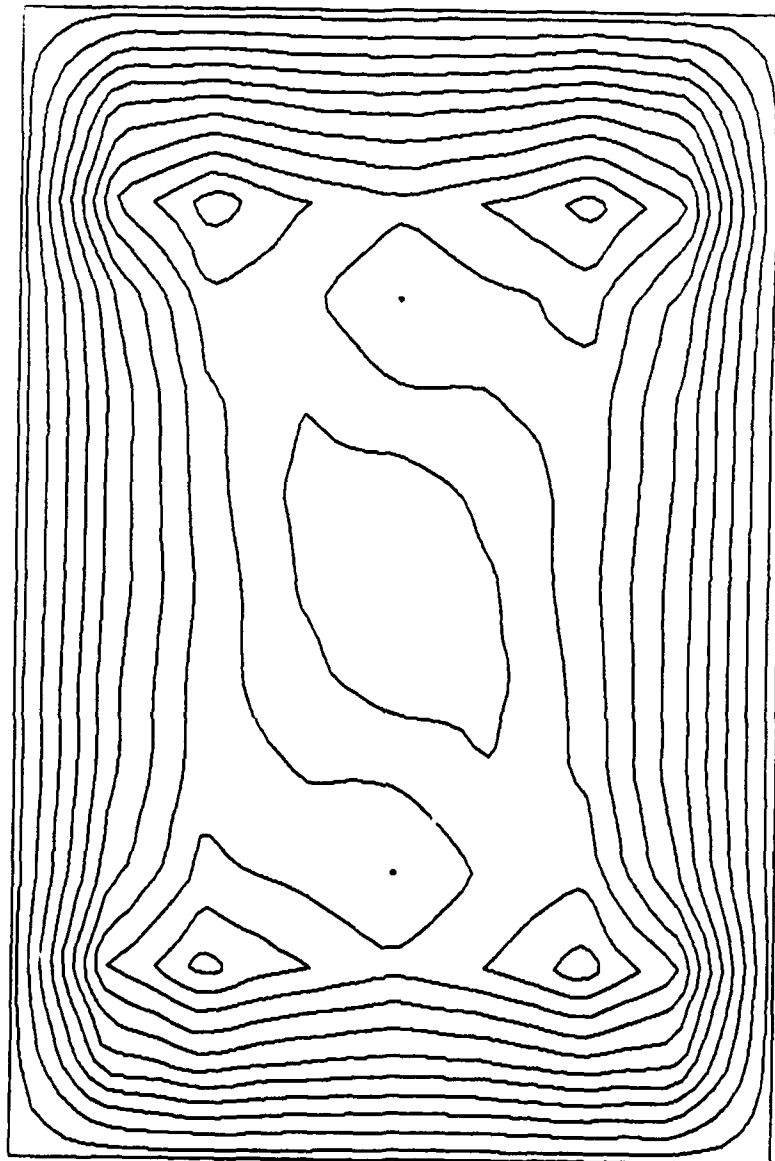


Fig 5.7 Radial Displacement Contour, 8" Wide Panel, No Cutout, v Free, Total Load = 3174 lbs (100% of Collapse Load).



**Fig 5.8** Radial Displacement Contour, 8" Wide Panel, No Cutout, v Fixed, Total Load = 3761 lbs (100% of Collapse Load).

and the 8" panel with no cutout (Fig 5.4), it appeared that the two conditions form an upper and lower bound for the experimental results. From a physical viewpoint, based upon scarring of the teflon tape, it seemed better to use the  $v$  fixed condition to model the response. Although the author believes that the actual experimental boundary conditions probably lies somewhere between the two extremes of fixed and free, all further analytical comparisons are made assuming that  $v$  is fixed along the vertical boundaries for the simply supported models. Because of this simplifying assumption, the STAGS collapse loads are expected to be slightly higher than the experimental results.

#### 5.1.2 Surface Imperfections

Janisse showed the greatest reduction in collapse load for uncut panels by modeling imperfections as three half sine waves in both the axial and circumferential directions [21]. It is felt that this imperfection modeling more closely approximates the experimental results (for uncut panels only) in part because the radial displacement pattern at collapse somewhat approximates this (refer Figs 5.5-8). It is noted that  $v$  is now assumed fixed along the vertical boundaries.

Imperfection models using one, two, or four half sine

waves all yielded higher collapse loads (from as little as 15% higher up to 75% higher) than the perfect panel model. The hypothesis is that since the buckled shape somewhat approximates three half sine waves in both the radial and axial directions, it requires less energy to move through an imperfection of a similar shape to the collapsed shape of the panel, than for the other imperfection models used. Hence, any imperfection models included in the following discussion consisted of the three half sine waves with an maximum amplitude of 0.005" ( $\approx$  one ply thickness).

With the imperfections included, the computer time required to reach collapse load was at least doubled (from 35000 CPU seconds to over 72000). The final reduction in load turned out to be small (Table 5.1, Figs 5.9-12), between 1-3%. This is especially true when considered with the very large reductions seen by Janisse [24] for solid panels (no cutout). For an equivalent ply lay-up and imperfection, his uncut panel with the same imperfection pattern collapsed at less than 25% of the bifurcation collapse load. Note: for a panel with no cutouts or imperfections, the bifurcation solution is essentially the same as the nonlinear solution ( $\approx$  3% variance). By modeling more precisely the imperfections typically seen in panels without cutouts, Starnes [30] saw collapse load reductions of only about 10%. Since collapse load of panels

with cutouts was much less sensitive to imperfections in the worst case form, it seems reasonable to assume sensitivity will also be less for other imperfection patterns such as those mentioned above.

When an imperfection model was tried with a cylindrical panel containing a large cutout it was found to be less sensitive to imperfections than the same panel with no cutout. Previous work by Tisler [35] seemed to bear this out. However, this was not the primary thrust of his work and therefore does not give much depth to this particular analysis. Unfortunately, no other work on cylinders with both large cutouts and imperfections was found to verify these results.

Table 5.1 Results by Comparing Perfect vs Imperfect Panels

Collapse Load, lbs			
Panels	Perfect	Imperfect	Reduction
12" SS	5060	5940	2.2%
8" SS	3761	3700	1.6%
12" US	2298	2260	1.7%
8" US	1382	1350	2.3%

MOTE: SS = Simply Supported, US = Unsupported

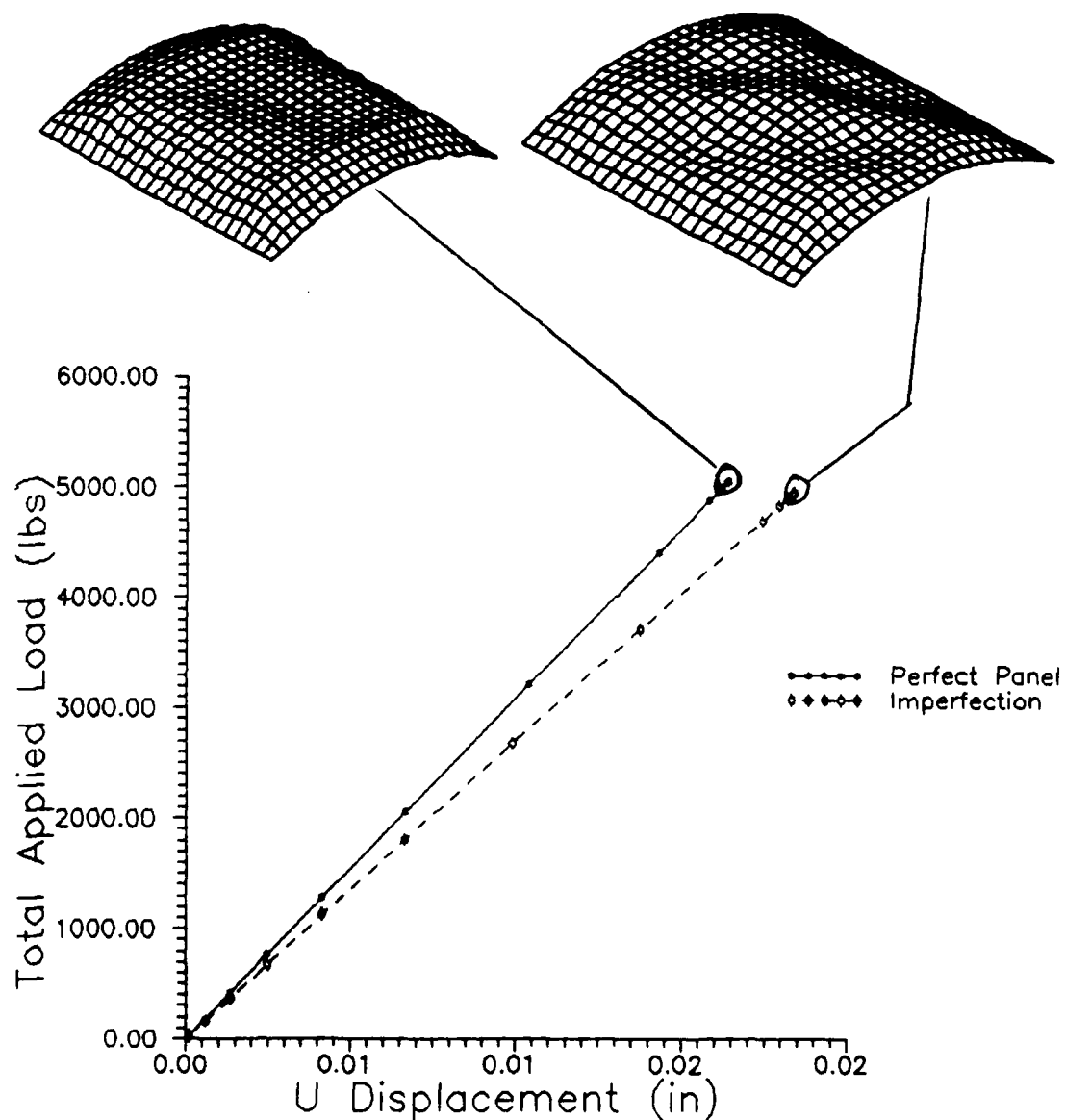


Fig 5.9 Load-Displacement, 12" Simply Supported Panel, Comparing Perfect vs Imperfection

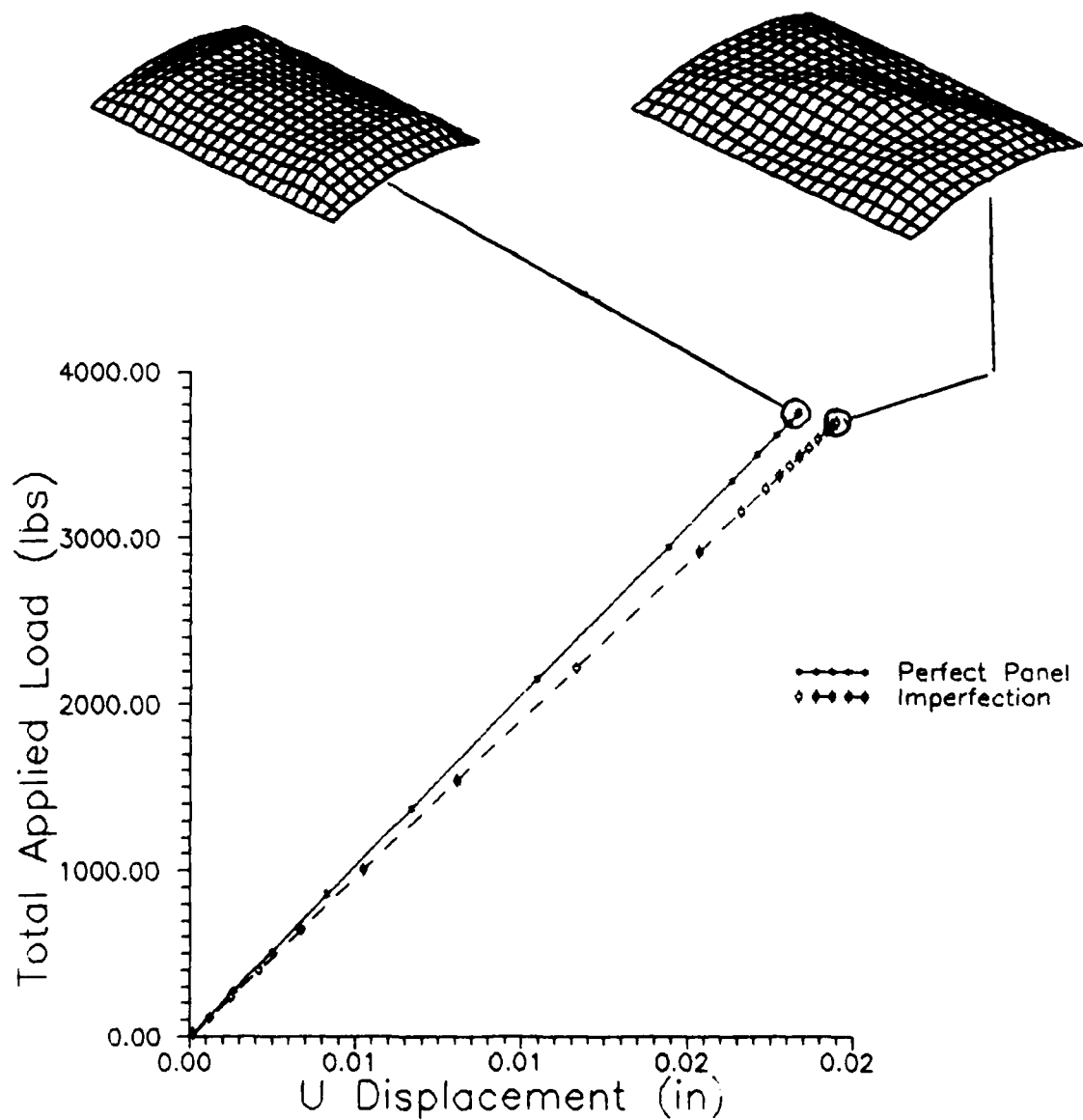
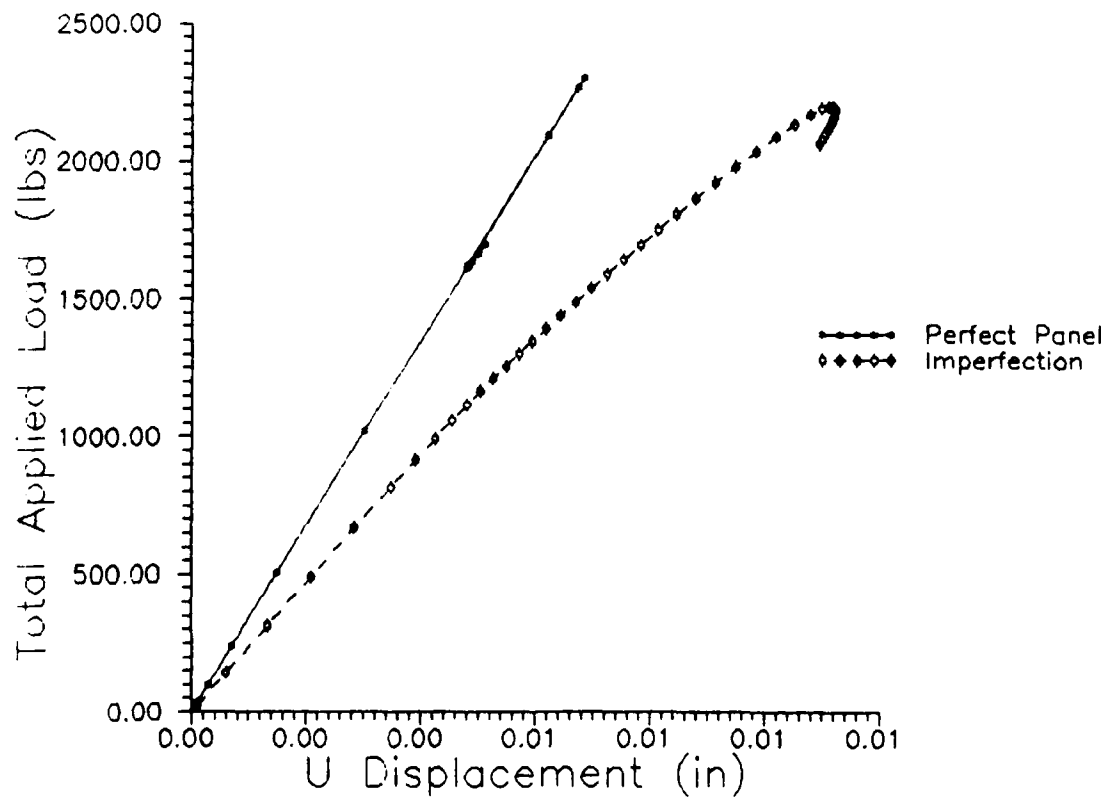


Fig 5.10 Load-Displacement, 8" Simply Supported Panel, Comparing Perfect vs Imperfection





**Fig 5.11 Load-Displacement, 12" Unsupported Panel, Comparing Perfect vs Imperfection**

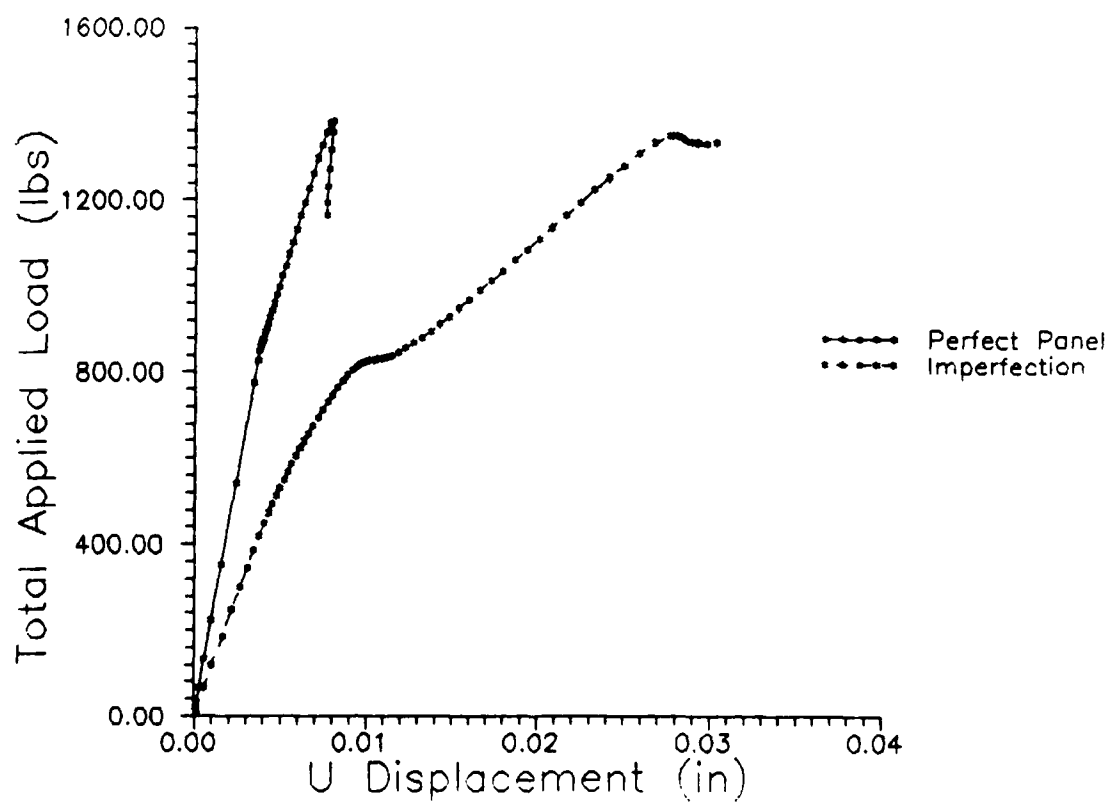


Fig 5.12 Load-Displacement, 8" Unsupported Panel, Comparing Perfect vs Imperfection

It should be noted at this point that for the solid panels with unsupported edges had extreme problems converging to a solution with the STAGS QUAFF 411 element. However, when the QUAFF 410 element was tried, along with the imperfections, STAGS did converge to solutions that were reasonable when compared to the experimental results. The author will discuss this in greater detail in Section 5.3.

The STAGS radial displacement collapse patterns (Figs 5.13-16) and isoparametric views (Figs 5.9-12) were much different for panels with imperfections than for panels without at the collapse load. This imperfection pattern alluded to earlier in the discussion is not the true experimental imperfection pattern, and the resulting collapse shapes are much different. For those models with an surface imperfection model, a trough (aligned with the  $-45^\circ$  outer angle ply) is distinctly formed whereas in the perfect model, the trough is barely distinguishable and is nearly perpendicular (aligned with the  $0^\circ$  ply). The experimental radial displacements were very similar to that predicted for panels with no imperfections. This indicates that initial imperfections do not control the displacement pattern to the extent seen in the analytical imperfection case. However, as evidenced in Figs 5.9-12, the initial imperfections do reduce the panel's stiffness (hence its ability to withstand additional energy created by increased

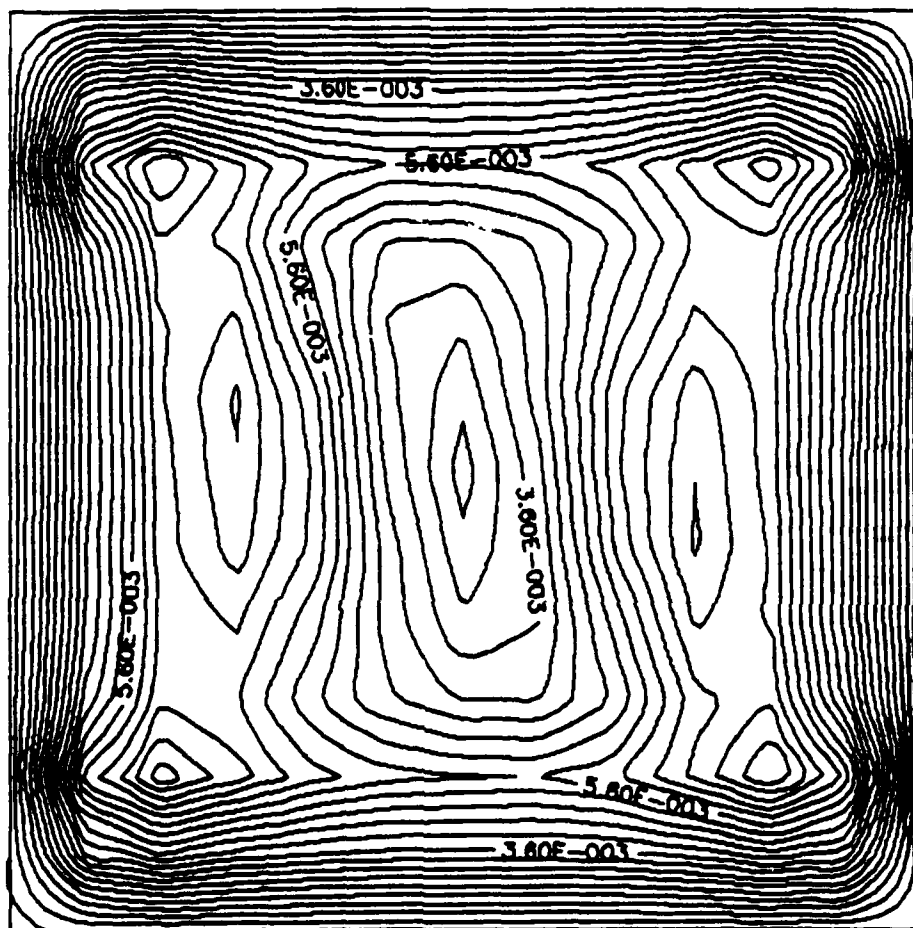


Fig 5.13 Radial Displacement Contour, 12" Wide Panel,  
No Cutout, Simply Supported, No Imperfection,  
Total Load = 5060 lbs (100% of Collapse Load)

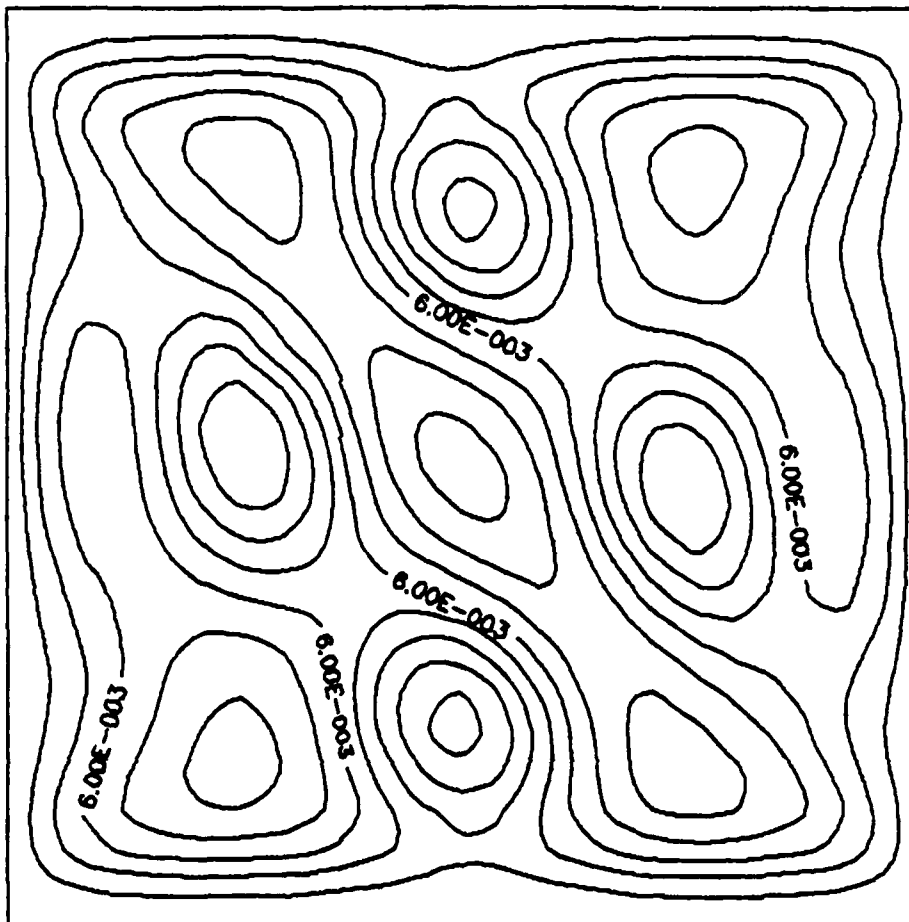


Fig 5.14 Radial Displacement Contour, 12" Wide Panel,  
No Cutout, Simply Supported, Imperfection,  
Total Load = 4899 lbs (100% of Collapse Load)

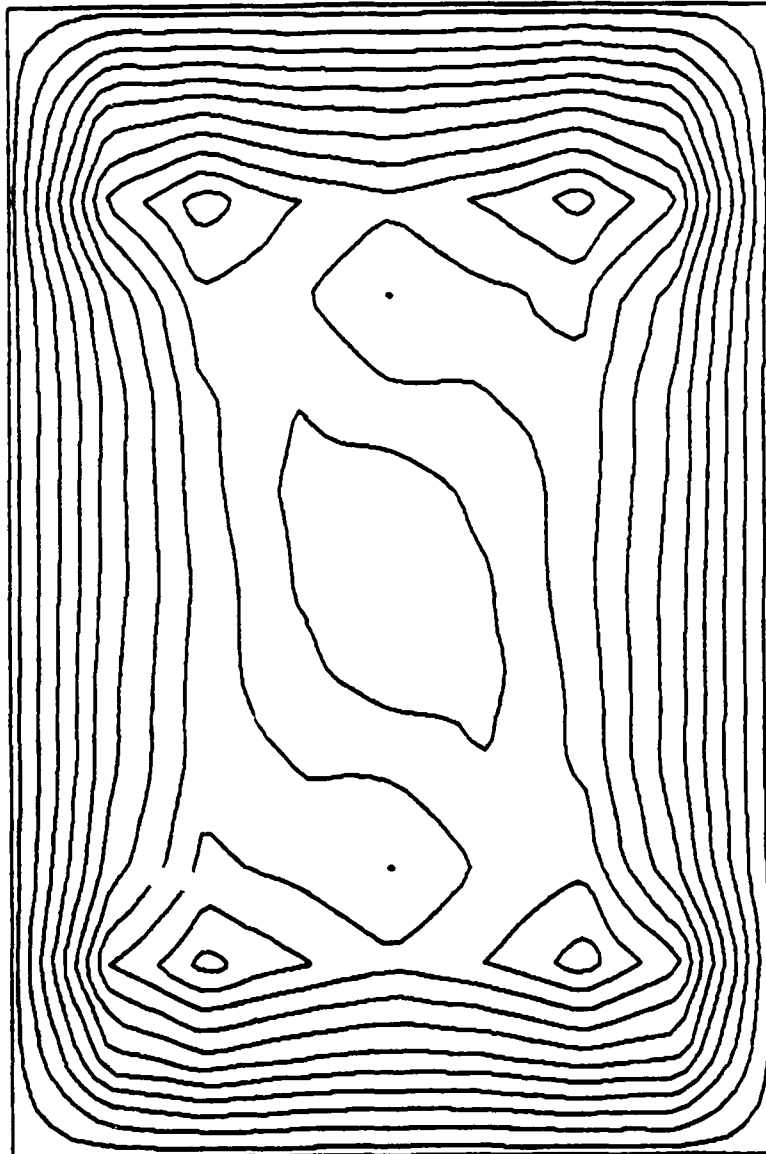
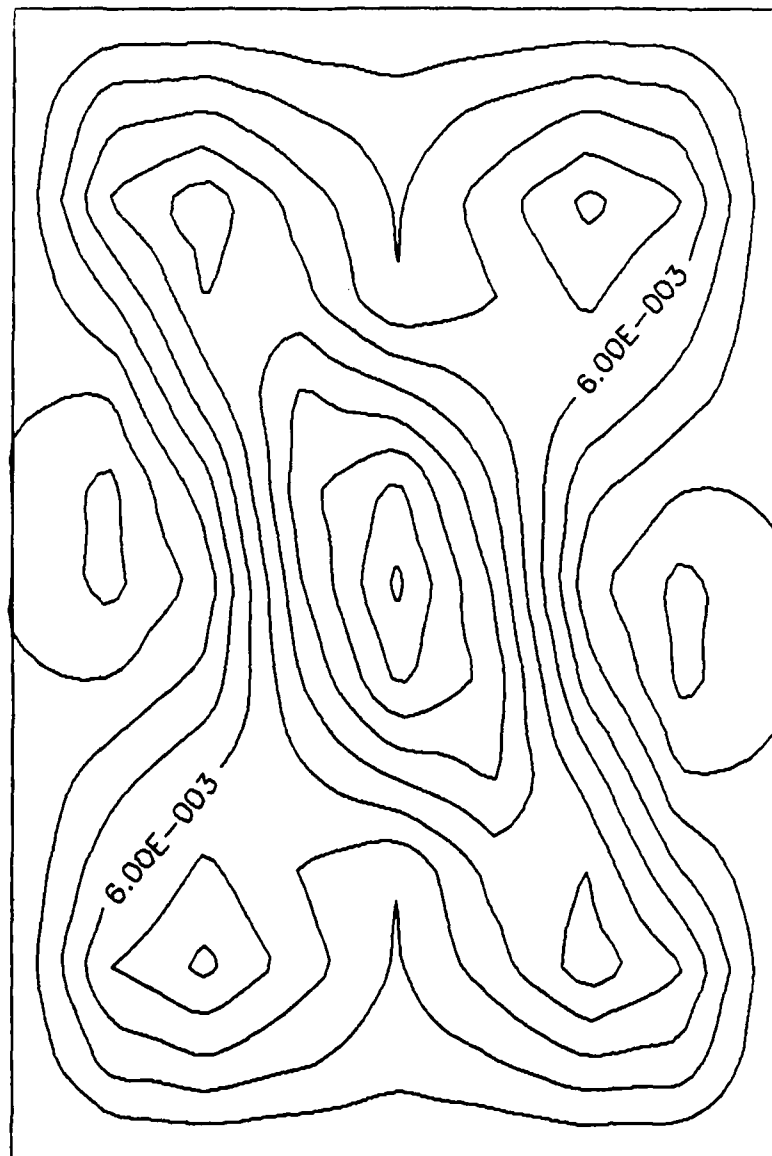


Fig 5.15 Radial Displacement Contour, 8" Wide Panel,  
No Cutout, Simply Supported, No Imperfection,  
Total Load = 3761 lbs (100% of Collapse Load)



**Fig 5.16** Radial Displacement Contour, 8" Wide Panel,  
No Cutout, Simply Supported, Imperfection,  
Total Load = 3749 lbs (100% of Collapse Load)

loading) over the duration of the load-displacement curve. It is important to notice that the unsupported panels are significantly affected by the initial imperfections. Although the analytical imperfection model used does not accurately reflect the experimental imperfections, it does demonstrate the inherent reduction in stiffness exhibited in the panel experimentally. Also, in the case of the unsupported panels, the imperfection model does indicate increased bending in the panel's response once it has entered the nonlinear region of loading. The reduction in collapse load due to initial imperfections is present for all the panels shown in the above figures. In the case of the simply supported panels, the analytical imperfection model demonstrated a small change in collapse load and stiffness ( $\approx 5-7\%$ ). In the unsupported panels the analytical imperfection model showed a small change in collapse load ( $\approx 5\%$ ), but a marked decrease in stiffness with a significant increase in bending (as much as a 35% increase in  $M_{xy}$ ).

Because of the small change in collapse load (less than 5%) at the cost of a substantial increase in computer time (over 75000 CPU seconds) and poor radial displacement predictions (it was not practical to use the methods needed to get the more accurate initial imperfection shape [30]), it was decided to perform the analytical checks without



imperfections for the panels with cutouts. It is assumed based on previous work [35] and the few computer models attempted in this effort that the 4" cutout panels are relatively insensitive to initial imperfections. The author feels that the large geometric imperfections for these panels dominate the panels response over the initial imperfections. As in assuming a fixed circumferential boundary condition ( $v$ ), the STAGS solution that assumes no initial imperfections should estimate higher collapse loads than is seen experimentally. Only the panels with no cutouts contain imperfection models, primarily due to the relatively small cost of running these models (only an increase of about 10000-15000 CPU seconds) and the marked change in stiffness and bending due to the presence of the initial imperfections.

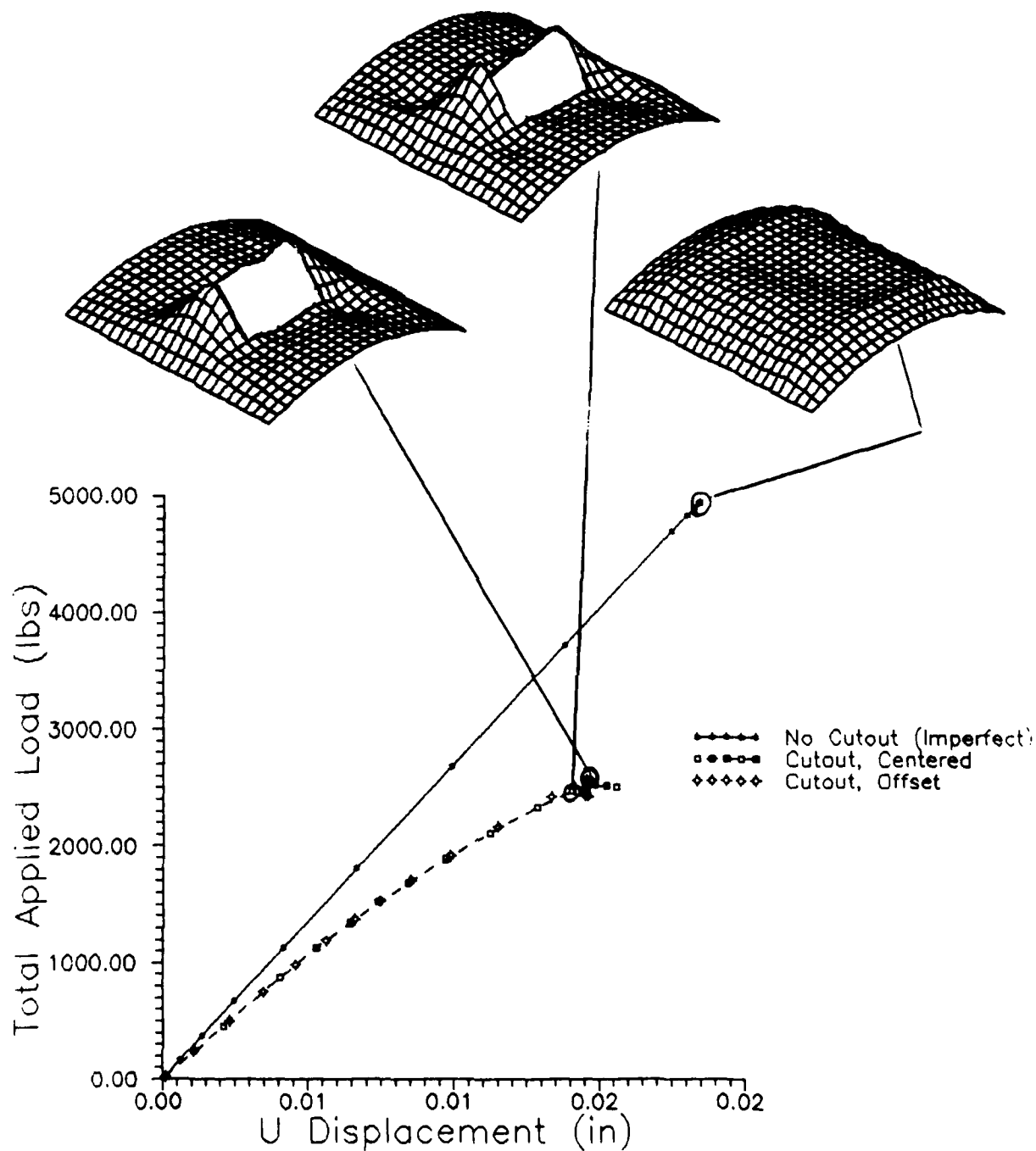
#### 5.1.3 Geometric Imperfections (Cutouts) & Eccentricity Effects

One of the major thrusts of this effort is studying the collapse characteristics of cylindrical composite shells due to the effects of large geometric imperfections (cutouts) and the effect of cutout eccentricity.

Load-displacement curves were generated for all twelve of the models mentioned in Section 3.1, Table 3.1 and are

shown in Figs 5.17-20 in composite form (meaning curves are shown together for the same boundary conditions and panel width). It should be noted that  $v$  is assumed fixed for all simply supported panels and that all panels with no cutouts do contain an initial imperfection model of three half sine wave in both the radial and circumferential directions. The maximum amplitude of these sine waves is one ply thickness (0.005").

By comparing values between the same class of panels, it is clear the effect cutouts have on the panel collapse characteristics. It is also evident the effect eccentricity has on the panel(s). In the case of the 12", simply supported panels, the 4" cutout decreases the collapse load by 51%. However cutout eccentricity actually increases the collapse load by a small amount (3%) over the centered cutout. Both panels with cutouts show an extensive amount of nonlinearity when compared with the panel that has no cutout. As Tisler [34], Hermesen [23], and Janisse [21] noted, this nonlinearity is caused by the large stress (axial and bending) redistribution occurring with large cutouts. The difference between the nonlinear collapse loads and buckling loads obtained by simpler and more efficient bifurcation analysis is seen to change with cutout size and location (Fig 5.21). As expected, for no cutouts with and no initial imperfections, the nonlinear and



**Fig 5.17 Load-Displacement, 12" Simply Supported Panel, Comparing Geometric Imperfections**

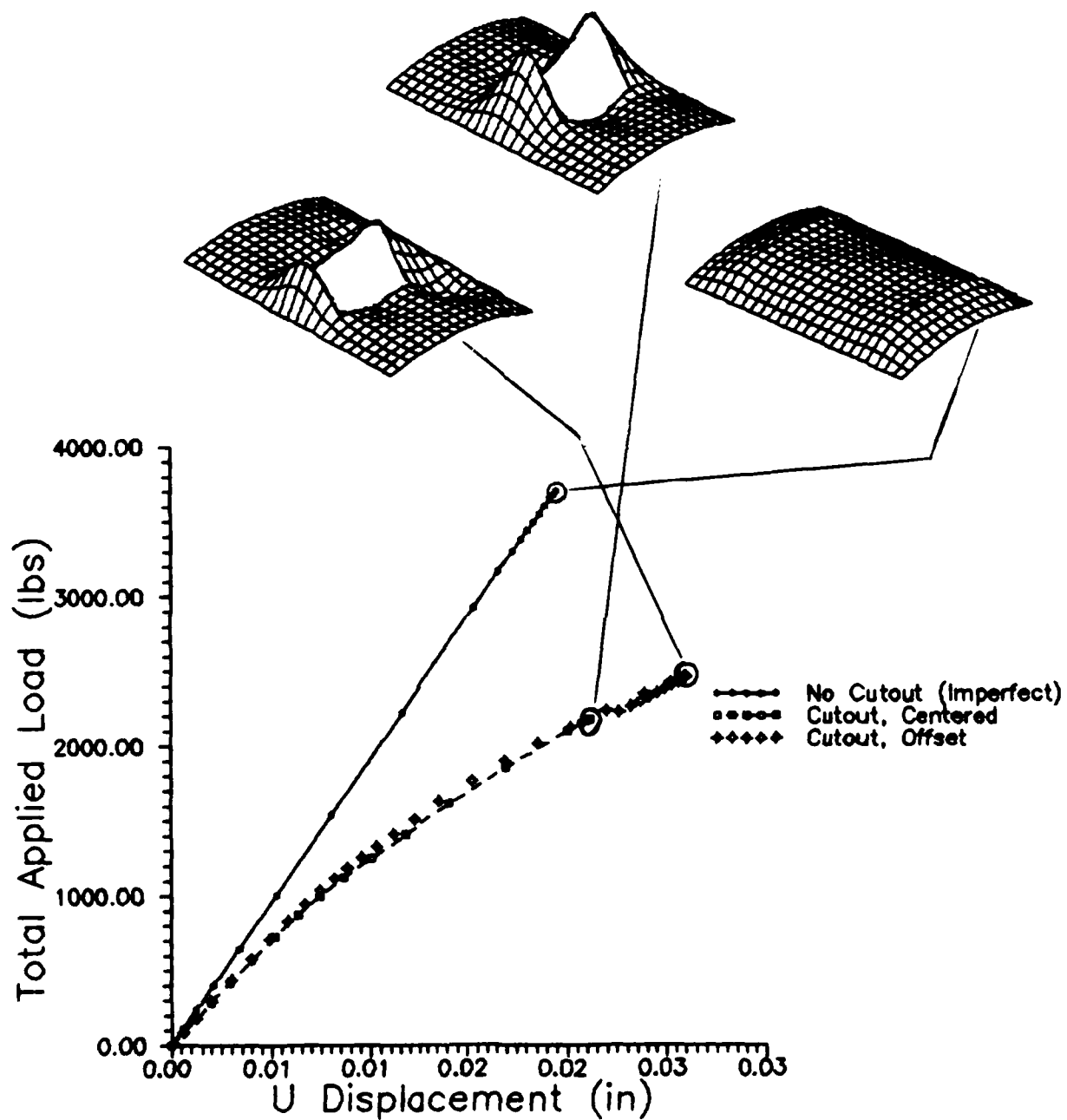


Fig 5.18 Load-Displacement, 8" Simply Supported Panel, Comparing Geometric Imperfections

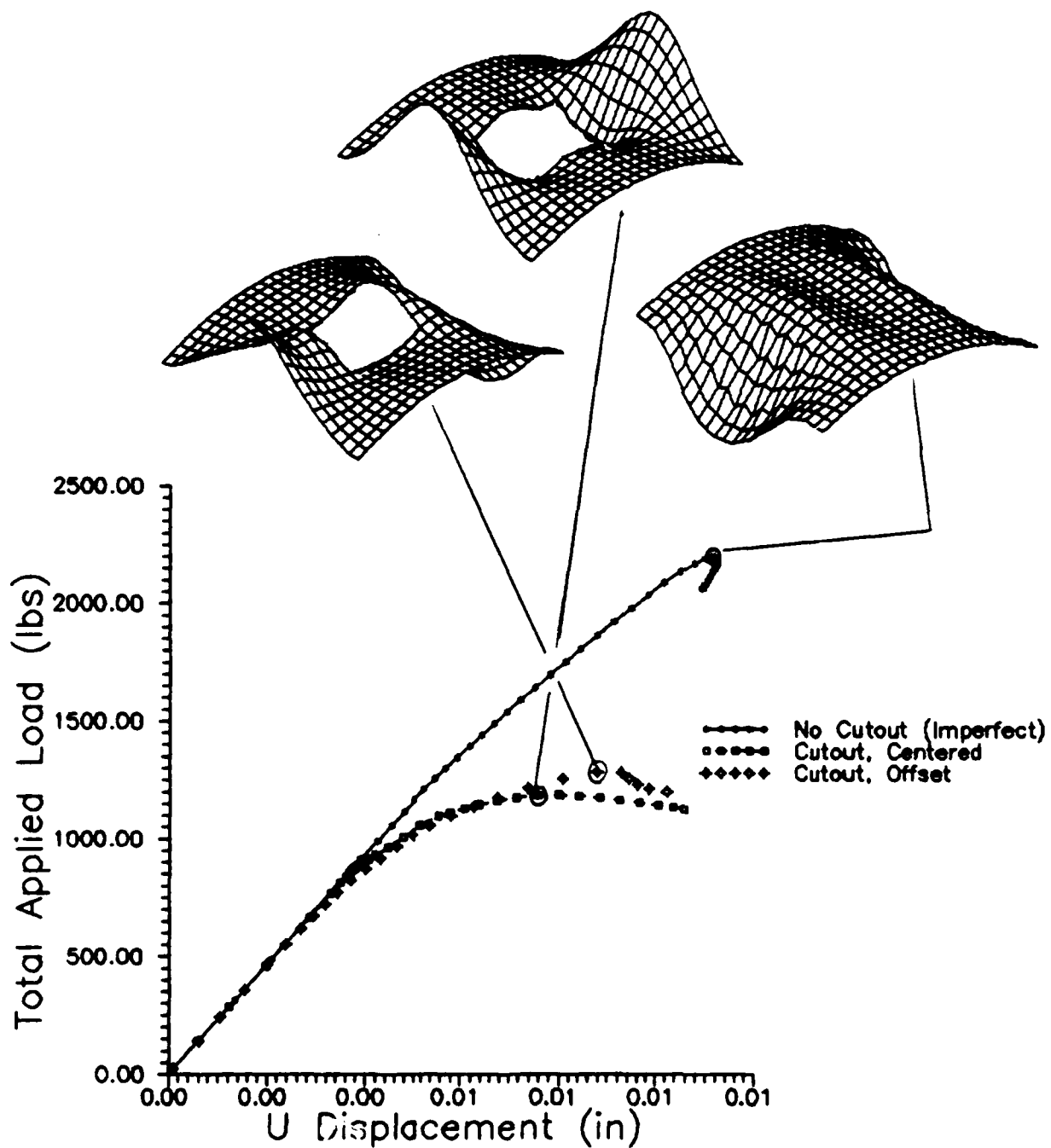


Fig 5.19 Load-Displacement, 12" Unsupported Panel, Comparing Geometric Imperfections

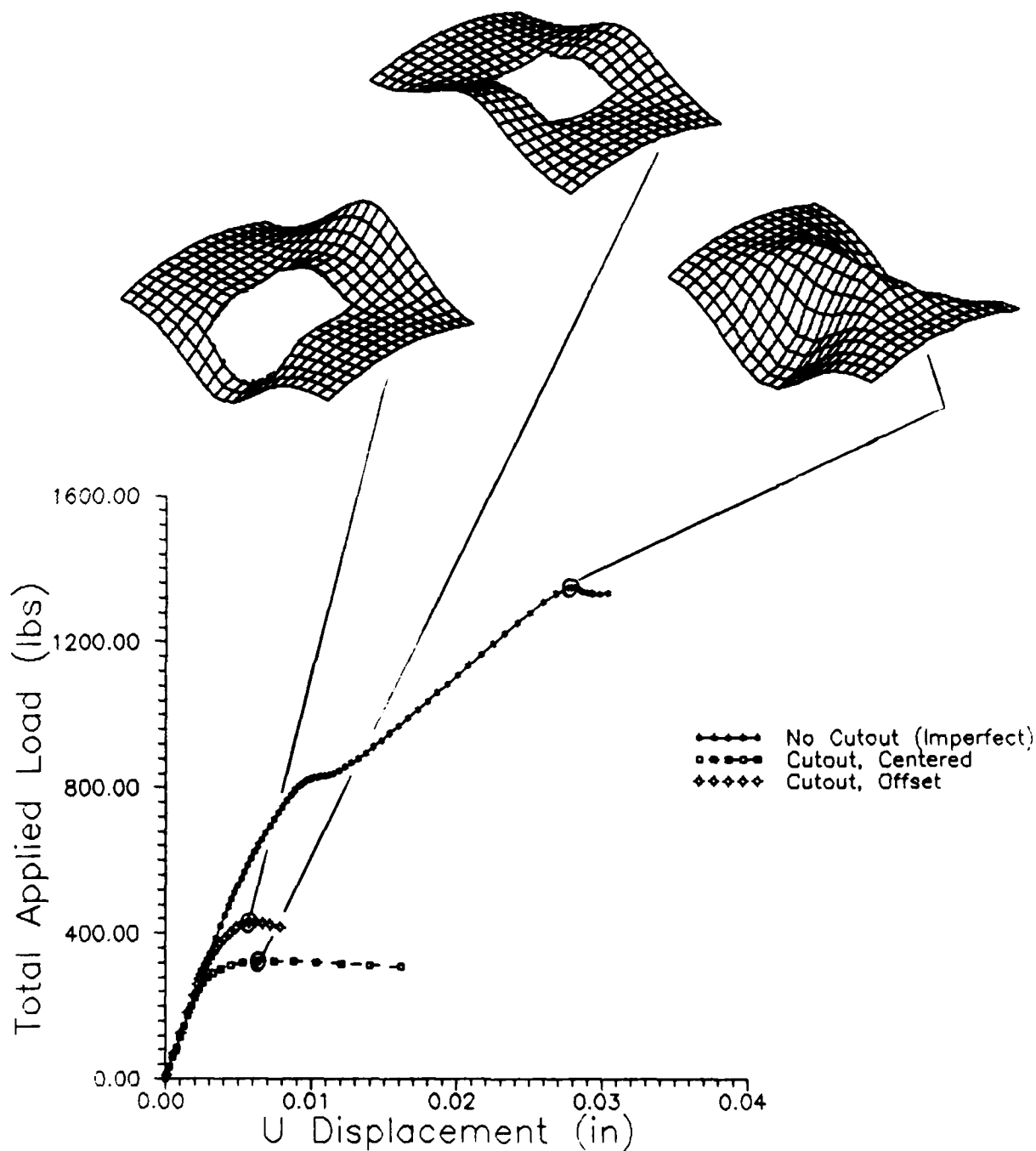


Fig 5.20 Load-Displacement, 8" Unsupported Panel, Comparing Geometric Imperfections

bifurcation values are the same. The 2" cutout does not have much stress redistribution, and the bifurcation value is higher than the nonlinear collapse load [21]. The opposite occurs for the 4" cutouts, with the bifurcation values becoming lower than the nonlinear results. The lower bifurcation values for the 4" cutouts is expected, since linear bifurcation methods do not consider the redistribution of moments and stresses. Instead, the bifurcation method assumes that the stresses and moments increase linearly from a small initial load. Fig 5.22 shows how the vertical stress profile ( $N_x$ ) in the panel with the 4" cutout, centered, changes. This  $N_x$  profile is taken along the left side of the cutout. The stress is greatest near the cutout at the beginning of loading, and shifts toward the vertical edges while loading is increased. At collapse, most of the load is carried along the vertical edges during loading. This shifting of the load to the supported edges allows for a much higher collapse load than is predicted by the linear bifurcation method. When the cutout is moved closer to one side, this redistribution occurs even more quickly. For the 4" centered cutout, the redistribution was essentially accomplished at 80% of the collapse load. For the 4" cutout, offset 1", the redistribution was accomplished at approximately 70% of the collapse load. This may indicate the reason why the

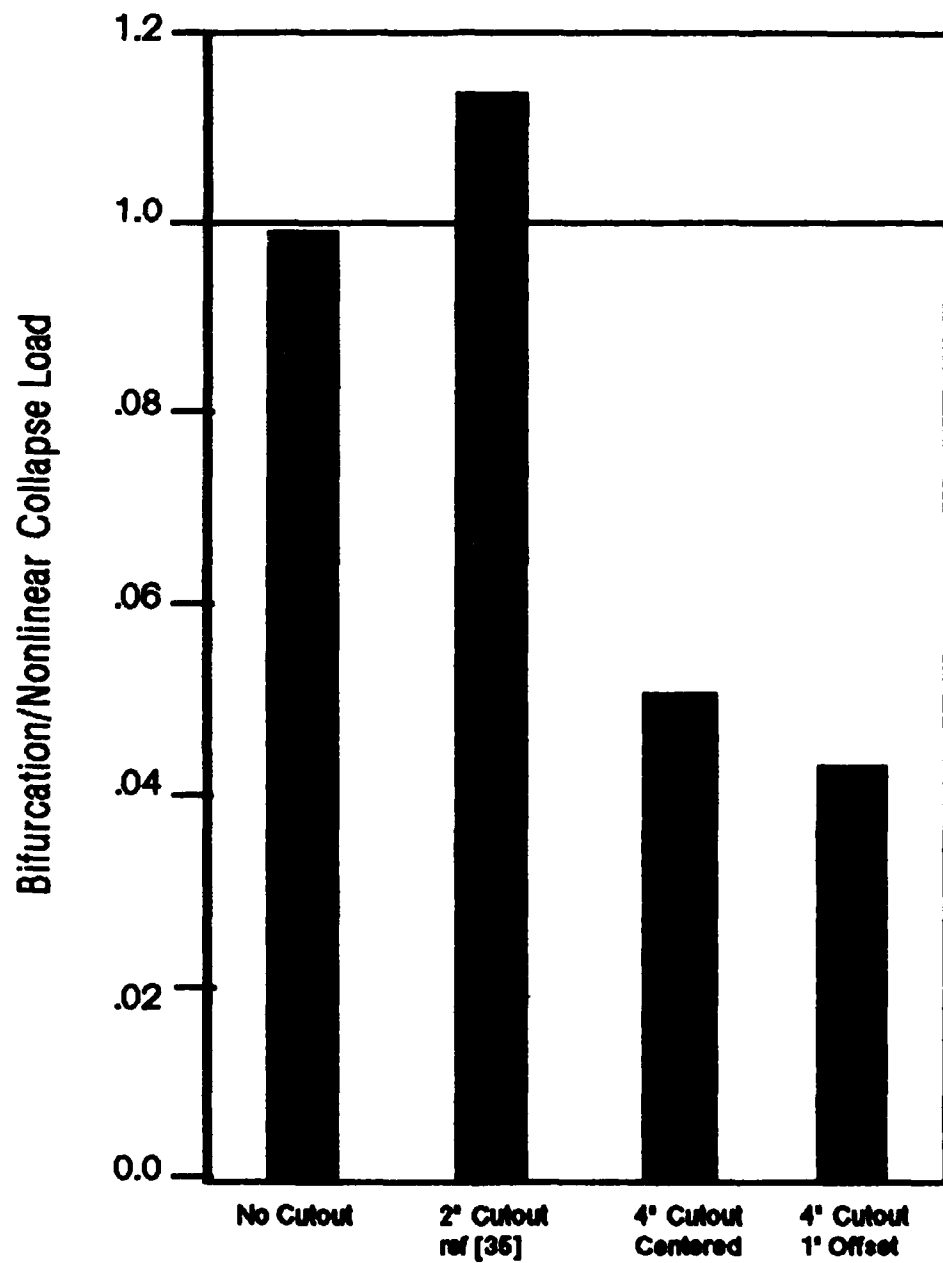


Fig 5.23 Bifurcation/Nonlinear Collapse Load for Varying Cutout Sizes & Location



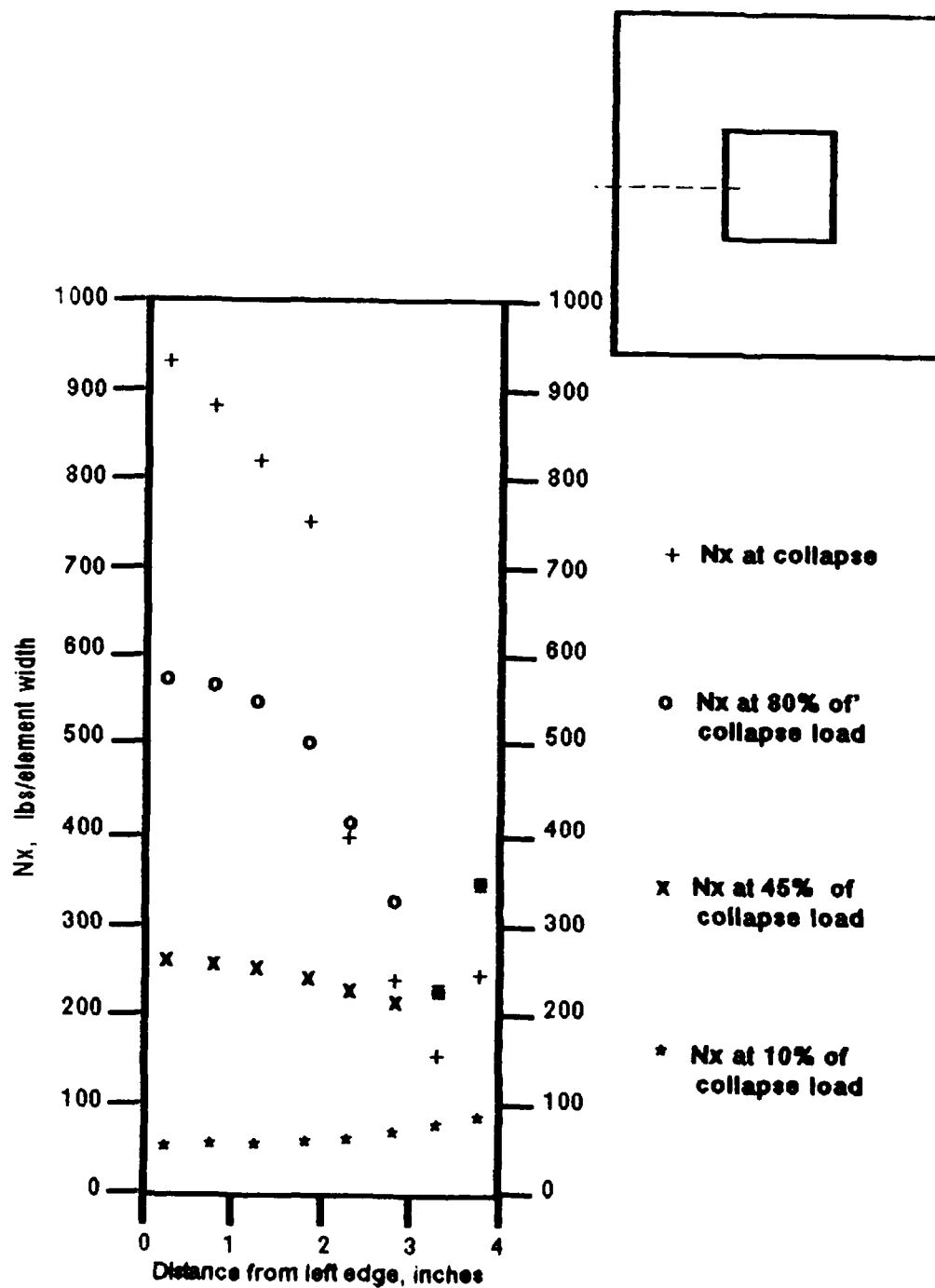


Fig 5.24 Values of  $N_x$  Along Side of Cutout, 12" Simply Supported Panel

eccentricity of the cutout leads to a slight increase in the total collapse load of the panel.

The same trend is noticed for the other three classes of panels. In the case of the 8" simply supported panel, the 4" centered cutout reduces the total collapse load by 43%. As in the 12" simply supported panels, eccentricity of the cutout increases collapse load by 3%. The smaller reduction in collapse load is attributed to the simply supported edges being closer to the cutout, thereby influencing the stress redistribution. Fig 5.23 shows how the vertical stress profile for the 8" panel with a centered cutout changes. As expected, the redistribution follows the pattern shown by the 12" panel with the off-center cutout. As the simply supported vertical edges are moved closer to the cutout, the stress redistribution occurs at a lower percentage of the total collapse load. For the 8" panel this occurred at approximately 65% of the collapse load. And for the 8" panel with the offset cutout, the redistribution occurred at approximately 50% of the collapse load.

For the 12" unsupported panels, the presence of a 4" centered cutout reduced the total collapse load by 46%. But when the cutout was offset 1", the collapse load is reduced only by 40%.

The 8" unsupported panels showed extreme sensitivity to

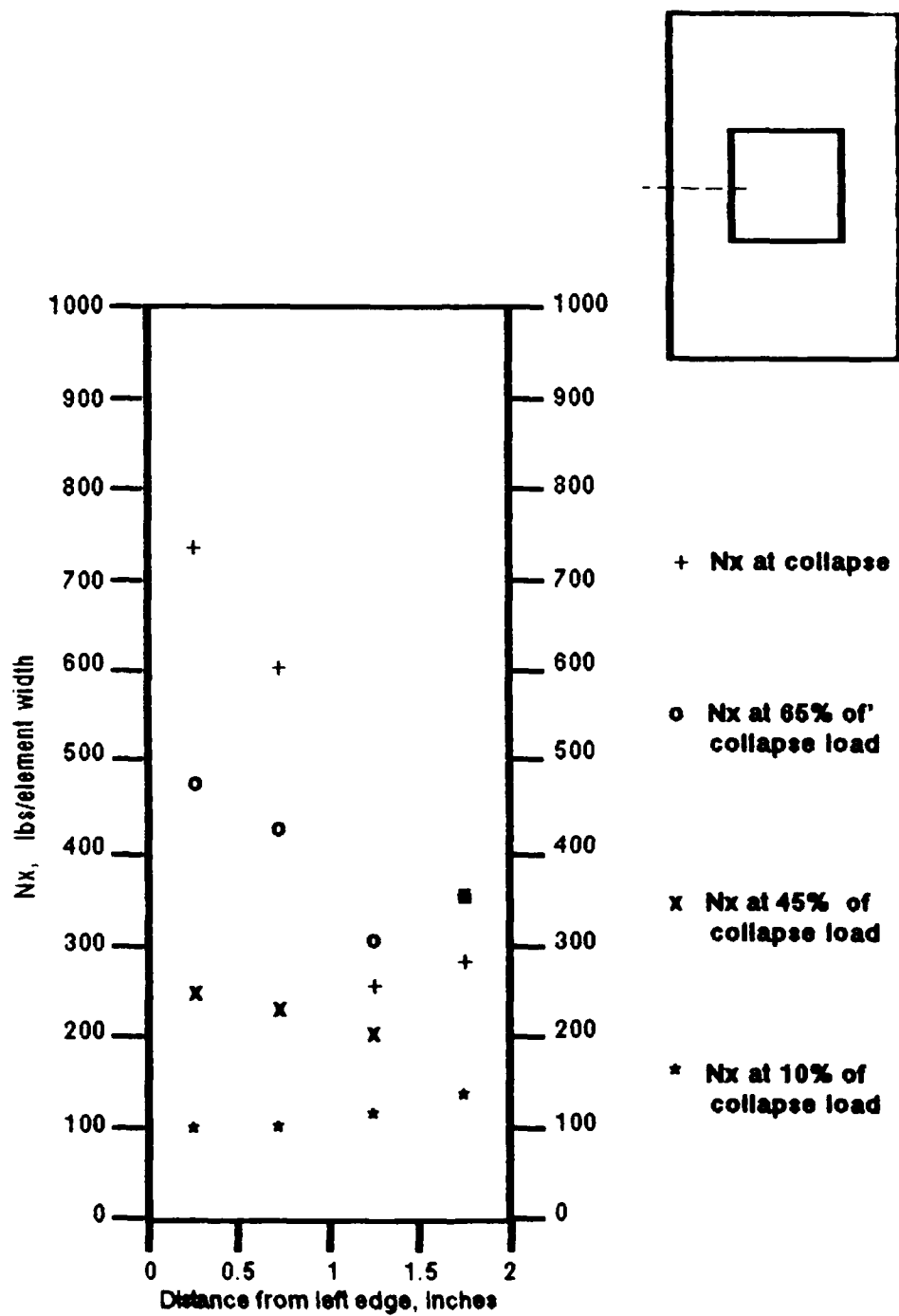


Fig 5.23 Values of  $N_x$  Along Side of Cutout, 8" Simply Supported Panel

the presence of cutouts. The 4" centered cutout reduced the total collapse load by 77%, and when the cutout was offset 1", the collapse load is reduced by 70%.

#### 5.1.4 Boundary Conditions

Another major thrust of this effort is studying the effect of changing the boundary conditions along the vertical edges of the composite panels. Load-displacement curves were generated in comparing six categories of panels based on panel geometry (width) and the existence of geometric imperfections. These are shown in Figs 5.24-29. In every circumstance, the removal of the vertical simple supports resulted in a significant decrease of the total collapse load. As stated before, all solid panels contain initial imperfection models of three half sine waves with amplitude of one ply thickness.  $v$  is assumed to be fixed for all simply supported panels. It is expected, based on these initial assumptions, that STAGS will converge to a solution with more stiffness than is seen experimentally.

Table 5.2 shows the tabulated comparison for the analytical results from STAGS. Fig 5.30 shows the comparison between simply supported/unsupported panels for each category. On the average, for the 12" panels, the reduction is 50-53%. For the 8" panels, the

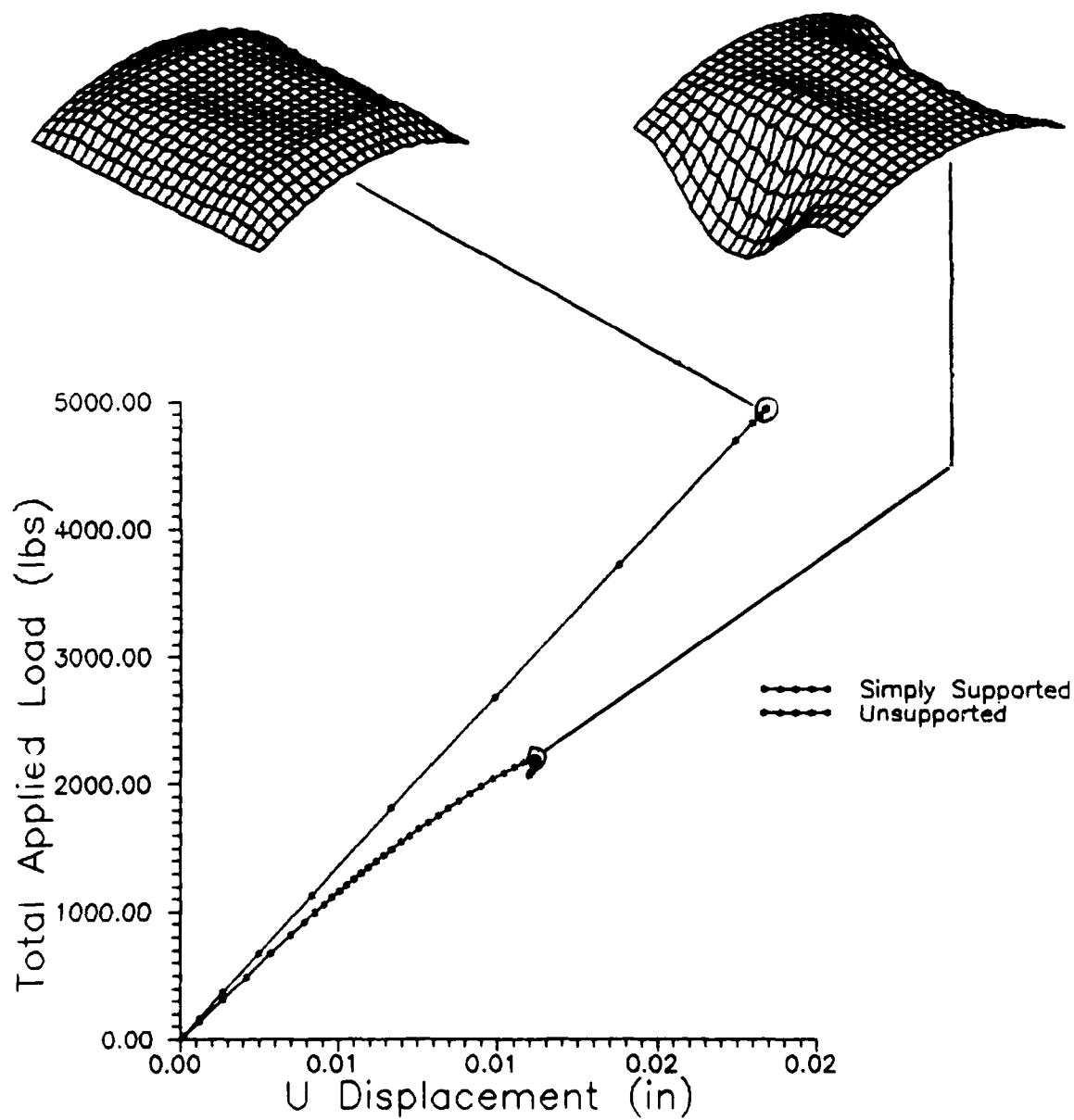


Fig 5.24 Load-Displacement, 12" Panels, No Cutout

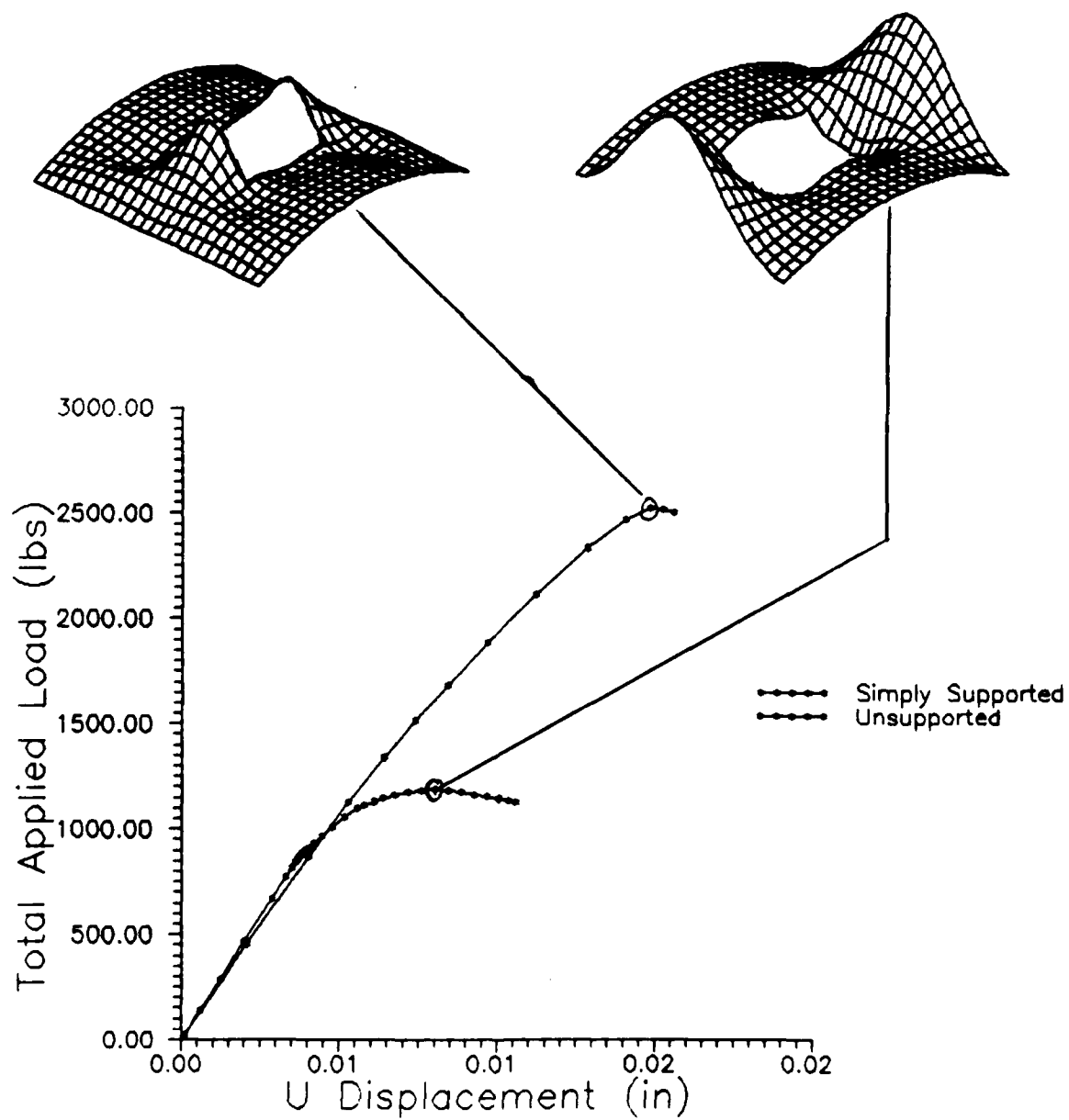


Fig 5.25 Load-Displacement, 12" Panels, 4" Cutout, Centered

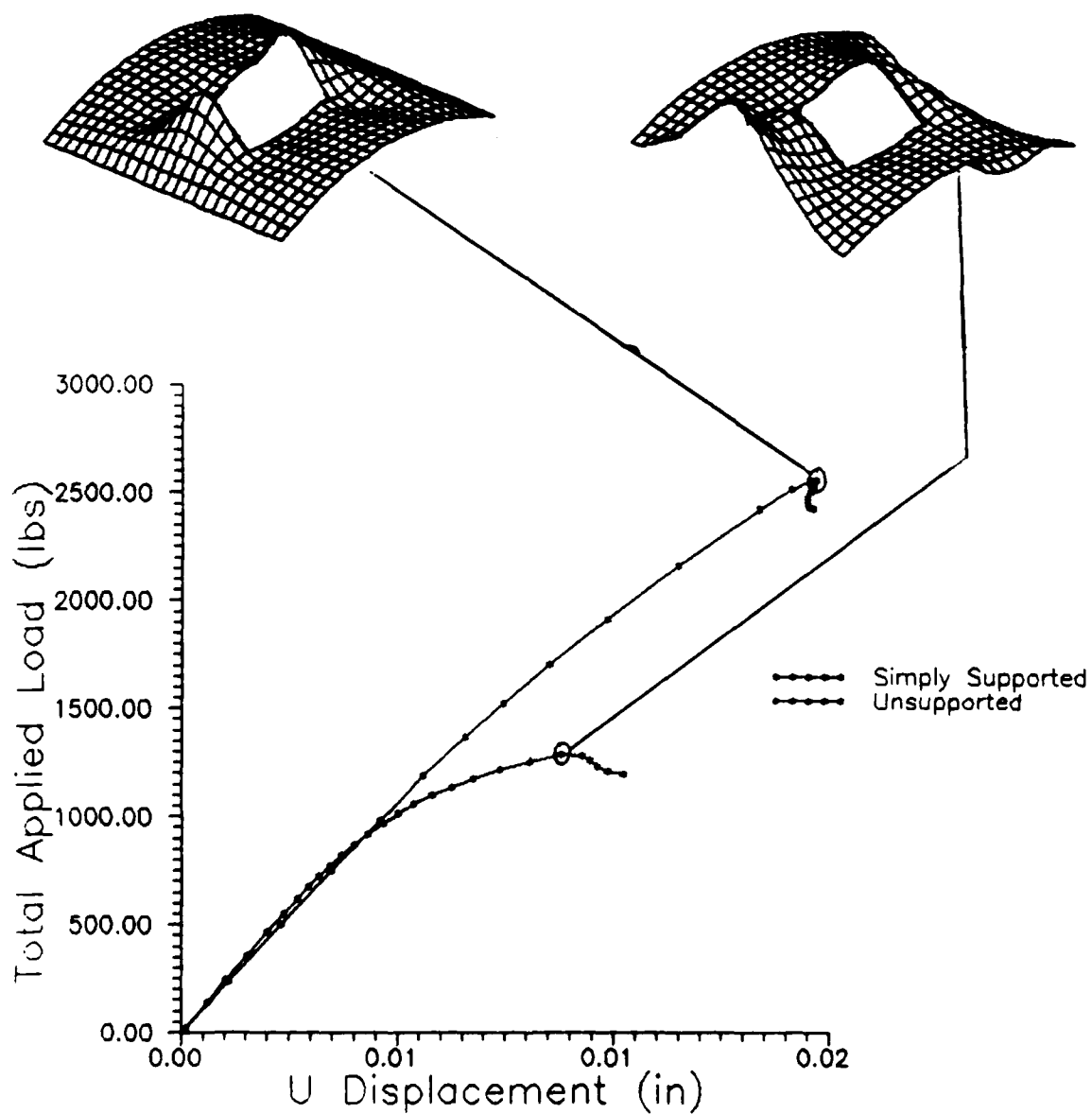


Fig 5.26 Load-Displacement, 12" Panels, 4" Cutout, 1" Offset

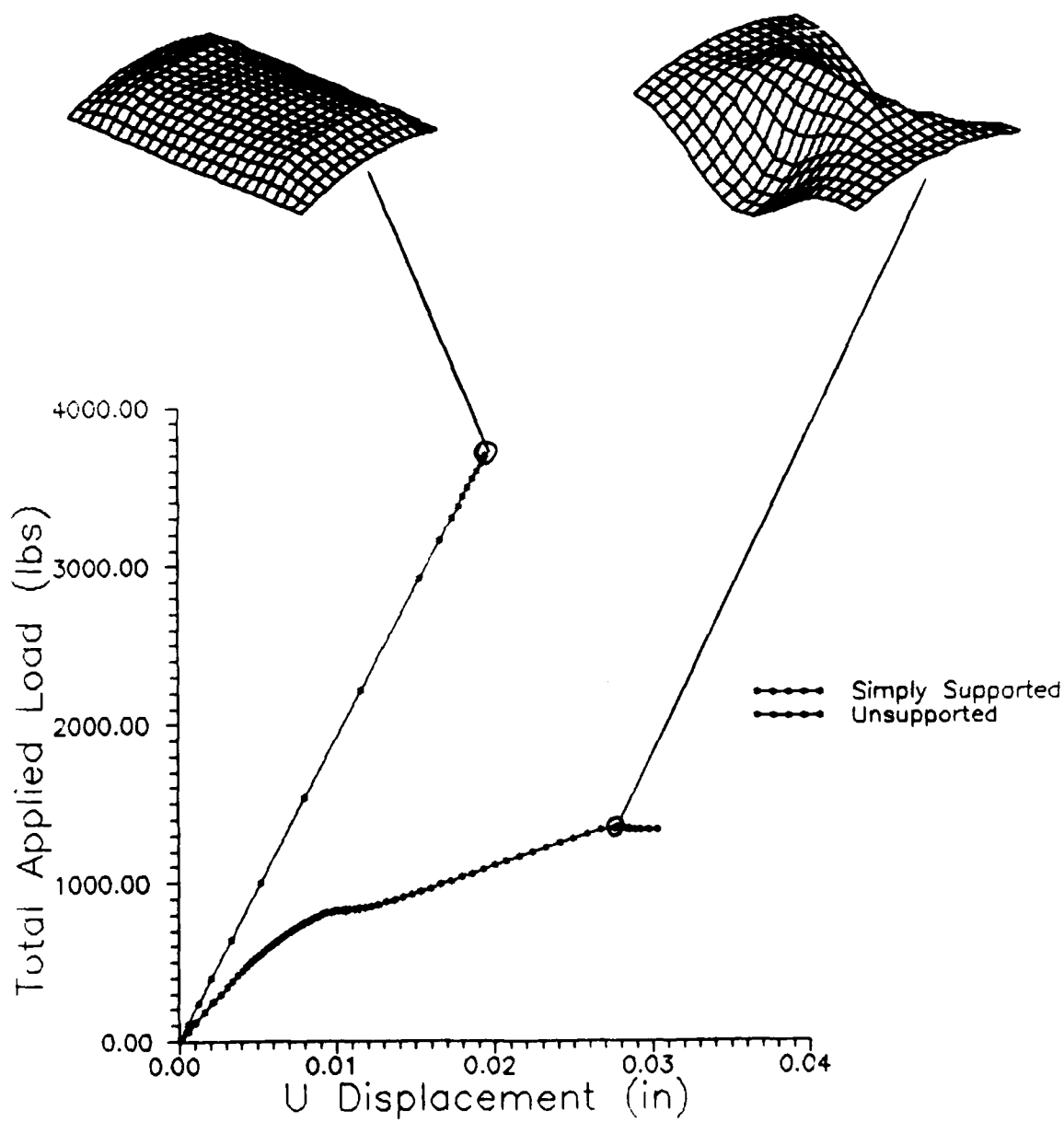


Fig 5.27 Load-Displacement, 8" Panels, No Cutout



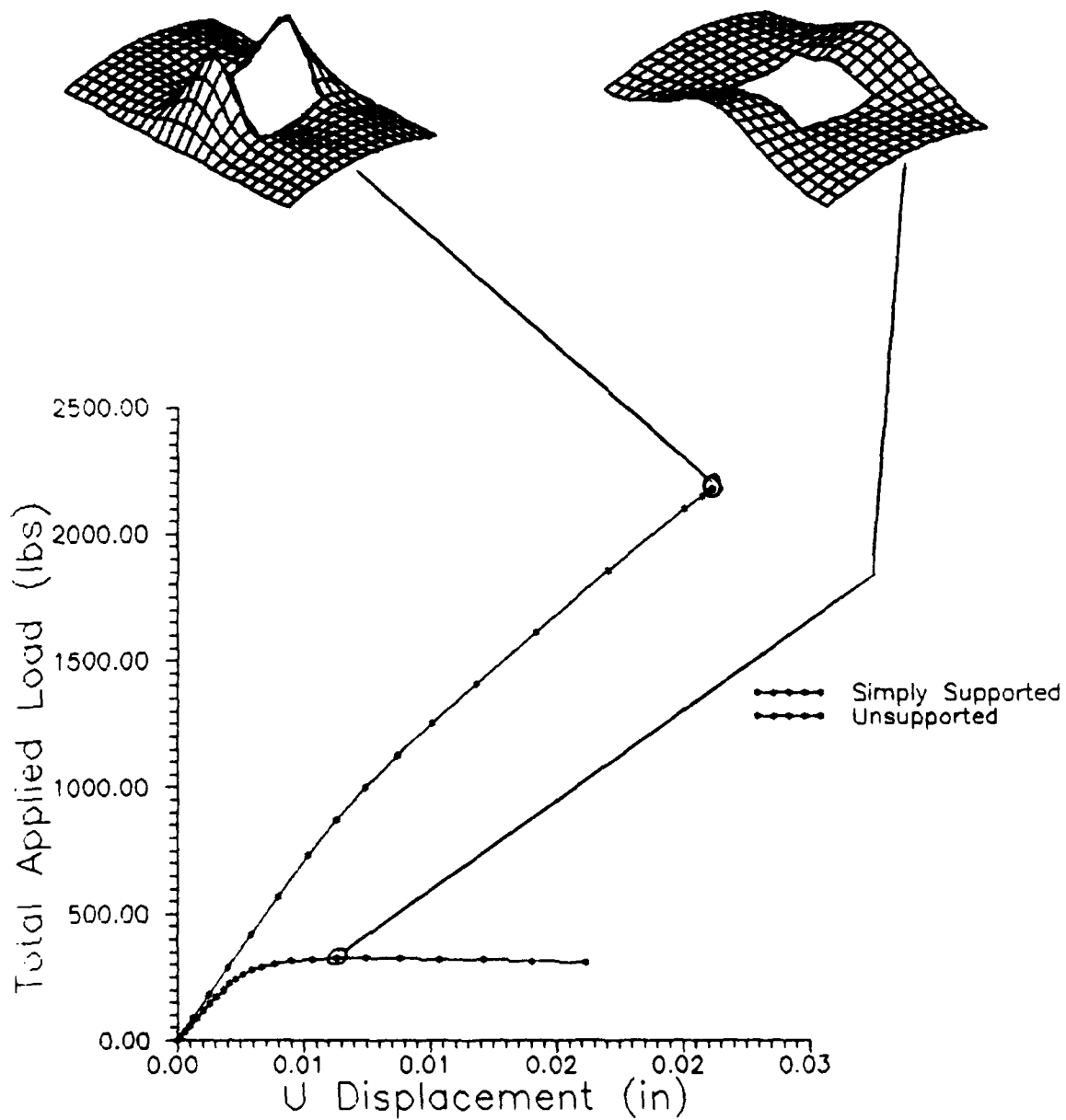


Fig 5.28 Load-Displacement, 8" Panels, 4" Cutout, Centered

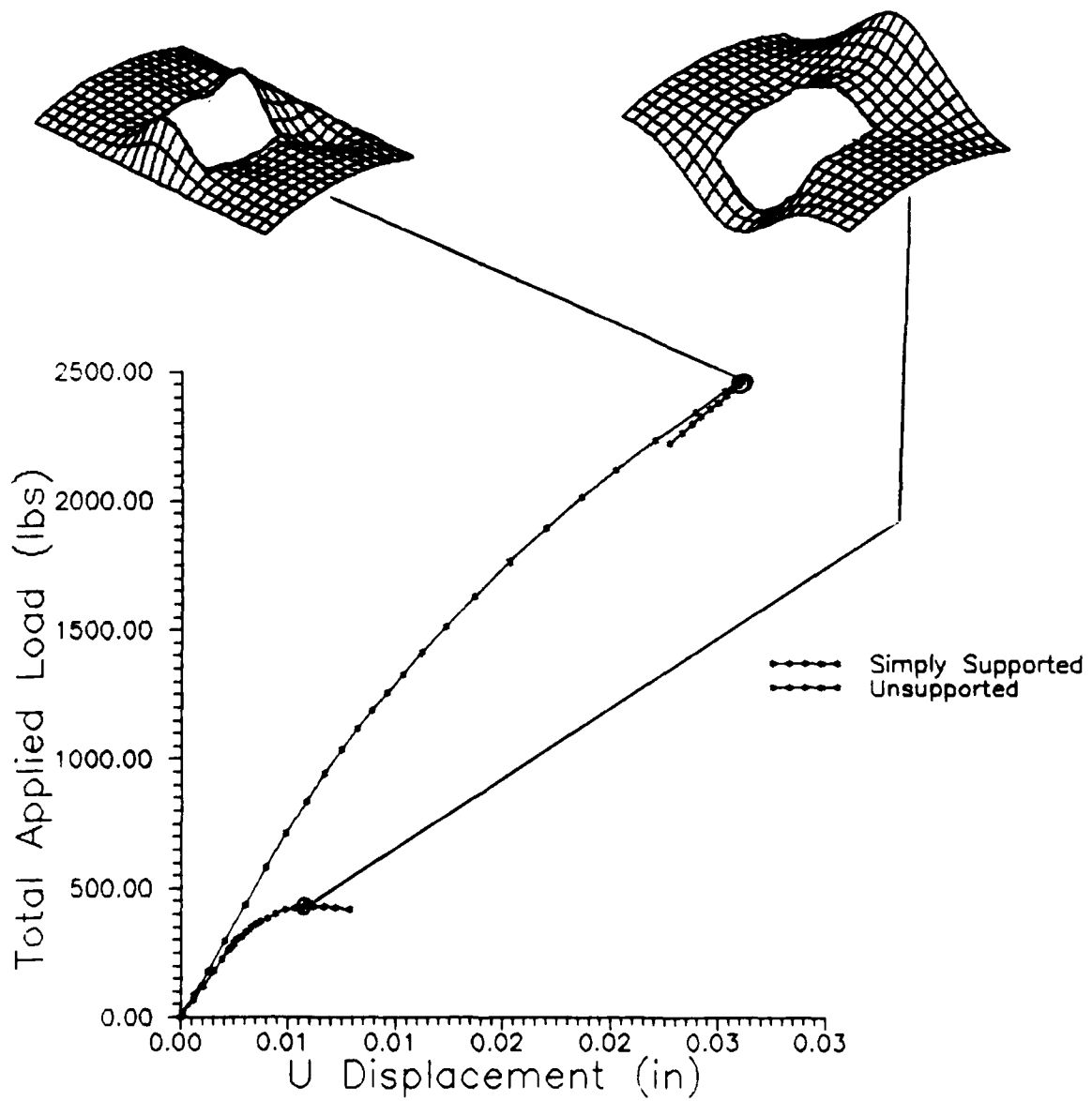


Fig 5.29 Load-Displacement, 8" Panels, 4" Cutout, 1" Offset

reduction is substantial, between 63-85%.

Table 5.2 Panel Results by Comparing Boundary Conditions

Panels	SS	US	Reduction
12", NC	4950	2260	54%
12", CC	2521	1186	53%
12", OC	2561	1284	50%
8", NC	3700	2260	63%
8", CC	2178	323	85%
8", OC	2465	460	81%

NOTE: NC = No Cutout, CC = Centered Cutout  
OC = Off center Cutout, SS = Simple  
Support, US = Unsupported

Of all the panels considered, the 8" wide panels showed and extreme reduction when the vertical supports are removed. Combine this with the presence of a geometric imperfection and the reduction is almost complete. A quick inspection of the data thus far indicates the 8" panels (with a geometric imperfection present) are behaving as if they were composed of two distinct columns that are joined by some material at the top and bottom. This in turn, indicates these panels are no longer behaving as shells but as thin, wide plates or (if the plates are oriented

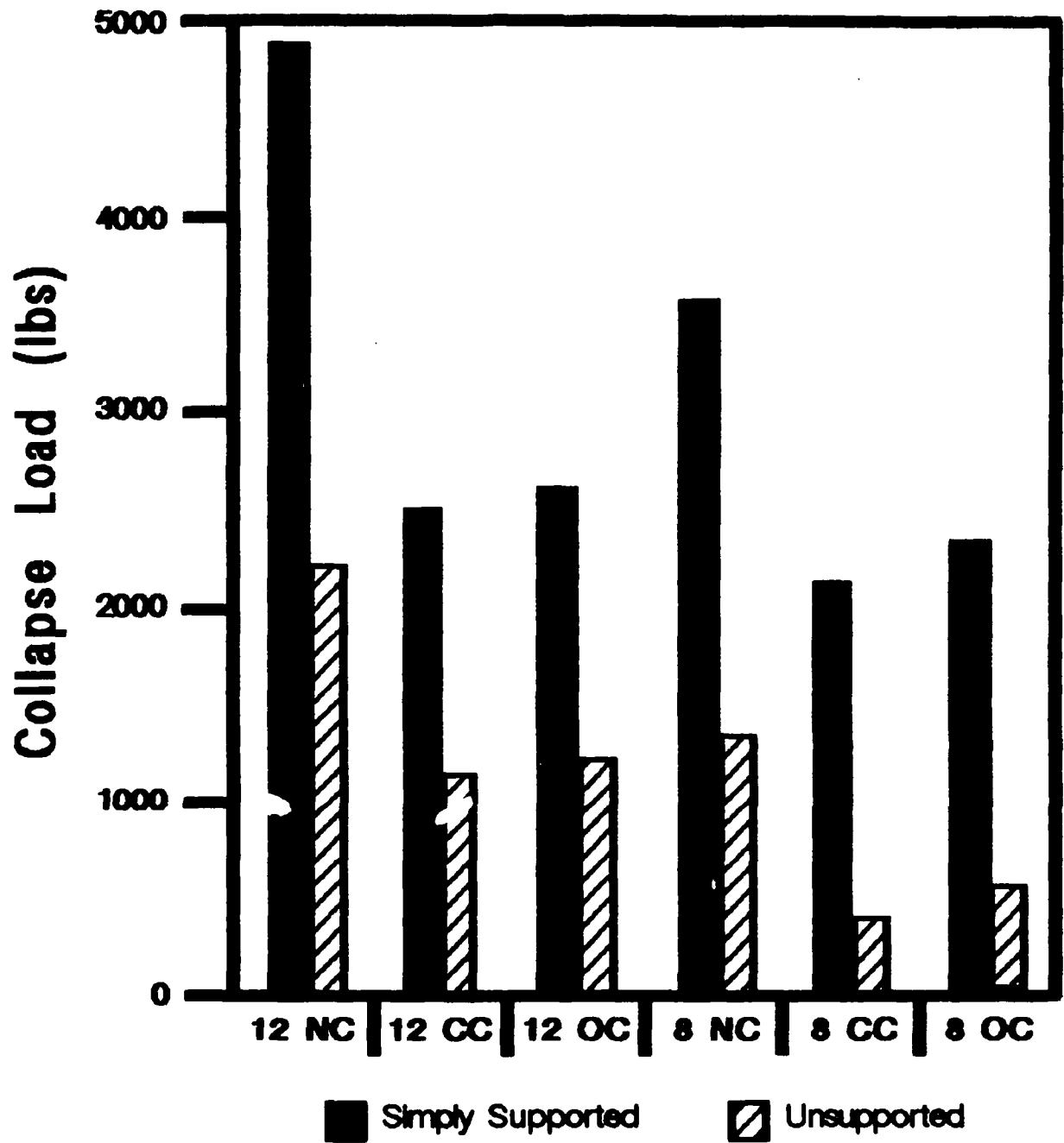


Fig 5.30 Comparing Simply Supported/Unsupported Panels

correctly) as columns. However, the author was unable to model this assumption using some simplified theoretical relations from [4,44]. By using the simplified column and plate relations (Euler column, Donnell approximation) the error between theory and the analytical results was an average of 40% with one model approaching 70%.

The only positive aspect of this assumption is that it may indicate why a panel, with an offset cutout, yields a higher collapse load. When offsetting a cutout by 1", this creates one column that is wider than in the case of the panel with a centered cutout, and may play a role in increasing the panel's overall stiffness. However, as is stated above, the panel's response is too complicated to be explained by relatively simple column and plate relations. Unfortunately, there exist no literature that addresses axially-loaded, cylindrical composite shells with large cutouts having unsupported vertical edges. Therefore, to gain a further understanding of this complex, nonlinear problem, further analytical and experimental research must be accomplished.

#### 5.1.5 Panel Geometry

The final major portion of this effort is considering boundary effects upon cylindrical composite shells which

have large geometric imperfections. Load-displacement curves were generated in comparing six categories of panels. These categories compared panel width while keeping the other parameters (boundary conditions, geometric imperfections) constant. These are shown in Figs 5.31-36. In every circumstance, the reduction in panel width for the same boundary conditions and the same geometric imperfection (or lack thereof) yielded a reduction in total collapse load. As stated before, all panels with no geometric imperfections contained an initial imperfection model of three half sine waves in both circumferential and radial directions with an amplitude of one ply thickness.  $v$  is assumed to be fixed for all simply supported panels. It is expected, based on these initial assumptions, that STAGS will converge to a solution with a higher collapse load than is seen experimentally.

Table 5.3 shows the comparison for the analytical results from STAGS. Fig 5.37 shows the comparison between 12" panels and 8" panels (assuming similar boundary conditions and geometric imperfections). As is shown in Table 5.3, the simply supported panels were not significantly affected by a reduction in panel width. It appears that the geometric imperfection is dominating panel's response, thereby minimizing the effect of changing the panel width. However, the unsupported panels are affected

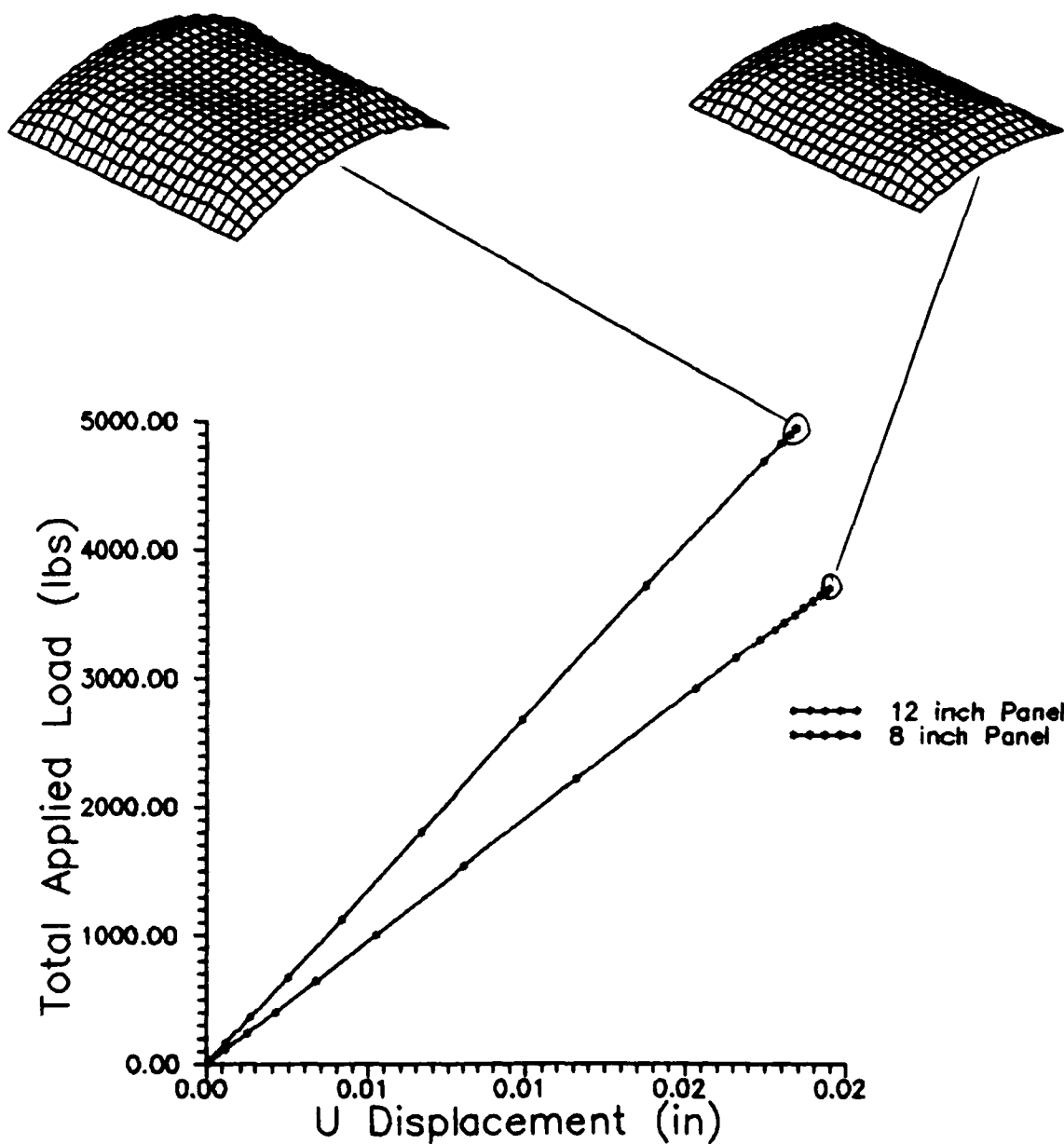


Fig 5.31 Load-Displacement, Simply Supported Panels with No Cutout

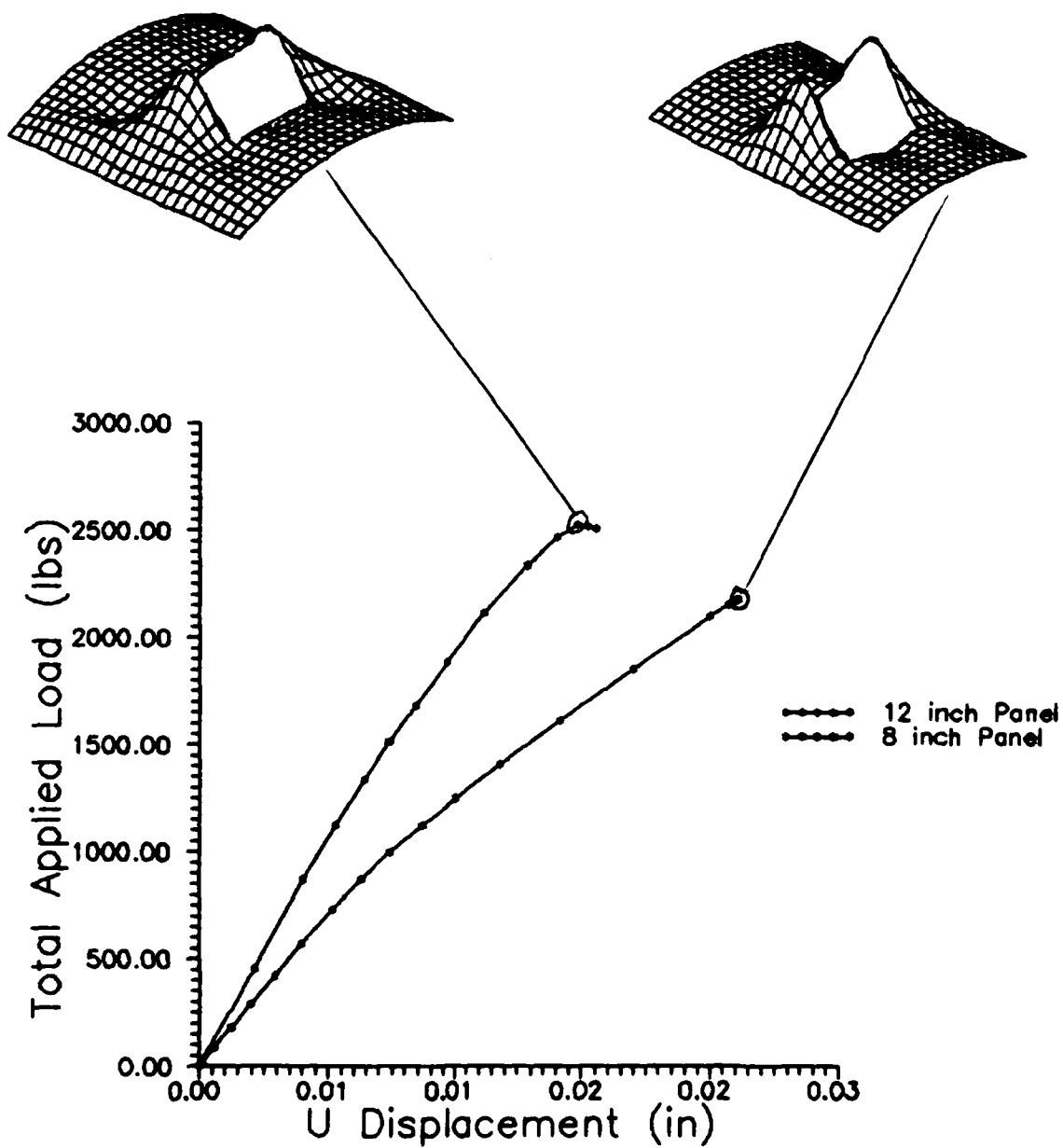


Fig 5.32 Load-Displacement, Simply Supported Panels with 4" Cutout, Centered



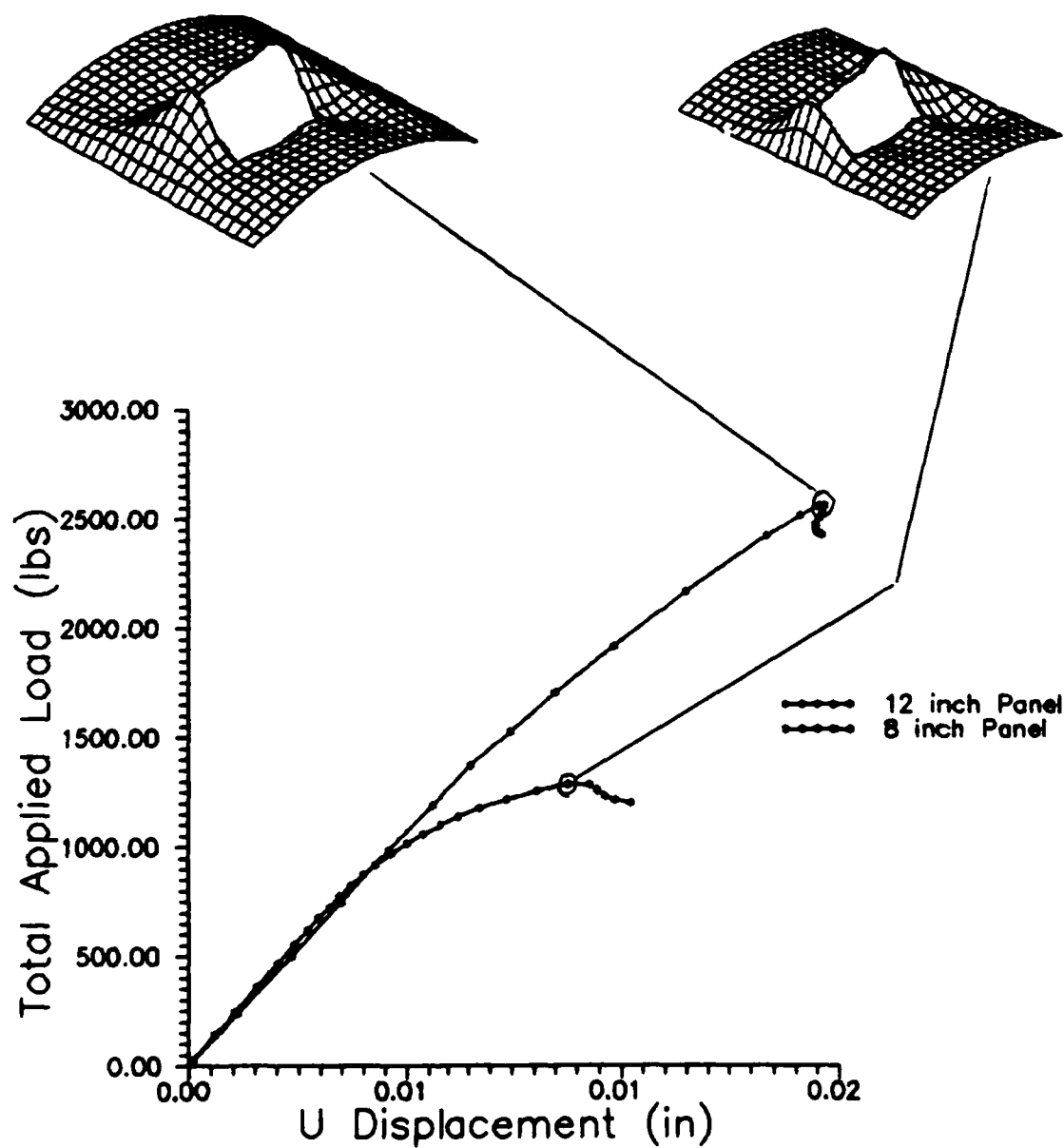


Fig 5.33 Load-Displacement, Simply Supported Panels with 4" Cutout, 1" Offset

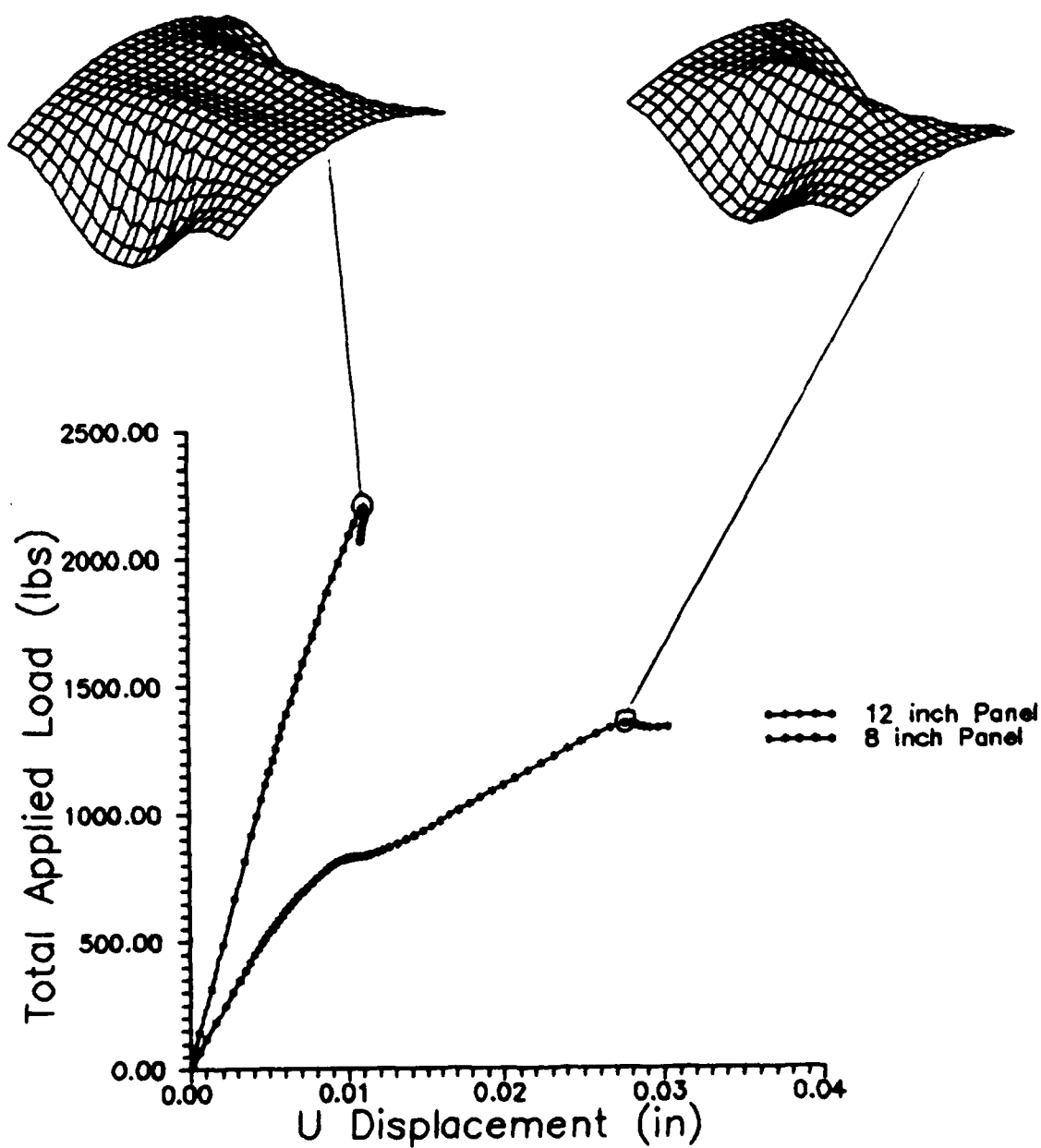


Fig 5.34 Load-Displacement, Unsupported Panels with No Cutout

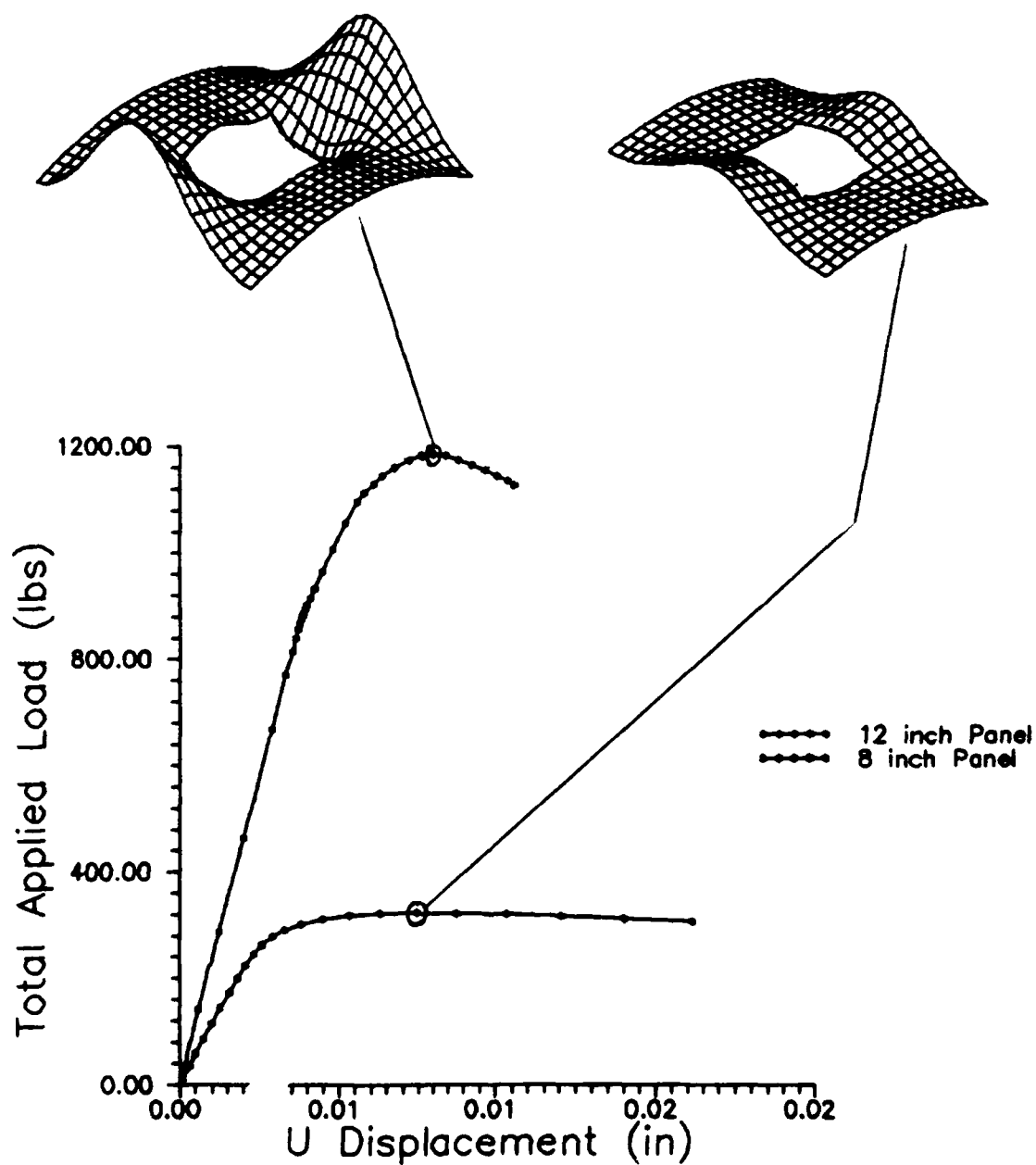


Fig 5.35 Load-Displacement, UnSupported Panels with 4" Cutout, Centered

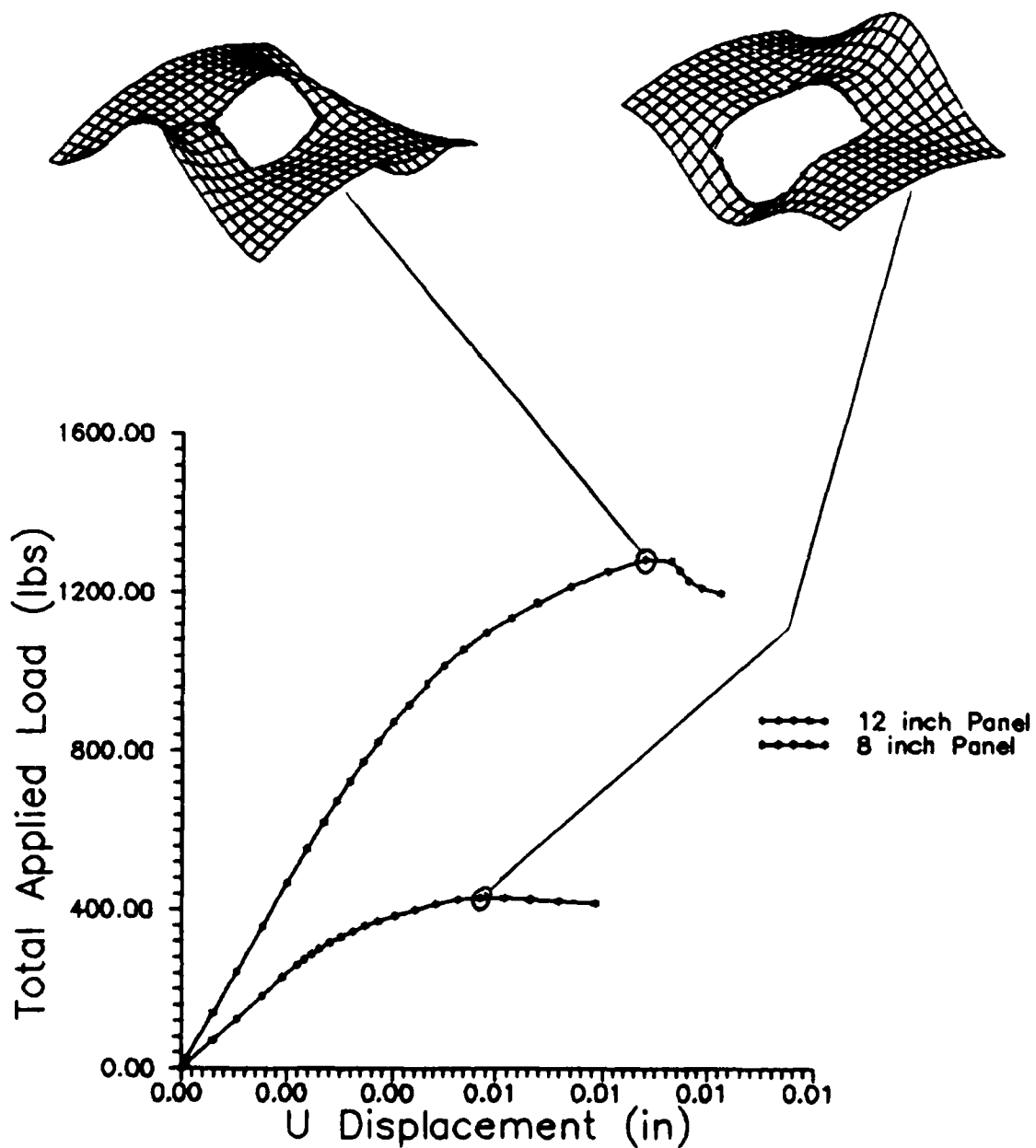


Fig 5.36 Load-Displacement, Simply Supported Panels with 4" Cutout, 1" Offset

by reducing the panel width. Combining this with the presence of a cutout creates a significant reduction of total collapse load, approximately 70%.

Table 5.3 Panel Results by Comparing Panel Geometry

Collapse Load. lbs			
Panels	12"	8"	Reduction
SS, NC	4950	3700	23.5%
SS, CC	2521	2178	13.6%
SS, OC	2561	2465	3.7%
US, NC	2260	1350	38.7%
US, CC	1186	323	72.8%
US, OC	1382	460	66.9%

NOTE: SS = Simply Supported, US = Unsupported,  
NC = No Cutout, CC = Centered Cutout,  
OC = Off center Cutout

It should be noted that the unsupported, 8" panels have demonstrated the greatest sensitivity in reduction of total collapse load and nonlinear response to the presence of geometric imperfections, boundary conditions, panel geometry or any combination of these three parameters. However, because of this high degree of sensitivity, and combining these parameters, characterizing the response of these

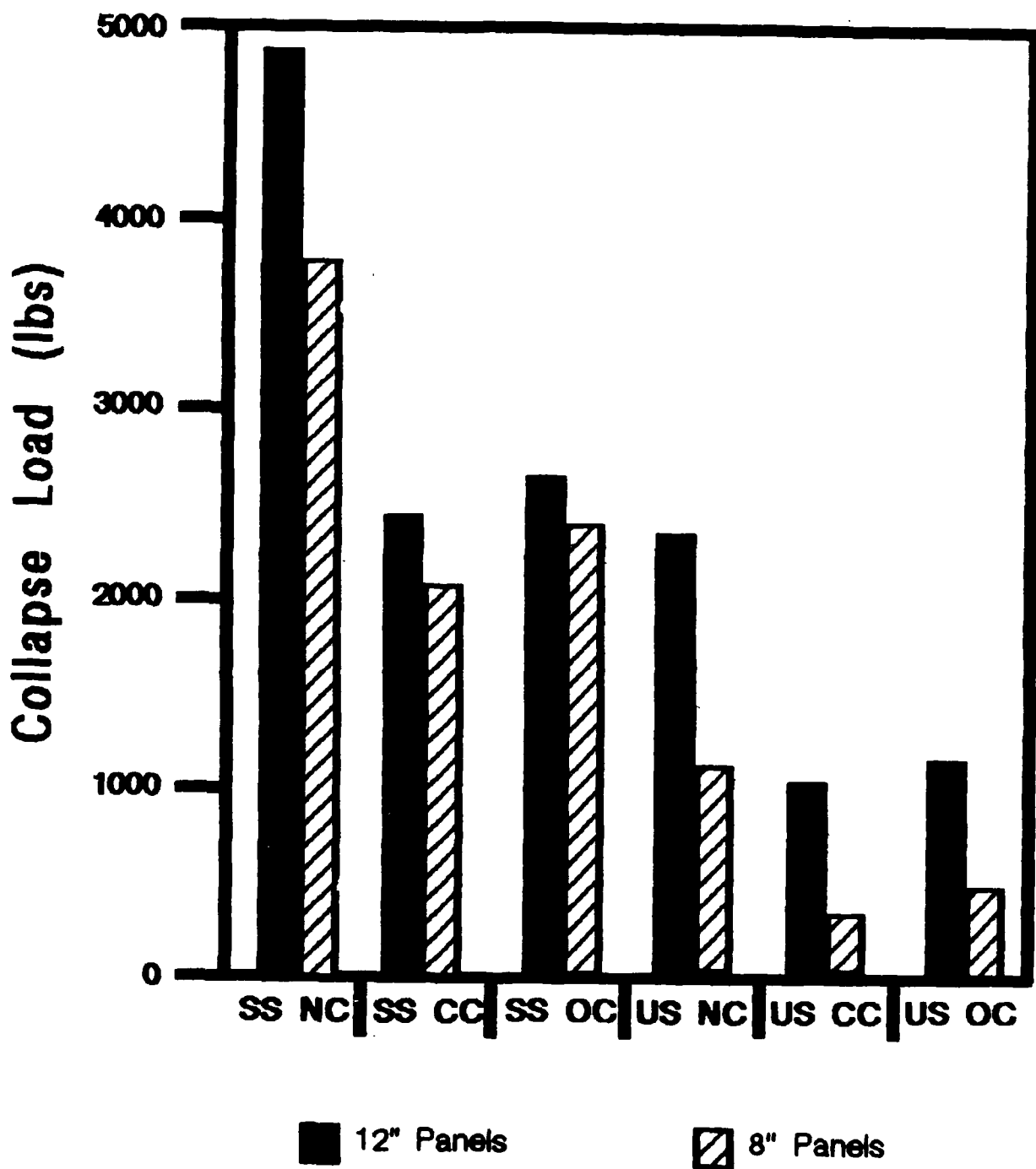


Fig 5.37 Comparing 12"/8" Panels for Similar Boundary Conditions and Geometric Imperfections

panels is extremely complex. Further work needs to be pursued before an adequate analysis can be accomplished.

## 5.2 Analytical Results - SHELL

At this time, only one model has been successfully run using the SHELL program with the full model using a fine mesh. This model is the 8" panel with a 4" cutout, centered and is unsupported along the vertical edges (refer Tables H.3-4). Four other models, full scale but with coarser meshes (1" elements), were completed. These models converged to solutions from 50-80% higher than the experimental values (refer to Table 5.4). As expected, using a mesh that modeled half of the panel, SHELL converged to a solution with a higher collapse load than STAGS (from 75-90% higher than STAGS). Table 5.5 compares these results. The solution for SHELL is quite good (312.8 lbs) when proper modeling techniques are utilized. The load-displacement curve for this model is shown in Fig 5.38.

At collapse,  $\psi_x$  was found to equal in magnitude  $\approx 29.2^\circ$  or 0.51 radians. This would indicate that through-the-thickness shear is present and should relax the panel's global stiffness. This in turn, reduces total collapse load and enhance the bending moment that occurs in the panel when it nears the collapse point. The SHELL program indicates

**Table 5.4 Comparing SHELL Models with Coarse Mesh Size  
(1" Elements) vs Experimental Results**

**Collapse Load, lbs**

Panels	Experimental	SHELL	% Difference
12" US, NC	1890	2782.7	47.2
12" US, CC	1093	1625.3	48.7
12" US, OC	1127	1702.8	51.1
8" US, NC	1311	2199.9	67.8
8" US, CC	300	527.4	75.8
8" US, OC	403	727.2	81.2

**Table 5.5 Comparing SHELL Models with Half Mesh Size  
(1/2" Elements) vs Experimental Results**

**Collapse Load, lbs**

Panels	Experimental	SHELL	% Difference
12" US, NC	1890	2956.0	56.4
12" US, CC	1093	1693.1	54.9
8" US, NC	1311	2375.5	81.2
8" US, CC	300	552.9	84.3

**NOTE:** SS= Simple Supports, US = Unsupported, NC = No  
Cutout, CC = Centered Cutout, OC = Off center Cutout



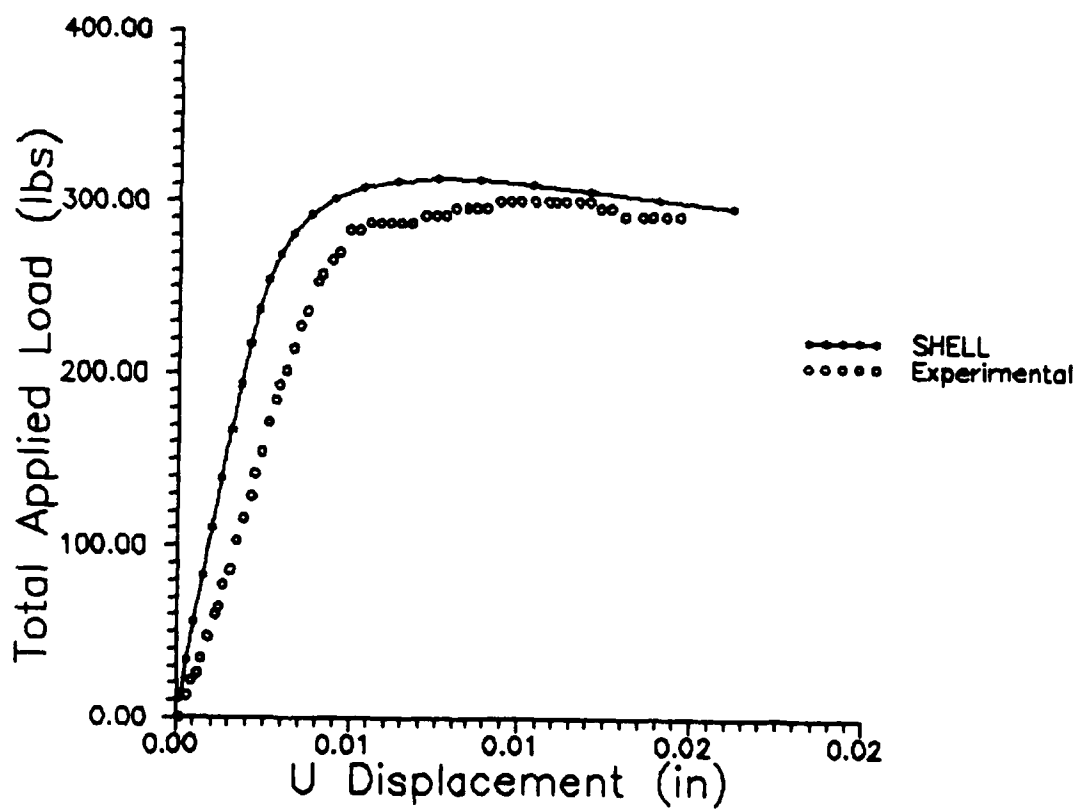


Fig 5.38 Load-Displacement, 8" Panel, Unsupported with 4" Cutout, Centered

this with the full model, refined mesh solution shown in Fig 5.38 which is less than STAGS.

The other models, with refined meshes, are being pursued at this moment, and will be presented in a paper at the AIAA conference in April, 1990. From all indications, SHELL is correctly predicting the behavior of the nonlinear response for the unsupported panels. Since SHELL incorporates through-the-thickness shear stress, the solution it converges to is realistic and accurate. However, further analysis must wait until comparisons can be made concerning all of the STAGS, SHELL models with the experimental data.

### 5.3 Experimental Results

The individual experimental panel results, as are the STAGS and SHELL results, are tabulated in Appendix H, Tables H.1-5. Load-displacement curves are generated for all twelve panels and are shown in Figs 5.39-50. We can see immediately that both STAGS and SHELL give predictions that are stiffer than the experimental results, which is expected. For the one model SHELL has converged to, SHELL predicts a more flexible panel than STAGS, which is expected. This can be attributed to the fact that through the thickness shear is present (due to the large angles of

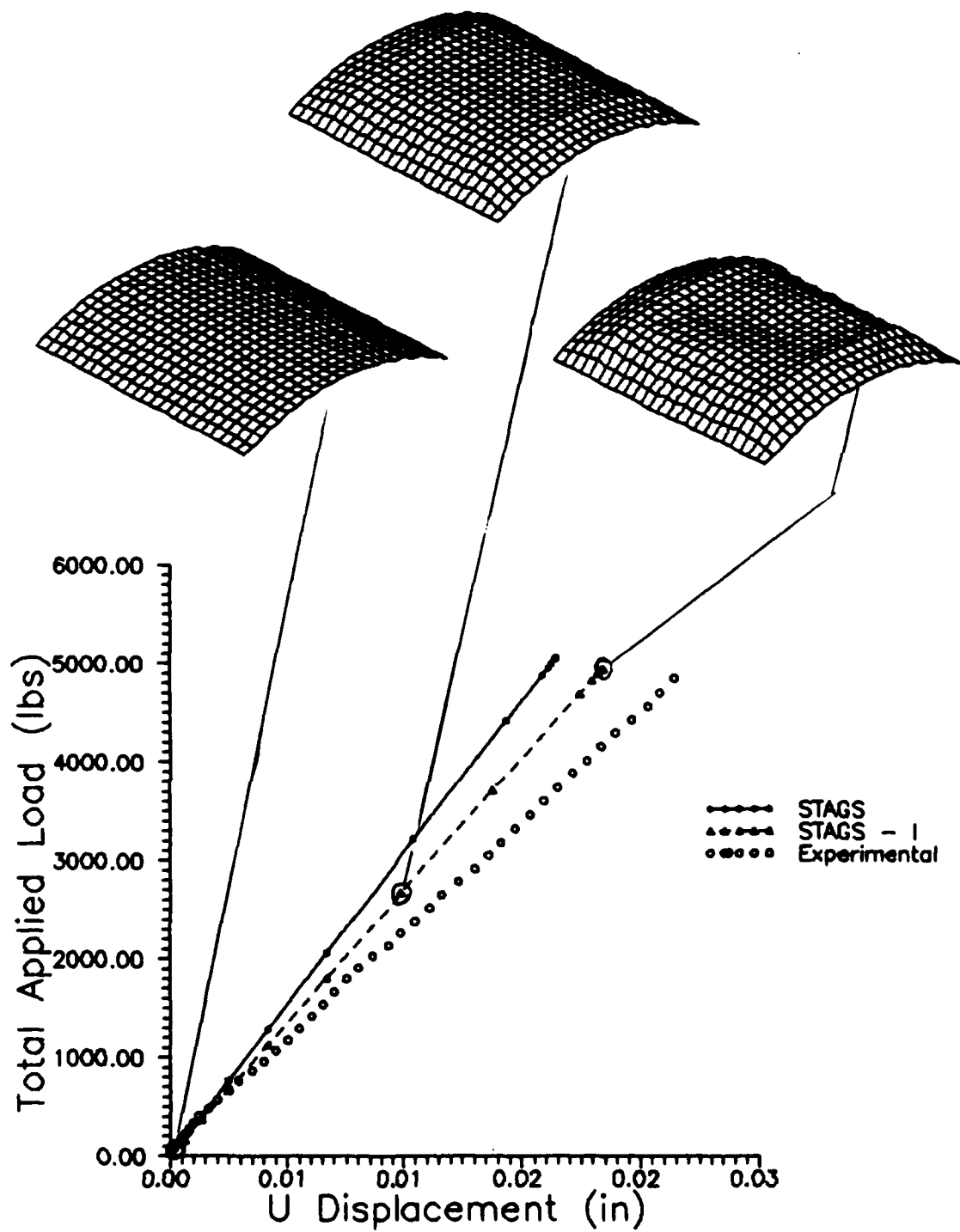


Fig 5.39 Load-Displacement, 12" Panel, Simply Supported, No Cutout

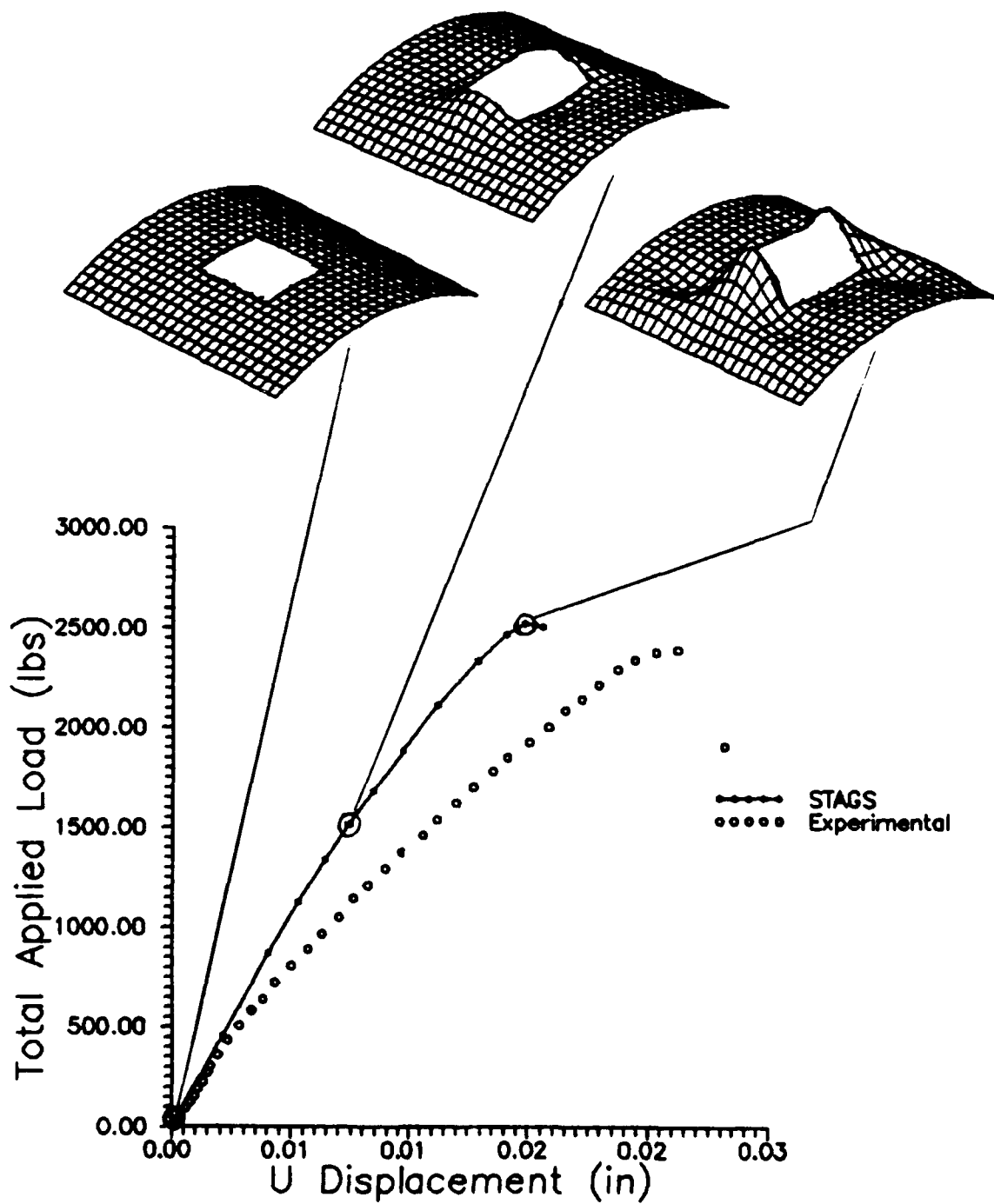


Fig 5.40 Load-Displacement, 12" Panel, Simply Supported, 4" Cutout, Centered

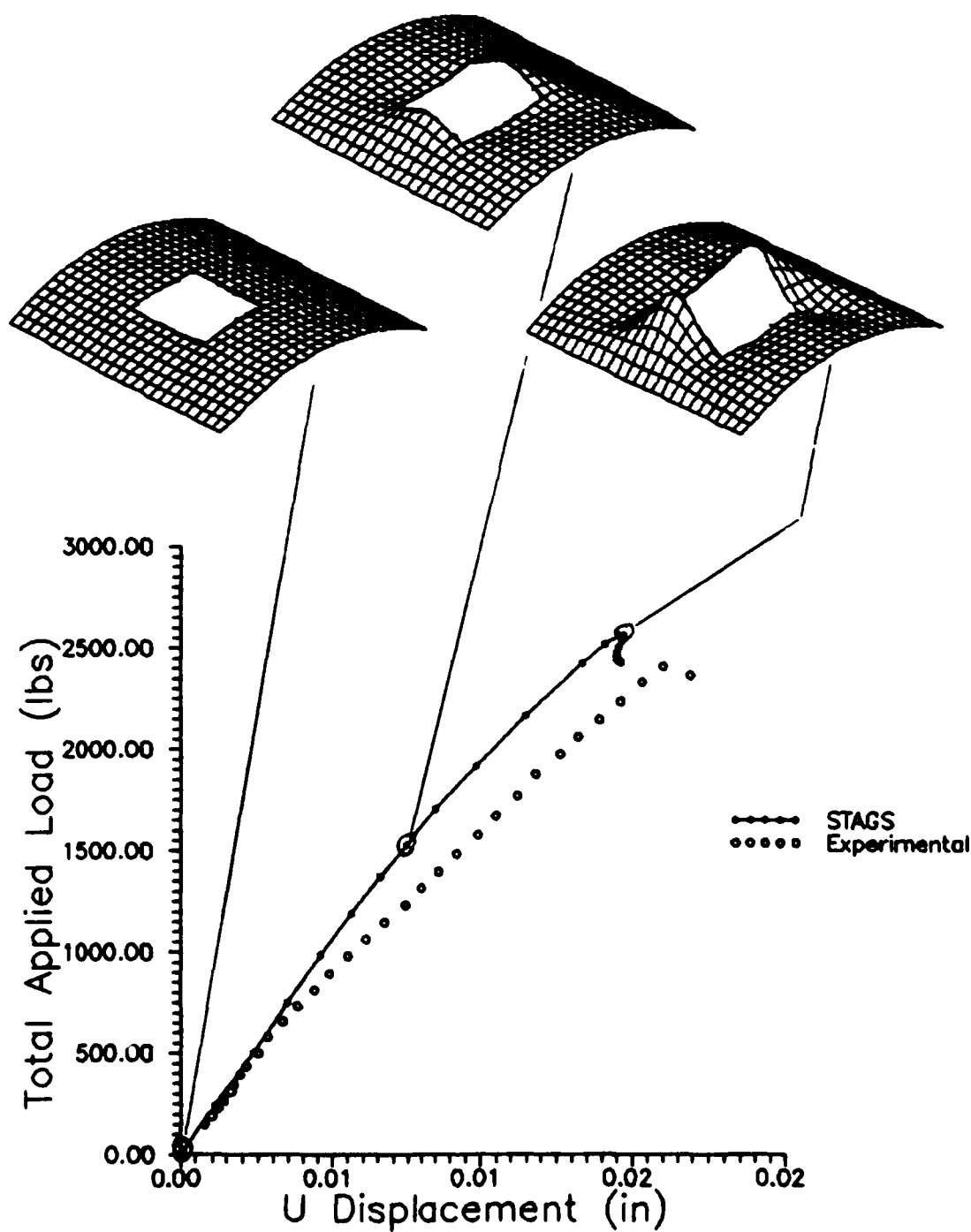


Fig 5.41 Load-Displacement, 12" Panel, Simply Supported, 4" Cutout, 1" Offset

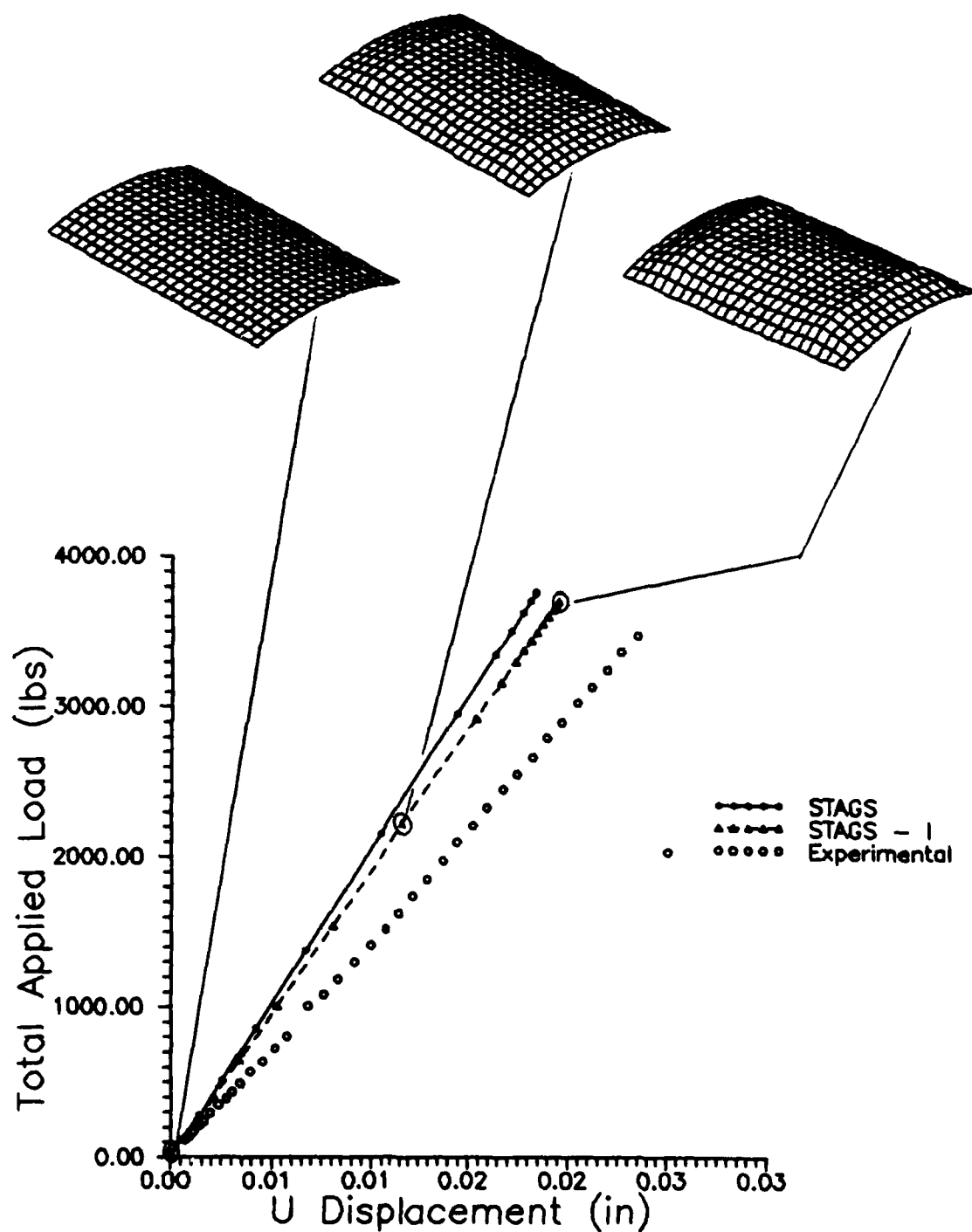


Fig 5.42 Load-Displacement, 8" Panel, Simply Supported, No Cutout

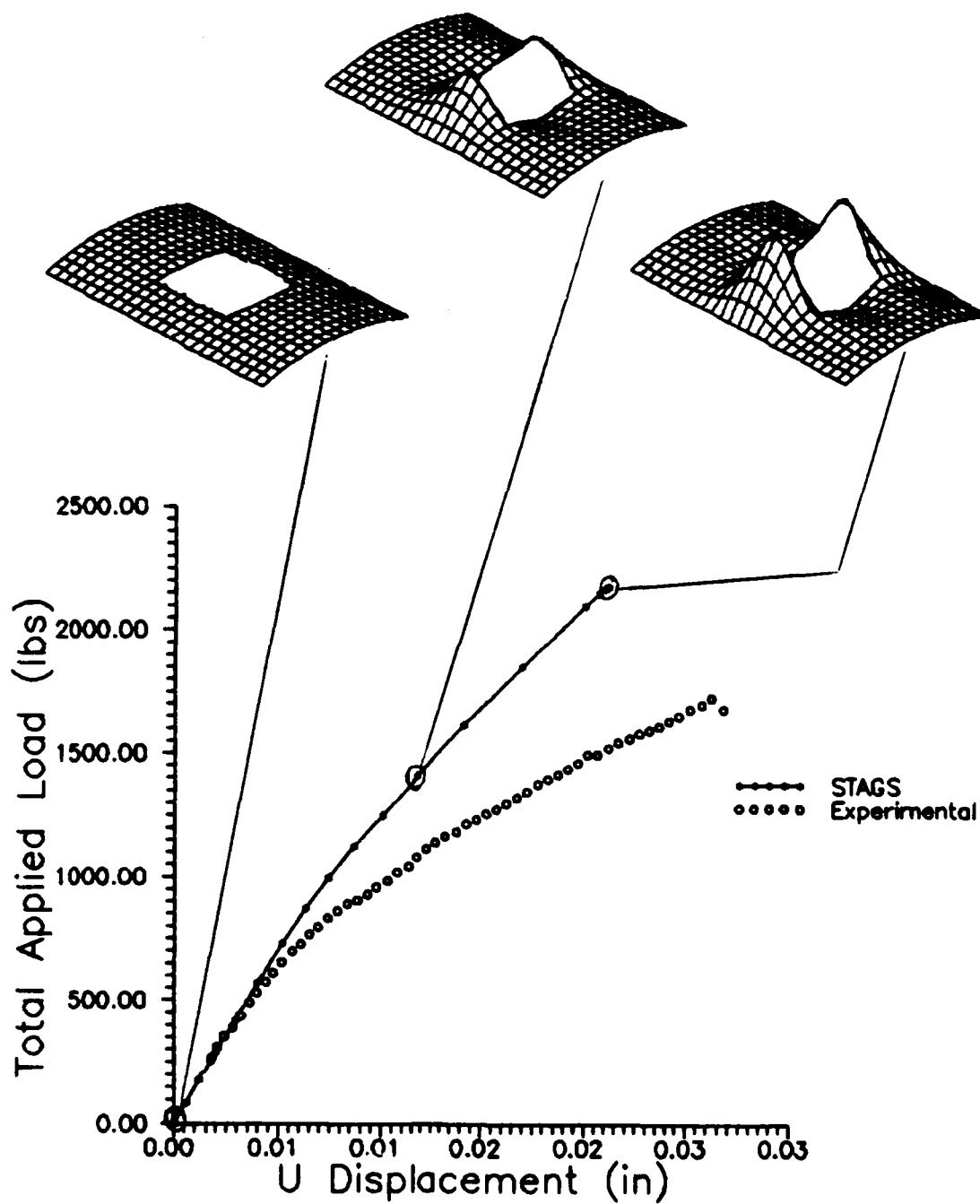


Fig 5.43 Load-Displacement, 8" Panel, Simply Supported, 4" Cutout, Centered

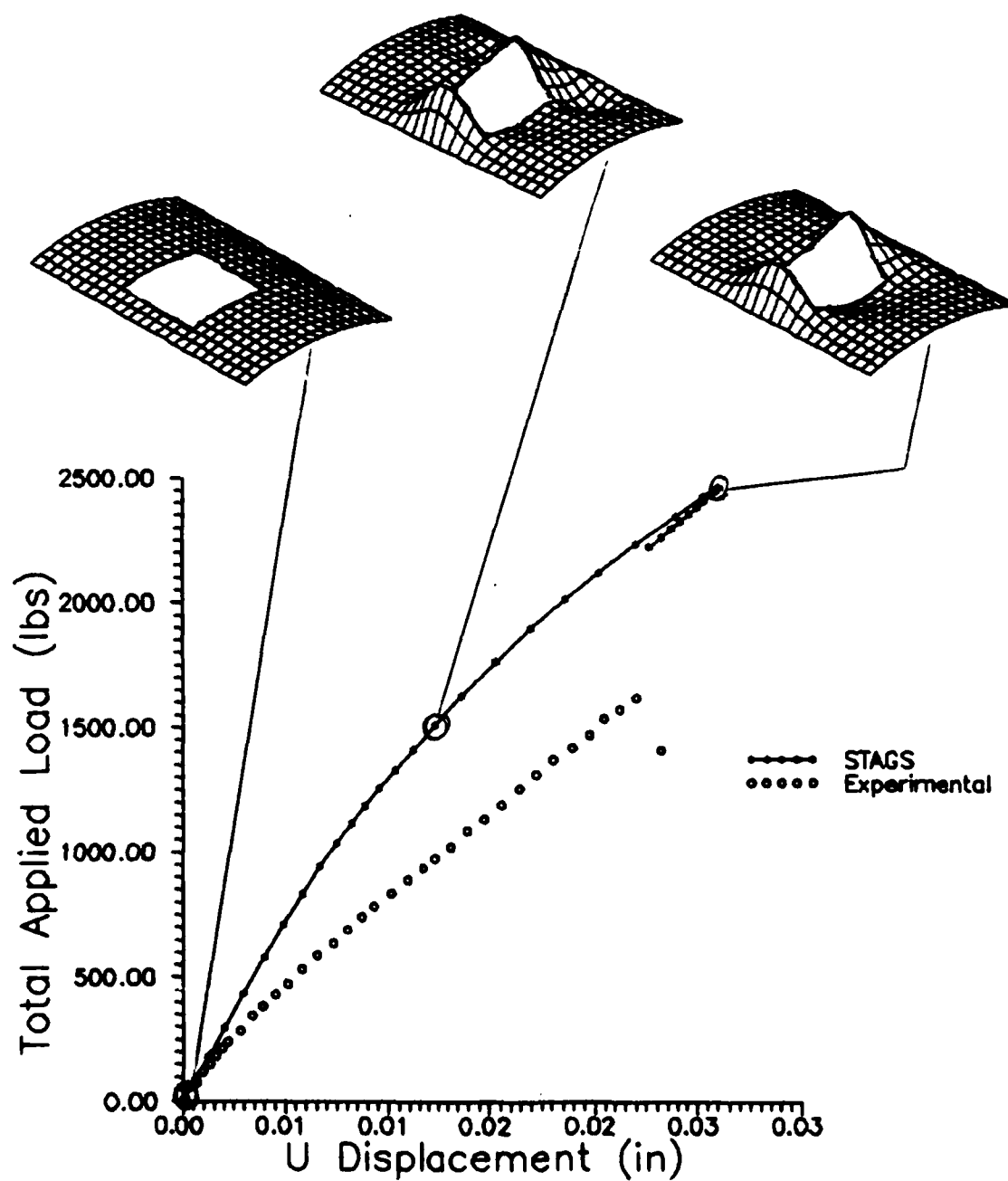


Fig 5.44 Load-Displacement, 8" Panel, Simply Supported, 4" Cutout, 1" Offset



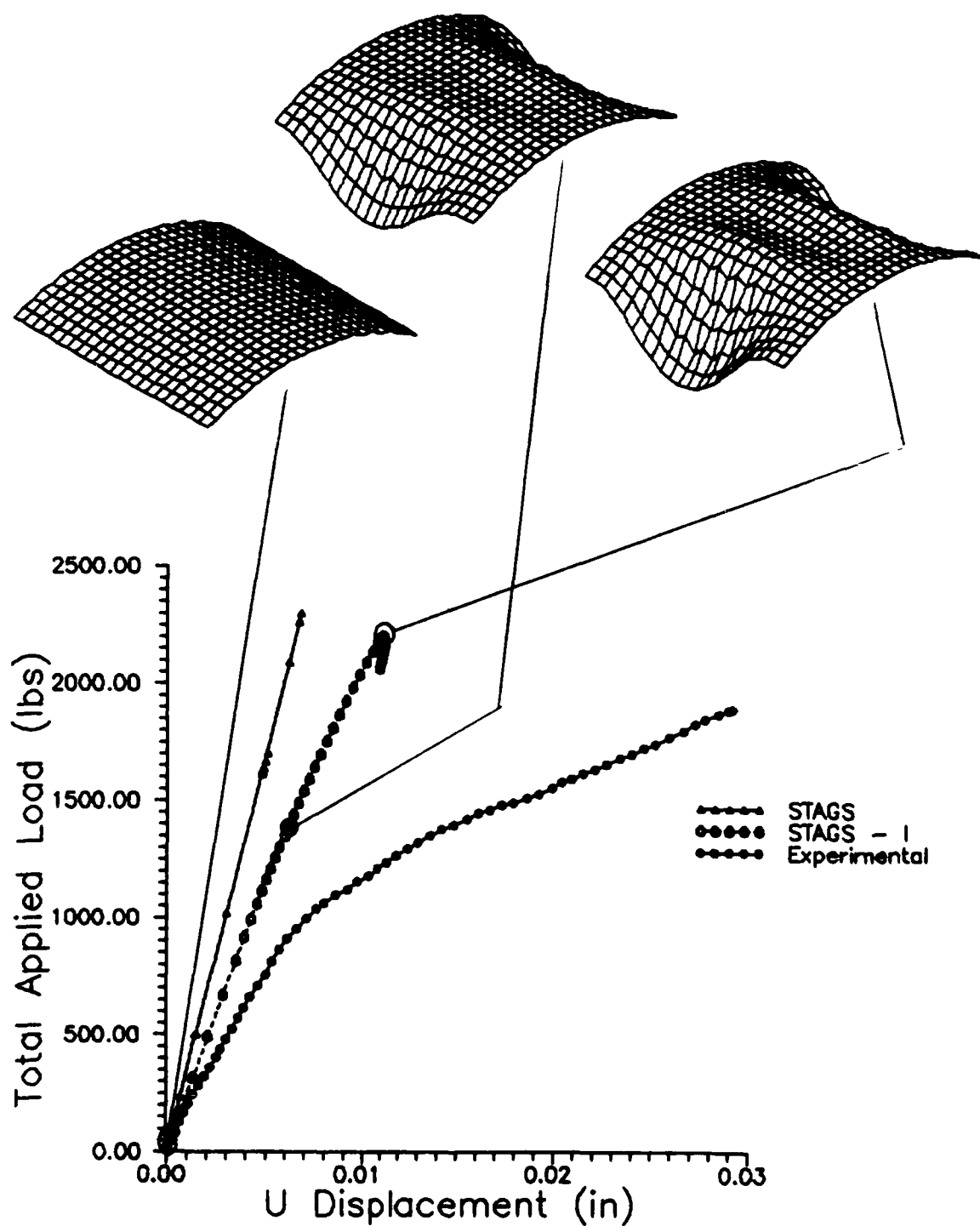


Fig 5.45 Load-Displacement, 12" Panel, Unsupported, No Cutout

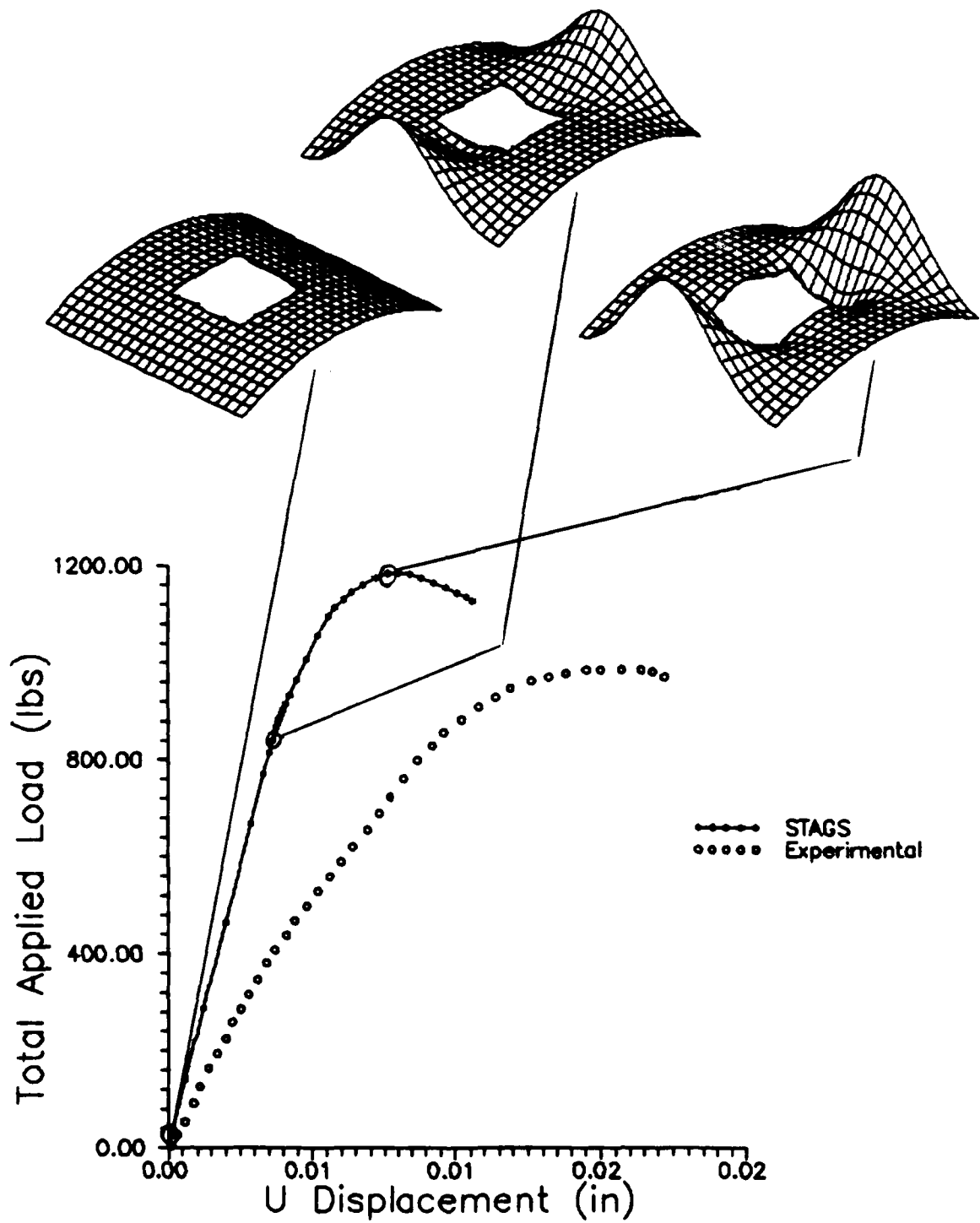


Fig 5.46 Load-Displacement, 12" Panel, Unsupported, 4" Cutout, Centered

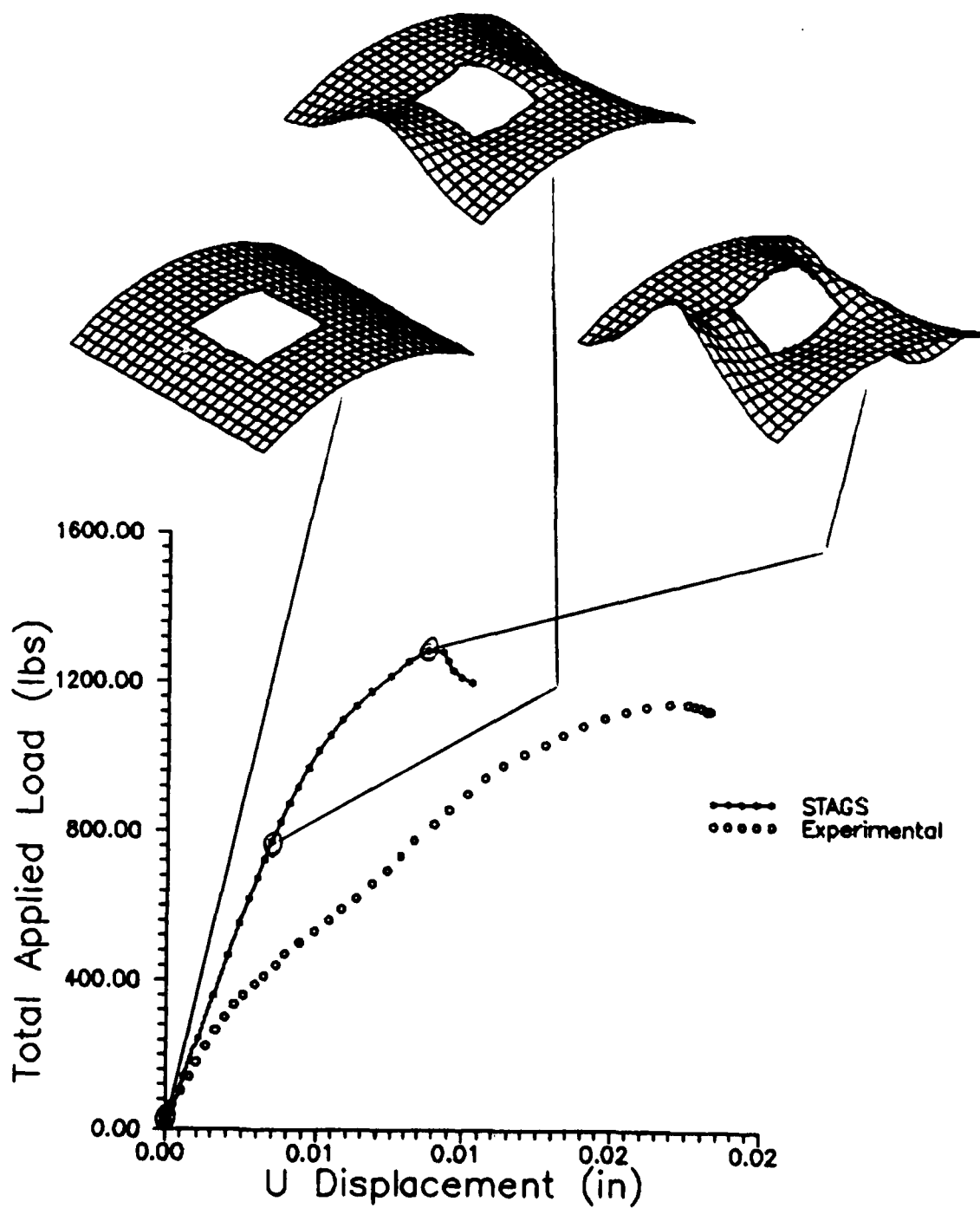


Fig 5.47 Load-Displacement, 12" Panel, Unsupported, 4" Cutout, 1" Offset

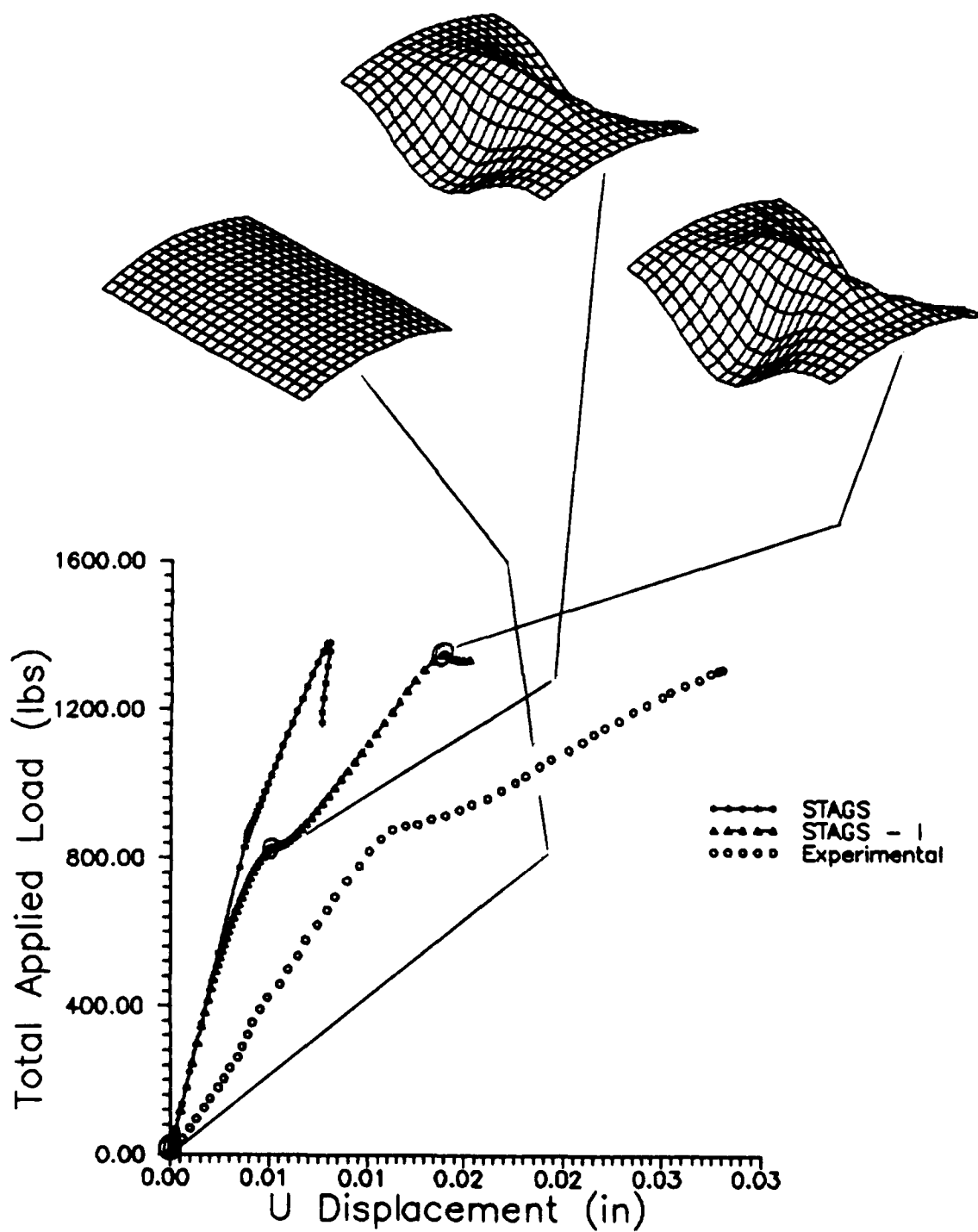


Fig 5.48 Load-Displacement, 8" Panel, Unsupported, No Cutout

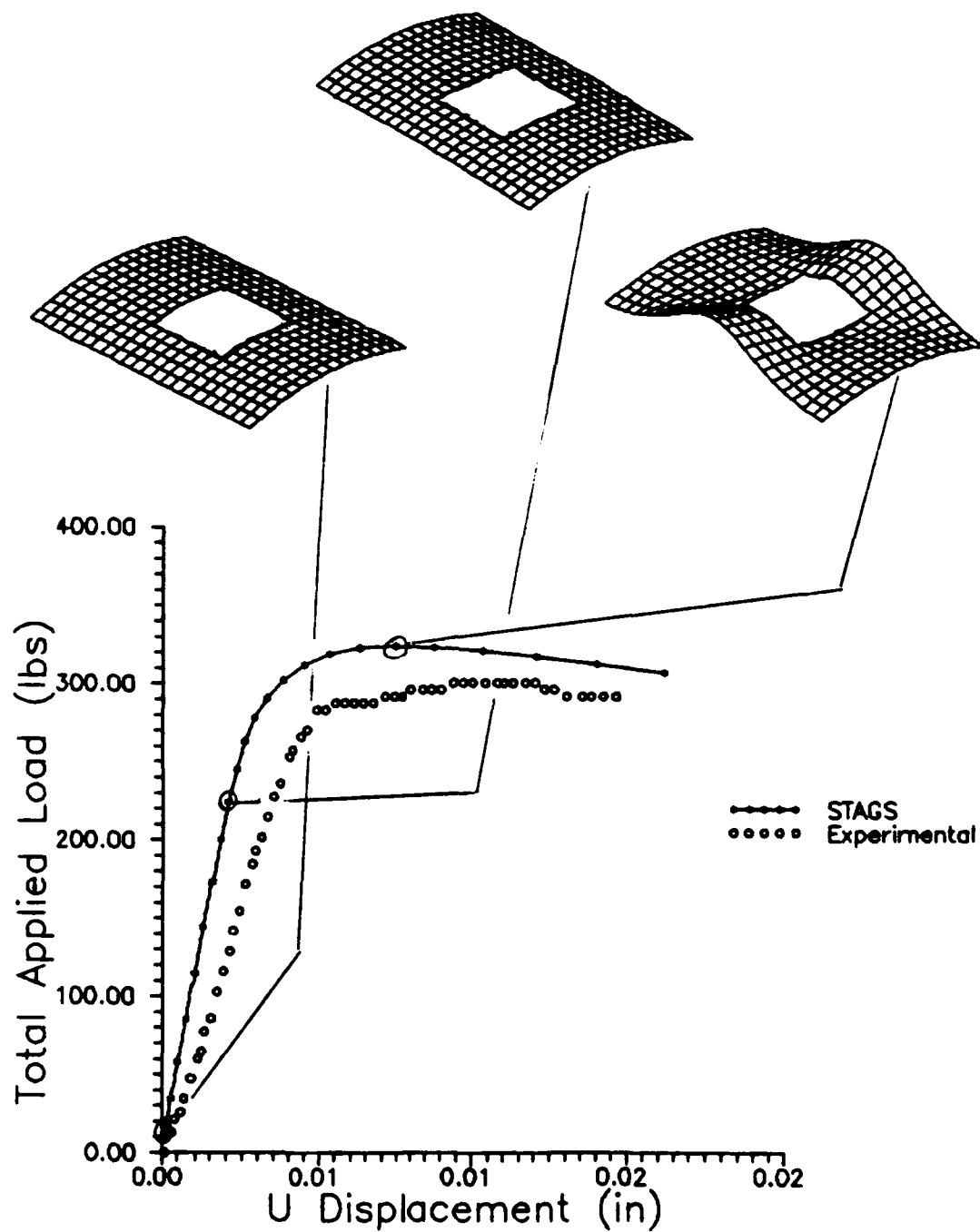


Fig 5.49 Load-Displacement, 8" Panel, Unsupported, 4" Cutout, Centered

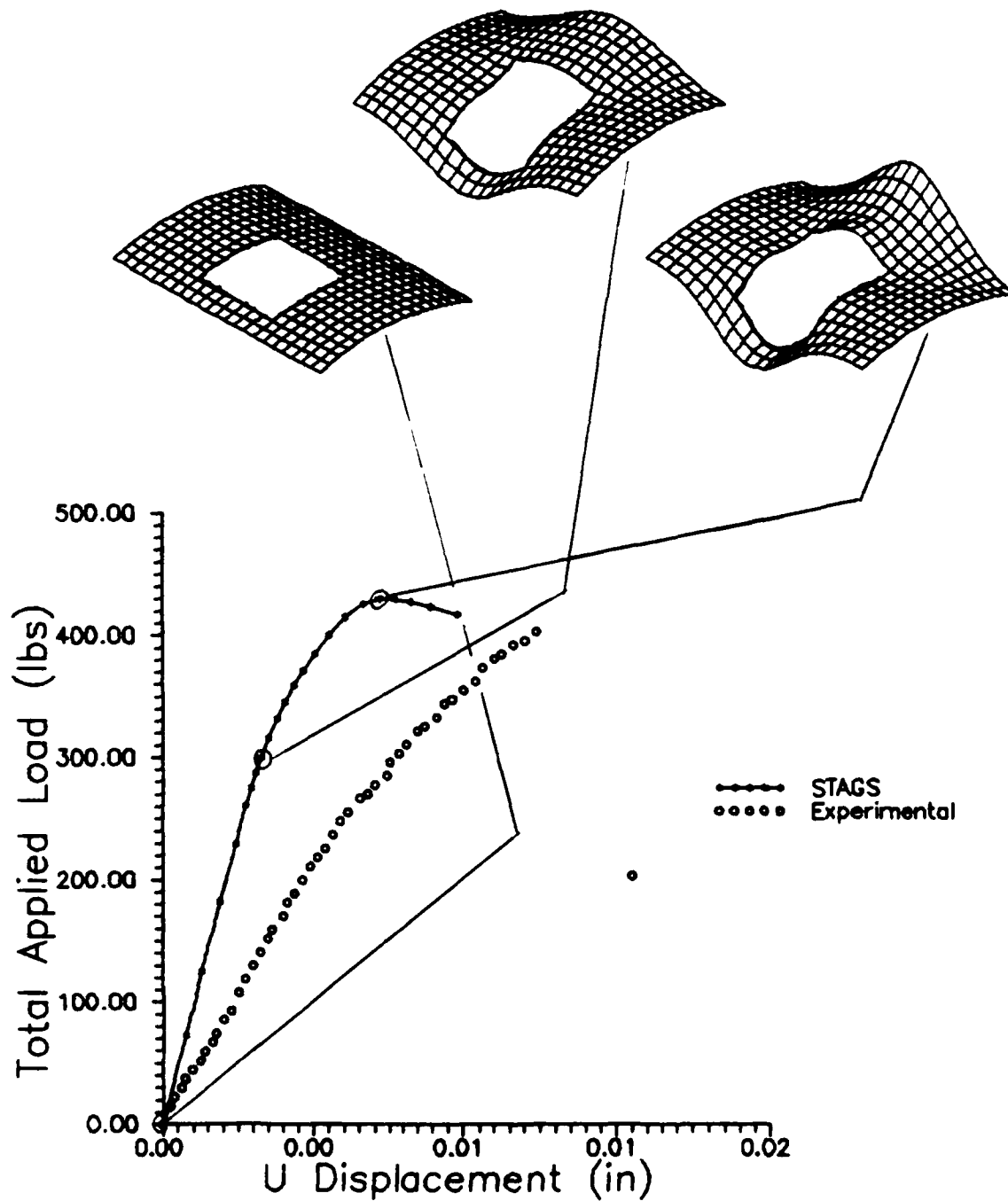


Fig 5.50 Load-Displacement, 8" Panel, Unsupported,  
4" Cutout, 1" Offset

rotation,  $\psi_x$ ) at collapse, which increases the panel's flexibility (or decreases panel stiffness).

Table 5.6 shows the comparison of experimental results with the analytical results from STAGS. Figs 5.51-54 show the comparison of STAGS/experimental collapse ratios for all twelve panels considered. It is evident from the load-displacement curves and the comparison figures that the 1986 version of STAGSC-1 with the corotational method is accurately modeling the panels' response to an axial-compression load. It appears that STAGS provides the best solutions for the 8" panels that are unsupported along the vertical edges. There are many possible reasons for this trend.

One possible answer can be shown through another model. It should be noted that STAGS failed to converge on the 12" unsupported panel that had no cutout using the QUAF 411 element. At first a mesh of 1/2" x 1/2" was tried. Then a coarser mesh of 1" x 1" was tried. Both models diverged at  $\approx$  1350 lbs, far short of the experimental results for this particular panel. Another model using the coarser mesh was tried, but incorporating the QUAF 410 element instead. When this model was run, STAGS converged to a solution of 2298 lbs with exactly the same stiffness as the 411 element had

Table 5.6 Panel Results by Comparing Experiment vs STAGS

Panels	Experiment	STAGS	% Difference
12", SS, NC	4851	4950	+ 2.0
12" SS, CC	2392	2521	+ 5.3
12" SS, OC	2406	2561	+ 6.1
8", SS, NC	3473	3700	+ 6.1
8", SS, CC	1918	2178	+11.9
8", SS, OC	1619	2465	+34.3
12", US, NC	1890	2260	+16.4
12", US, CC	1093	1186	+ 7.9
12", US, OC	1127	1284	+12.2
8", US, NC	1311	1350	+ 2.9
8", US, CC	300	323	+ 7.1
8", US, OC	403	460	+12.4

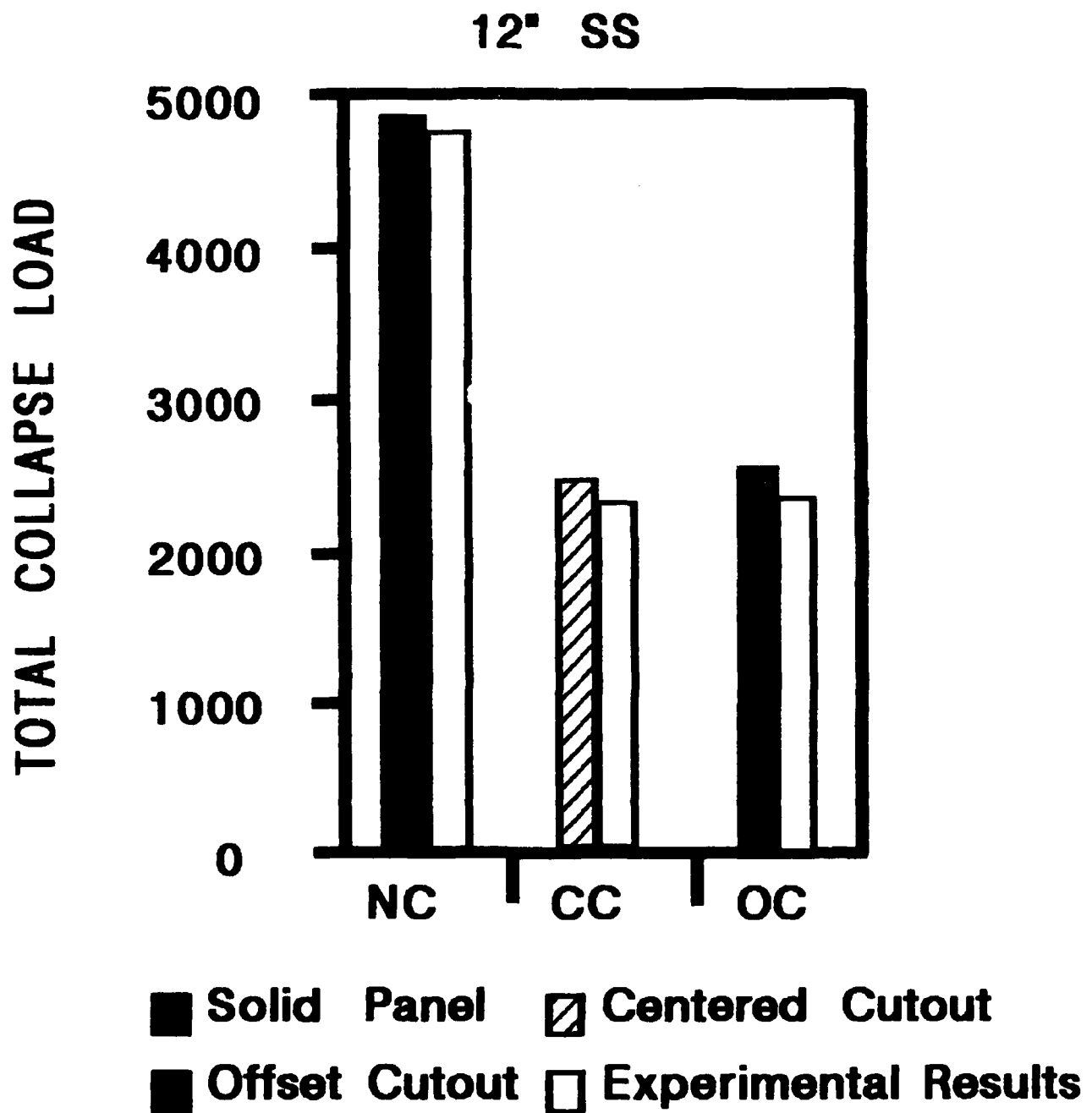
NOTE: SS = Simply Supported, US = Unsupported, NC = No Cutout, CC = Centered Cutout, OC = Off center Cutout.

when it diverged at 1350 lbs. The author believes the problem may lie not in the code itself, but in the computer system the code operates on. The VAX 8550 operates on 12-13 significant figures, even at double precision. When a fine mesh is used, or an element with many DOF's (such as the 411) the global stiffness arrays can grow to several

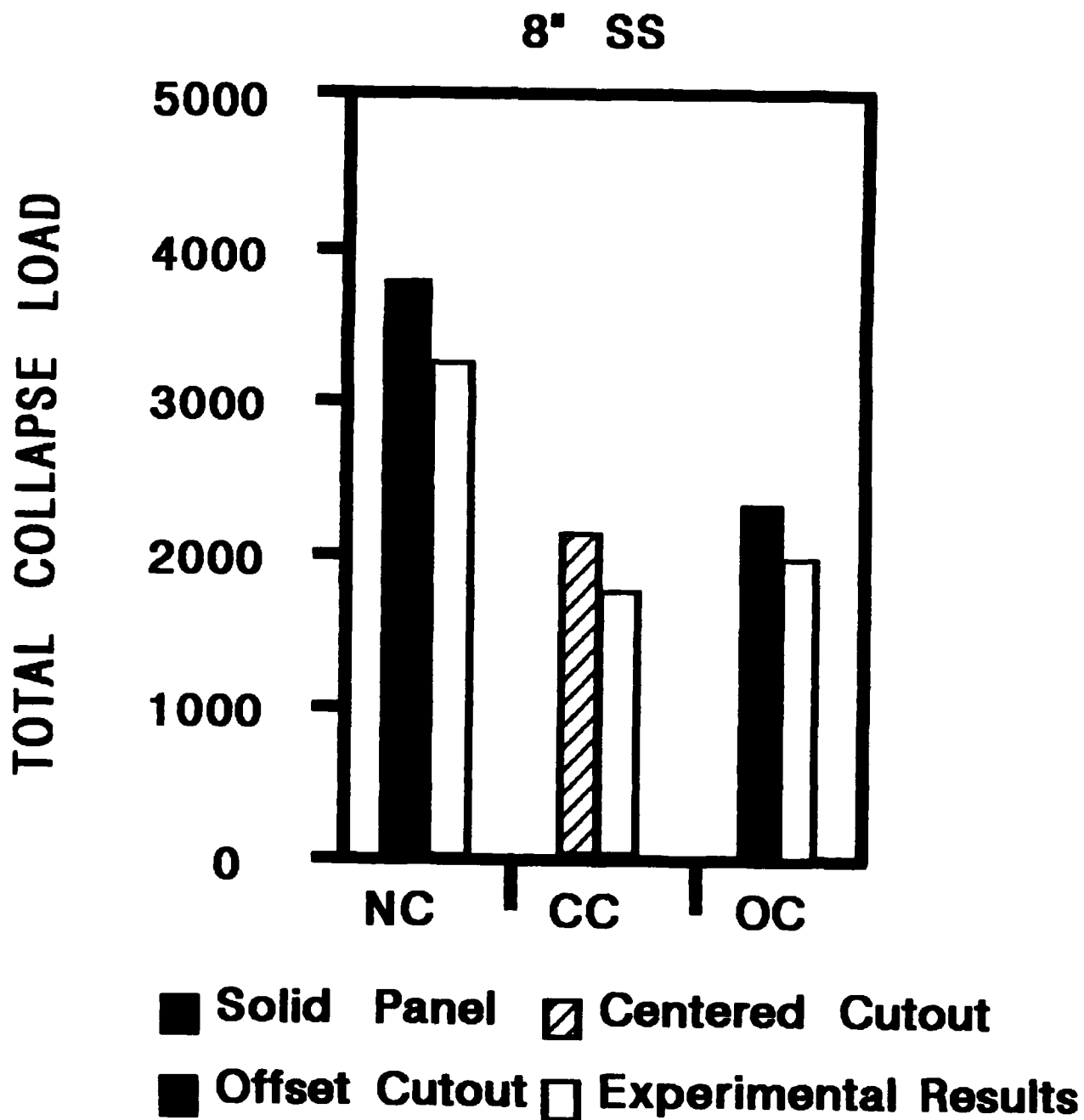


thousand equations. As these equations are iterated upon using the modified Newton-Raphson method, the error introduced by VAX will continue to grow (due to the smaller number of significant figures) until the model either converges to an unrealistic solution, or completely diverges. This was seen by Janisse [21] when he used both the VAX and the Cyber to run STAGS. The only possible way to verify this hypothesis is to run the same model, with the 411 element, on the Cyber (which has 12 significant digits at single precision alone) and determine if the model converges or not.

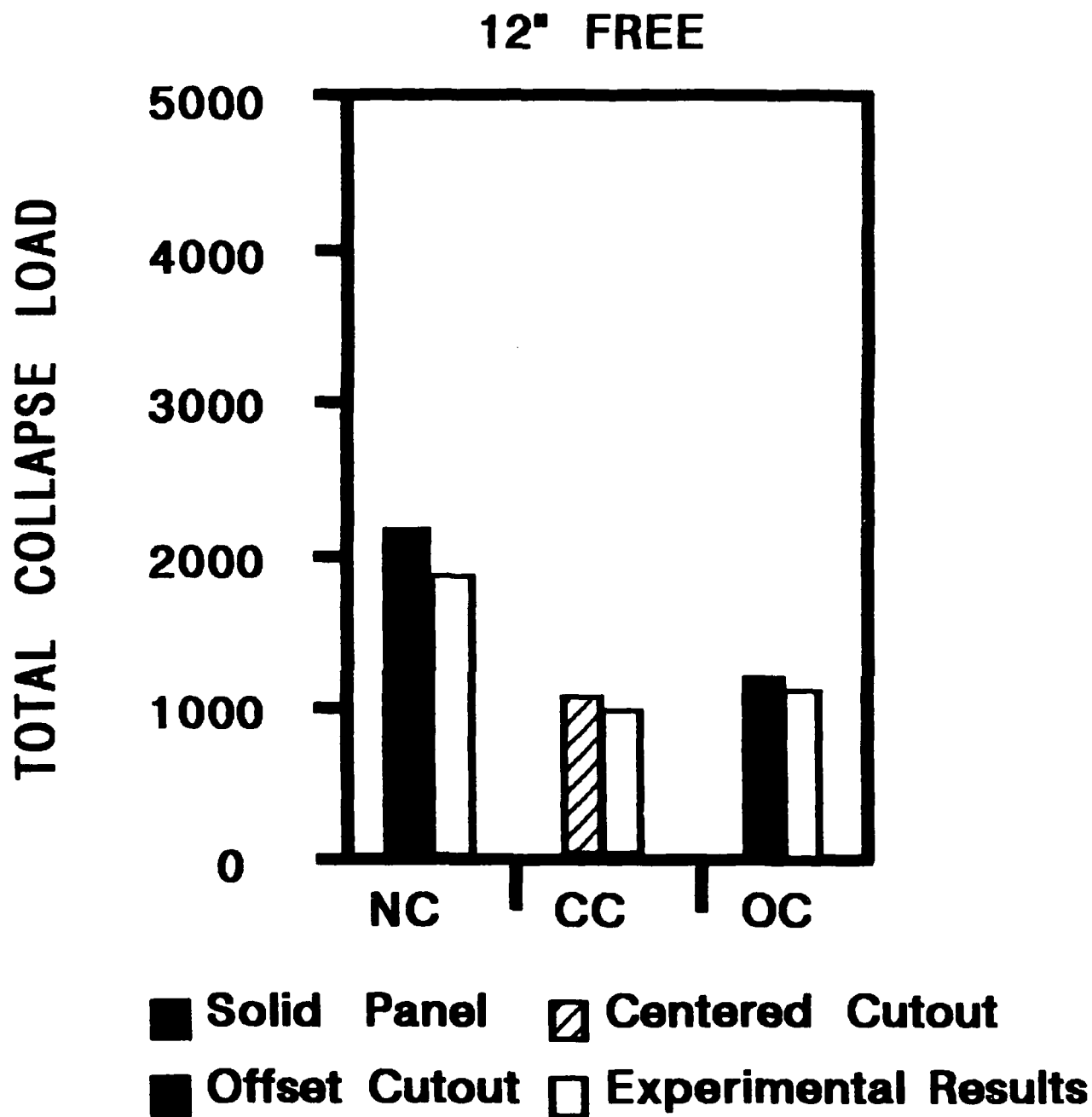
Based on this hypothesis, the author believes that STAGS may be converging to accurate solutions on the 8" models for exactly the same reason. These models require less DOF, therefore the matrices iterated upon for solution are smaller, and the induced error is thereby minimized. The author acknowledges the possibility of other answers as to why STAGS gave superior answers for the 8" models, but believes the hypothesis mentioned above is viable.



**Fig 5.51 STAGS/Experimental Collapse Ratios for 12" Simply Supported Panels Considered**



**Fig 5.52 STAGS/Experimental Collapse Ratios for 8" Simply Supported Panels Considered**



**Fig 5.53 STAGS/Experimental Collapse Ratios for 12" Unsupported Panels Considered**

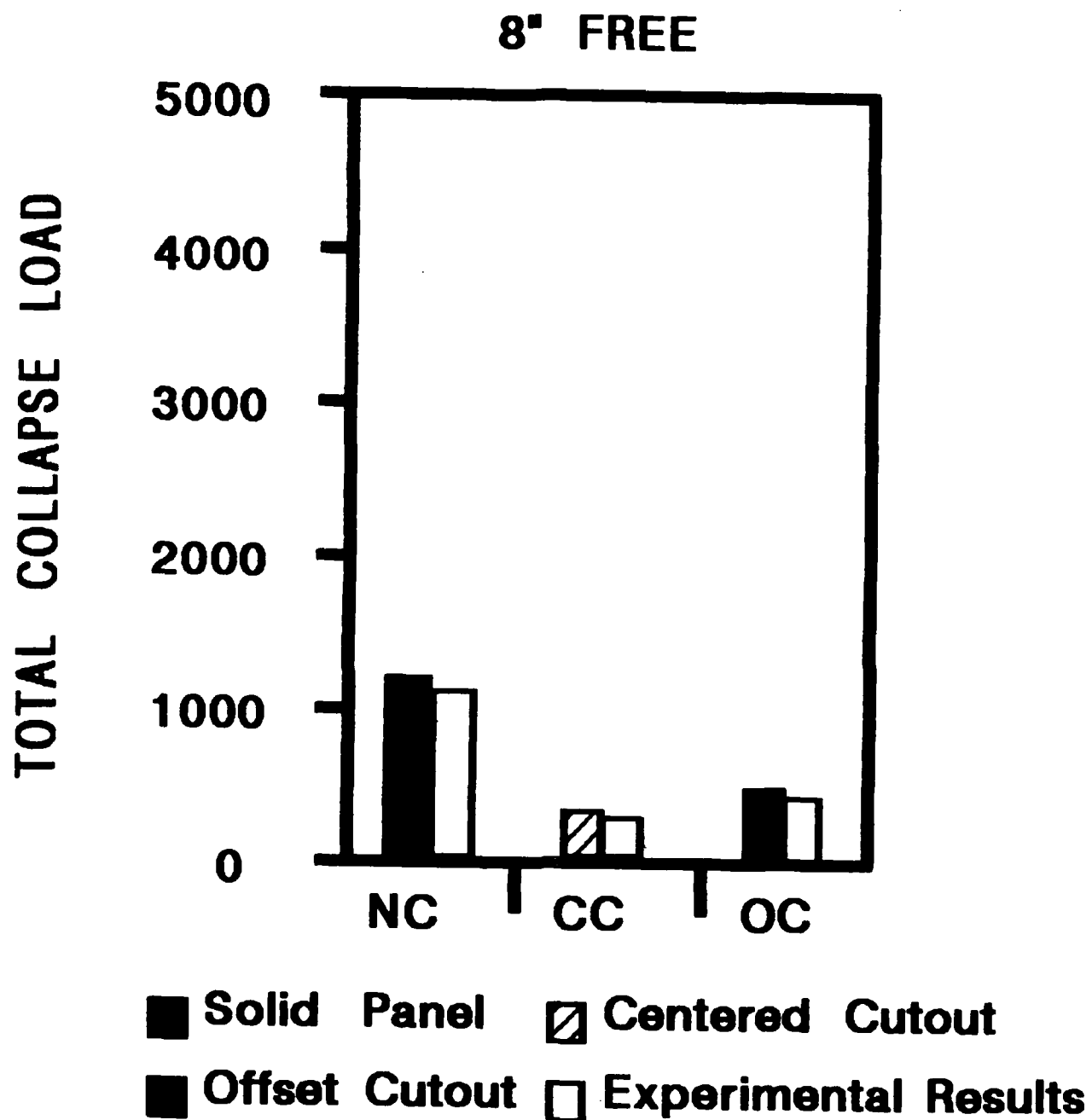


Fig 5.54 STAGS/Experimental Collapse Ratios for 8" Unsupported Panels Considered

Upon studying Figs 5.51-54, it is clear that STAGS is handling large cutouts, eccentricity, and a large nonlinear response due to free vertical edges very well. The imperfection model used on the solid panels, albeit a crude approximation of the true, initial surface imperfections of the panels, allows STAGS to better predict the bending moments that occur near the total collapse load of the panels. However, as is evident in Figs 5.39-5.50, the imperfection model leaves much to be desired. STAGS is only able to predict a small portion of the magnitude of the bending moments that exist when the panel(s) enter the nonlinear portion of the load-displacement curve.

In spite of under estimating the bending moments, STAGS predicts quite well the radial displacement pattern that is seen experimentally through the LVDT measurements. For brevity, none of these curves are included. Unlike the results Tisler [35] reported, STAGS did not demonstrate a softening of the panel. It is believed that this is due to the advancements in the code made through the corotational (updated Lagrangian scheme) method.

The experimental radial deformation pattern, while very similar to that seen for a perfect panel, is much different than what is predicted using the initial imperfection model. Combining this with the fact that all the panels had different, random initial imperfection patterns and yet

still failed in the same manner, we conclude that large cutouts dominate the panel(s)' response to axial compression. The initial imperfections play a role in the response only in those panels that do not have geometric imperfections.

At the point of collapse, for the simply supported panels, the panel is seen to snap into a new form. Although this snap-through is more dramatic for the solid panels, those panels with 4" cutouts did exhibit a secondary mode. This was seen for both 12" and 8" panels (Figs 5.55-56). As is mentioned in [35], apparently enough energy is retained by the vertical supports to force the panel(s) to collapse, via a bifurcation-like approach, into a secondary mode. A possible contribution to this may be the surface imperfection along the cutout edges causing energy to buildup in a different manner than STAGS predicts. The solid panel with free vertical edges also acted as having a secondary mode (Figs 5.57-58). It is thought that the panel, since there are no vertical supports to add stiffness, essentially acts as plate and therefore exhibits the secondary mode once collapse is achieved.

For those panels with free vertical edges and geometric imperfections, the panels did not exhibit any snap-through phenomenon (Figs 5.59-62). Instead, once the total collapse load is achieved, the panel continues its displacement

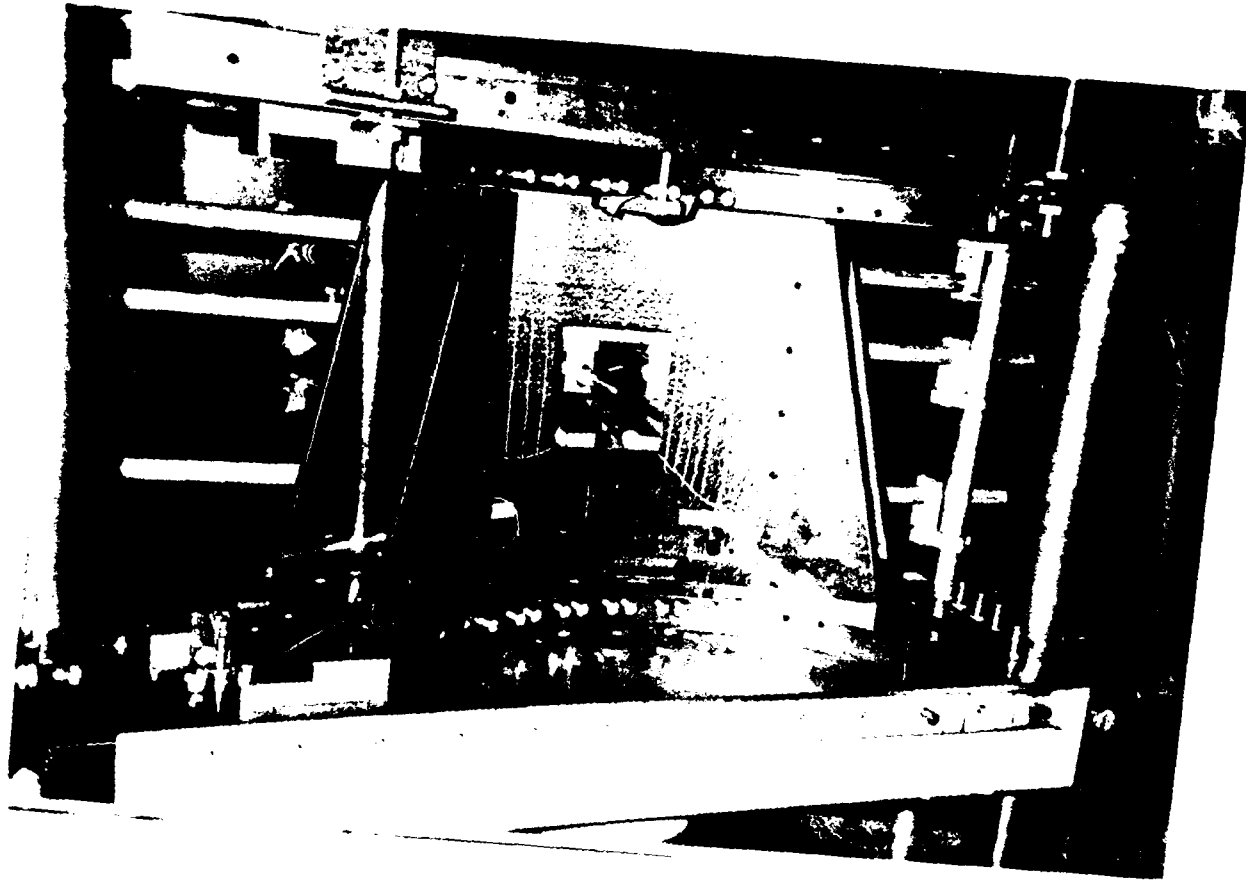


Fig 5.55 Picture of 12" Simply Supported Panel with  
4" Cutout, Centered Prior Collapse Snap -  
Through



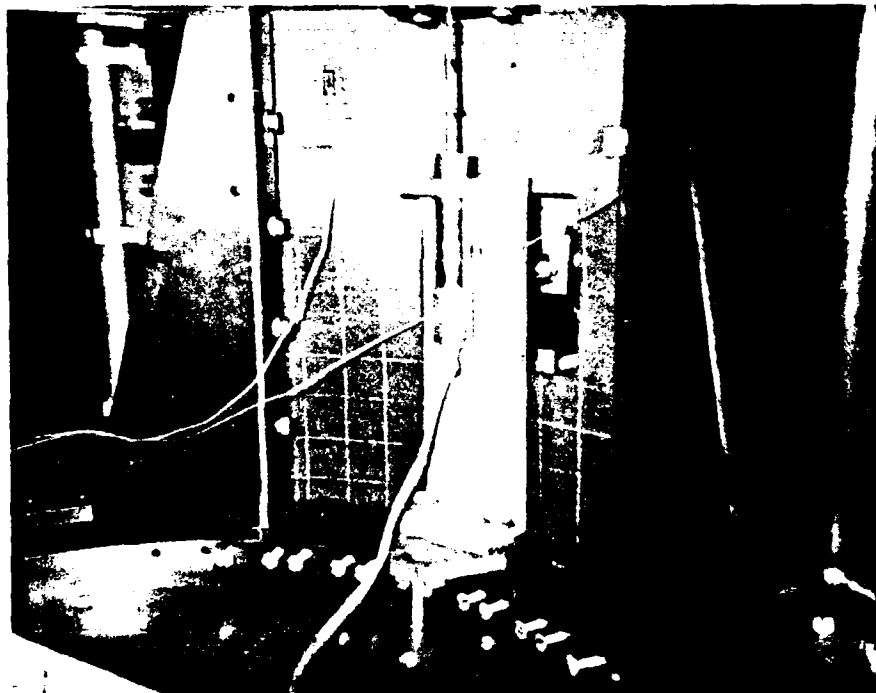


Fig 5.56 Pictures of 12" Simply Supported Panel with  
4" Cutout, Centered After Collapse Snap -  
Through



Fig 5.57 Picture of 12" Unsupported Panel, No Cutout,  
Prior to Collapse Snap-Through

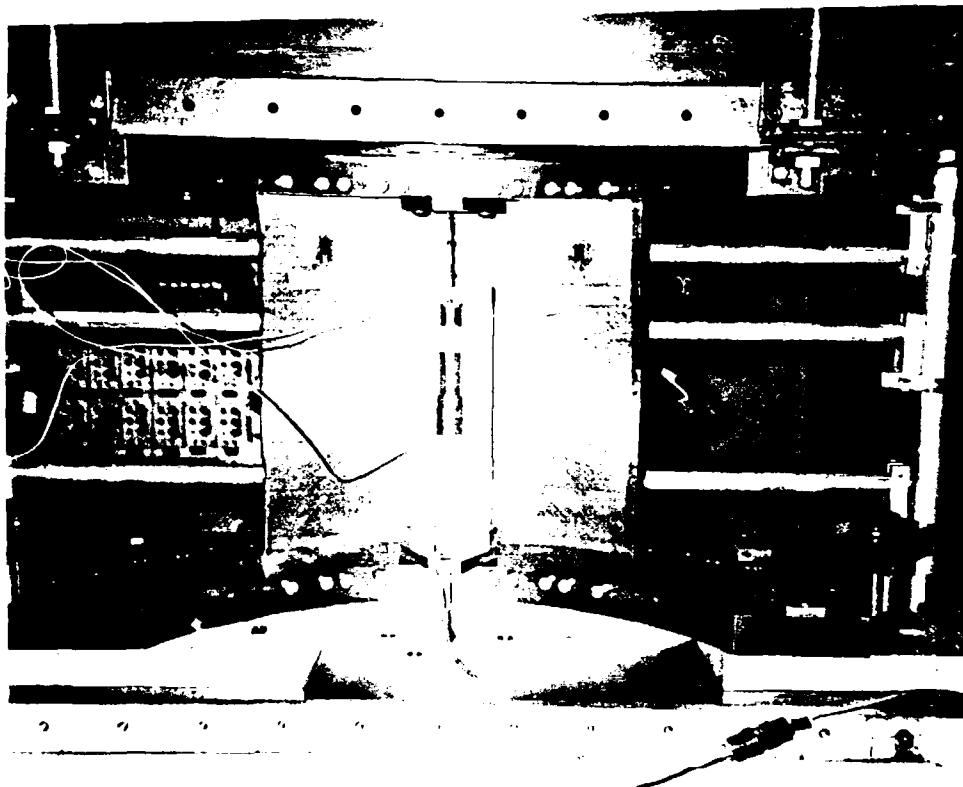


Fig 5.58 Picture of 12" Unsupported Panel, No Cutout,  
After to Collapse Snap-Through

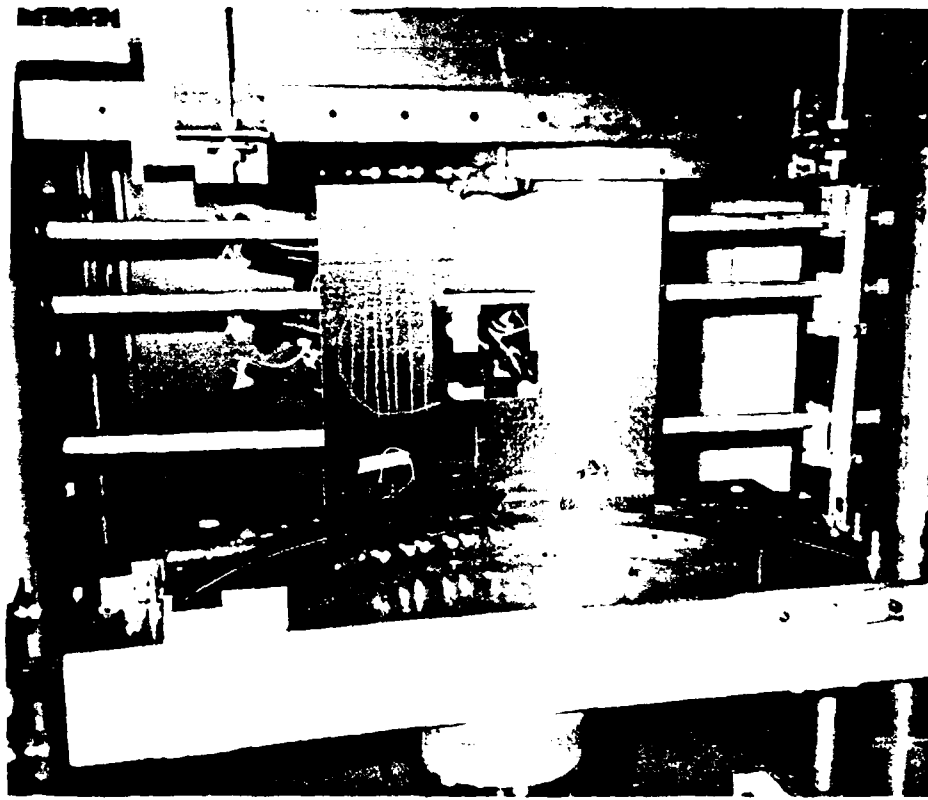


Fig 5.59 Picture of 12" Unsupported Panel with 4" Cutout  
Prior to Collapse

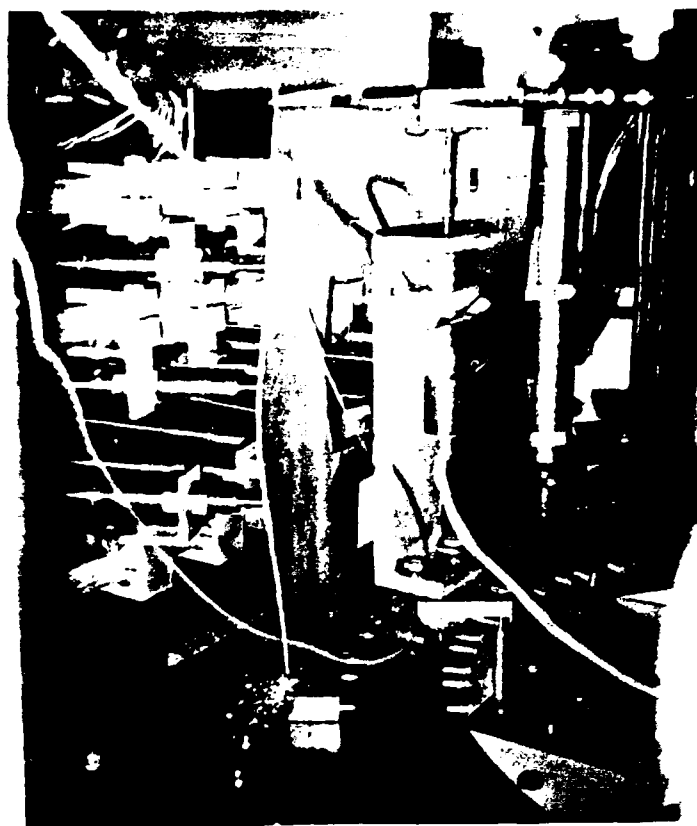


Fig 5.60 Pictures of 12" Unsupported Panel with 4" Cutout  
After to Collapse



Fig 5.61 Picture of 8" Unsupported Panel with 4" Cutout  
Prior to Collapse

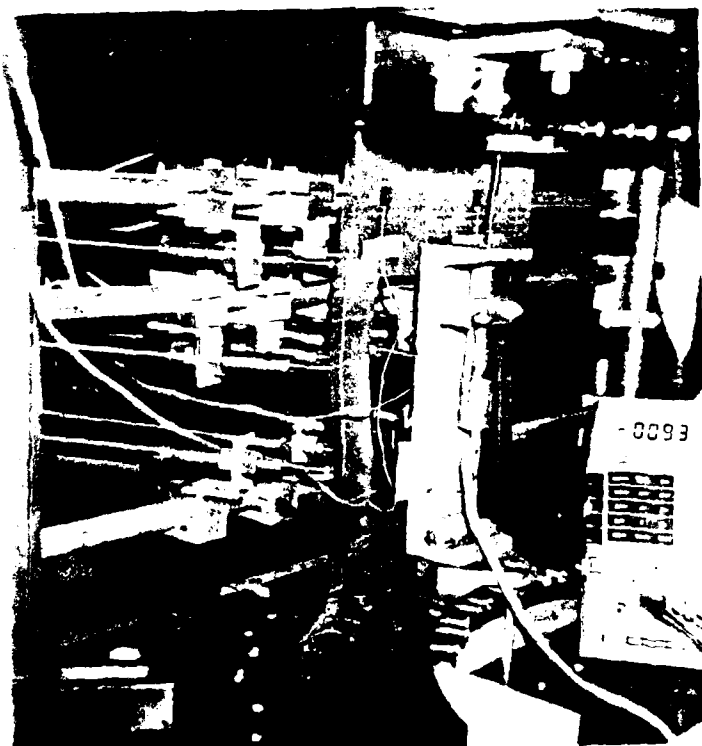
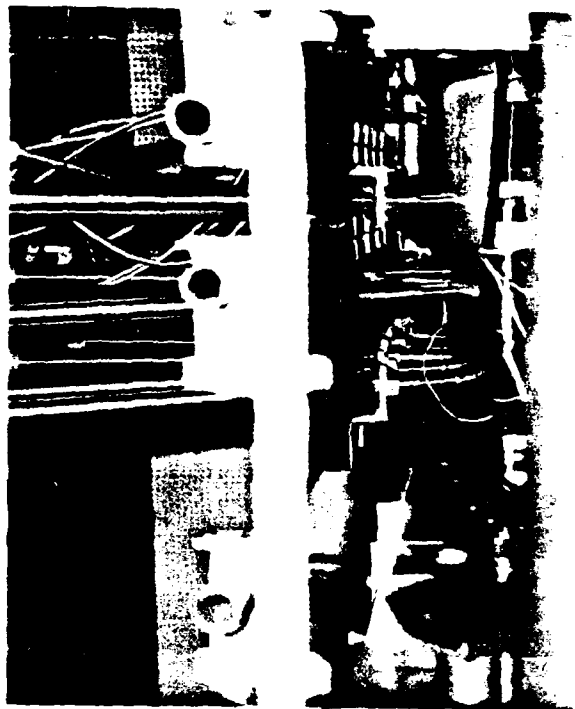


Fig 5.62 Pictures of 8" Unsupported Panel with 4" Cutout  
After to Collapse

bending moments through the nonlinear portions of the pattern until the loading is removed.

In all, STAGS and SHELL predicts the general displacement pattern, both axially and radially, very well. When the imperfection models are included, STAGS does predict an increase in load-displacement curves. STAGS and SHELL also accurately predicts, the effects of boundary conditions, geometric imperfections, eccentricity, and panel geometry upon composite shell response to axial compression.

#### 5.4 Residual Stress

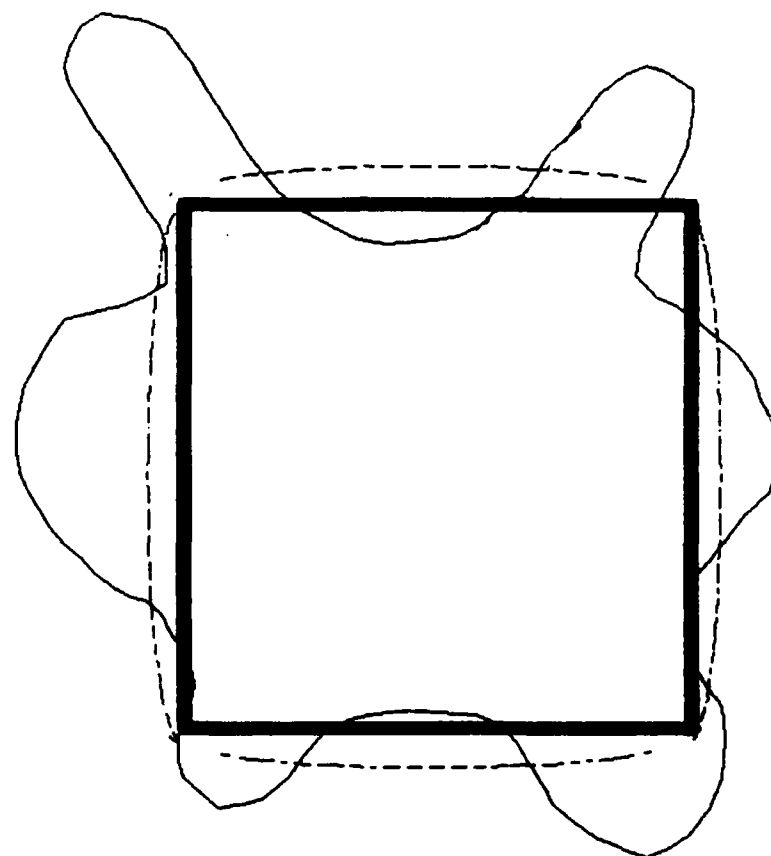
The results of the residual stress test showed little change in the strain in the axial direction ( $\approx 10 \mu$  strain). The circumferential direction, however, saw a relatively large change in surface strain ( $\approx 75 \mu$  strain). How much of this could be attributed to experimental error is unclear. Although the panel was measured before cutting while freely resting, the curved panel is very sensitive to bending stresses. Some bending stress may have been caused by merely resting the panel on the wooden cutout form (refer Section 3.3, Fig 3.18).

Assuming the experimental findings are correct, it remains to compare these stresses to stresses during axial compression. The change in strain appears to be in bending



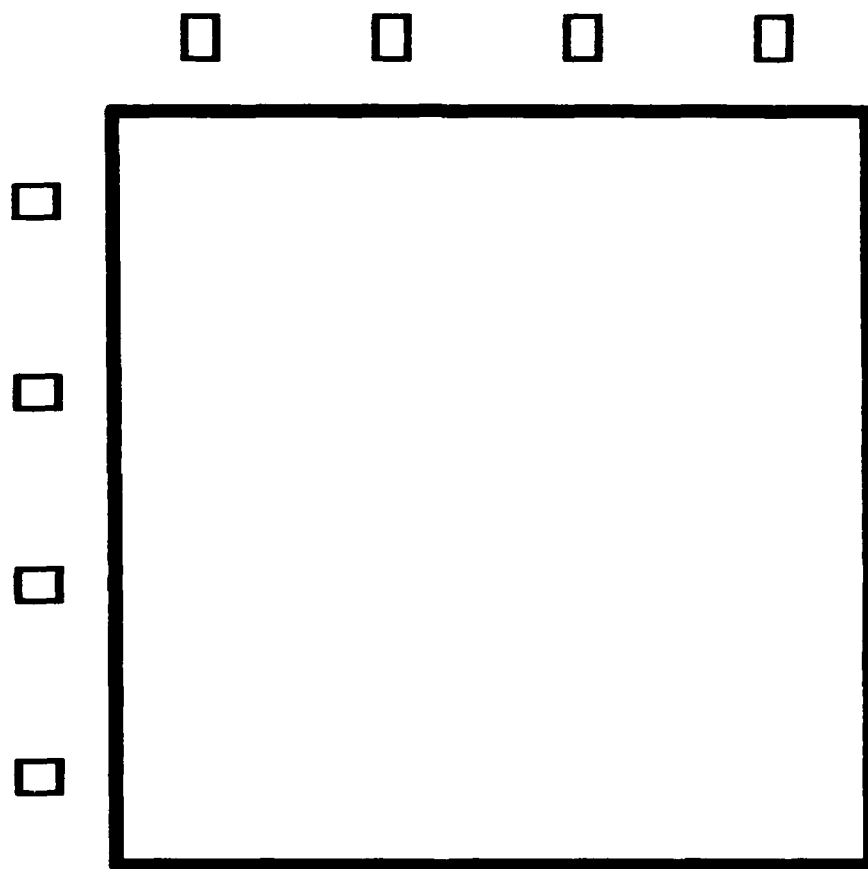
stress present due to curing the panel during the manufacturing process. This means that the maximum change in stress occurred at the outer surface where the strain rosettes were positioned. This change in bending stress was of equal and opposite magnitude on the opposing side of the panel, and zero at the center of the panel.

Since the change in stress in the axial direction was negligible ( $\approx 14$  psi), interest is in the stress in the circumferential direction. The change in stress in the circumferential direction (at the outermost ply) that corresponds to the measured change in strain varied from 450 psi at the corners to 750 psi at the center of the cutout. A plot of the circumferential stress at collapse is shown in Fig 5.63, where the stress magnitude is measured for the cutout edge, positive outward. It is seen that the change in stresses are much smaller in magnitude than the stresses from loading. These results differ greatly from Tisler's [31] results. The author believes this is due mainly to the experimental approach taken between this effort and Tisler's. Tisler used a single strain rosette, placed in the center of the cutout. This single rosette could, at best, give a rough global approximation of the change in stress due to removing the cutout. The approach used in this effort incorporated 16 strain rosettes (Fig 5.64) on the front and back of the panel. These rosettes were placed



- Magnitude of circumferential stress change measured, approximately 450 to 750 psi
- ~~~~~ Magnitude of circumferential stress (N ) near cutout edge as predicted by STAGS, ranges in magnitude from -1430 psi to +2557 psi
- Magnitude is measured positively outward from the cutout edge, negative is inward

**Fig 5.63** Circumferential Stress Near Cutout Edge at Collapse as Compared to Stress Change Measured



**NOTE: Strain rosettes are spaced 1" apart  
and 1/2" of the cutout**

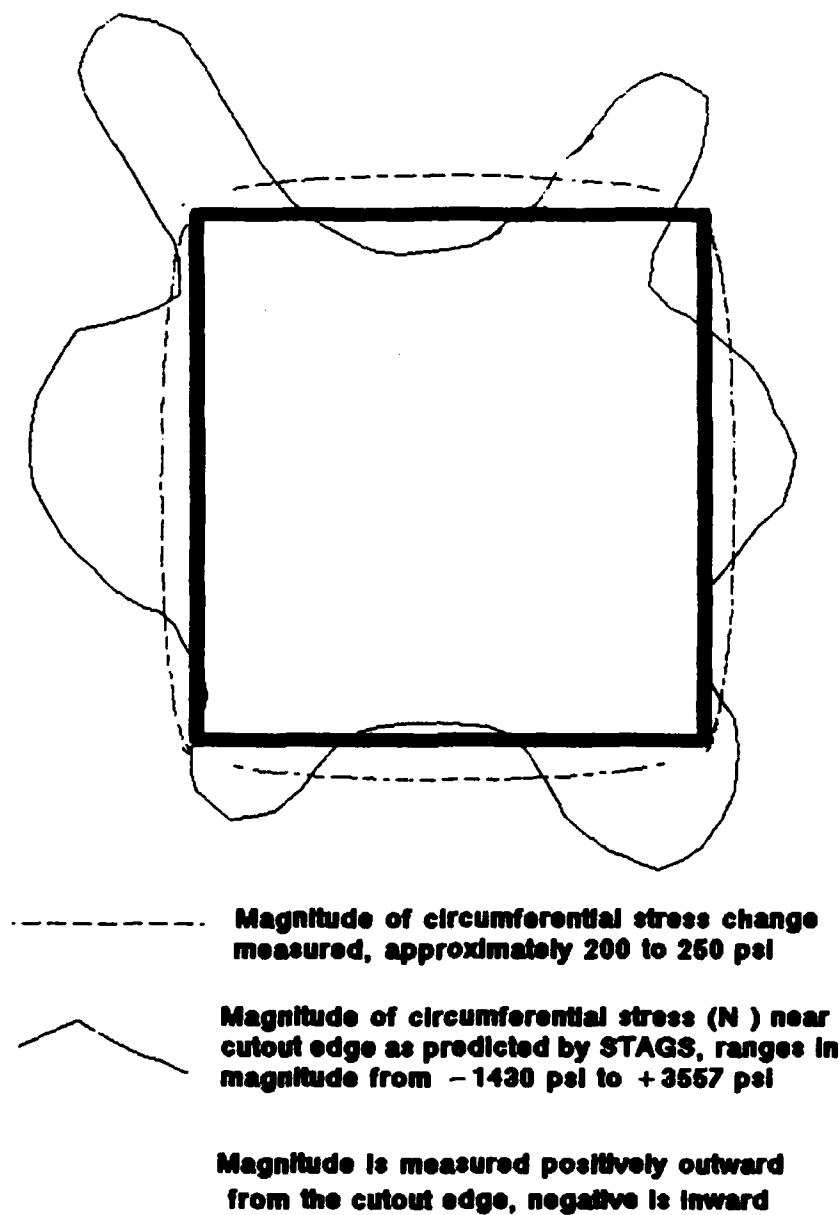
**Fig 5.64 Schematic of Residual Stress Test Showing  
Placement of Strain Rosettes**

0.5" away from the cutout to allow clearance for the router used in removing the cutout (refer Section 3.3, Fig 3.19). Although this is relatively small distance, it may be great enough to begin relieving the change in stresses. However, the author believes the results generated from this experimental approach give a clearer picture as to the magnitude and shape of the residual stress than before. It is seen to be at least 50% less than stresses from loading at collapse.

At this point it is unclear as to the importance this change in stress is to the panel(s)' collapse. How much (if any) of the error in the STAGS and SHELL solutions can be attributed to residual stress changes is unclear. We have seen that based on the previous work, along with this effort, this is a subject that warrants further study. It is evident that residual stress changes exist. What needs to be determined is the role these stress changes play in the collapse of cylindrical composite shells. A statistical study should be made in determining the stress concentrations along the edges of the cutout (as was done in this effort) should provide a clearer picture as to the importance of considering residual stress in the collapse analysis. The the only references available on this subject are for isotropic materials with circular holes in plates and do not consider cylindrical composite shells with large

cutouts. Since this is the case, a methodology of incorporating these residual stresses into the collapse analysis along with a larger data base need to be developed.

One final note, there is some concern about inducing residual stress by forcing the experimental panels to fit the curvature of the test fixture. While the panel(s) are curing in the autoclave, the original radius of curvature is no longer held constant due to the anisotropy of the laminate. Hence the panel, once curing was completed, now has a random radius of curvature throughout. However, the test fixture was machined with a constant radius of curvature of 12" (the original curvature for the laminate when it was manufactured). By forcing the panel into this constant radius of curvature, it is felt that internal stresses may be induced, thereby decreasing panel stiffness and at the same time increasing the bending moment seen in the nonlinear panel response. By referring to Section 3.3, Fig 3.17, the reader is reminded that a reading was taken from the strain rosettes while the panel was strapped to the hole cutting support. It is felt that this closely parallels the situation when the panel was fit into the experimental test fixture. An analysis was accomplished, similar to the actual residual stress test and is shown in Fig 5.85. It was determined that forcing the panel to assume a constant radius of curvature generated a maximum of



**Fig 5.85** Circumferential Stress Near Cutout Edge at Collapse as Compared to Stress Change Measured

250 lbs. Granted, this is a small amount (only 9% of the total collapse load) but it is of enough magnitude that it can be considered in the analysis if so desired.

## 6. CONCLUSIONS

1. It is still unclear whether the vertical boundary condition of circumferential movement ( $v$ ) is fixed or free. From the analysis presented in Chapter 5, it appears the true boundary condition for the experimental panels is somewhere in between the two extremes. The  $v$  free condition does not reduce panel stiffness, but it will reduce the total collapse load for the panels. For those panels with no cutouts the reduction is  $\approx 8\%$ . For those panels with 4" cutouts, the reduction is 18%. This is because the majority of the load is carried along the vertical edge if there is a large cutout present. With a solid panel, the load remains evenly distributed.
2. Small radial imperfections effects become less crucial when cutout are present, and are almost negligible when large cutouts are introduced. The impact of these imperfections is minimal when compared to the effect of the cutouts on the panel(s)' response. However, these small imperfections do play a role in those panels no having a cutout. STAGS has shown that using an initial imperfection model using three half sine waves in both the radial and circumferential directions with an



amplitude of one ply thickness (0.005") indicates a reduction in stiffness for both simply supported panels (5-10%) and unsupported panels (15-35%). For the unsupported panels, this reduction in stiffness included a marked increase in bending for the nonlinear portion of the load-displacement curves.

3. The presence of geometric imperfections (cutouts) reduces the panel's total collapse load by  $\approx 50\%$  (up to 77% for the unsupported 8" panels). Offsetting the cutout to introduce eccentricity did not reduce the collapse load as expected. Instead, STAGS predicted a slight increase in total collapse load (3% for simply supported panels and 7-10% for unsupported panels) which is verified by experimental results. This increase in loading may be due to the redistribution of stress that occurs between the cutout and the vertical edges. If the reader considers the 12" simply supported panel with a 4" centered cutout as the baseline: then as the boundary is moved closer, the stress ( $N_x$ ) redistribution occurs at a lower percentage of the total collapse load than is seen for the baseline. Thus in the case of eccentricity, the smaller "column" or side of the panel redistributes its stress at a lower magnitude of stress, and the wider

column will keep an even distribution at a higher magnitude of stress. There may be some localized buckling due to the smaller column reaching its maximum stress at a lower magnitude of axial loading, but from a global viewpoint, the panel will respond with an essentially increased stiffness.

4. The vertical boundary conditions have a significant impact on the total collapse load. By removing the vertical supports, total collapse load of the panel (ignoring the effect of cutouts or panel width) is reduced by at least 40% and up to 75%. This is due to essentially removing the  $\pm 45^\circ$  plies from the panel's stiffness matrix (which is half of the ply lay-up) since there is no vertical support to constrain these plies. Hence, the  $\approx 50\%$  reduction in total collapse load for all six panels when the vertical supports are removed.
5. By reducing the panel's width and thereby placing the effects of the vertical boundary condition near the cutout, a reduction in collapse load is seen. The effect of panel geometry is not as significant to the panel's response when considering cutouts or boundary conditions of the panel for the simply supported

panels. This is not true for the unsupported panels. For the simply supported panels, geometric imperfections (cutouts) and removing the boundary conditions have a greater impact than reducing the width of the panel. The unsupported panels are very sensitive to the presence of cutouts and reducing panel width. Both conditions have approximately the same result, a large decrease in panel stiffness and therefore a significant decrease in total collapse load.

6. The unsupported panels demonstrated the greatest sensitivity to presence of cutouts. By removing one-third to half of the effective cross-section of the panel to carry a load, the panel could see a reduction in total collapse load of up to 75%. The same holds true from reducing panel width from 12" to 8". The response of these panels is highly nonlinear with significant rotations occurring at the point of collapse along the free vertical edge. These large rotations may indicate the presence of through-the-thickness shear which reduces panel stiffness and therefore total collapse load.

7. STAGS appears quite able to handle large displacements and rotations exhibited by the panels. Although STAGS may predict higher stiffnesses for the panels, this is to be expected. The imperfection model used forces the random imperfections known to exist on the experimental panels into a uniform pattern through the sine wave approximation which minimizes the amount of bending moment introduced into the model as it nears the collapse load. Residual stress (due to curing and enforcing a constant radius of curvature) is not considered. For the simply supported panels, the v free or fixed boundary condition is still unclear. Yet STAGS accurately predicts the panel's response in terms of load, axial displacement, and radial displacement.
8. SHELL predicts more accurately than STAGS for those panels that undergo large displacements ( $\approx .02"$ ) and/or large rotations ( $\approx 15-17^\circ$ ). This is due to transverse shear reducing the panel's stiffness. This reduction in stiffness is seen through a reduction in total collapse load, an increase in the bending moments, and an increase in the magnitude of radial displacements.
9. Both STAGS and SHELL are useful analysis tools. STAGS is more advantageous for analyzing general shell shapes

(either isotropic or anisotropic material) that undergo small, moderate, and even large displacements and/or rotations. On the other hand, STAGS ignores three-dimensional effects and cannot adequately conduct nonlinear vibrational analysis. SHELL has the advantage of incorporating transverse shear effects into its analysis, its strain-displacement relationships are based upon the exact nonlinear, shell strain-displacement relationships, and the additional capability of nonlinear vibrational analysis (both static and dynamic). However, SHELL can only analyze cylindrical shell structures or plate structures.

10. Residual stress is created by removing the cutout. It is fairly uniform in the circumferential direction and practically nonexistent in the axial direction. The magnitude of this stress is approximately 750 lbs (assuming worst case). When comparing this to the total collapse load (2521 lbs) it is evident that residual stress does not dominate nor greatly influence the panel's response. It is felt the presence of the cutout itself dominates the reduction in total collapse load that is seen. However, residual stress should not be ignored.

## 7. RECOMMENDATIONS

1. Further analysis need to be accomplished on the initial imperfection model. It is believed the additional bending seen in the nonlinear resonse of the panel is due to radial surface imperfections. One method is mark out the finite element model on the surface of the panel. Assume a uniform radius of curvature through the midplane of the panel. Then determine, at each node point on the panel the change, in terms of displacement, from this uniform plane of constant radius of curvature. Then input these displacements into the model used in STAGS as initial imperfection and the solve the model for equilibrium as load is increase. This should provide a solution that approximates the experimental results more closely. Another method is to incorporate the techniques Starnes [30] used into STAGS. The author realizes this is not a simple problem, but it is felt to be important enough to be pursued.
2. More analysis needs to be accomplished on the cylindrical shells that have free vertical edges. SHELL indicates that through-the-thickness shear is important at the onset of collapse. This shear effect

could reduced panel stiffness and thereby decrease total collapse load. It may also enhance the bending moment that begins to dominate the panel's response in the nonlinear region.

3. Verification is still needed on the experimental vertical boundary conditions, whether  $v$  is free or fixed. One solution is model the panel such that on the vertical edges, every other node has  $v$  free and the rest have  $v$  fixed. The author acknowledges this is not the actual circumstances seen in the experimental setup, but this model could give a better approximation for the true boundary conditions.

## 8. BIBLIOGRAPHY

1. Ugral, A. C., Stresses in Plates and Shells, McGraw-Hill Book Co., 1981.
2. Saada, A. S., Elasticity Theory and Applications, Pergommen Press, 1974.
3. Sanders, J. L. "Nonlinear Theories for Thin Shells," Qtr. of Applied Math, Vol XXI, No. 1 (1962).
4. Leissa, A. W. Buckling of Laminated Composite Plates and Shell Panels. AFWAL-TR-85-3069. Air Force Flight Dynamics Laboratory, Wright-Patterson AFB OH, June 1985.
5. Sobel, L. H., Weller, T., and Agarwal, B. L., "Buckling of Cylindrical Panels Under Axial Compression," Computers and Structures, 6: 29-35 (February 1976).
6. Almroth, B. O. "Influence of Edge Conditions on the Stability of Axially Compressed Cylindrical Shells," AIAA Journal, 4: 134-14 (1969).
7. Andreev, L. V. et al., "Nonlinear Deformation of a Cylindrical Panel Under Axial Compression," Soviet Applied Mechanics, 17: 270-274 (September 1981).
8. Rehfield, L. W. and Hallauer, W. L., Jr., "Edge Restraint Effect on Buckling of Compressed Curved Panels," AIAA Journal, 6: 187-189 (January 1980).
9. Becker, M. L., Palazotto, A. N., and Khot, N. S., "Instability of Composite Panels," Journal of Aircraft, 18: 739-743 (September 1981).
10. Tvergaard, V., "Buckling of Elastic-Plastic Cylindrical Panel Under Axial Compression," International Journal of Solid Structures, 13: 957-970 (1977).
11. Brogan, F. and Almroth, B. O., "Buckling of Cylinders with Cutouts," AIAA Journal, 8: 236-238 (February 1970).
12. Garashchuk, I. N., and Chernyshenko, I. S., "Numerical Investigation of the Stress State of a Cylindrical Shell with a Circular Hole," Soviet Applied Mechanics, 15: 484-488 (December 1979).



13. Almroth, B. O. and Holmes, A. M. C., "Buckling of Shells with Cutouts Experiment and Analysis," International Journal of Solid Structures, 8: 1057-1071 (August 1972).
14. Almroth, B. O., et al., "Stability of Cylinders with Circular Cutouts," AIAA Journal, 11: 1582-1584 (November 1973).
15. Almroth, B. O., and Brogan, F. A. "Bifurcation Buckling as an Approximation of the Collapse Load for General Shells," AIAA Journal, 10: 463-467 (April 1972).
16. Becker, M. L., Palazotto, A. N., and Khot, N. S., "Experimental Investigation of the Instability of Composite Cylindrical Panels," Experimental Mechanics, 22: 372-376 (October 1982).
17. Bauld, N. R., Jr., and Satyamurthy, K., Collapse Load Analysis for Plates and Shells. AFFDL-TR-79-3038. Air Force Flight Dynamics Laboratory, Wright-Patterson AFB OH, December 1970.
18. Harper, James G. Buckling Analysis of Laminated Composite Circular Cylindrical Shells. MS Thesis, AFIT/GAE/AA/78D-8. School of Engineering, Air Force Institute of Technology (AU), Wright-Patterson AFB OH, December 1979.
19. Becker, Marvin L. Analytical/Experimental Investigation of the Instability of Composite Cylindrical Panels. MS Thesis, AFIT/GAE/AA/79D-3. School of Engineering, Air Force Institute of Technology (AU), Wright-Patterson AFB OH, December 1979.
20. Hebert, John S. Analytical/Experimental Linear Bifurcation of Curved Cylindrical Composite Panels. MS Thesis, AFIT/GAE/AA/82D-14. School of Engineering, Air Force Institute of Technology (AU), Wright-Patterson AFB OH, December 1982.
21. Janisse, T. C. and Palazotto, A. N., "Collapse Analysis of Cylindrical Composite Panel with Cutouts," AIAA Journal of Aircraft, 21: 731-733 (September 1984).
22. Lee, C. E., and Palazotto, A. N., "Nonlinear Collapse Analysis of Composite Cylindrical Panels with Small Cutouts or Notches," Composite Structures, 4: 217-229 (1985).

23. Hermesen, M. F., and Palazotto, A. N., "The Effects of Cutout Location and Material Degradation on the Collapse of Composite Cylindrical Panels," Non-Linear Analysis and NDE of Composite Material Vessels and Components, (Edited by Hui, D., Duke, J. C., and Chung, H.) ASME PVP vol. 115 and NDE vol. 3: 43-57 (1986).
24. Dennis, S. T. and Palazotto, A. N., "The Effects of Large Movement on a Composite Cylindrical Shell with Cutouts," 30th AIAA Conf., Mobile AL, paper no.89-1398, to appear in Nonlinear Mechanics (1989).
25. Linneman, P. E. Vibration and Buckling Characteristics of Composite Cylindrical Panels Incorporating the Effects of a Higher Order Shear Theory. MS Thesis, AFIT/GA/AA/88D-6. School of Engineering, Air Force Institute of Technology (AU), Wright-Patterson AFB OH, December 1988.
26. Cook, R. D. Concepts and Applications of Finite Element Analysis for Plates and Panels. (Second Edition). John Wiley and Sons, 1981.
27. User's Manual for STAGS, Volume 1 Theory. Structural Mechanics Laboratory, Lockheed Palo Alto Research Laboratory, Palo Alto CA, 1981.
28. Zienkiewicz, O. C. The Finite Element Method (The third, expanded and revised edition of The Finite Element Method in Engineering Sciences). McGraw-Hill Book Company (UK) Limited, 1977.
29. Lee, Cathy E. Numerical Determination of the Effects of Boundary Conditions on the Instability of Composite Panels with Cutouts. MS Thesis, AFIT/GAE/AA/83D-4. School of Engineering, Air Force Institute of Technology (AU), Wright-Patterson AFB OH, December 1983.
30. Starnes, J. H. and Knight, N. F., "Postbuckling Behavior of Selected Graphite-Epoxy Cylindrical Panels Loaded in Axial Compression," 27th Structures, Structural Dynamics, and Materials Conference, San Antonio TX, May 19-21 1986, AIAA 86-0881.
31. Knight, N. F., and Starnes, J. H., "Postbuckling Behavior of Axially Compressed Graphite Epoxy Cylindrical Panels with Circular Holes," Collapse Analysis of Structures, (ed. by L. H. Sobel) ASME, PVP Vol. 84, (1984).

32. Palazotto, A. N., and Tisler, T. W., "Experimental Collapse Determination of Cylindrical Composite Panels with l=Large Cutouts under Axial Load," Composite Structures, 4: 61-78 (1989).
33. Palazotto A. N., and Tisler. T. W., "Considerations of Cutouts in Composite Cylindrical Panels," Computers & Structures, Vol. 29, No. 6, pp 1101-1110, (1988).
34. Tisler, T. W., and Palazotto, A. N., "Insight into the Collapse of Composite Cylindrical Panels with Cutouts: Analysis and Experimentation," Recent Advances in Structural Dynamics, (ed. by H. Chung and H. D. Fisher) ASME, PVP Vol. 124 (1987).
35. Tisler, Thomas W. Collapse Analysis of Cylindrical Composite Panels with Large Cutouts Under an Axial Load. MS Thesis, AFIT/GAE/AA/86D-1. School of Engineering, Air Force Institute of Technology (AU), Wright-Patterson AFB OH, December 1986.
36. Egan, G. S., and Palazotto A. N., "The Analysis of a Composite Shell Structure," 30th AIAA/ASME Structures, Structural Dynamics and Materials Conference, Mobile AL, Paper No. 89-1297, to appear in AIAA Journal (1989).
37. Egan, Gregory S. Nonlinear Finite Element Analysis of a General Composite Shell. MS Thesis, AFIT/GAE/AA/88D-12. School of Engineering, Air Force Institute of Technology (AU), Wright-Patterson AFB OH, December 1988.
38. Palazotto, A. N., "An Experimental Study of a Curved Composite Cutout," Composite Materials: Testing and Design (Eighth Conference), ASTM STP 972. Ed. by J. D. Whitcomb, pp 191-202 (1988).
39. Riks, E., "On the Numerical Solution of Snapping Problems in the Theory of Elastic Stability," SUDAAR No. 401, Stanford University, Stanford, CA, 1970.
40. Dennis, S. T., and Palazotto A. N., "The Effects of Large Movement on a Composite Cylindrical Shell with Cutouts", 30th AIAA/ASME Structures, Structural Dynamics and Materials Conference, Mobile AL, Paper No. 89-1398, AIAA Journal (Oct 1989).

41. Dennis, Scott T. Large Displacement and Rotational Formulation for Laminated Cylindrical Shells Including Parabolic Transverse Shear. Ph.D. Dissertation, AFIT/DS/AA/88-1. School of Engineering, Air Force Institute of Technology (AU), Wright-Patterson AFB OH, May, 1988 (AD-A194871).
42. Sobel, L. H. and Thomas, K. Evaluation of the STAGSC-1 Shell Analysis Program. WARD-10881. Westinghouse Advanced Reactors Division, Madison PA, August 1981.
43. Almroth, B. O. and Brogran, F. A. Numerical Procedures for Analysis of Structural Shells. AFWAL-TR-80-3128. Air Force Flight Dynamics Laboratory, Wright-Patterson AFB OH, March 1981.
44. Brush, D. O., and Almroth, B. O. Buckling of Bars, Plates, and Shells. McGraw-Hill, 1975.
45. Jones, R. M. Mechanics of Composite Materials. Hemisphere Publishing Corporation, 1975.
46. Rankin, C. C., et al. "Enhancements to the STAGS Computer Code." NASA Contract Report 4000, November 1986.
47. Rankin, C. C. and Brogan, F. A. "An Element-Independent Corotational Procedure for the Treatment of Large Rotations," in Collapse Analysis of Structures, ed. by L. H. Sobel, ASME, PVP Vol. 84, 1984.
48. Bathe, K. J. and Ho, L. W. "Some Results in the Analysis of Thin Shell Structures," Nonlinear Finite Element Analysis in Structural Mechanics. Ed. by W. Wunderlich, E. Stein, and K. J. Bathe, 1981, Springer - Verlag Berlin, Heidelberg, NY, (125-150).
49. Riks, E. "An Incremental Approach to the Solution of Snapping and Buckling Problems," International Journal of Solids and Structures, 15: 529-551 (1979).
50. Wempner, G. A. "Discrete Approximations Related to Nonlinear Theories of Solids," International Journal of Solids and Structures, 7: 1581-1599 (1971).

51. Tsai, C. T. and Palazotto, A. N. "A Modified Riks Approach to Composite Shell Snapping Using High-Order Shear Deformation Theory," accepted for publication in Journal of Computers and Structures (1989).
52. Horban, B. A. The Effects of Through-the-Thickness Delaminations on Curved Composite Panels. MS Thesis, AFIT/GAE/AA/85D-8. School of Engineering, Air Force Institute of Technology (AU), Wright-Patterson AFB OH, Dec 1985.
53. Wilder, B. L. A Study of Damage Tolerance in Curved Composite Panels. MS Thesis, AFIT/GAE/AA/88D-2. School of Engineering, Air Force Institute of Technology (AU), Wright-Patterson AFB OH, Dec 1988.
54. Broek, D. Elementary Engineering Fracture Mechanics. Martinus Nijhoff Publishers, Dordrecht, Netherlands, 1987.
55. Crisfield, M. A., "A Fast Incremental/Iterative Solution Procedure That Handles 'Snap-Through'," Computers and Structures, 13: 55-62 (1981).
56. Bowlus, J. A., Palazotto, A. N., and Whitney, J. M., "Vibration of Symmetrically Laminated Rectangular Plates Considering Deformation and Rotary Inertia," AIAA Journal, 25: 1500-1511 (Nov 1987).
57. Bowlus, John A. The Determination of the Natural Frequencies and Mode Shapes For Anisotropic Laminated Plates Including the Effects of Shear Deformation and Rotary Inertia. MS Thesis, AFIT/GA/AA/85S-1. School of Engineering, Air Force Institute of Technology (AU), Wright-Patterson AFB OH, September 1985.
58. Palardy, Real F. The Buckling and Vibration of Composite Plates Using the Levy Method Considering Shear Deformation and Rotary Inertia. MS Thesis, AFIT/GAE/AA/87D-16. School of Engineering, Air Force Institute of Technology (AU), Wright-Patterson AFB, OH, December 1987.
59. Reddy, J. N., and Liu, C. F., "A Higher-Order Shear and Deformation Theory of Laminated Elastic Shells," Int J Eng Sci. 23: 319-330 (Mar 1985).

Appendix A: Derivation of STAGSC-1 Nonlinear  
Strain Displacement Equations

Since one of the primary strengths of the STAGS computer programs is its ability to analyze shells nonlinearly, a derivation of the nonlinear kinematics is presented.

To start the derivation, a few assumptions need to be made. STAGS uses plate elements to model a shell structure. These plate elements are considered thin so that the in-plane displacements,  $u$  and  $v$ , and the normal displacements,  $w$ , are functions of only two space variables [27]. A plane stress assumption is made whereby  $\gamma_{xy}$ ,  $\gamma_{yz}$ ,  $\epsilon_z$ , and  $\sigma_z$  are considered negligible. And finally, the Kirchhoff-Love hypothesis applies for strains away from the mid-plane.

Consider a line segment as shown in Fig A.1 oriented in its undeformed and deformed state (represented by an \*). From Fig A.1, it is evident that the deformed state can be related to the undeformed state by [27]:

$$\begin{aligned}x^* &= x + u \\z^* &= z + w\end{aligned}\tag{A.1}$$

and the differential change in distance by [27]:

$$dx^* = dx(1 + u_{,x})$$

$$dz^* = dx w_{,z} \quad (A.2)$$

$$(ds^*)^2 = (dx^*)^2 + (dz^*)^2$$

By subtracting the first two equations of Eqn (A.2) into the last equation it follows that [27]:

$$\left(\frac{ds}{dx}\right)^2 - 1 = 2u_{,x} + (u_{,x})^2 + (w_{,x})^2 \quad (A.3)$$

Using the definition of strain [27],

$$\epsilon_x = (ds^* - dx)/dx \quad (A.4)$$

and then rearranging it to get an alternate form [27],

$$\epsilon_x + 1/2 \epsilon_x^2 = 1/2 \left[ \left(\frac{ds}{dx}\right)^2 - 1 \right] \quad (A.5)$$

Substituting Eqn (A.3) into Eqn (A.5) and assuming the strain is small so that  $\epsilon_x^2$  can be ignored gives [27]:

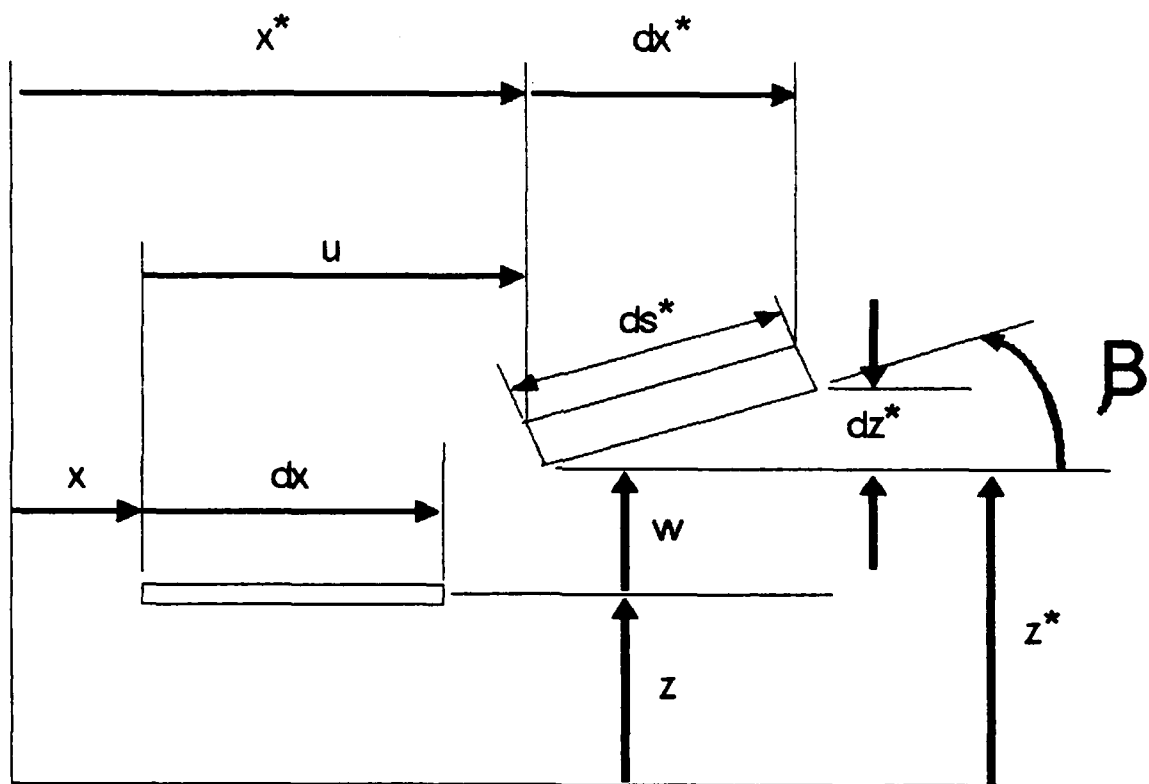


Fig A.1 Line Element in Undeformed and Deformed State [26]



$$\epsilon_x = u_{,x} + 1/2(u_{,x}^2 + w_{,x}^2) \quad (A.6)$$

So far the analysis for this line element has been only in one plane. If this element is in the mid-plane of a plate element, the rotation of this line element about the normal has to be considered. If this rotation is included in Eqn (A.6) as in Sanders' nonlinear shell equations, and rewritten to reflect mid-plane strain, the result is:

$$\epsilon_x^0 = u_{,x} + 1/2(u_{,x}^2 + w_{,x}^2 + \phi^2) \quad (A.7)$$

where in Sanders' equations [3]

$$\phi = 1/2(u_{,y} - v_{,x}) \quad (A.8)$$

The term that should be included in Eqn (A.7) to represent this rotation in the x-direction about the normal, for a flat plate, is  $v_{,x}$ . This does not imply the use of Sander's equation in STAGS, just the importance of defining a normal rotation term for flat plates representing a shell geometry. Substituting this term in Eqn (A.7) results in [27]:

$$\epsilon_x^0 = u_{,x} + 1/2(u_{,x}^2 + w_{,x}^2 + v_{,x}^2) \quad (A.9)$$

Following this same line of reasoning, the other two mid-plane terms  $\epsilon_y^0$  and  $\gamma_{xy}^0$  can be written as [27]:

$$\begin{aligned}\epsilon_y^0 &= v_{,y} + 1/2(u_{,y}^2 + w_{,y}^2 + v_{,y}^2) \\ \gamma_{xy}^0 &= u_{,y} + v_{,x} + (u_{,x}u_{,y} + v_{,x}v_{,y} + w_{,x}w_{,y})\end{aligned}\quad (A.10)$$

Now if the Kirchhoff hypothesis is included, where strains away from the mid-plane are due to the following curvatures:

$$\begin{aligned}\chi_x &= -w_{,xx} \\ \chi_y &= -w_{,yy} \\ \chi_{xy} &= -w_{,xy}\end{aligned}\quad (A.11)$$

the full expression for strain in the plate element can be written from Eqn's (A.9), (A.10), and (A.11) as:

$$\begin{aligned}\epsilon_x &= \epsilon_x^0 - z\chi_x \\ \epsilon_y &= \epsilon_y^0 - z\chi_y \\ \epsilon_{xy} &= \epsilon_{xy}^0 - z\chi_{xy}\end{aligned}\quad (A.12)$$

This kinematic formulation allows for large displacements and moderate rotations with small strains (due to the Kirchhoff hypothesis).

## Appendix B: Derivation of Nonlinear Strain Displacement Equations

As in STAGS, one of the primary strengths of SHELL is its ability to analyze shells nonlinearly. Therefore a short derivation of the underlying nonlinear kinematics is presented. It is important to note that the elements used in SHELL are not plate elements but true shell elements. Also, SHELL incorporates a parabolic distribution of through the thickness shear strain.

Therefore, a method to incorporate three-dimensional (3-D) effects is to specialize the general 3-D strain displacement relations expressed in arbitrary orthogonal curvilinear coordinates. These are derived in several elasticity texts, see Eqn (2.10) or reference [2] for example.

The following derivation is based on Linneman's [25] work. It is presented here as a means to give the reader the basic understanding of the methodology of incorporating 3-D effects (transverse shear) into the 2-D strain displacement relations. This derivation is not how SHELL is formulated, but demonstrates to the reader a simpler method of incorporating transverse shear effects into the strain displacement relations than is shown in [41].

The coordinate system for a circular cylindrical shell

panel and the degrees of freedom used in [25] are shown in Fig B.1. The  $x$  and  $y$  axes are located at the mid-surface of the laminate ( $z = 0$ ). The degrees of freedom  $u_0(x,y,t)$ ,  $v_0(x,y,t)$ , and  $w(x,y,t)$  are the laminate mid surface displacements in the  $x$ ,  $y$ , and  $z$  directions, respectively. The degrees of freedom  $\psi_x(x,y,t)$  and  $\psi_y(x,y,t)$  are the rotations of the laminate cross section from the normal at the mid surface with respect to the  $x$  and  $y$  axes, respectively.  $R$  is the radius of curvature,  $h$  the laminate thickness,  $a$  the length in the  $x$ -direction and  $b$  the length

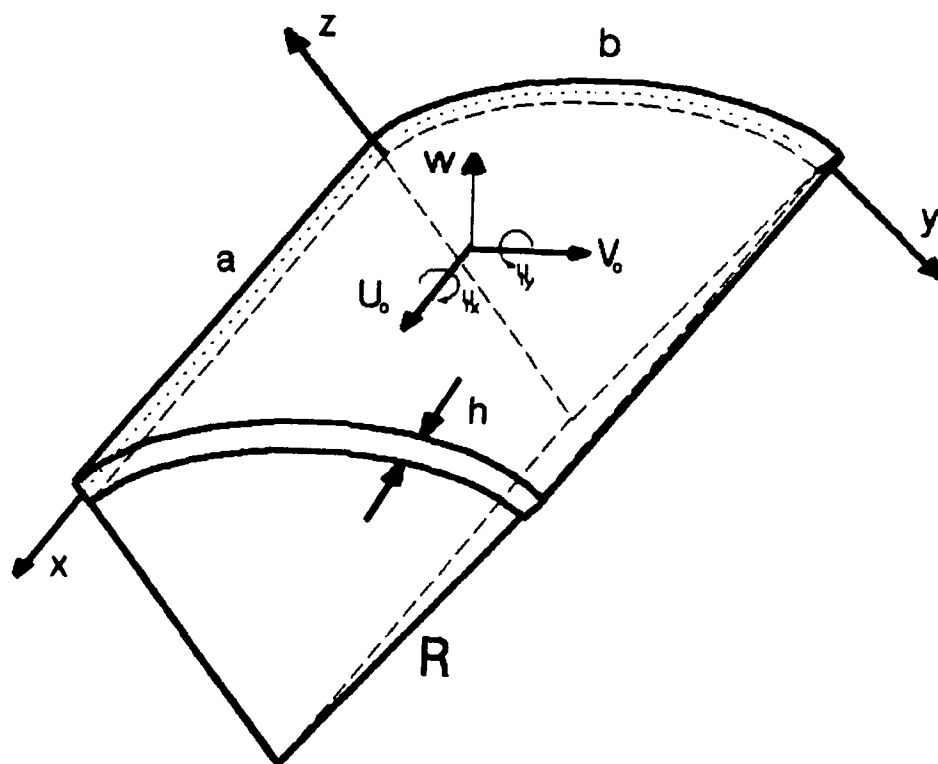
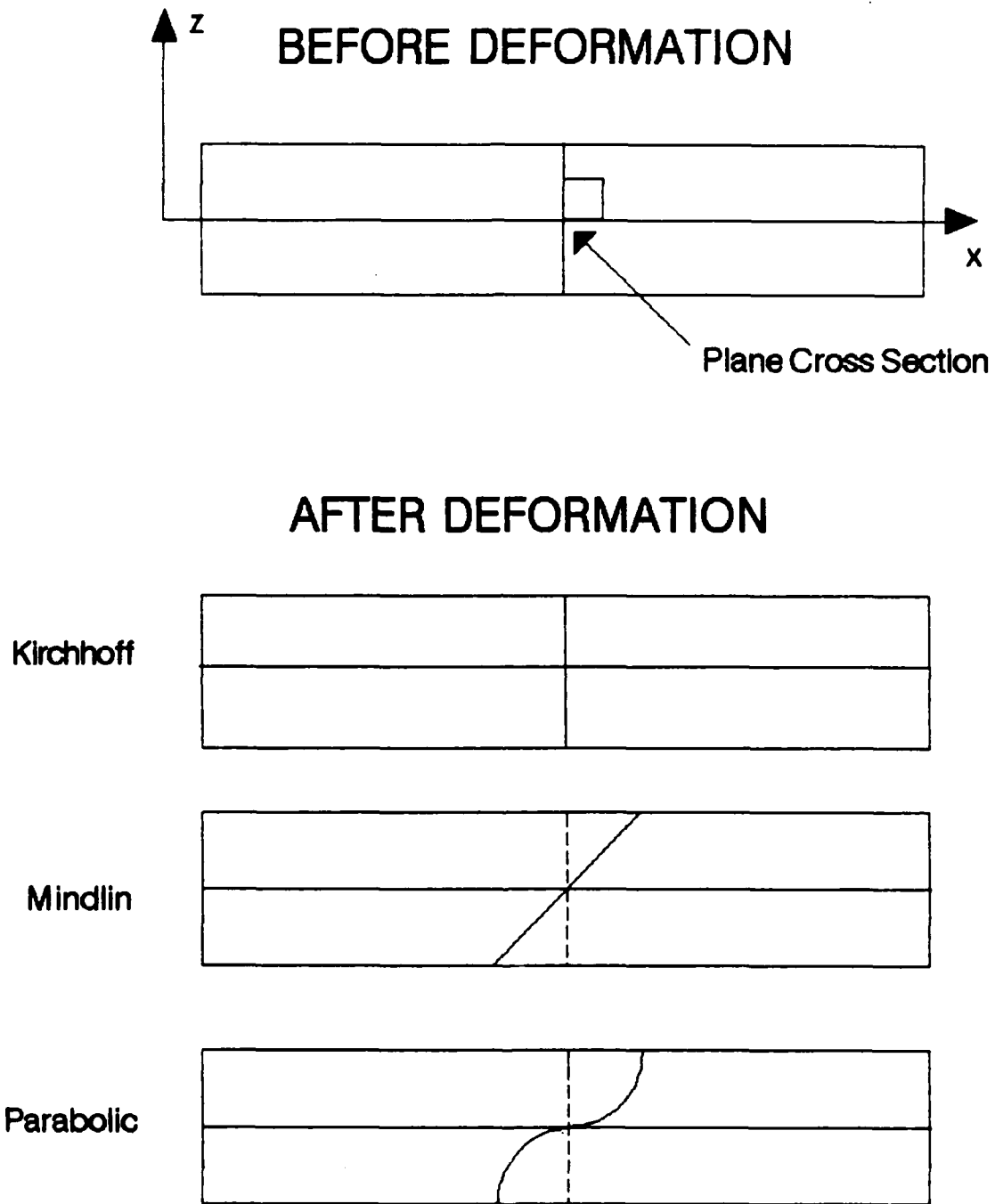


Fig B.1 Shell Panel Coordinates and Degrees of Freedom

in the y-direction.

In order to determine the displacement field, the transverse shear strains,  $\gamma_{xz}$  and  $\gamma_{yz}$ , need to be modeled. In classical laminated shell theory, through the thickness shear deformation is neglected according to the Kirchhoff-Love hypothesis that plane cross sections remain plane and perpendicular to the laminate mid-surface after deformation. A displacement field that is a first order function of  $z$  is required in classical shell theory. Bowls [56,57] and Palardy [58] in their flat plate work modelled transverse shear strain using Mindlin plate theory, which also requires the use of a first order displacement field. Mindlin plate theory assumes the cross section remain plane, but is allowed to rotate from the normal with respect to the mid surface after deformation. The assumption of no cross sectional warping introduces error, especially at the top and bottom surfaces of the laminate, since the model does not match the boundary conditions of zero transverse shear there. This error is reduced by the introduction of shear correction factor. SHELL models transverse shear strain parabolically wherein the strains are maximum at the laminate mid-surface and are zero at the top and bottom surfaces, satisfying the boundary conditions. Fig B.2 illustrates the various transverse shear concepts discussed above.



**Fig B.2 Transverse Shear Strain Models**

To achieve the desired parabolic transverse shear, a higher order displacement field is required, as opposed to the first order displacement field used in the Classical and Mindlin cases. The coordinate displacements in the x and y directions, u and v, will be cubic functions of z; the displacement in the z-direction, w, will be constant with respect to z. From Reddy [59] and Saada [2], the generalized displacement field is:

$$\begin{aligned} u(x,y,z,t) &= u_0 + z\psi_x + z^2\theta_1 + z^3\theta_1 \\ v(x,y,z,t) &= \left(1 + \frac{z}{R}\right)v_0 + z\psi_y + z^2\theta_2 + z^3\theta_2 \quad (B.1) \\ w(x,y,z,t) &= w \end{aligned}$$

where  $\theta_1$ ,  $\theta_2$ ,  $\theta_1$ , and  $\theta_2$  will be chosen to satisfy the boundary conditions of zero transverse shear strain at the laminate top and bottom surfaces.

Linear orthogonal curvilinear coordinates are used to develop the strain-displacement relations for simplicity. For a circular cylindrical shell panel these relations reduce to [25]:

$$\begin{aligned}
\epsilon_x &= u_{,x} \\
\epsilon_y &= \frac{1}{1 + \frac{z}{R}} \left( v_{,y} + \frac{w}{R} \right) \\
\gamma_{xy} &= \frac{1}{1 + \frac{z}{R}} u_{,y} + v_{,x} \\
\gamma_{yz} &= \frac{1}{1 + \frac{z}{R}} \left( w_{,y} - \frac{v}{R} \right) + v_{,z} \\
\gamma_{xz} &= u_{,z} + w_{,x}
\end{aligned} \tag{B.2}$$

where  $(\ )_{,x}$  represents partial differentiation with respect to  $x$  and so on.  $\epsilon_z$  is assumed equal to zero. This implies that a change in length in the normal ( $z$ ) direction of a cross section perpendicular to the mid surface is not considered, and is regarded as an accepted inconsistency in plate and shell theory. In reality,  $\epsilon_z$  is not zero, but is small compared to the other strains. For the laminate, it means there are no discontinuities in  $\epsilon_z$  at the lamina boundaries, but they too are small.

The Donnell cylindrical shell panel equations assume  $\frac{z}{R} \approx 0$  in Eqn (B.2). As shown in [25], this assumption limits Donnell theory to be valid only for small  $\frac{h}{R}$  ratios. With no transverse shear, the maximum  $h/R$  limit under Donnell assumptions is approximately 1/500 [59]. As will be shown, with transverse shear included, the Donnell equations



are valid up to  $h/R$  equal to approximately 1/50 [59].

For simplicity assume  $\frac{z}{R} \approx 0$  for the transverse shear strains,  $\gamma_{xz}$  and  $\gamma_{yx}$ , only. (The limitations of the model resulting from these simplifications are discussed in Appendix A of [25]). For the membrane strains ( $\epsilon_x$ ,  $\epsilon_y$ , and  $\gamma_{xy}$ ) the following polynomial expansion is made:

$$\frac{1}{1 + \frac{z}{R}} \approx 1 - \frac{z}{R} \quad (B.3)$$

This approximation allows the strain-displacement relations to be valid for deep panels, with an  $\frac{h}{R}$  maximum limit of approximately 1/5 (See [24,25]). The transverse shear strains in Eqn (B.2) become:

$$\begin{aligned} \gamma_{yz} &= v_{,z} + w_{,y} - \frac{v}{R} \\ \gamma_{xz} &= u_{,z} + w_{,x} \end{aligned} \quad (B.4)$$

If one sets  $\gamma_{yz}(x,y,\pm h/2,t) = 0$  and  $\gamma_{xz}(x,y,\pm h/2,t) = 0$  to satisfy the laminate boundary conditions, then from Eqn (B.1) it can be shown that (see Appendix A [25]):

$$\begin{aligned}
\theta_1 &= \theta_2 = 0 \\
\theta_1 &= k(\psi_x + w_{,x}) \\
\theta_2 &= k(\psi_y + w_{,y})
\end{aligned} \tag{B.5}$$

where  $k = -\frac{4}{3h^2}$ . The displacement field becomes:

$$\begin{aligned}
u(x,y,z,t) &= u_o + z\psi_x + z^3k(\psi_x + w_{,x}) \\
v(x,y,z,t) &= \left(1 + \frac{z}{R}\right)v_o + z\psi_y + z^3k(\psi_y + w_{,y}) \\
w(x,y,z,t) &= w
\end{aligned} \tag{B.6}$$

Using this displacement field in Eqn (B.2), the strain displacement relations become:

$$\begin{aligned}
\epsilon_x &= u_{o,x} + 2\psi_{x,x} + z^3k(\psi_{x,x} + w_{,xx}) \\
\epsilon_y &= v_{o,y} + \frac{w}{R} + 2\psi_{y,y} - \frac{1}{R}z^2\psi_{y,y} \\
&\quad + z^3k(\psi_{y,y} + w_{,yy}) - \frac{1}{R}z^4k(\psi_{y,y} + w_{,yy}) \\
\gamma_{xy} &= u_{o,y} + v_{o,x} + z\left(\psi_{x,y} + \psi_{y,x} + \frac{1}{2R}(v_{o,x} - u_{o,y})\right) \\
&\quad - \frac{1}{R}z^2\psi_{x,y} + z^3k(\psi_{x,y} + \psi_{y,x} + 2w_{,xx}) \\
&\quad - \frac{1}{R}z^4k(\psi_{x,y} + w_{,xy}) \\
\gamma_{yx} &= \psi_y + w_{,y} + 3kz^2(\psi_y + w_{,y}) \\
\gamma_{xz} &= \psi_x + w_{,x} + 3kz^2(\psi_x + w_{,x})
\end{aligned} \tag{B.7}$$

Shorthand notation can be introduced to rewrite the strains as follows:

$$\begin{Bmatrix} \epsilon_x \\ \epsilon_y \\ \gamma_{xy} \\ \gamma_{yz} \\ \gamma_{xz} \end{Bmatrix} = \begin{Bmatrix} \epsilon_x^0 \\ \epsilon_y^0 \\ \gamma_{xy}^0 \\ \gamma_{yz}^0 \\ \gamma_{xz}^0 \end{Bmatrix} + z \begin{Bmatrix} \kappa_x^0 \\ \kappa_y^0 \\ \kappa_{xy}^0 \\ 0 \\ 0 \end{Bmatrix} + z^2 \begin{Bmatrix} 0 \\ \kappa_y^1 \\ \kappa_{xy}^1 \\ \kappa_{yz}^1 \\ \kappa_{xz}^1 \end{Bmatrix} + z^3 \begin{Bmatrix} \kappa_x^2 \\ \kappa_y^2 \\ \kappa_{xy}^2 \\ 0 \\ 0 \end{Bmatrix} + z^4 \begin{Bmatrix} 0 \\ \kappa_y^3 \\ \kappa_{xy}^3 \\ 0 \\ 0 \end{Bmatrix} \quad (\text{B.8})$$

(Note the superscripts on the  $\kappa$  terms are not exponents. They are for identification purposes only and simply distinguish among the high and low order curvature terms). The strains at the laminate mid surface are [25]:

$$\begin{Bmatrix} \epsilon_x^0 \\ \epsilon_y^0 \\ \gamma_{xy}^0 \\ \gamma_{yz}^0 \\ \gamma_{xz}^0 \end{Bmatrix} = \begin{Bmatrix} u_{0,x} + \frac{w}{R} \\ v_{0,x} + v_{0,x} \\ u_{0,y} + v_{0,y} \\ \psi_y + w_{,y} \\ \psi_x + w_{,x} \end{Bmatrix} \quad (\text{B.9})$$

and the curvature terms ( $\kappa$ ) due to bending and shear deformation are defined as follows [25]:

$$\begin{Bmatrix} \chi_{x^0}^0 \\ \chi_{y^0}^0 \\ \chi_{xy}^0 \end{Bmatrix} = \begin{Bmatrix} \psi_{x,x} \\ \psi_{y,y} \\ \psi_{x,x} + \psi_{y,x} + \frac{1}{2R}(\psi_{o,x} - u_{o,y}) \end{Bmatrix}$$

$$\begin{Bmatrix} \chi_y^1 \\ \chi_{xy}^1 \\ \chi_{yz}^1 \\ \chi_{xz}^1 \end{Bmatrix} = \begin{Bmatrix} -\frac{1}{R} \psi_{y,y} \\ -\frac{1}{R} \psi_{x,y} \\ 3k(\psi_y + w_{,y}) \\ 3k(\psi_x + w_{,x}) \end{Bmatrix}$$

(B.10)

$$\begin{Bmatrix} \chi_{x^2}^2 \\ \chi_{y^2}^2 \\ \chi_{xy}^2 \end{Bmatrix} = \begin{Bmatrix} k(\psi_{x,x} + w_{,xx}) \\ k(\psi_{y,y} + w_{,yy}) \\ k(\psi_{x,y} + \psi_{y,x} + 2w_{,xy}) \end{Bmatrix}$$

$$\begin{Bmatrix} \chi_y^3 \\ \chi_{xy}^3 \end{Bmatrix} = \begin{Bmatrix} -\frac{1}{R} k(\psi_{y,y} + w_{,yy}) \\ -\frac{1}{R} k(\psi_{x,y} + w_{,xy}) \end{Bmatrix}$$

## Appendix C: Variational Formulation

Both STAGS and SHELL are energy based finite element programs dependent upon variational formulation. The following presentation of this formulation is given for better understanding.

For the static case where the motion of the system can be ignored, the total potential energy of a system,  $\Pi_p$ , can be given as:

$$\Pi_p = U - W \quad (C.1)$$

where  $U$  is the internal strain energy of the system and  $W$  is the external work due to applied forces. For a conservative system, the change in total potential energy is independent of path [27]. The equations of equilibrium can then be derived from the first variation of total potential energy [27]. In equation form, the principle of virtual work is:

$$\delta \Pi_p = \delta U - \delta W = 0 \quad (C.2)$$

The expression for the internal strain energy is [26]:

$$U = \int_V (\epsilon)^T [D] (\epsilon) dV \quad (C.3)$$

where  $(\epsilon)$  is the strain vector for the body and  $[D]$  is the material matrix. Taking the variation of Eqn (C.3) results in:

$$\delta U = \frac{1}{2} \int_V \delta(\epsilon)^T [D] (\epsilon) dV + \frac{1}{2} \int_V (\epsilon)^T [D] \delta(\epsilon) dV \quad (C.4)$$

or alternatively by taking the transpose of the last expression in Eqn (C.4) and adding it to the remaining term results in:

$$\delta U = \int_V \delta(\epsilon)^T [D] (\epsilon) dV = \int_V \delta(\epsilon)^T (\sigma) dV \quad (C.5)$$

Now one defines the differential operator,  $[L]$ , which acts on the general displacements,  $(u)$ , to get [28]:

$$(\epsilon) = [L](u) \quad (C.6)$$

Next one can define the shape functions,  $[N]$ , to describe the general displacements in terms of nodal displacements (parameters),  $(a)$ , of the element where:

$$(u) = [N](a) \quad (C.7)$$

If one substitutes Eqn (C.7) into Eqn (C.6) the results give:

$$(\epsilon) = [L][N](a) \quad (C.8)$$

Or alternatively, defining a matrix [B] such that [28]:

$$[B] = [L][N] \quad (C.9)$$

Then Eqn (C.8) can be written as:

$$(\epsilon) = [B](a) \quad (C.10)$$

Finally, one can take the variation of Eqn (C.10), transpose it, and substitute it into Eqn (C.5) resulting in:

$$\delta U = \delta(a)^T \int_V [B]^T(\sigma) dV \quad (C.11)$$

In order to get the full expression for the variation of the potential energy, assume that the work term has been defined in terms of nodal displacements, (a), and forces, (f), such that:

$$W = (a)^T(f) \quad (C.12)$$

Taking the variation of Eqn (C.12), combining it with Eqn

(C.11),, and substituting these equations into Eqn (C.2) results in:

$$\delta \Pi_p = \delta(a)^T \left\{ \int_V [B]^T(\sigma) dV - (f) \right\} = 0 \quad (C.13)$$

Finally, defining a term,  $(\Psi)$ , which represents the sum of the external and internal forces (inside braces, Eqn (C.13)) [28]:

$$(\Psi) = \int_V [B]^T(\sigma) dV - (f) = 0 \quad (C.14)$$

or alternatively after integration,

$$(\Psi) = [K](a) - (f) = 0 \quad (C.15)$$

where  $[K]$  is the stiffness matrix.



## Appendix D: Classical Laminated Plate Theory

The shells analyzed in this thesis are made of composite materials. STAGSC-1, the computer program used in the analysis, uses flat plates to model a shell surface. Because of this, a review of composite plate theory is presented.

To start the formulation, a few of the classical laminated plate assumptions need to be made. The laminate is assumed to consist of perfectly bonded plies where this bond is assumed infinitesimally thin and does not allow shear deformation within itself (i.e. the displacements between plies is continuous; no slip between plies) [45]. Also, the laminate is thin so that the in-plane displacements,  $u$  and  $v$ , as well as the normal displacement,  $w$ , are functions of only two in-plane space variables ( $x$  and  $y$ ) [27]. A plane stress assumption is assumed to where  $\epsilon_z$ ,  $\gamma_{xz}$ ,  $\gamma_{yz}$ , and  $\sigma_z$  are assumed to equal zero. Finally, out of plane strains are due to curvatures as in the Kirchhoff hypothesis for plates.

Fig D.1 shows the coordinate system, the associated displacements, and the force and moment resultants ( $N_x$ ,  $M_x$ , etc. respectively) on the laminate [45]. The  $x$ - $y$  plane of Fig D.1 coincides with the reference axis. From these assumptions, a general expression can be written for the

strains in the laminate using the Kirchhoff hypothesis as (see Appendix A, Eqn (A.12)):

$$\begin{Bmatrix} \epsilon_x \\ \epsilon_y \\ \gamma_{xy} \end{Bmatrix} = \begin{Bmatrix} \epsilon_x^o \\ \epsilon_y^o \\ \gamma_{xy}^o \end{Bmatrix} - z \begin{Bmatrix} \chi_x \\ \chi_y \\ \chi_{xy} \end{Bmatrix} \quad (D.1)$$

where  $\epsilon_x^o$ ,  $\epsilon_y^o$ , and  $\gamma_{xy}^o$  represent in-plane strains and the terms  $\chi_x$ ,  $\chi_y$ , and  $\chi_{xy}$  are curvatures. The curvature terms are defined as:

$$\begin{Bmatrix} \chi_x \\ \chi_y \\ \chi_{xy} \end{Bmatrix} = \begin{Bmatrix} w_{,xx} \\ w_{,yy} \\ 2w_{,xy} \end{Bmatrix} \quad (D.2)$$

The kinematic relations for the laminate (Eqn (D.1)) can be substituted into the constitutive equation for the laminate resulting in [45]:

$$\begin{Bmatrix} \sigma_x \\ \sigma_y \\ \tau_{xy} \end{Bmatrix} = \begin{bmatrix} \bar{Q}_{11} & \bar{Q}_{12} & \bar{Q}_{16} \\ \bar{Q}_{12} & \bar{Q}_{22} & \bar{Q}_{26} \\ \bar{Q}_{16} & \bar{Q}_{26} & \bar{Q}_{66} \end{bmatrix}_k \left\{ \begin{Bmatrix} \epsilon_x^o \\ \epsilon_y^o \\ \gamma_{xy}^o \end{Bmatrix} - z \begin{Bmatrix} \chi_x \\ \chi_y \\ \chi_{xy} \end{Bmatrix} \right\} \quad (D.3)$$

where the subscript k refers to the ply layer and the  $\bar{Q}$  (transformed reduced stiffnesses) quantities are defined as follows [45]:

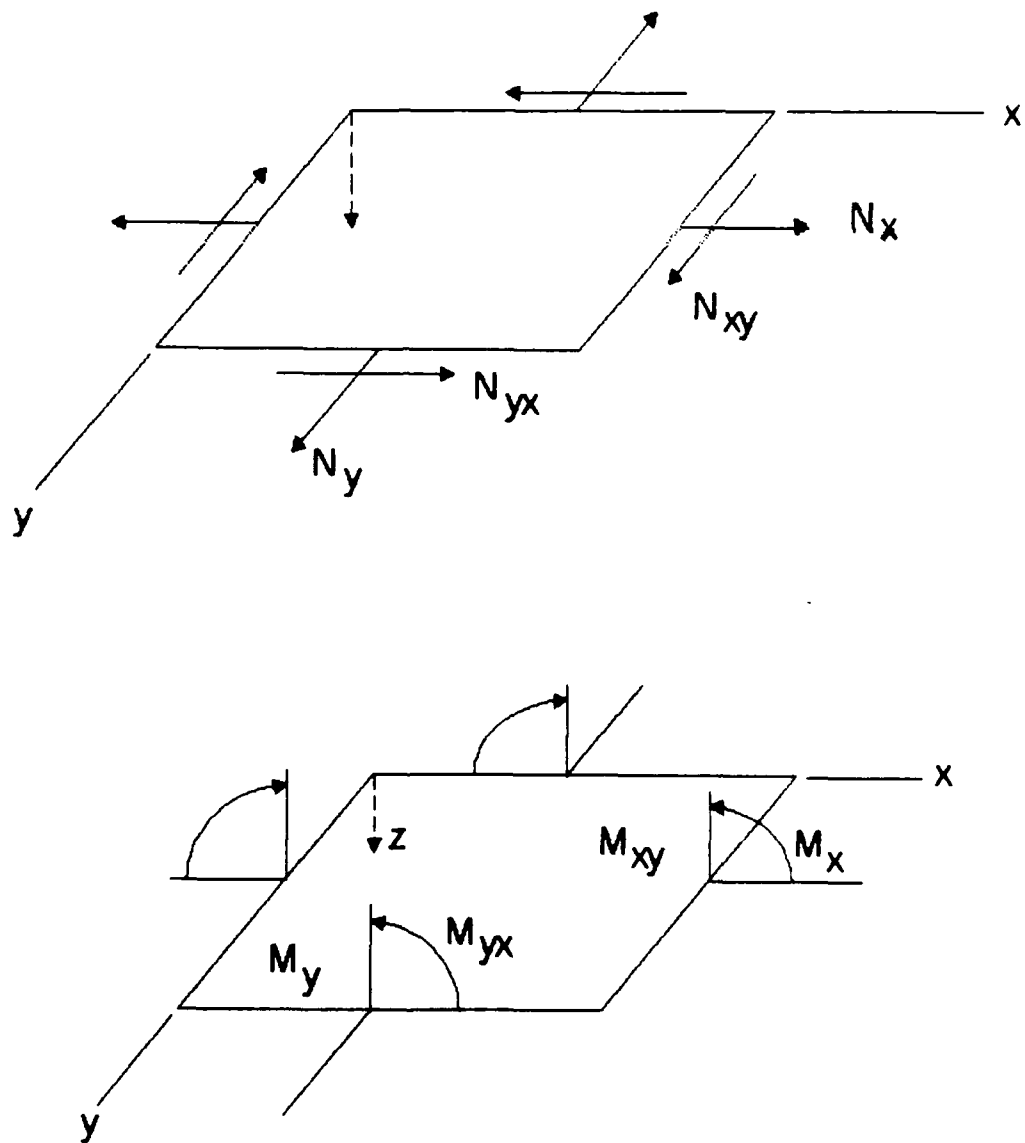


Fig D.1 Coordinate System, Displacements, and Force and Moment Resultants

$$\begin{aligned}
\bar{Q}_{11} &= Q_{11} \cos^4 \theta + 2(Q_{12} + Q_{66}) \sin^2 \theta \cos^2 \theta + Q_{22} \sin^4 \theta \\
\bar{Q}_{12} &= (Q_{11} + Q_{22} + 4Q_{66}) \sin^2 \theta \cos^2 \theta + Q_{12} (\sin^4 \theta + \cos^4 \theta) \\
\bar{Q}_{22} &= Q_{11} \sin^4 \theta + 2(Q_{12} + Q_{66}) \sin^2 \theta \cos^2 \theta + Q_{22} \cos^4 \theta \\
\bar{Q}_{16} &= (Q_{11} - Q_{12} - 2Q_{66}) \sin \theta \cos^3 \theta \\
&\quad + (Q_{12} - Q_{22} + Q_{66}) \sin^3 \theta \cos \theta \\
\bar{Q}_{26} &= (Q_{11} - Q_{12} - 2Q_{66}) \sin^3 \theta \cos \theta \\
&\quad + (Q_{12} - Q_{22} + Q_{66}) \sin \theta \cos^3 \theta \\
\bar{Q}_{66} &= (Q_{11} - Q_{22} - 2Q_{66} - 4Q_{66}) \sin^2 \theta \cos^2 \theta \\
&\quad + Q_{66} (\sin^4 \theta + \cos^4 \theta)
\end{aligned} \tag{D.4}$$

The  $Q$  terms (reduced stiffnesses) in Eqn (D.4) are functions of the material properties as follows [45]:

$$\begin{aligned}
Q_{11} &= \frac{E_1}{1 - \nu_{12} \nu_{21}} \\
Q_{12} &= \frac{\nu_{12} E_2}{1 - \nu_{12} \nu_{21}} = \frac{\nu_{21} E_1}{1 - \nu_{12} \nu_{21}} \\
Q_{22} &= \frac{E_2}{1 - \nu_{12} \nu_{21}} \\
Q_{66} &= G_{12}
\end{aligned} \tag{D.5}$$

The angle  $\theta$  in Eqn (D.4) is the angle between the principle axis ( $x, y, z$ ) and the material axis (1,2,3) as in Fig D.2.

The force and moment resultants (forces and moments per unit length) acting on a composite plate can be found by

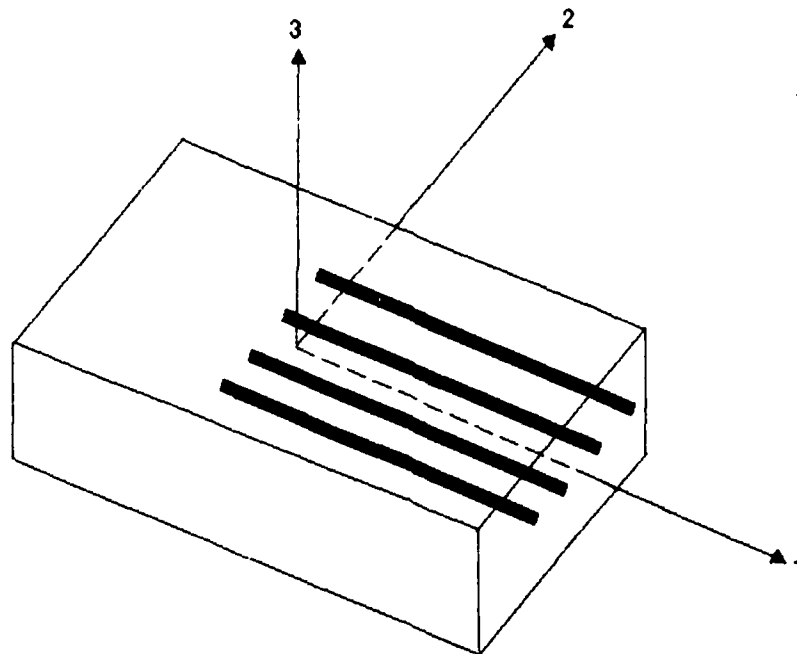
integrating the stresses in each ply through the plate thickness, for example [45]:

$$N_x = \int_{-t/2}^{t/2} \sigma_x dz \quad (D.6)$$

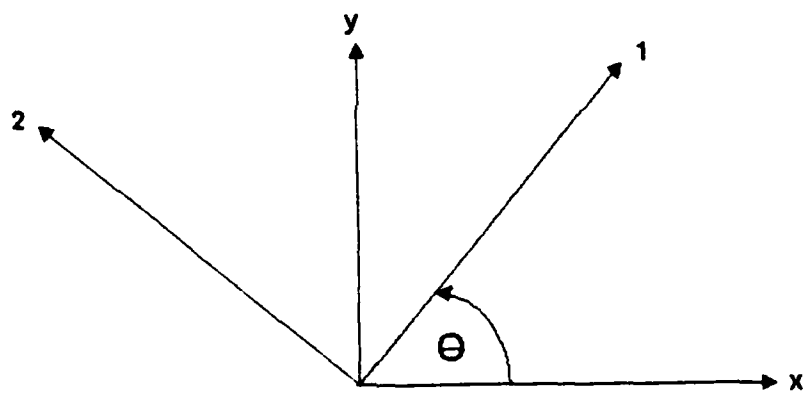
$$M_x = \int_{-t/2}^{t/2} \sigma_x z dz$$

These force and moment resultants are shown in Fig D.1. All of the force and moment resultants are put in vector form for an N-layered laminate and the results are [45]:

$$\begin{Bmatrix} N_x \\ N_y \\ N_{xy} \end{Bmatrix} = \int_{-t/2}^{t/2} \begin{Bmatrix} \sigma_x \\ \sigma_y \\ \tau_{xy} \end{Bmatrix} dz = \sum_{k=1}^N \int_{z_{k-1}}^{z_k} \begin{Bmatrix} \sigma_x \\ \sigma_y \\ \tau_{xy} \end{Bmatrix} dz \quad (D.7)$$



(a)



(b)

(a) Fiber (1 - 2) Axis System (b) Transformation into Structural Axis System

Figure D.2 Principal ( $x, y, z$ ) and Material (1, 2, 3) Axis Systems

and,

$$\begin{Bmatrix} M_x \\ M_y \\ M_{xy} \end{Bmatrix} = \int_{-t/2}^{t/2} \begin{Bmatrix} \sigma_x \\ \sigma_y \\ \tau_{xy} \end{Bmatrix} z \, dz = \sum_{k=1}^N \int_{z_{k-1}}^{z_k} \begin{Bmatrix} \sigma_x \\ \sigma_y \\ \tau_{xy} \end{Bmatrix} z \, dz \quad (D.8)$$

where  $z_k$  and  $z_{k-1}$  are defined in Fig D.3.

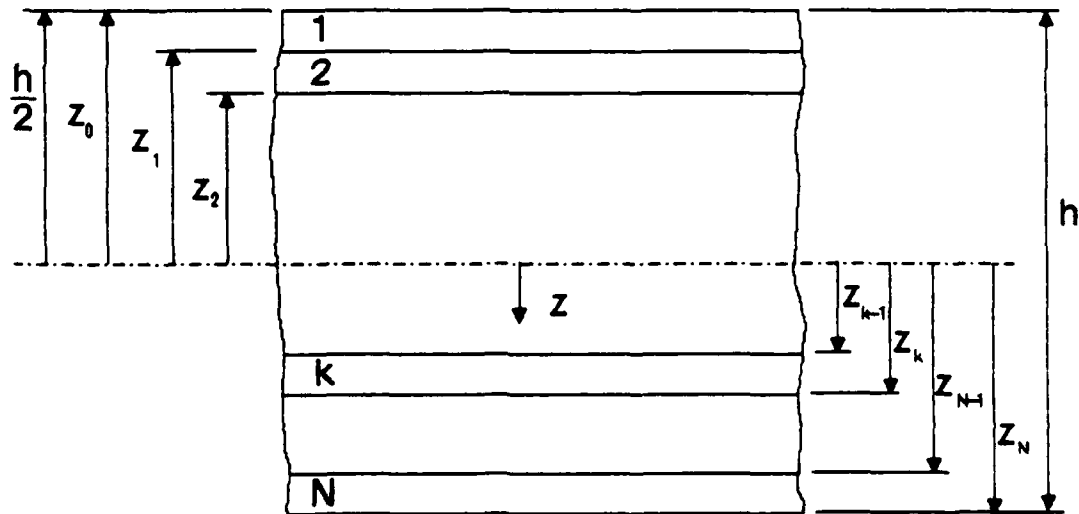


Figure D.3 Geometry of an N-Layered Laminate [45]

Substituting Eqn (D.3) into Eqns (D.7) and (D.8)

yields:

$$\begin{Bmatrix} N_x \\ N_y \\ N_{xy} \end{Bmatrix} = \sum_{k=1}^N \begin{bmatrix} \bar{Q}_{11} & \bar{Q}_{12} & \bar{Q}_{12} \\ \bar{Q}_{12} & \bar{Q}_{22} & \bar{Q}_{26} \\ \bar{Q}_{16} & \bar{Q}_{26} & \bar{Q}_{66} \end{bmatrix}_k \left\{ \int_{z_{k-1}}^k \begin{Bmatrix} \epsilon_x^o \\ \epsilon_y^o \\ \gamma_{xy}^o \end{Bmatrix} dz - \int_{z_{k-1}}^k \begin{Bmatrix} \chi_x \\ \chi_y \\ \chi_{xy} \end{Bmatrix} z dz \right\} \quad (D.9)$$

$$\begin{Bmatrix} N_x \\ N_y \\ N_{xy} \end{Bmatrix} = \sum_{k=1}^N \begin{bmatrix} \bar{Q}_{11} & \bar{Q}_{12} & \bar{Q}_{12} \\ \bar{Q}_{12} & \bar{Q}_{22} & \bar{Q}_{26} \\ \bar{Q}_{16} & \bar{Q}_{26} & \bar{Q}_{66} \end{bmatrix}_k \left\{ \int_{z_{k-1}}^k \begin{Bmatrix} \epsilon_x^o \\ \epsilon_y^o \\ \gamma_{xy}^o \end{Bmatrix} dz - \int_{z_{k-1}}^k \begin{Bmatrix} \chi_x \\ \chi_y \\ \chi_{xy} \end{Bmatrix} z dz \right\}$$

The stiffness matrix  $[\bar{Q}]$  has been removed from the integrals in Eqn (D.9) because it is constant within a lamina but must be included within the summation of force and moment resultants for each ply [45]. Since strain and curvature terms in Eqn (D.9) are not functions of  $z$  but are mid-plane values, they can be removed from the integration and summation signs [45]. After integrating the remaining terms, the results are [45]:

$$\begin{Bmatrix} N_x \\ N_y \\ N_{xy} \\ M_x \\ M_y \\ M_{xy} \end{Bmatrix} = \begin{bmatrix} [A] & [B] \\ [B] & [D] \end{bmatrix} \begin{Bmatrix} \epsilon_x^o \\ \epsilon_y^o \\ \gamma_{xy}^o \\ \chi_x \\ \chi_y \\ \chi_{xy} \end{Bmatrix} \quad (D.10)$$



where,

$$\begin{aligned}A_{ij} &= \sum_{k=1}^N (\bar{a}_{ij})_k (z_k - z_{k-1}) \\B_{ij} &= \frac{1}{2} \sum_{k=1}^N (\bar{a}_{ij})_k (z_k^2 - z_{k-1}^2) \\D_{ij} &= \frac{1}{3} \sum_{k=1}^N (\bar{a}_{ij})_k (z_k^3 - z_{k-1}^3)\end{aligned}\tag{D.11}$$

## Appendix E: Anisotropic Cylindrical Shell

### Theory Including Through the Thickness

#### Shear Strain

Lamination theory incorporates constitutive relationships for orthotropic lamina through the shell panel thickness resulting in expressions which approximate force resultants in terms of displacement functions. This theory provides concepts which are required in the subsequent development of the equations of motion and boundary conditions. The constitutive relationships are developed for the basic lamina and then to the end result, the structural laminate. The end results of this section are the laminate stiffness terms and force resultants. The following derivation is based upon Appendix B and [25] for simplicity.

The plane stress constitutive relationships for a single orthotropic layer in the principle coordinate system shown in Fig E.1 are [45]:

$$\begin{aligned} \begin{Bmatrix} \epsilon_x \\ \epsilon_y \\ \gamma_{xy} \end{Bmatrix} &= \begin{bmatrix} S_{11} & S_{12} & 0 \\ S_{12} & S_{22} & 0 \\ 0 & 0 & S_{66} \end{bmatrix} \begin{Bmatrix} \sigma_x \\ \sigma_y \\ \tau_{xy} \end{Bmatrix} \\ \begin{Bmatrix} \gamma_{yz} \\ \gamma_{xz} \end{Bmatrix} &= \begin{bmatrix} S_{44} & 0 \\ 0 & S_{55} \end{bmatrix} \begin{Bmatrix} \tau_{yz} \\ \tau_{xz} \end{Bmatrix} \end{aligned} \quad (E.1)$$

Note that  $\sigma_z = 0$  for plane stress. That is, the individual lamina are considered thin enough that the average of  $\sigma_z$

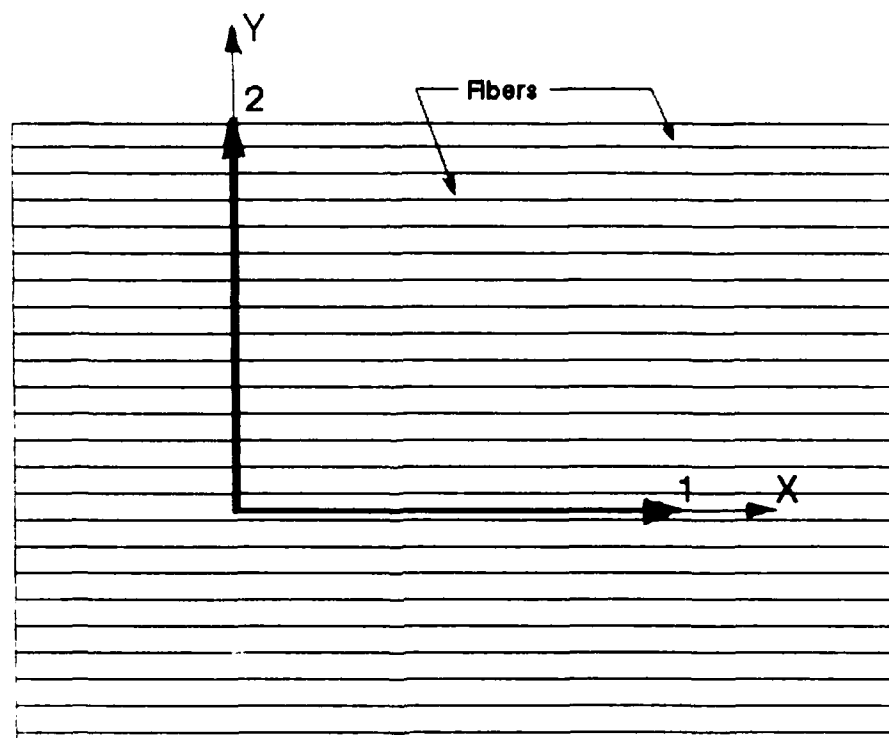


Figure E.1 Lamina Material Coordinates

across the thickness is negligible. The  $S_{ij}$  terms are compliance terms and may be written in terms of the lamina engineering constants as [45]:

$$\begin{aligned}
 S_{11} &= \frac{1}{E_1} \\
 S_{12} &= -\frac{\nu_{12}}{E_2} \\
 S_{22} &= \frac{1}{E_2} \\
 S_{66} &= \frac{1}{G_{12}} \\
 S_{44} &= \frac{1}{G_{23}} \\
 S_{55} &= \frac{1}{G_{13}}
 \end{aligned}
 \tag{E.2}$$

where  $E_i$  are Young's moduli in the  $i_{th}$  direction,  $\nu_{ij}$  is Poisson's ratio for transverse strain in the  $j_{th}$  direction when stressed in the  $i_{th}$  direction, and  $G_{ij}$  is the shear modulus in the  $i$ - $j$  plane.

Eqn (E.1) may be inverted to give the relationships of the stresses in terms of the strains [45]:

$$\begin{Bmatrix} \sigma_x \\ \sigma_y \\ \tau_{xy} \end{Bmatrix} = \begin{bmatrix} Q_{11} & Q_{12} & 0 \\ Q_{12} & Q_{22} & 0 \\ 0 & 0 & Q_{66} \end{bmatrix} \begin{Bmatrix} \epsilon_x \\ \epsilon_y \\ \gamma_{xy} \end{Bmatrix} \quad (E.3)$$

$$\begin{Bmatrix} \tau_{yz} \\ \tau_{xz} \end{Bmatrix} = \begin{bmatrix} Q_{44} & 0 \\ 0 & Q_{55} \end{bmatrix} \begin{Bmatrix} \gamma_{yz} \\ \gamma_{xz} \end{Bmatrix}$$

where  $Q_{ij}$  are the reduced stiffness terms and are defined as [45]:

$$\begin{aligned} Q_{11} &= \frac{E_1}{1 - \nu_{12}\nu_{21}} \\ Q_{12} &= \frac{\nu_{12}E_2}{1 - \nu_{12}\nu_{21}} = \frac{\nu_{21}E_1}{1 - \nu_{12}\nu_{21}} \\ Q_{22} &= \frac{E_2}{1 - \nu_{12}\nu_{21}} \\ Q_{66} &= G_{12} \\ Q_{44} &= G_{23} \\ Q_{55} &= G_{31} \end{aligned} \quad (E.4)$$

A structural laminate consists of N lamina oriented at different angles with respect to each other. The previous constitutive relations apply only to Fig E.1 where the lamina-fixed 1-2 axis system is aligned with the laminate (or global) x-y axis system. If the 1-2 axis system is not aligned with the x-y axis system but rather is at an angle  $\theta$  (see Fig E.2), the reduced stiffness matrix,  $[Q_{ij}]$ , must

be transformed. The transformation matrices applied to the stiffness terms in Eqn (E.3) to reflect the shift in the lamina axes are defined below [45]:

$$\begin{aligned} \text{For } \begin{bmatrix} Q_{11} & Q_{12} & 0 \\ Q_{12} & Q_{22} & 0 \\ 0 & 0 & Q_{66} \end{bmatrix}, \quad T &= \begin{bmatrix} c^2 & s^2 & -2cs \\ s^2 & c^2 & 2cs \\ cs & -cs & c^2 - s^2 \end{bmatrix} \\ \text{For } \begin{bmatrix} Q_{44} & 0 \\ 0 & Q_{55} \end{bmatrix}, \quad T &= \begin{bmatrix} c & -s \\ s & c \end{bmatrix} \end{aligned} \quad (\text{E.5})$$

where  $c = \cos(\theta)$  and  $s = \sin(\theta)$ . The transformed stiffness matrices become [45]:

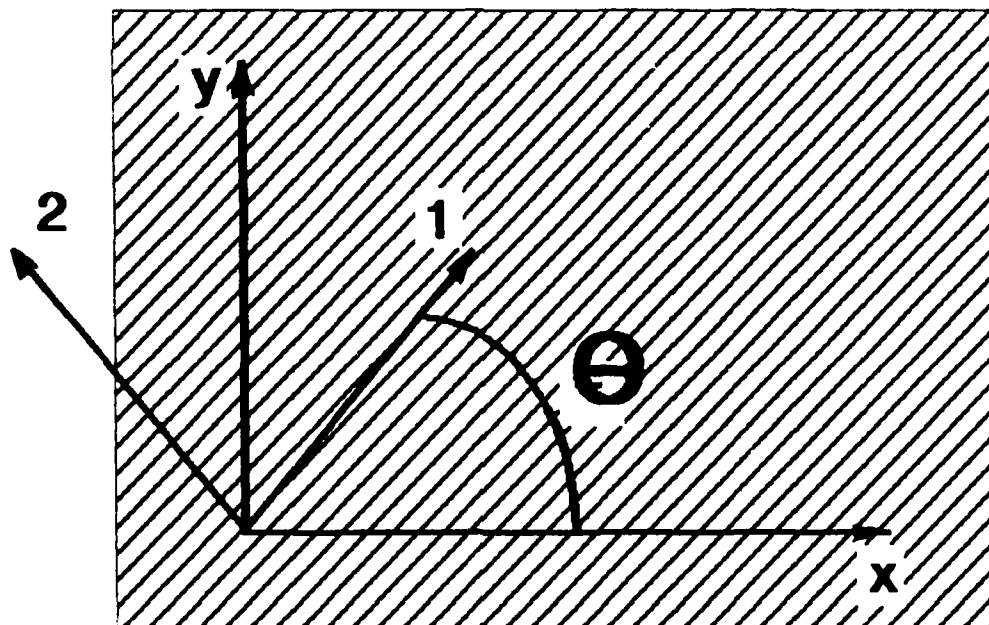


Fig E.2 Arbitrary Lamina Coordinates

$$\begin{bmatrix} \bar{Q}_{ij} \end{bmatrix} = \begin{bmatrix} T \end{bmatrix} \begin{bmatrix} Q_{ij} \end{bmatrix} \begin{bmatrix} T \end{bmatrix}^T \quad (E.6)$$

From [37], the lamina constitutive relationships can now be expressed in laminate coordinates as:

$$\begin{aligned} \begin{Bmatrix} \sigma_x \\ \sigma_y \\ \tau_{xy} \end{Bmatrix}_k &= \begin{bmatrix} \bar{Q}_{11} & \bar{Q}_{12} & \bar{Q}_{16} \\ \bar{Q}_{12} & \bar{Q}_{22} & \bar{Q}_{26} \\ \bar{Q}_{16} & \bar{Q}_{26} & \bar{Q}_{66} \end{bmatrix}_k \begin{Bmatrix} \epsilon_x \\ \epsilon_y \\ \gamma_{xy} \end{Bmatrix} \\ \begin{Bmatrix} \tau_{yz} \\ \tau_{xz} \end{Bmatrix}_k &= \begin{bmatrix} \bar{Q}_{44} & \bar{Q}_{45} \\ \bar{Q}_{45} & \bar{Q}_{55} \end{bmatrix}_k \begin{Bmatrix} \gamma_{yz} \\ \gamma_{xz} \end{Bmatrix} \end{aligned} \quad (E.7)$$

where  $k$  denotes the  $k_{th}$  lamina and the individual  $\bar{Q}_{ij}$  are computed as [45]:

$$\begin{aligned} \bar{Q}_{11} &= Q_{11} \cos^4 \theta + 2(Q_{12} + 2Q_{66}) \sin^2 \theta \cos^2 \theta + Q_{22} \sin^4 \theta \\ \bar{Q}_{12} &= (Q_{11} + Q_{22} - 4Q_{66}) \sin^2 \theta \cos^2 \theta + Q_{12} (\sin^4 \theta + \cos^4 \theta) \\ \bar{Q}_{22} &= Q_{11} \sin^4 \theta + 2(Q_{12} + 2Q_{66}) \sin^2 \theta \cos^2 \theta + Q_{22} \cos^4 \theta \\ \bar{Q}_{16} &= (Q_{11} - Q_{12} - 2Q_{66}) \sin \theta \cos^3 \theta \\ &\quad + (Q_{12} - Q_{22} + 2Q_{66}) \sin^3 \theta \cos \theta \\ \bar{Q}_{26} &= (Q_{11} - Q_{12} - 2Q_{66}) \sin^3 \theta \cos \theta \\ &\quad + (Q_{12} - Q_{22} + 2Q_{66}) \sin \theta \cos^3 \theta \\ \bar{Q}_{66} &= (Q_{11} + Q_{22} - 2Q_{12} - 2Q_{66}) \sin^2 \theta \cos^2 \theta \\ &\quad + Q_{66} (\sin^4 \theta + \cos^4 \theta) \\ \bar{Q}_{44} &= Q_{44} \cos^4 \theta + Q_{55} \sin^4 \theta \\ \bar{Q}_{45} &= (Q_{44} - Q_{55}) \cos \theta \sin \theta \\ \bar{Q}_{55} &= Q_{44} \sin^4 \theta + Q_{55} \cos^4 \theta \end{aligned} \quad (E.8)$$

Finally, as an example, we can substitute in the expressions for the strains in Appendix B, Eqn (B.8) into the the constitutive relations in Eqn (E.7). The stress in the  $k_{th}$  lamina of the structural laminate is expressed as [45]:

$$\begin{aligned} \begin{Bmatrix} \sigma_x \\ \sigma_y \\ \tau_{xy} \end{Bmatrix}_k &= \begin{bmatrix} \bar{Q}_{11} & \bar{Q}_{12} & \bar{Q}_{16} \\ \bar{Q}_{12} & \bar{Q}_{22} & \bar{Q}_{26} \\ \bar{Q}_{16} & \bar{Q}_{26} & \bar{Q}_{66} \end{bmatrix}_k \left( \begin{Bmatrix} \epsilon_x^0 \\ \epsilon_y^0 \\ \gamma_{xy}^0 \end{Bmatrix} + z \begin{Bmatrix} \chi_x^0 \\ \chi_y^0 \\ \chi_{xy}^0 \end{Bmatrix} + z^2 \begin{Bmatrix} 0 \\ \chi_y^1 \\ \chi_{xy}^1 \end{Bmatrix} \right. \\ &\quad \left. + z^3 \begin{Bmatrix} \chi_x^2 \\ \chi_y^2 \\ \chi_{xy}^2 \end{Bmatrix} + z^4 \begin{Bmatrix} 0 \\ \chi_y^3 \\ \chi_{xy}^3 \end{Bmatrix} \right) \quad (E.9) \\ \begin{Bmatrix} \tau_{yz} \\ \tau_{xz} \end{Bmatrix}_k &= \begin{bmatrix} \bar{Q}_{44} & \bar{Q}_{45} \\ \bar{Q}_{45} & \bar{Q}_{55} \end{bmatrix}_k \left( \begin{Bmatrix} \gamma_{yz}^0 \\ \gamma_{xz}^0 \end{Bmatrix} + z^2 \begin{Bmatrix} \chi_{yz}^1 \\ \chi_{xz}^1 \end{Bmatrix} \right) \end{aligned}$$

The resultant forces and moments and the higher order resultant quantities acting on the laminate are obtained by integrating the stresses in each lamina through the laminate thickness. Thus, for a laminate with N lamina shown in Fig E.3. The resultant forces and moments and higher order quantities are:



$$\begin{aligned}
\begin{Bmatrix} N_1 \\ N_2 \\ N_6 \end{Bmatrix}, \begin{Bmatrix} M_1 \\ M_2 \\ M_6 \end{Bmatrix}, \begin{Bmatrix} S_1 \\ S_2 \\ S_6 \end{Bmatrix}, \begin{Bmatrix} P_1 \\ P_2 \\ P_6 \end{Bmatrix}, \begin{Bmatrix} L_1 \\ L_2 \\ L_6 \end{Bmatrix} &= \int_{-h/2}^{h/2} \begin{Bmatrix} \sigma_x \\ \sigma_y \\ \tau_{xy} \end{Bmatrix} (1, z, z^2, z^3, z^4) dz \\
&= \sum_{k=1}^N \int_{z_{k-1}}^{z_k} \begin{Bmatrix} \sigma_x \\ \sigma_y \\ \tau_{xy} \end{Bmatrix} (1, z, z^2, z^3, z^4) dz \quad (E.10) \\
\begin{Bmatrix} Q_2 \\ Q_1 \end{Bmatrix}, \begin{Bmatrix} R_2 \\ R_1 \end{Bmatrix} &= \int_{-h/2}^{h/2} \begin{Bmatrix} \tau_{yz} \\ \tau_{xz} \end{Bmatrix} (1, z^2) dz = \sum_{k=1}^N \int_{z_{k-1}}^{z_k} \begin{Bmatrix} \tau_{yz} \\ \tau_{xz} \end{Bmatrix} (1, z^2) dz
\end{aligned}$$

where  $\{N_i\}$  and  $\{Q_i\}$  are the resultant forces,  $\{M_i\}$  are the resultant moments, and  $\{S_i\}$ ,  $\{P_i\}$ ,  $\{L_i\}$ , and  $\{R_i\}$  are the higher order quantities resulting from the higher order strain displacement relations.

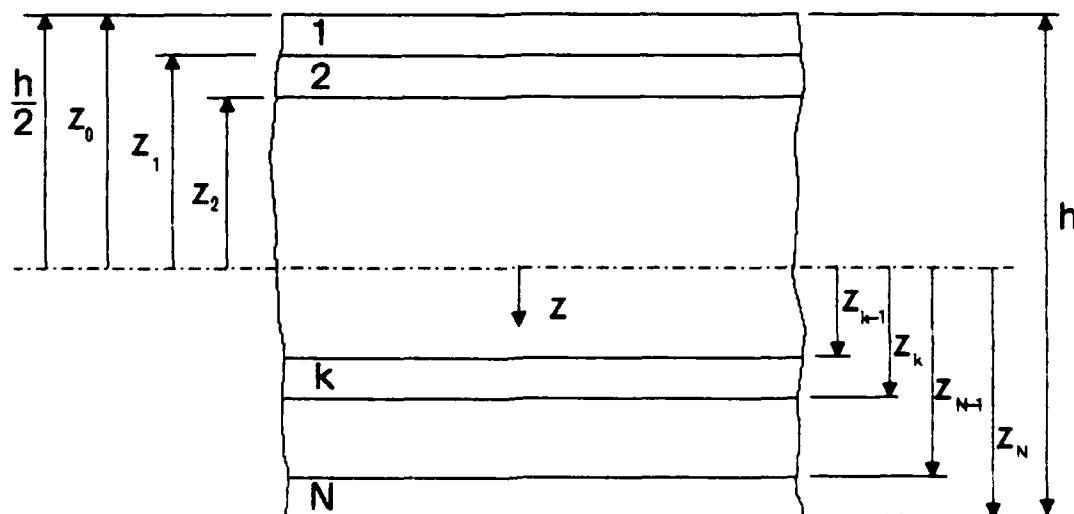


Fig E.3 Geometry of an N-Layered Laminate [45]

By substituting Eqn (E.9) into Eqn (E.10), thereby expressing the stresses in terms of the mid-surface displacement quantities and the transformed reduced stiffness matrices, the integration is simplified because the mid-surface values are independent of  $z$  and can come out of the integral and summation signs [45]. This allows the following notation to be adopted for the integrated laminate stiffness matrices:

$$(A_{ij}, B_{ij}, D_{ij}, E_{ij}, F_{ij}, G_{ij}, H_{ij}, I_{ij}, J_{ij}) = \quad (E.11a)$$

$$\sum_{k=1}^N \begin{bmatrix} \bar{Q}_{11} & \bar{Q}_{12} & \bar{Q}_{16} \\ \bar{Q}_{12} & \bar{Q}_{22} & \bar{Q}_{26} \\ \bar{Q}_{16} & \bar{Q}_{26} & \bar{Q}_{66} \end{bmatrix}_k \int_{z_{k-1}}^{z_k} (1, z, z^2, z^3, z^4, z^5, z^6, z^7, z^8) dz$$

$$i, j = 1, 2, 6$$

For the transverse shear:

$$(A_{ij}, D_{ij}, F_{ij}) = \sum_{k=1}^N \begin{bmatrix} \bar{Q}_{44} & \bar{Q}_{45} \\ \bar{Q}_{45} & \bar{Q}_{55} \end{bmatrix}_k \int_{z_{k-1}}^{z_k} (1, z^2, z^4) dz \quad (E.11b)$$

$$i, j = 4, 5$$

Now, Eqn (E.10) may be written as:

$$\begin{Bmatrix} N_1 \\ N_2 \\ N_6 \end{Bmatrix} \quad \begin{Bmatrix} M_1 \\ M_2 \\ M_6 \end{Bmatrix} \quad \begin{Bmatrix} S_1 \\ S_2 \\ S_6 \end{Bmatrix} \quad \begin{Bmatrix} P_1 \\ P_2 \\ P_6 \end{Bmatrix} \quad \begin{Bmatrix} L_1 \\ L_2 \\ L_6 \end{Bmatrix} = \begin{bmatrix} [A_{ij}] & [B_{ij}] & [D_{ij}] & [E_{ij}] & [F_{ij}] \\ [B_{ij}] & [D_{ij}] & [E_{ij}] & [F_{ij}] & [G_{ij}] \\ [D_{ij}] & [E_{ij}] & [F_{ij}] & [G_{ij}] & [H_{ij}] \\ [E_{ij}] & [F_{ij}] & [G_{ij}] & [H_{ij}] & [I_{ij}] \\ [F_{ij}] & [G_{ij}] & [H_{ij}] & [I_{ij}] & [J_{ij}] \end{bmatrix} \begin{Bmatrix} \epsilon_x^0 \\ \epsilon_y^0 \\ \gamma_{xy}^0 \end{Bmatrix} \quad \begin{Bmatrix} x_x^0 \\ x_y^0 \\ x_{xy}^0 \end{Bmatrix} \quad \begin{Bmatrix} 0 \\ x_y^1 \\ x_{xy}^1 \end{Bmatrix} \quad \begin{Bmatrix} x_x^2 \\ x_y^2 \\ x_{xy}^2 \end{Bmatrix} \quad \begin{Bmatrix} 0 \\ x_{yz}^3 \\ x_{xy}^3 \end{Bmatrix} \quad (E.12a)$$

$i, j = 1, 2, 6$

$$\begin{Bmatrix} Q_2 \\ Q_1 \end{Bmatrix} = \begin{bmatrix} A_{44} & A_{45} & D_{44} & D_{45} \\ A_{45} & A_{55} & D_{45} & D_{55} \end{bmatrix} \begin{Bmatrix} \gamma_{yz}^0 \\ \gamma_{xz}^0 \end{Bmatrix} \quad (E.12b)$$

$$\begin{Bmatrix} R_2 \\ R_1 \end{Bmatrix} = \begin{bmatrix} D_{44} & D_{45} & A_{44} & A_{45} \\ D_{45} & D_{55} & A_{45} & A_{55} \end{bmatrix} \begin{Bmatrix} x_{yz}^1 \\ x_{xz}^1 \end{Bmatrix}$$

where the large matrix above is (15 x 15) and each of its sub-matrices are the (3 x 3) matrices in Eqns (E.11a) and (E.11b).

## Appendix F: Derivation of the Tangent Stiffness Matrix

The tangent stiffness matrix is a nonlinear stiffness matrix used in the Newton-Raphson (see section 2.2.7) for solving a nonlinear set of equations. There are other techniques for solving these equations, but STAGSC-1 and SHELL uses the Newton-Raphson (or modified Newton-Raphson), and thus the derivation of the tangent stiffness matrix is of interest in this thesis. This appendix derives the tangent stiffness matrix for STAGS only. The tangent stiffness matrix development for SHELL is similar but has more terms and is much more complex. See reference [37] for a more complete derivation of SHELL's stiffness matrix.

The tangent stiffness matrix is derived for a flat plate element, a STAGS type element, in a general way without any reference to any specific shape functions. See reference [43] for the specific shape functions used in STAGS. Although the derivation is conducted in general coordinates, STAGS uses isoparametric coordinates in its nonlinear stiffness matrix formulation.

To start the derivation, a form of the tangent stiffness matrix is found from the energy expression. Consider ( $\Psi$ ), the sum of external and internal generalized forces (Appendix C, Eqn (C.14)), which is given as [28]:

$$(\Psi) = \int_V [B]^T (\sigma) dV - (f) \quad (F.1)$$

where,

$(\sigma)$  = vector of stresses

$(f)$  = nodal forces of the element

and  $[B]$  is defined as the product of the differential operator matrix,  $[L]$ , operating on the element shape functions,  $[N]$ . In an equilibrium state  $(\Psi)$  (Eqn (F.1)) will equal zero. The strain displacement relations can be written (to include the  $[B]$  matrix) as:

$$(\epsilon) = [L][N](a) = [B](a) \quad (F.2)$$

where  $(a)$  is the nodal displacement vector. In the case of a nonlinear stiffness matrix (i.e. tangent stiffness matrix),  $[B]$  is redefined as [28]:

$$[B] = [B_0] + [B_1] \quad (F.3)$$

where,

$[B_0]$  = constant

$[B_1]$  = function of displacements

In order to use the Newton-Raphson method, a relation between  $\delta(a)$  and  $\delta(\Psi)$  must be found. Taking the variation of Eqn (F.1) with respect to  $\delta(a)$  gives the relation needed and is given as [28]:

$$\delta(\Psi) = \int_V \delta[B]^T(\sigma)dV + \int_V [B]^T\delta(\sigma)dV = [K_T]\delta(a) \quad (F.4)$$

where  $[K_T]$  is the tangent stiffness matrix. In this derivation, strain is assumed small therefore the equation,

$$(\sigma) = [D] \left( (\epsilon) - (\epsilon_0) + (\sigma_0) \right) \quad (F.5)$$

still applies, where  $[D]$  is the material matrix and the subscripts indicate initial values of stresses and strains. With Eqns (F.2), (F.3), and (F.5), the variational terms in Eqn (F.4) can be rewritten as:

$$\delta(\sigma) = [D]\delta(\epsilon) = [D][B]\delta(a) \quad (F.6a)$$

and

$$\delta[B]^T = \delta[B_L]^T \quad (F.6b)$$

With Eqns (F.6a) and (F.6b), Eqn (F.4) becomes:

$$\delta(\Psi) = \int_V \delta[B_L]^T(\sigma) dV + \int_V [B]^T [D] [B] dV \delta(a) \quad (F.7)$$

The first term in Eqn (F.7) contains the initial stress matrix,  $[K\sigma]$ , while the last term turns out to be the linear and the nonlinear stiffness matrices,  $[K_0]$  and  $[K_L]$  respectively, after substituting Eqn (F.3) in for  $[B]$  [28]. The three stiffness matrices contained in Eqn (F.7) are:

$$\begin{aligned} [K_0] &= \int_V [B_0]^T [D] [B_0] dV \\ [K_L] &= \int_V \left( [B_0]^T [D] [B_L] + [B_L]^T [D] [B_L] \right. \\ &\quad \left. + [B_L]^T [D] [B_L] \right) dV \\ [K\sigma] \delta(a) &= \int_V \delta[B_L]^T(\sigma) dV \end{aligned} \quad (F.8)$$

The full expression for the tangent stiffness matrix can now be written as:

$$[K_T] = [K_0] + [K_L] + [K\sigma] \quad (F.9)$$

With an expression for the elements contained in the tangent stiffness matrix (Eqn (F.9)), the derivation can now

determine the terms contained in the matrices that make up the tangent stiffness matrix.

The next steps in the derivation include formulating the kinematic relations, introducing the material matrix, and giving the displacement relations. Recalling the strain expression from Appendix A (Eqn (A.12)) written in vector form and rearranged to reflect in-plane and bending strains [28]:

$$(\epsilon) = \begin{Bmatrix} \epsilon_x \\ \epsilon_y \\ \gamma_{xy} \\ -w_{,xx} \\ -w_{,yy} \\ -2w_{,xy} \end{Bmatrix} \quad (F.10)$$

where the distance for the mid-plane,  $z$ , is incorporated in the material matrix (see Appendix D). If Eqn (F.4) is rewritten, separating linear and nonlinear terms due to in-plane and bending strains, the results are [28]:

$$(\epsilon) = \begin{Bmatrix} \epsilon^p \\ \epsilon^b \end{Bmatrix} + \begin{Bmatrix} \epsilon^p_L \\ 0 \end{Bmatrix} + \begin{Bmatrix} \epsilon^b_L \\ 0 \end{Bmatrix} \quad (F.11)$$



where,

$(\epsilon_o^p)$  = linear in-plane strains

$(\epsilon_o^b)$  = linear bending strains

$(\epsilon_L^p)$  = nonlinear in-plane strains in u and v

$(\epsilon_L^b)$  = nonlinear in-plane strains in w

Incorporating the linear constitutive relationship, the material matrix [D], for a composite material (derived in Appendix D), is given as:

$$[D] = \begin{bmatrix} [A] & [B] \\ [B] & [D] \end{bmatrix} \quad (F.12)$$

Since the distance from the mid-plane, z, has been incorporated in this matrix, the integration indicated in Eqn (F.9) for  $[K_o]$ ,  $[K_L]$ , and  $[K_\sigma]$  reduces to an area integral.

Finally, the displacements are defined in terms of nodal displacements using the shape functions for the plate element. If for example, an element similar to the QUAF 410 is considered (see [37]), which has four corner nodes and six degrees of freedom per node, the displacements can be given as:

$$\begin{Bmatrix} u \\ v \\ w \end{Bmatrix} = [N](a_e) \quad (F.13)$$

The vector of element nodal displacements,  $(a_e)$ , can be subdivided into displacements that influence in-plane (superscript p) and bending (superscript b) as [28]:

$$\begin{aligned} (a_i^p) &= \begin{Bmatrix} u_i \\ v_i \\ \beta_i \end{Bmatrix} \\ (a_i^b) &= \begin{Bmatrix} w_i \\ w_{,x_i} \\ w_{,y_i} \end{Bmatrix} \end{aligned} \quad (F.14)$$

where  $\beta$  represents an average rotation about the normal (similar to  $\phi$  in Eqn (A.8)).

In order to proceed further it is necessary to expand the expression for  $[B]$ . From Eqn (F.3) it was shown that [28]:

$$[B] = [B_0] + [B_1] \quad (F.15)$$

where,

$$[B_0] = \begin{bmatrix} [B^p] & 0 \\ (3 \times 12) & \\ 0 & [B^b] \\ & (3 \times 12) \end{bmatrix} \quad (F.16a)$$

and

$$[B_L] = \begin{bmatrix} [B_L^p] & [B_L^b] \\ (3 \times 12) & (3 \times 12) \\ 0 & 0 \end{bmatrix} \quad (F.16b)$$

The matrices  $[B_o^p]$  (linear in-plane) and  $[B_o^b]$  (linear bending) are standard matrices and are derived in reference [28] with the exception that in the derivation  $[B_o^p]$  the normal rotation term,  $\beta$  (Eqn (F.14)), must be included as a degree of freedom at each node. The matrices  $[B_L^p]$  and  $[B_L^b]$  are found by taking a variation of  $(\epsilon_L^p)$  and  $(\epsilon_L^b)$  (Eqn (F.11)) respectively, with respect to the nodal degrees of freedom (a).

In matrix form  $(\epsilon_L^p)$  can be written as:

$$(\epsilon_L^p) = \frac{1}{2} \begin{bmatrix} u_{,x} & 0 & v_{,x} & 0 \\ 0 & u_{,y} & 0 & v_{,y} \\ u_{,y} & u_{,x} & v_{,y} & v_{,x} \end{bmatrix} \begin{Bmatrix} u_{,x} \\ u_{,y} \\ v_{,x} \\ v_{,y} \end{Bmatrix} \quad (F.17)$$

or [28]:

$$(\epsilon_L^p) = \frac{1}{2} [R^p] (\theta^p) \quad (F.18)$$

The vector  $(\theta^p)$  can be related to the in-plane (u and v) nodal degrees of freedom as:

$$(\epsilon^P) = \begin{Bmatrix} u, \\ u, \\ v, \\ v, \end{Bmatrix}_{\begin{smallmatrix} x \\ y \\ x \\ y \end{smallmatrix}} = [G^P]_{(4 \times 12)} (a^P)_{(12 \times 1)} \quad (F.19)$$

where  $[G^P]$  is a matrix of coordinates and  $(a^P)$  is the vector of nodal displacements (Eqn (F.14)). The next step involves taking the variation  $(\epsilon_L^P)$ . To do this Eqn (F.17) is rewritten as:

$$(\epsilon_L^P) = \begin{Bmatrix} 1/2 u,^2 + 1/2 v,^2 \\ 1/2 u,^2 + 1/2 v,^2 \\ u, u, + v, v, \\ u, u, + v, v, \end{Bmatrix}_{\begin{smallmatrix} x \\ y \\ x \\ y \end{smallmatrix}} \quad (F.20)$$

Taking the variation of Eqn (F.20) gives:

$$\delta(\epsilon_L^P) = \begin{Bmatrix} u, \delta u, + v, \delta v, \\ u, \delta u, + v, \delta v, \\ u, \delta u, + u, \delta u, + v, \delta v, + v, \delta v, \\ u, \delta u, + u, \delta u, + v, \delta v, + v, \delta v, \end{Bmatrix}_{\begin{smallmatrix} x \\ y \\ x \\ y \end{smallmatrix}} \quad (F.21)$$

Rewriting yields:

$$\delta(\epsilon_L^P) = \begin{bmatrix} u, & 0 & v, & 0 \\ 0 & u, & 0 & v, \\ u, & u, & v, & v, \\ u, & u, & v, & v, \end{bmatrix}_{\begin{smallmatrix} x \\ y \\ x \\ y \end{smallmatrix}} \delta \begin{Bmatrix} u, \\ u, \\ v, \\ v, \end{Bmatrix}_{\begin{smallmatrix} x \\ y \\ x \\ y \end{smallmatrix}} \quad (F.22)$$

where the first matrix on the right hand side equals  $[R^P]$  (Eqn (F.18)) and the last matrix can be written from Eqn

(F.19) as:

$$\delta \begin{Bmatrix} u, x \\ u, y \\ v, x \\ v, y \end{Bmatrix} = \begin{matrix} [G^P] \\ (4 \times 12) \end{matrix} \delta \begin{matrix} (a^P) \\ (12 \times 1) \end{matrix} \quad (F.23)$$

since  $[G^P]$  is a function of coordinates only.

Using the definition of  $[R^P]$  in Eqn (F.18) along with Eqn (F.23), Eqn (F.22) can be written as:

$$\delta(\epsilon_L^P) = [R^P] [G^P] \delta(a^P) \quad (F.24)$$

From Eqn (F.24) the resulting expression for  $[B_L^P]$  is, by definition,

$$\begin{matrix} [B_L^P] \\ (3 \times 12) \end{matrix} = \begin{matrix} [R^P] \\ (3 \times 4) \end{matrix} \begin{matrix} [G^P] \\ (4 \times 12) \end{matrix} \quad (F.25)$$

Following the same line of reasoning used to find  $[B_L^P]$  from  $(\epsilon_L^P)$ , one can find from:

$$(\epsilon_L^b) = \frac{1}{2} \begin{bmatrix} w, x & 0 \\ 0 & w, y \\ w, y & w, x \end{bmatrix} \begin{Bmatrix} w, x \\ w, y \end{Bmatrix} \quad (F.26)$$

or from [28]:

$$(\epsilon_L^b) = 1/2 [R^b](\theta^b) \quad (F.27)$$

that:

$$\begin{matrix} [B^b] \\ (3 \times 12) \end{matrix} = \begin{matrix} [R^b] & [G^b] \\ (3 \times 2) & (2 \times 12) \end{matrix} \quad (F.28)$$

where  $[G^b]$  is composed of derivatives of the shape functions that are contained in the expression for  $w$ .

With the expressions for  $[B_0]$  and  $[B_1]$  determined (Eqns (F.16a) and (F.16b)), the material matrix defined (Eqn (F.12)), and recalling that the volume integral has been reduced to an area integral (Eqn (F.12)), the expressions for linear and nonlinear stiffness matrices ( $[K_0]$  and  $[K_1]$ ) can be determined. If one uses Eqn (F.8) and, after some manipulation,

$$[K_0]_{(2 \times 24)} = \int_A \begin{bmatrix} [B_0^p]^T [A] [B_0^p] & [B_0^p]^T [B] [B_0^p] \\ [B_0^p]^T [B] [B_0^p] & [B_0^p]^T [D] [B_0^p] \end{bmatrix} dA \quad (F.29)$$

and

$$[K_L]_{(2 \times 24)} = \int_A \begin{bmatrix} [1] & [2] \\ [2] & [3] \end{bmatrix} \quad (F.30)$$

where,

$$[1] = [B_o^p]^T [A] [B_L^p] + [B_L^p]^T [A] [B_L^p] + [B_L^p]^T [A] [B_o^p] \quad (F.31)$$

$$[2] = [B_o^p]^T [A] [B_L^b] + [B_L^p]^T [A] [B_L^b] + [B_L^p]^T [B] [B_o^b] \quad (F.32)$$

$$[3] = [B_o^b]^T [B] [B_L^b] + [B_L^b]^T [A] [B_L^b] + [B_L^b]^T [B] [B_o^b] \quad (F.33)$$

The final expression necessary for the tangent stiffness matrix is the initial stress matrix  $[K\sigma]$ . Recalling Eqn (F.8), rewritten for convenience as:

$$[K\sigma] \delta(a) = \int_V \delta[B_L]^T (\sigma') dV \quad (F.34)$$

The stresses,  $(\sigma')$ , are defined in terms of the in-plane (superscript p) and bending (superscript b) stresses as [28]:

$$(\sigma') = \begin{Bmatrix} N_x & N_y & N_{xy} & M_x & M_y & M_{xy} \end{Bmatrix} = \begin{Bmatrix} \sigma'^p \\ \sigma'^b \end{Bmatrix} \quad (F.35)$$

where the primes on the stresses indicates stress resultants, not true stresses, and the true stress

resultants are given in Appendix D (Eqn (D.6)). The stress resultants are average values over the element. This also implies that integration through the thickness has been completed thereby reducing the integration of Eqn (F.34) to that of an area. Now, define the variation of  $[B_L]^T$  in Eqn (F.34) from Eqn (F.16b) as:

$$\delta[B_L]^T = \begin{bmatrix} \delta[B_L^P] & 0 \\ \delta[B_L^B] & 0 \end{bmatrix} \quad (F.36)$$

Substituting Eqns (F.24) and (F.25) into Eqn (F.36) and then substituting that result, as well as Eqn (F.35), into Eqn (F.34) gives [28]:

$$[K\sigma] \delta(a) = \int_A \begin{bmatrix} [G^P]^T \delta[R^P]^T & 0 \\ [G^B]^T \delta[R^B]^T & 0 \end{bmatrix} \begin{Bmatrix} N_x \\ N_y \\ N_{xy} \\ M_x \\ M_y \\ M_{xy} \end{Bmatrix} \quad (F.37)$$

Expanding Eqn (F.37), rewriting it in terms of in-plane (superscript p) and bending (superscript b) expressions and then expressions results in:



$$[K\sigma^p]_{(12 \times 12)} \delta(a^p)_{(12 \times 1)} = \int_A [G^p]_{(12 \times 4)}^T \delta[R^p]_{(4 \times 3)}^T \begin{Bmatrix} N_x \\ N_y \\ N_{xy} \end{Bmatrix} dA \quad (F.38a)$$

and

$$[K\sigma^b]_{(12 \times 12)} \delta(a^b)_{(12 \times 1)} = \int_A [G^b]_{(12 \times 2)}^T \delta[R^b]_{(2 \times 3)}^T \begin{Bmatrix} N_x \\ N_y \\ N_{xy} \end{Bmatrix} dA \quad (F.38b)$$

The following steps involve finding expressions for  $[K\sigma^b]$  and  $[K\sigma^p]$ .

Starting with Eqn (F.38a) and rewriting the last two matrices on the right hand side using Eqn (F.17) gives:

$$\delta[R^p]^T \begin{Bmatrix} N_x \\ N_y \\ N_{xy} \end{Bmatrix} = \begin{bmatrix} \delta u_{,x} & 0 & \delta u_{,y} \\ 0 & \delta u_{,y} & \delta u_{,x} \\ \delta v_{,x} & 0 & \delta v_{,y} \\ 0 & \delta v_{,y} & \delta v_{,x} \end{bmatrix} \begin{Bmatrix} N_x \\ N_y \\ N_{xy} \end{Bmatrix} \quad (F.39)$$

Expanding the right side of Eqn (F.39) and also taking the variation, recalling that  $N_x$ ,  $N_y$ , and  $N_{xy}$  are constants (Eqn (F.35)), results in:

$$\delta[R^P]^T \begin{Bmatrix} N_x \\ N_y \\ N_{xy} \end{Bmatrix} = \begin{Bmatrix} N_x \delta u_{,x} + N_{xy} \delta u_{,y} \\ N_y \delta v_{,y} + N_{xy} \delta u_{,x} \\ N_x \delta v_{,x} + N_{xy} \delta v_{,y} \\ N_y \delta v_{,y} + N_{xy} \delta v_{,x} \end{Bmatrix} \quad (F.40)$$

Rewriting Eqn (F.40) in matrix form gives:

$$\delta[R^P]^T \begin{Bmatrix} N_x \\ N_y \\ N_{xy} \end{Bmatrix} = \begin{bmatrix} N_x & N_{xy} & 0 & 0 \\ N_y & N_{xy} & 0 & 0 \\ 0 & 0 & N_x & N_{xy} \\ 0 & 0 & N_y & N_{xy} \end{bmatrix} \delta \begin{Bmatrix} u_{,x} \\ u_{,y} \\ v_{,x} \\ v_{,y} \end{Bmatrix} \quad (F.41)$$

Recalling Eqn (F.23) and substituting into Eqn (F.41) gives:

$$\delta[R^P]^T \begin{Bmatrix} N_x \\ N_y \\ N_{xy} \end{Bmatrix} = \begin{bmatrix} N_x & N_{xy} & 0 & 0 \\ N_y & N_{xy} & 0 & 0 \\ 0 & 0 & N_x & N_{xy} \\ 0 & 0 & N_y & N_{xy} \end{bmatrix} [G^P] \delta(a^P) \quad (F.42)$$

Substituting Eqn (F.42) into Eqn (F.38a) results in an expression for  $[K\sigma^P]$ :

$$([K\sigma^P])_{(12 \times 12)} = \int_A ([G^P]^T)_{(12 \times 4)} \begin{bmatrix} N_x & N_{xy} & 0 & 0 \\ N_y & N_{xy} & 0 & 0 \\ 0 & 0 & N_x & N_{xy} \\ 0 & 0 & N_y & N_{xy} \end{bmatrix} ([G^P])_{(4 \times 12)} dA \quad (F.43)$$

With the same type of derivation used to find  $[K\sigma^p]$ ,  $[K\sigma^b]$  can be found. The resulting expression for  $[K\sigma^b]$  is:

$$[K\sigma^b]_{(12 \times 12)} = \int_A [G^b]_{(12 \times 2)}^T \begin{bmatrix} N_x & N_{xy} \\ N_{xy} & N_y \end{bmatrix} [G^b]_{(2 \times 12)} dA \quad (F.44)$$

With Eqns (F.43) and (F.44), the full expression for the initial stress matrix can be written as:

$$[K\sigma]_{(24 \times 24)} = \begin{bmatrix} [K\sigma^p]_{(12 \times 12)} & 0 \\ 0 & [K\sigma^b]_{(12 \times 12)} \end{bmatrix} \quad (F.45)$$

## Appendix G: Using STAGSC-1

The STAGSC-1 finite element code was originally developed for use on the Cyber. The 1986 STAGSC-1 version is capable of running both on the Cyber and VMS based systems such as Digital Equipment's VAX 11/785 or VAX 8550. When running STAGS on these machines, because of the limited time allowed for interactive use, each model must be submitted in batch form. Fig G.1 demonstrates a typical .COM file that will run STAGS in batch form. Fig G.2 shows the proper VMS syntax needed to submit the .COM file to the STAGS queue.

### SUBFILE.COM:

```
$ SET VERIFY
$ SET DEFAULT GAE89D:[SSCHIMME.STAGS]
$ ASSIGN FILENAME.INP FOR005
$ ASSIGN FILENAME.OUT1 FOR006
$ ASSIGN FILENAME.MOD FOR021
$ ASSIGN FILENAME.DAT FOR002
$ ASSIGN FILENAME.INP FOR025
$ RUN STAGS$DIR:STAGS1
$ COPY FILENAME.DAT FILENAME.DAT
$ ASSIGN FILENAME.BIN FOR005
$ ASSIGN FILENAME.OUT2 FOR006
$ ASSIGN FILENAME.RST FOR020
$ ASSIGN FILENAME.SOD FOR022
$ RUN STAGS$DIR:ET
$ DEL FOR009.DAT
$ PUR SUBFILE.COM
$ EXIT
```

Fig G.1 Typical Command File for Batch Execution

```
$ SUBMIT/QUE=SYS$STAGS/NOTIFY/NAME=STAGS/KEEP/LOG=GAE89D:  
[SSCHIMME.STAGS]FILENAME.LOG/NOPRINTER SUBFILE.COM
```

Fig G.2 VMS Syntax for Submitting Batch File

Unlike the STAGS Cyber version, the VMS based code requires two separate files for STAGS to run. The first file is called the .INP file. It is exactly the same as the input deck file for the Cyber based code. The second file is called the .BIN file. This file controls the STAGS2 phase for the solution algorithm. Examples of both files are given in Figs G.3 through G.10. The reader is suggested to refer heavily to Ref 27 while looking at these examples for clarification.

Some of the models used for STAGS required tremendously large amount of CPU time (100000+ CPU seconds). On the D1 record, the user specifies the amount of CPU time STAGS is supposed to run for the model. The author normally used 90000 (because of the combination of using 0.5" mesh and using the QUAF 411 element) as most of the models considered large rotations ( $\approx 30^\circ$ ). These large rotations required a substantial number iterations and cutting the load step in order to converge to a solution. This tends to drive the required CPU time for solution upward in a somewhat exponential manner. STAGS allows for only 5 characters for

S121.INP:

NONLINEAR ANALYSIS, 12" PANEL, NO CUTOUT	\$A1
3,1,1,1,0,0,1	\$B1
1	\$B2
1,0,1	\$B3
.0001,.0002,.04	\$C1
0,90000,40,-20,-1,.00001	\$D1
25,25	\$F1
1	\$I1
20.461E6,0.0205,.8638E6,1.,1.,1.3404E6,1.	\$I2
1,1,8	\$K1
1,.005,0.0,1	\$K2
1,.005,-45.0,0	\$K2
1,.005,45.0,0	\$K2
1,.005,90.0,1	\$K2
1,.005,90.0,1	\$K2
1,.005,45.0,1	\$K2
1,.005,-45.0,1	\$K2
1,.005,0.0,1	\$K2
5	\$M1
0.0,12.0,0.0,57.2958,12.0	\$M2A
1	\$M5
411	\$N1
0,0,0,0,0	\$P1
100,000	\$P2
100,100	\$P2
000,000	\$P2
100,100	\$P2
1	\$Q1
1,1	\$Q2
1.0,-1,1,1,0	\$Q3
1,0,0,0,0,1	\$R1

S121.BIN

NONLINEAR ANALYSIS, 12" PANEL, NO CUTOUT	\$P1
.0001,.0005,.04	\$P2
0,90000,40,-20,-1,.00001	\$P3
1	\$P4

Fig G.3 Input Deck for 12x12 Panel, Simply Supported,  
No Cutout

S122.INP:

NONLINEAR ANALYSIS, 12" PANEL, 4" CUTOUT, CENTERED	\$A1
3,1,1,1,0,0,1	\$B1
1	\$B2
1,0,1	\$B3
.0001,.0002,.04	\$C1
0,90000,40,-20,-1,.00001	\$D1
25,25	\$F1
1	\$I1
20.461E6,0.0205,.8638E6,1.,1.,1.3404E6,1.	\$I2
1,1,8	\$K1
1,.005,0.0,1	\$K2
1,.005,-45.0,0	\$K2
1,.005,45.0,0	\$K2
1,.005,90.0,1	\$K2
1,.005,90.0,1	\$K2
1,.005,45.0,1	\$K2
1,.005,-45.0,1	\$K2
1,.005,0.0,1	\$K2
5	\$M1
0.0,12.0,0.0,57.2958,12.0	\$M2A
1	\$M5
411,0,0,1	\$N1
9,17,9,17	\$N8
0,0,0,0,0	\$P1
100,000	\$P2
100,100	\$P2
000,000	\$P2
100,100	\$P2
1	\$Q1
1,1	\$Q2
1.0,-1,1,1,0	\$Q3
1,0,0,0,0,1	\$R1

S122.BIN

NONLINEAR ANALYSIS, 12" PANEL, 4" CUTOUT, CENTERED	\$P1
.0001,.0005,.04	\$P2
0,90000,40,-20,-1,.00001	\$P3
1	\$P4

Fig G.4 Input Deck for 12x12 Panel, Simply Supported,  
4" Cutout, Centered

S123.INP:

NONLINEAR ANALYSIS, 12" PANEL, 4" CUTOUT, 1" OFFSET	\$A1
3,1,1,1,0,0,1	\$B1
1	\$B2
1,0,1	\$B3
.0001,.0002,.04	\$C1
0,90000,40,-20,-1,.00001	\$D1
25,25	\$F1
1	\$I1
20.461E6,0.0205,.8638E6,1.,1.,1.3404E6,1.	\$I2
1,1,8	\$K1
1,.005,0.0,1	\$K2
1,.005,-45.0,0	\$K2
1,.005,45.0,0	\$K2
1,.005,90.0,1	\$K2
1,.005,90.0,1	\$K2
1,.005,45.0,1	\$K2
1,.005,-45.0,1	\$K2
1,.005,0.0,1	\$K2
5	\$M1
0.0,12.0,0.0,57.2958,12.0	\$M2A
1	\$M5
411,0,0,1	\$N1
9,17,7,15	\$N8
0,0,0,0,0	\$P1
100,000	\$P2
100,100	\$P2
000,000	\$P2
100,100	\$P2
1	\$Q1
1,1	\$Q2
1.0,-1,1,1,0	\$Q3
1,0,0,0,0,1	\$R1

S121.BIN

NONLINEAR ANALYSIS, 12" PANEL, 4" CUTOUT, 1" OFFSET	\$P1
.0001,.0005,.04	\$P2
0,90000,40,-20,-1,.00001	\$P3
1	\$P4

Fig G.5 Input Deck for 12x12 Panel, Simply Supported,  
4" Cutout, 1" Offset



S82.INP:

NONLINEAR ANALYSIS, 8" PANEL, 4" CUTOUT	\$A1
3,1,1,1,0,0,1	\$B1
1	\$B2
1,0,1	\$B3
.0001,.0002,.04	\$C1
0,90000,40,-20,-1,.00001	\$D1
25,17	\$F1
1	\$I1
20.461E6,0.0205,.8638E6,1.,1.,1.3404E6,1.	\$I2
1,1,8	\$K1
1,.005,0.0,1	\$K2
1,.005,-45.0,0	\$K2
1,.005,45.0,0	\$K2
1,.005,90.0,1	\$K2
1,.005,90.0,1	\$K2
1,.005,45.0,1	\$K2
1,.005,-45.0,1	\$K2
1,.005,0.0,1	\$K2
5	\$M1
0.0,12.0,0.0,38.1972,12.0	\$M2A
1	\$M5
411,0,0,1	\$N1
9,17,5,13	\$N8
0,0,0,0,0	\$P1
100,000	\$P2
100,100	\$P2
000,000	\$P2
100,100	\$P2
1	\$Q1
1,1	\$Q2
1.0,-1,1,1,0	\$Q3
1,0,0,0,0,1	\$R1

S82.BIN

NONLINEAR ANALYSIS, 8" PANEL, 4" CUTOUT	\$P1
.0001,.0005,.04	\$P2
0,90000,40,-20,-1,.00001	\$P3
1	\$P4

Fig G.6 Input Deck for 8x12 Panel, Simply Supported,  
4" Cutout, Centered

F122.INP:

NONLINEAR ANALYSIS, 12" PANEL, 4" CUTOUT, FREE EDGES	\$A1
3,1,1,1,0,0,1	\$B1
1	\$B2
1,0,1	\$B3
.0001,.0002,.04	\$C1
0,90000,40,-20,-1,.00001	\$D1
23,25	\$F1
1	\$I1
20.461E6,0.0205,.8638E6,1.,1.,1.3404E6,1.	\$I2
1,1,8	\$K1
1,.005,0.0,1	\$K2
1,.005,-45.0,0	\$K2
1,.005,45.0,0	\$K2
1,.005,90.0,1	\$K2
1,.005,90.0,1	\$K2
1,.005,45.0,1	\$K2
1,.005,-45.0,1	\$K2
1,.005,0.0,1	\$K2
5	\$M1
0.0,11.0,0.0,57.2958,12.0	\$M2A
1	\$M5
411,0,0,1	\$N1
8,16,9,17	\$N8
0,0,0,0,0	\$P1
100,000	\$P2
111,111	\$P2
000,000	\$P2
111,111	\$P2
1	\$Q1
1,1	\$Q2
1.0,-1,1,1,0	\$Q3
1,0,0,0,0,1	\$R1

F122.BIN

NONLINEAR ANALYSIS, 12" PANEL, 4" CUTOUT, CENTERED	\$P1
.0001,.0005,.04	\$P2
0,90000,40,-20,-1,.00001	\$P3
1	\$P4

Fig G.7 Input Deck for 12x11 Panel, Unsupported,  
4" Cutout, Centered

F82.INP:

NONLINEAR ANALYSIS, 8" PANEL, 4" CUTOUT, CENTERED	\$A1
3,1,1,1,0,0,1	\$B1
1	\$B2
1,0,1	\$B3
.0001,.0002,.04	\$C1
0,90000,40,-20,-1,.00001	\$D1
23,17	\$F1
1	\$I1
20.461E6,0.0205,.8638E6,1.,1.,1.3404E6,1.	\$I2
1,1,8	\$K1
1,.005,0.0,1	\$K2
1,.005,-45.0,0	\$K2
1,.005,45.0,0	\$K2
1,.005,90.0,1	\$K2
1,.005,90.0,1	\$K2
1,.005,45.0,1	\$K2
1,.005,-45.0,1	\$K2
1,.005,0.0,1	\$K2
5	\$M1
0.0,11.0,0.0,38.1972,12.0	\$M2A
1	\$M5
411,0,0,1	\$N1
8,16,5,13	\$N8
0,0,0,0,0	\$P1
100,000	\$P2
111,111	\$P2
000,000	\$P2
111,111	\$P2
1	\$Q1
1,1	\$Q2
1.0,-1,1,1,0	\$Q3
1,0,0,0,0,1	\$R1

F82.BIN

NONLINEAR ANALYSIS, 8" PANEL, 4" CUTOUT, CENTERED	\$P1
.0001,.0005,.04	\$P2
0,90000,40,-20,-1,.00001	\$P3
1	\$P4

Fig G.8 Input Deck for 8x11 Panel, Unsupported,  
4" Cutout, Centered

S121-I.INP:

NONLINEAR ANALYSIS, 12" PANEL, NO CUTOUT	\$A1
3,1,1,1,0,0,1	\$B1
1	\$B2
1,0,1	\$B3
.0001,.0002,.04	\$C1
0,90000,40,-20,-1,.00001	\$D1
25,25	\$F1
1	\$I1
20.461E6,0.0205,.8638E6,1.,1.,1.3404E6,1.	\$I2
1,1,8	\$K1
1,.005,0.0,1	\$K2
1,.005,-45.0,0	\$K2
1,.005,45.0,0	\$K2
1,.005,90.0,1	\$K2
1,.005,90.0,1	\$K2
1,.005,45.0,1	\$K2
1,.005,-45.0,1	\$K2
1,.005,0.0,1	\$K2
5	\$M1
0.0,12.0,0.0,57.2958,12.0	\$M2A
1,1	\$M5
6.0,28.6479,4.0,19.0986,.005	\$M6
411	\$N1
0,0,0,0,0	\$P1
100,000	\$P2
100,100	\$P2
000,000	\$P2
100,100	\$P2
1	\$Q1
1,1	\$Q2
1.0,-1,1,1,0	\$Q3
1,0,0,0,0,1	\$R1

S121I.BIN

NONLINEAR ANALYSIS, 12" PANEL, NO CUTOUT	\$P1
.0001,.0005,.04	\$P2
0,90000,40,-20,-1,.00001	\$P3
1	\$P4

Fig G.9 Input Deck for 12x12 Panel, Simply Supported,  
No Cutout, with Imperfection

S121V.INP:

NONLINEAR ANALYSIS, 12" PANEL, NO CUTOUT	\$A1
3,1,1,1,0,0,1	\$B1
1	\$B2
1,0,1	\$B3
.0001,.0002,.04	\$C1
0,90000,40,-20,-1,.00001	\$D1
25,25	\$F1
1	\$I1
20.461E6,0.0205,.8638E6,1.,1.,1.3404E6,1.	\$I2
1,1,8	\$K1
1,.005,0.0,1	\$K2
1,.005,-45.0,0	\$K2
1,.005,45.0,0	\$K2
1,.005,90.0,1	\$K2
1,.005,90.0,1	\$K2
1,.005,45.0,1	\$K2
1,.005,-45.0,1	\$K2
1,.005,0.0,1	\$K2
5	\$M1
0.0,12.0,0.0,5757.2958,12.0	\$M2A
1	\$M5
411	\$N1
0,0,0,0,0	\$P1
100,000	\$P2
110,100	\$P2
000,000	\$P2
110,100	\$P2
1	\$Q1
1,1	\$Q2
1.0,-1,1,1,0	\$Q3
1,0,0,0,0,1	\$R1

S121V.BIN

NONLINEAR ANALYSIS, 12" PANEL, NO CUTOUT	\$P1
.0001,.0005,.04	\$P2
0,90000,40,-20,-1,.00001	\$P3
1	\$P4

Fig G.10 Input Deck for 12x12 Panel, Simply Supported,  
No Cutout, with V Free

NSEC variable. Thus, the user cannot specify more than 99999 CPU seconds. In this case, the STAGS restart capability must be used. Fig G.11 demonstrates the .COM file needed to accomplish a STAGS restart.

SUBFILE.COM:

```
$ SET VERIFY
$ SET DEFAULT GAE89D:[SSCHIMME.STAGS]
$ ASSIGN FILENAME.BIN FOR005
$ ASSIGN FILENAME.OUT3 FOR006
$ COPY FILENAME.SOD FILENAME.RST
$ COPY FILENAME.DAT FOR002
$ ASSIGN FILENAME.RST FOR020
$ ASSIGN FILENAME.SOD FOR022
$ RUN STAGS$DIR:ET
$ PUR SUBFILE.COM
$ EXIT
```

Fig G.11 Typical Command File for Batch Restart

Besides a new .COM file, the .BIN file needs to be modified. In the C1 deck, the starting load is set to correspond to the final load completed in the prior run. It is strongly recommended that the user chooses not the last load step but the second to the last step. This ensures that the model, when restarted, will essentially follow the same equilibrium path before STAGS stopped execution. The increment should also be matched to a more appropriate value,

usually the increment last being used by STAGS before execution was terminated. The step number in the D1 deck is changed to match the incremental load value being used as a starting point for the restart in deck C1. Fig G.12 demonstrates a .BIN file modified for a STAGS restart. Submit the modified .BIN file through the .COM file as before (See Fig G.2).

S122.BIN:

NONLINEAR ANALYSIS, 12" PANEL, 4" CUTOUT, RESTART	\$P1
3.9217E-04.,00001,.04	\$P2
27,75000,40,-20,-1,.00001	\$P3
1	\$P4

Fig G.12 Modified Control File for Restart Execution

## Appendix H: Miscellaneous Information

The following are tabulated results for the STAGS and SHELL analytical models and the experimental results.

NOTE: SS = Simply Supported, US = Unsupported, NC = No Cutout, CC = Centered Cutout, OC = Offcenter Cutout.

Table H.1 Individual Panel Results, STAGS

Collapse Load, lbs

Panels	Perfect	Imperfect	V Free
12", SS, NC	5060	4950	4754
12" SS, CC	2521	N/A	N/A
12" SS, OC	2561	N/A	N/A
8", SS, NC	3761	3700	3174
8", SS, CC	2178	N/A	N/A
8", SS, OC	2465	N/A	N/A
12", US, NC	2298	2260	N/A
12", US, CC	1186	N/A	N/A
12", US, OC	1284	N/A	N/A
8", US, NC	1382	1350	N/A
8", US, CC	323	N/A	N/A
8", US, OC	460	N/A	N/A



Table H.2 Individual Panel Results, STAGS

Top Edge Displacement, in

Panels	Perfect	Imperfect	V Free
12", SS, NC	.016433	.01842	.015437
12" SS, CC	.014823	N/A	N/A
12" SS, OC	.014535	N/A	N/A
8", SS, NC	.018334	.019454	.015457
8", SS, CC	.021156	N/A	N/A
8", SS, OC	.026007	N/A	N/A
12", US, NC	.0068329	.011109	N/A
12", US, CC	.0088393	N/A	N/A
12", US, OC	.0087854	N/A	N/A
8", US, NC	.0080207	.027807	N/A
8", US, CC	.0087811	N/A	N/A
8", US, OC	.0071766	N/A	N/A

Table H.3 Individual Panel Results, SHELL

Collapse Load, lbs

Panels	Perfect
12", US, NC	
12", US, CC	
12", US, OC	
8", US, NC	
8", US, CC	312.8
8", US, OC	

Table H.4 Individual Panel Results, SHELL

Top Edge Displacement, in

Panels	Perfect
12", US, NC	
12", US, CC	
12", US, OC	
8", US, NC	
8", US, CC	.0098
8", US, OC	

Table H.5 Individual Panel Results, Experimental

Panels	Collapse Load, lb	Displacement, in
12", SS, NC	4851	.0219
12" SS, CC	2392	.0212
12" SS, OC	2406	.016
8", SS, NC	3473	.0242
8", SS, CC	1918	.02165
8", SS, OC	1619	.022
12", US, NC	1890	.0291
12", US, CC	1093	.0172
12", US, OC	1127	.0182
8", US, NC	1311	.0279
8", US, CC	300	.0123
8", US, OC	403	.0099

VITA

Scott A. Schimmels [REDACTED]  
[REDACTED] [REDACTED]  
[REDACTED]

[REDACTED] entered the United States Air Force Academy where he received a Bachelor of Science Degree in Engineering Mechanics (concentration in Materials) in 1984. He was stationed at Eglin AFB in July 1984 and worked as a Munitions Design Engineer in the Air Force Armament Lab (AFATL). After serving 4 years at Eglin AFB, he was accepted into the graduate Aeronautical Engineering program at the Air Force Institute of Technology in May 1988.

[REDACTED] [REDACTED]  
[REDACTED]

# REPORT DOCUMENTATION PAGE

Form Approved  
OMB No. 0704-0188

1a. REPORT SECURITY CLASSIFICATION <b>UNCLASSIFIED</b>		1b. RESTRICTIVE MARKINGS	
2a. SECURITY CLASSIFICATION AUTHORITY		3. DISTRIBUTION / AVAILABILITY OF REPORT Approved for public release; distribution unlimited	
2b. DECLASSIFICATION / DOWNGRADING SCHEDULE			
4. PERFORMING ORGANIZATION REPORT NUMBER(S)  AFIT/GAE/ENY/89D-33		5. MONITORING ORGANIZATION REPORT NUMBER(S)	
6a. NAME OF PERFORMING ORGANIZATION  SCHOOL OF ENGINEERING	6b. OFFICE SYMBOL (If applicable) AFIT/ENY	7a. NAME OF MONITORING ORGANIZATION	
6c. ADDRESS (City, State, and ZIP Code)  Air Force Institute of Technology Wright-Patterson AFB OH 45433-6583		7b. ADDRESS (City, State, and ZIP Code)	
8a. NAME OF FUNDING / SPONSORING ORGANIZATION  AFOSR	8b. OFFICE SYMBOL (If applicable)	9. PROCUREMENT INSTRUMENT IDENTIFICATION NUMBER	
8c. ADDRESS (City, State, and ZIP Code)  Bolling AFB Wash DC		10. SOURCE OF FUNDING NUMBERS	
		PROGRAM ELEMENT NO.	PROJECT NO.
		TASK NO.	WORK UNIT ACCESSION NO.
11. TITLE (Include Security Classification) (U) INVESTIGATION OF COLLAPSE CHARACTERISTICS OF CYLINDRICAL COMPOSITE PANELS WITH LARGE CUTOUTS			
12. PERSONAL AUTHOR(S) Scott A. Schimmels, Capt, USAF			
13a. TYPE OF REPORT MS Thesis	13b. TIME COVERED FROM _____ TO _____	14. DATE OF REPORT (Year, Month, Day) 1989 December	15. PAGE COUNT 316
16. SUPPLEMENTARY NOTATION			
17. COSATI CODES		18. SUBJECT TERMS (Continue on reverse if necessary and identify by block number)	
FIELD	GROUP	SUB-GROUP	
II	04		
20	II		
		Composites Cylindrical Panels Cutouts	
		Finite Elements Nonlinear Analysis Transverse Shear	
19. ABSTRACT (Continue on reverse if necessary and identify by block number)			
<p>Thesis Advisor: Dr Anthony Palazotto Professor Department of Aeronautical and Astronautical Engineering</p> <p>ABSTRACT ON BACK</p>			
20. DISTRIBUTION / AVAILABILITY OF ABSTRACT <input checked="" type="checkbox"/> UNCLASSIFIED/UNLIMITED <input type="checkbox"/> SAME AS RPT. <input type="checkbox"/> DTIC USERS		21. ABSTRACT SECURITY CLASSIFICATION <b>UNCLASSIFIED</b>	
22a. NAME OF RESPONSIBLE INDIVIDUAL Dr Anthony Palazotto		22b. TELEPHONE (Include Area Code) (513) 255-3517	22c. OFFICE SYMBOL AFIT/ENY

Block 19 Abstract

↙  
In order to better understand the collapse properties of composite shells, an analysis of cylindrical panels with large cutouts (11-17% of surface area) was conducted with two finite element codes (STAGSC-1 and SHELL). These results were then compared to experimental findings. Existence of cutout, eccentricity of cutout, boundary conditions, and panel width are varied to see how each affected the collapse load. In addition, the release of residual strain due to placing the cutout within the panel was evaluated.

It was found that placing a cutout in the panel and/or removing the vertical supports reduced the total collapse load by at least 50%. Surface imperfections were seen to reduce the collapse load, but more importantly these imperfections accurately predicted the nonlinear response of the shell. STAGSC-1 accurately predicted the composite panels' response to axial compression. Transverse shear was seen to be important if the panels' free edges underwent 15-17% or more of rotation. Hence the SHELL program gave better results than STAGSC-1 for those panels that saw rotations greater than 17%. The residual stress test showed there was a measureable change in strain due to cutting the panel. However, the magnitude of this change is minimal when compared to the total collapse load of the shell. *These findings*